Raman Scattering and Optical Spectroscopies of Individual Pristine and Functionalized Carbon Nanotubes

Huy-Nam Tran

Collège Doctoral du Languedoc-Roussillon

THÈSE

Pour obtenir le grade de

Docteur

Délivré par **Université de Montpellier**

Préparée au sein de l'école doctorale **I2S**
Et de l'unité de recherche **Laboratoire Charles Coulomb**

Spécialité : **Physique**

Présentée par **Huy Nam TRAN**

RAMAN SCATTERING AND OPTICAL SPECTROSCOPIES OF INDIVIDUAL PRISTINE AND FUNCTIONALIZED CARBON NANOTUBES

Soutenue le 15 décembre 2015 devant le jury composé de

M. Ahmed-Azmi ZAHAB, Prof., Université de Montpellier	Directeur de thèse
M. Matthieu PAILLET, Dr., Université de Montpellier	Co-Directeur de thèse
M. Pierre PETIT, Dr., Université de Strasbourg	Rapporteur
M. Valentin N. POPOV, Prof., Université de Sofia	Rapporteur
M. Alfonso SAN MIGUEL, Prof., Université Lyon 1	Examinateur
Mme. Lucyna FIRLEJ, Prof., Université de Montpellier	Examinateur
M. Thibaut JARROSSON, Dr., ENSC Montpellier	Invité

UNIVERSITÉ MONTPELLIER

ACKNOWLEDGEMENT

This work was performed in the team “Structures Carbonées de Basse Dimensionnalité” of the Laboratoire Charles Coulomb of the University of Montpellier. I would like to thank everyone who helped me in past three years.

First of all, I would like to thank my supervisors, Prof. Ahmed-Azmi Zahab, and Dr. Matthieu Paillet for their support and guidance during my PhD thesis. I am also grateful to Dr. Jean-Louis Sauvajol for his valuable advices and corrections of my manuscript.

I would like to thank my jury members, Prof. Valentin N. Popov, Dr. Pierre Petit, Prof. Alfonso San Miguel, Prof. Lucyna Firlej and Dr. Thibaut Jarrosson who agreed to evaluate my work.

I reserve my thanks for Dr. Jean-Roch Huntzinger and Dr. Antoine Tiberj for the help in the use of the “Octave software” for the fit of the Raman excitation profiles.

I am thankful for the helpful discussion with Dr. Dmitry Levshov and Dr. Thierry Michel.

I am also thanks to the colleagues of technical staff of the lab, namely: David Maurin, Raymond Aznar, Said Tahir for their help during the Raman/absorption experiments and sample preparations.

I want to thank Adoration Gabillard, Tina Rabeharivelo and Jean-Christophe Art who gave me the instructions about administrative protocols.

Many thanks are due to the all collaborators, without them this thesis was impossible. The suspended carbon nanotubes were prepared by Dr. Xuan Tinh Than. Dr. Jean-Christophe Blancon and his colleagues of the “Institut Lumière et Matière” of the University of Lyon performed the absorption measurements on the carbon nanotubes. I would like thank Dr. Raul Arenal of the University of Aragon for the electron microscopy and electron diffraction experiments on the carbon nanotubes. I would like thank Dr. Jean-Pierre Lère-Porte, Dr. Thibaut Jarrosson for the chemical functionalization of DWNTs with diazonium group, and Dr. Bortolamiol Tifania and Dr. Emmanuel Flahaut for the chemical functionalization of DWNTs with FITC molecules. I would like to thank other PhD students for the friendship in past three years.

I would like to thank the ANR project “Gambit” for the financial support of my research activities in this PhD work.

I want to thank Chau's family for their helps during three years in Montpellier.

A special acknowledgement goes to my girlfriend, Hoa, who loved and supported me during the periods of my PhD.

Finally, I am forever grateful to my parents for their immense love, understanding and encouragement throughout my life. All the support that they have provided me over the years was the greatest gift in the world.

I would like to end with my special thanks in advance to anyone who is reading this thesis for your patience and I hope you will enjoy it.

Huy Nam Tran

ABSTRACT

This work concerns the study of mono- and double-walled carbon nanotubes. It contains two distinct parts: (i) the first part is devoted to the understanding of the intrinsic optical and phonon properties of individual carbon nanotubes; (ii) the second part reports an experimental investigation of the properties of covalently and non-covalently functionalized double-walled carbon nanotubes.

Concerning the study of the intrinsic properties of the individual carbon nanotubes, new information was obtained by coupling Raman spectroscopy data, including the measurement of the excitation profiles of different Raman-active modes, with optical absorption and electronic diffraction data. From a general point of view, our approach put in evidence the complementarity of the Raman spectroscopy and electronic diffraction for “the most probable” assignment of the structure of the nanotubes.

Among the results obtained on individual single-walled carbon nanotubes (SWNTs), one can underline the confirmation of the excitonic character of the optical transitions by combining optical absorption and Raman excitation profiles on the same nanotubes, and the evidence of an unexpected behavior of the relative intensities of the LO and TO components of the G-modes. The study of the index-identified individual double-walled carbon nanotubes has permitted to understand the role of the inter-walls distance in the frequency shifts of the radial breathing-like modes (RBLM) and G-modes, by associating a given inter-walls distance to a negative (positive) internal pressure when this distance is larger (smaller) than 0.34 nm. On the other hand, the role of quantum interferences in the evolution with the excitation energy of the intensities of the LO and TO components of the G-modes was clearly identified. Finally, the assignment of the optical transitions, measured by absorption spectroscopy, of index-identified DWNTs was proposed.

The study of the properties of functionalized DWNTs was performed by combining Raman spectroscopy, UV-visible-NIR absorption and photoluminescence (PL), including maps of photoluminescence excitation (PLE), on suspensions of DWNTs before and after functionalization: (i) covalently by using diazonium, (ii) covalently and non-covalently (π stacking) by using dye molecules. This work is a contribution to the debate on an essential question for the use of the DWNTs in opto-electronic devices, namely: “Do the DWNTs they luminesce? And if yes, what is the origin of the luminescence?". The presence of photoluminescence in our samples of DWNTs was established, and the study of its evolution with various kinds and degrees of functionalization states that PL can only result from inner tubes (intrinsic PL of DWNTs), or from SWNTs generated by the extrusion of the internal tubes of DWNTs during the preparation of the suspensions. On the other hand, one must emphasize the evidence of an energy transfer from the dye molecules towards the internal tube when such molecules are covalently grafted on the outer tube.

RÉSUMÉ

Ce travail, qui concerne l'étude des nanotubes de carbone mono- et double parois, comporte deux volets distincts: (i) une compréhension des propriétés optiques et phononiques intrinsèques des nanotubes de carbone individuels, (ii) une approche expérimentale originale des propriétés des nanotubes de carbone double-parois fonctionnalisés de manières covalente et non-covalente.

Concernant l'étude des propriétés intrinsèques des nanotubes de carbone individuels, des informations originales ont été obtenues en couplant des résultats de spectroscopie Raman, incluant la mesure des profils d'excitation des différents modes, avec des données d'absorption optique et de diffraction électronique. De manière générale, l'approche que nous avons développée a mis en avant la complémentarité de la spectroscopie Raman et de la diffraction électronique pour l'identification « la plus probable » de la structure de chaque tube.

Parmi les résultats obtenus sur les tubes mono-paroi (SWNTs) individuels, on peut souligner la confirmation originale du caractère excitonique des transitions optiques obtenue en combinant des données d'absorption et de profils d'excitation Raman, ainsi que la mise en évidence d'un comportement inattendu des rapports d'intensité des composantes LO et TO des modes G.

L'étude des nanotubes de carbone double-parois (DWNTs) individuels de structures clairement identifiées a permis de comprendre le rôle de la distance inter-tubes dans les déplacements en fréquence des modes Raman (modes de respiration (RBLM) et modes G), en associant à une distance inter-tube donnée une pression interne négative (positive) quand cette distance est supérieure (inférieure) à 0.34 nm. D'autre part, le rôle des effets d'interférences quantiques dans l'évolution avec l'énergie d'excitation des intensités des composantes LO et TO des modes G a été clairement identifié. Enfin, une attribution de l'origine des transitions optiques, mesurées par spectroscopie d'absorption, de différents DWNTs a été proposée.

L'étude des propriétés de DWNTs fonctionnalisés a été réalisée en couplant des expériences de spectroscopie Raman, d'absorption UV-visible-NIR et de photoluminescence (PL), incluant les cartes d'excitation de la photoluminescence (PLE), sur des suspensions de DWNTs avant et après fonctionnalisation, (i) covalente via un groupement diazonium, (ii) covalente et non-covalente (π stacking) par un colorant. Ce travail présente une contribution au débat sur une question essentielle pour l'utilisation des DWNTs dans des dispositifs opto-électroniques, à savoir : « les DWNTs luminescent-ils ? Et si oui, quelle est l'origine de la luminescence ? ». La présence de photoluminescence dans nos échantillons de DWNTs est établie, et l'étude de son évolution avec différents types et degrés de fonctionnalisation démontre qu'elle ne peut provenir que des tubes internes des DWNTs (PL intrinsèque aux DWNTs), ou de SWNTs générés par l'extrusion des tubes internes de DWNTs durant la préparation des suspensions. D'autre part, on peut souligner la mise en évidence d'un transfert d'énergie du colorant vers le tube interne quand le colorant est greffé de manière covalente sur la tube externe.

Contents

MANUSCRIPT PRESENTATION

Carbon-based nanomaterials are ubiquitous materials in modern day condensed matter physics and materials science. Among them, carbon nanotubes have been considered as one of the promising candidates for realistic applications in mechanics [1-3], electronics [4-6], photonics and optoelectronics [7] due to their unique and fascinating properties. In addition, carbon nanotubes provide new paradigms to investigate the fundamental properties of one-dimensional systems. Indeed, carbon nanotubes represent an intriguing nanoscale laboratory for studying fundamental quantum behaviors, quasi-particle interactions, and the limit of the approximations we use for understanding them. Although a huge number of investigations about carbon nanotubes have been reported, the understanding of some specific properties, including optical and phonon properties, has to be precised.

The general objective of this work is to investigate the properties of individual single-walled carbon nanotubes (SWNTs) and double-walled carbon nanotubes (DWNTs). The manuscript is divided in two parts: A) the first part is devoted to the understanding of the intrinsic optical and phonon properties of individual and isolated index-identified carbon nanotubes; B) the second part reports experimental investigations of the properties of covalently and non-covalently functionalized individual double-walled carbon nanotubes.

The manuscript is organized in six chapters.

The first chapter gives general information on the structure, electronic and optical properties of carbon nanotubes. A state of art concerning the phonons properties in SWNTs and DWNTs is summarized in chapter 2. Both chapters provide all the information that are necessary to know for the understanding of the experimental results reported in the present work.

The part A of this manuscript is devoted to the investigation of intrinsic properties of individual SWNTs and DWNTs.

The chapter 3 is devoted to the study of intrinsic properties of individual free-standing semiconducting SWNTs by combining the information obtained by Raman resonance scattering, optical absorption, and electron diffraction measurements. The information derived from Raman and electron diffraction measurements allow us to assign the chiral indices (n,m) of individual SWNTs. These assignments are used to precise the understanding of the optical absorption data measured by spatial modulation spectroscopy.

In the following, we focus on the information which can be derived from the analysis of the Raman excitation profiles (REPs). We detail the results obtained on two individual free-standing semiconducting SWNTs. Firstly, by combining optical absorption data and REPs measured on the (23,7) SWNT, one discuss the nature of the optical transition: band-to-band or excitonic.

Secondly, we discuss the effects of quantum interferences on the REPS of the Raman-active modes of the (30,1) SWNT. Indeed, in this tube, the proximity of the $E_{33}+\hbar\omega_G$ and E_{44} transitions ($\hbar\omega_G$ is the energy of the G-modes) is one of the conditions which allow the observation of interference effects. Finally, the TO/LO intensity ratio is measured in several SWNTs around different optical transitions.

The chapter 4 is the counterpart of chapter 3 for individual free-standing DWNTs.

First, we detail an approach to evaluate the diameters of the inner and outer tubes from the knowledge of the experimental in-phase and out-of-phase radial breathing-like modes (RBLMs). On this basis, the structural assignments of inner and outer tubes are derived thanks to additional electron diffraction data. These assignments are used to understand the absorption data measured on several DWNTs by spatial modulation spectroscopy. For the first time, to the best of our knowledge, quantum interferences effects are put in evidence on the REPs of the (16,12)@(27,10) DWNT.

The part B of this manuscript is mainly devoted to a fundamental debate in DWNT: “Do the DWNTs luminesce? And if yes, what is the origin of the luminescence?" The investigation of functionalized individual DWNTs is a method to answer at this question.

In the chapter 5, we report and discuss Raman, optical absorption and photoluminescence data measured on aqueous suspensions of pristine and functionalized individual SWNTs and DWNTs wrapped in surfactants. Covalent functionalization, by using diazonium salts, and covalent and non-covalent functionalization, by using dye molecules, have been studied. A complete characterization of the samples is reported. The nature and the degree of functionalization of the outer tubes of DWNTs are identified by combining Raman spectroscopy and UV-VIS-NIR absorption. In the following, the origin of the PL which is observed in our suspensions of DWNTs is discussed. On the other hand, the features of the energy transfer of the dye molecules towards the internal tubes of DWNTs are investigated.

Finally, the chapter 6 presents the overall conclusions of this works and provides suggestions for future research on SWNTs and DWNTs.

CHAPTER 1 : AN INTRODUCTION TO THE PROPERTIES OF CARBON NANOTUBES

Carbon-based nanostructures are considered as one of the most important classes of materials. Carbon-based nanostructures exhibit different dimensionalities: fullerene (0D), nanotube (1D), graphene (2D), nano-diamond (3D). These materials are expected to play an important role in nanoscience and nanotechonology in the 21st century due to their extraordinary chemical and physical properties.

Carbon nanotubes (CNTs), firstly synthesized and observed by Iijima in 1991 [8], will be concerned in this thesis. During the last twenty years, a lot of theoretical and experimental investigations were performed on CNTs in order to study their unique properties and to develop their potential applications.

Carbon nanotubes such as double-walled (DWNTs), triple-walled (TWNTs), and multi-walled carbon nanotubes (MWNTs) are structures composed of coaxial two single-walled carbon nanotubes (SWNT) for DWNTs, three coaxial SWNTs for TWNTs…, or M coaxial SWNTs for MWNTs. Because the basic building-block of all the CNTs is a single-walled carbon nanotube, it is important to review the SWNT's properties.

In the part A of this chapter, the main fundamental properties of SWNTs are summarized:

- The atomic structure and geometry of SWNTs are described.

-The electronic band structure of SWNTs, calculated within a tight binding model, is presented. It can be reminded that, due to their one-dimensional character, the electronic and optical properties of SWNTs show specific features.

-The phonon modes and their q-dispersion, which are important information for the understanding of Raman data, are presented. Especially, the relations between phonons in graphene and SWNT are discussed.

- In a part B, we introduce the structure, electronic bands and phonons of DWNTs. Indeed, the study of DWNTs was the main focus of my work during this PhD.

PART A: Properties of SWNTs

1.1. Atomic structure and geometry of graphene and SWNTs

1.1.1. Graphene

A carbon atom has six electrons and their electronic ground state configuration is $1s^2 2s^2 2p^2$. The two electrons in 1s orbitals, called core electrons, do not participate at any chemical reaction. The remaining four electrons, called valence electrons, occupy the $2s^2 2p^2$ orbitals. In condensed phase, the four valence electrons give rise to $2s^2$, $2p_x^1$, $2p_y^1$ and $2p_z^1$ orbitals which are important in forming covalent bonds in carbon materials (molecule and solid). In condensed phase, since the energy difference between the upper 2p energy levels and the lower 2s levels is small compared with the binding energy of the chemical bonds, the electronic wave functions for the four valence electrons can mix with each other to form the so-called hybrid orbitals. In carbon, three possible hybridizations occur, namely: sp, sp^2 and sp^3 hybridizations. In sp^2 hybridization, the 2s orbital and two of the 2p orbitals are hybridized (Figure 1.1a).

As a basis for the s and p states of the graphene lattice, one choses sp^2 hybrids in the Oxy plane and p_z-orbital perpendicular to this plane (Figure 1.1b). In graphene lattice, strongly covalent σ bonds, formed by sp^2 hybrids, are in-plane and form an angle of 120° from one to another. For each carbon atom, p_z-orbital, called π orbital, exists normal to the plane (Figure 1.1c). From the Figure 1.1d, only the π bands contribute to the electronic properties of graphene because the bonding π and anti-bonding π* cross the Fermi level.

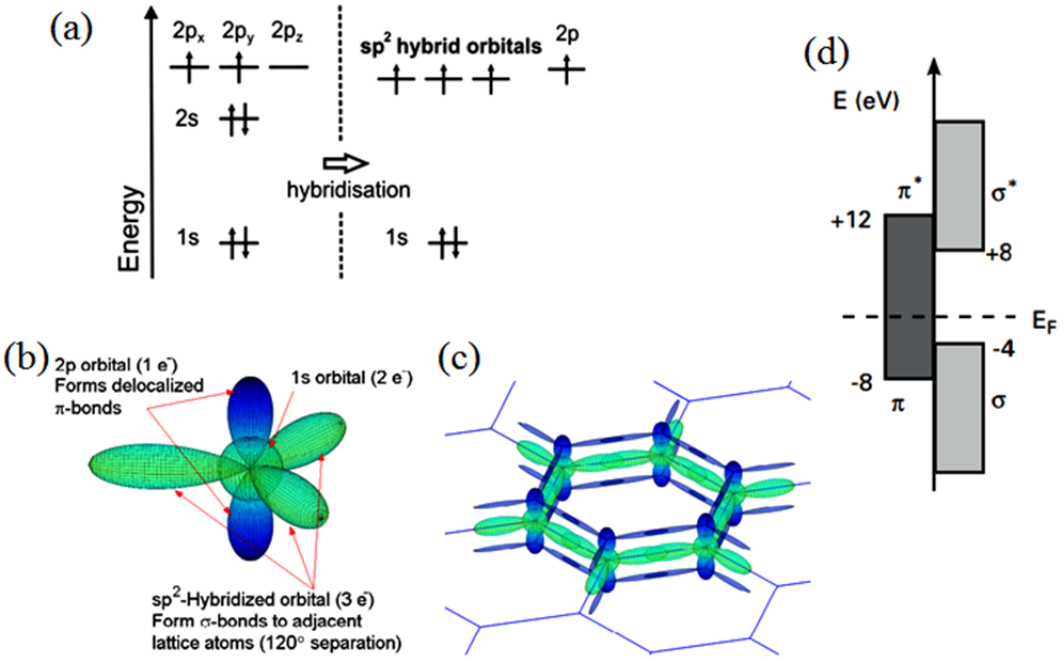

***Figure 1.1**: Atomic orbital diagram of a carbon atom. (a) Ground state and sp^2 hybridization, (b) sp^2-hybridized orbital, (c) graphene lattice structure, and (d) the bonding and anti-bonding π state lie in the vicinity of the Fermi level (E_F). (adapted from ref [9, 10]).*

Graphene sheet is a single atom layer of carbon. Figure 1.2a shows the hexagonal lattice of graphene with a triangular unit cell. In the real space, the basis vectors $\overrightarrow{a_1}$ and $\overrightarrow{a_2}$ of a unit cell can be written as:

$$\overrightarrow{a_1} = a\left(\frac{\sqrt{3}}{2}, \frac{1}{2}\right); \overrightarrow{a_2} = a\left(\frac{\sqrt{3}}{2}, -\frac{1}{2}\right) \qquad (1.1)$$

where that $a = \sqrt{3}\, a_{C\text{-}C}$, with $a_{C\text{-}C} = 1.42$ Å is the carbon-carbon distance in graphene.

The Figure 1.2b presents a reciprocal lattice with the first Brillouin zone (grey hexagon) of graphene. By using the condition $a_i b_j = 2\pi\delta_{ij}$, the reciprocal basis vectors $\overrightarrow{b_1}$ and $\overrightarrow{b_2}$ can be expressed as:

$$\overrightarrow{b_1} = \frac{1}{a}\left(\frac{2\pi}{\sqrt{3}}, 2\pi\right); \overrightarrow{b_2} = \frac{1}{a}\left(\frac{2\pi}{\sqrt{3}}, -2\pi\right) \qquad (1.2)$$

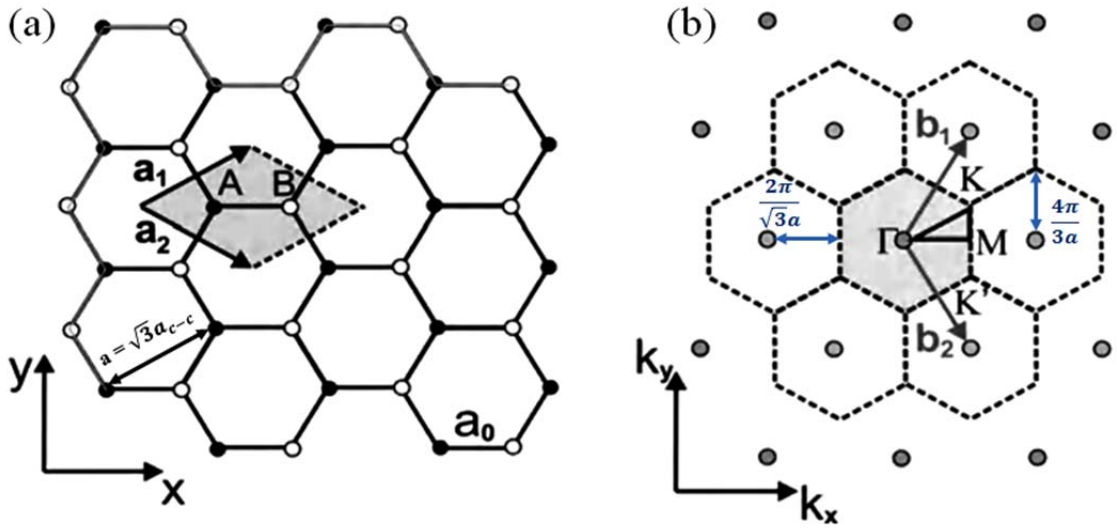

Figure 1.2*: (a) 2D honeycomb lattice of graphene in real space, a1 and a2 are the unit vectors of the primitive cell. (b) Reciprocal lattice with basis vector b1 and b2. (adapted from Ref [9]).*

The high symmetry points (Γ, M, K and K') of the first Brillouin zone are also indicated. The coordinates of two important points K and K' (known as Dirac points) in reciprocal lattice are:

$$K = \frac{1}{a}\left(\frac{2\pi}{\sqrt{3}}, \frac{2\pi}{3}\right);\ K' = \frac{1}{a}\left(\frac{2\pi}{\sqrt{3}}, -\frac{2\pi}{3}\right); \qquad (1.3)$$

The coordinate of the M point is:

$$M = \frac{2\pi}{\sqrt{3}a} \qquad (1.4)$$

1.1.2. Single-walled carbon nanotube

Conceptually, a single-walled carbon nanotube (SWNT) can be viewed as a rolled-up sheet of graphene and it is thus common to describe its atomic structure from the graphene lattice vectors.

Because of the surface curvature, a re-hybridization process including a certain amount of σ character in a π type orbital takes place ($sp^{2+\varepsilon}$ orbital) changing both its chemical and physical properties.

The particular roll orientation, (called chirality), of the graphene sheet defines different kind of SWNTs (Figure 1.3a). The chirality is defined by the chiral (or circumferential) vector $\overrightarrow{C_h}$ given by:

$$\overrightarrow{C_h} = n\,\overrightarrow{a_1} + m\,\overrightarrow{a_2} \qquad (1.5)$$

where (n, m) is a pair of integers and ($\overrightarrow{a_1}$, $\overrightarrow{a_2}$) is the pair of basis vectors of the graphene lattice.

The diameter of a SWNT is defined from the modulus of the chiral vector:

$$d = \frac{|\overrightarrow{C_h}|}{\pi} = \frac{\sqrt{3}a_{C-C}\sqrt{m^2+mn+n^2}}{\pi} \qquad (1.6)$$

The chiral angle θ, (0º - 30º), is the angle between the chiral vector and the direction $\overrightarrow{a_1}$.

$$\theta = \arctan\left(\frac{m\sqrt{3}}{2n+m}\right) \qquad (1.7)$$

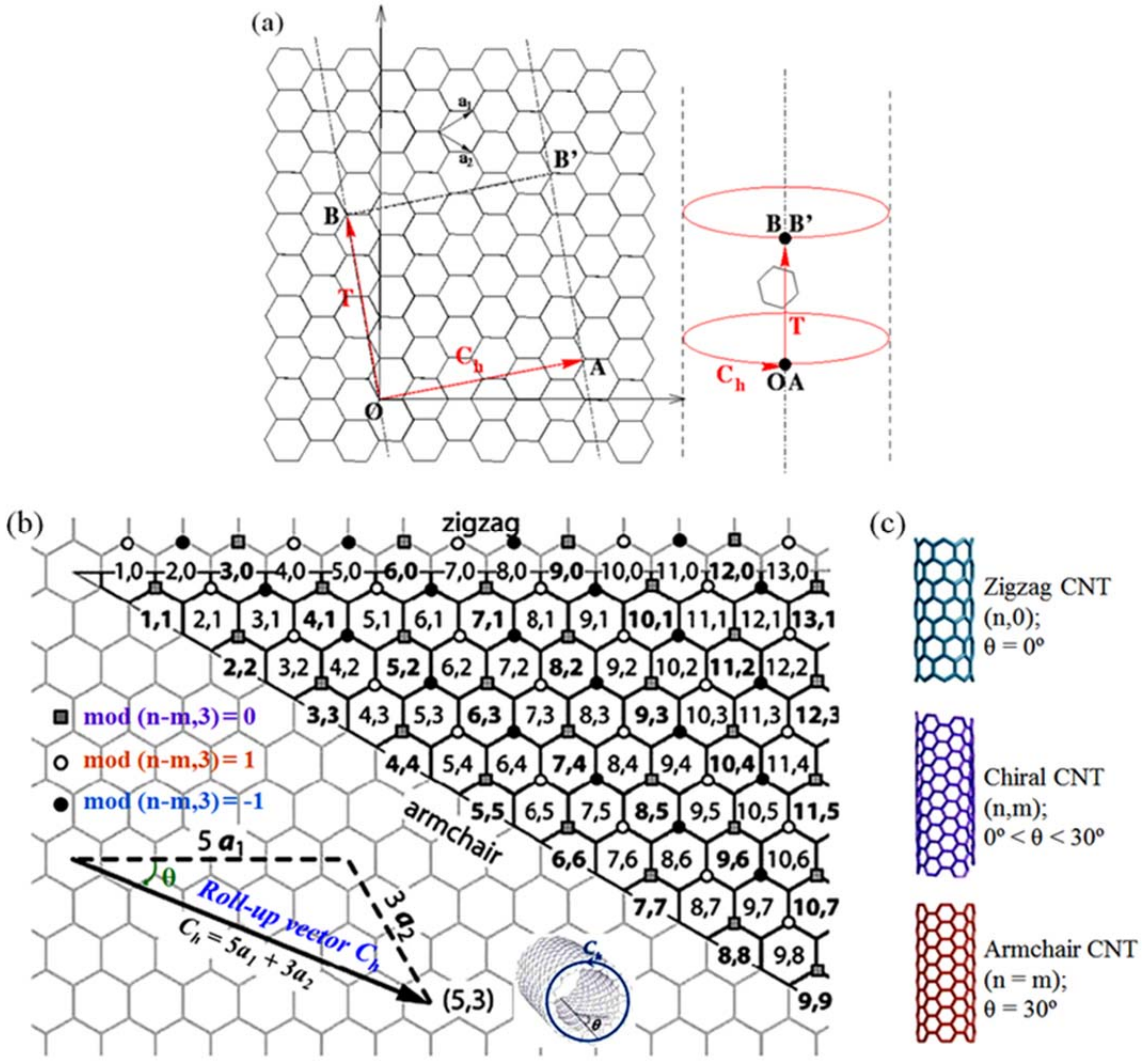

***Figure 1.3**: (a) The structure of a SWNT (from ref [11]), (b, c) Classification of the SWNT as a function of their chiral indices (n,m) (adapted from ref [12]).*

Based on the chiral angle, three types of SWNTs are defined, namely armchair, zigzag, and chiral SWNTs (Figure 1.3c).

- The armchair nanotubes correspond to the condition n = m or θ = 30º.
- The zigzag nanotubes correspond to the condition n = 0 or θ = 0º.
- All others SWNTs are called chiral tubes with 0º < θ < 30º.

The translational vector $\vec{T}$ is defined as the smallest unit vector which is perpendicular to $\overrightarrow{C_h}$.

$$\vec{T} = \frac{2n+m}{d_R}\overrightarrow{a_1} - \frac{2n+m}{d_R}\overrightarrow{a_2} \qquad (1.8)$$

where the greatest common divisor (gcd) d_R is defined.

$$\gcd(2n+m, 2m+n)\ d_R = \begin{cases} d\ if\ (n-m) is\ not\ a\ multiple\ of\ 3d \\ 3d\ if\ (n-m) is\ a\ multiple\ of\ 3d \end{cases}$$

where d is the greatest common divisor (gcd) of n and m.

1.2. Electronic band structure of graphene and SWNTs

1.2.1. The electronic band structure of graphene

The first calculation of electronic structure of graphene was obtained by using a simple nearest neighbor tight-binding model (NNTB model) where only π electrons are considered [13].

The energy eigenvalues $E_{g2D}(\vec{k})$ of 2D graphene is given by expression:

$$E_{g2D}(\vec{k}) = \frac{\epsilon_{2p} \pm tw(\vec{k})}{1 \pm sw(\vec{k})} \qquad (1.9)$$

where ε_{2p}: site energy of the $2p_z$ atomic orbital (orbital energy), t: the nearest neighbor carbon-carbon interaction (transfer) energy between π orbital (usually it holds in the range: -3 eV - -2.5 eV), s: denotes the overlap of the electronic wave function on adjacent sites. The + (–) signs in the numerator and denominator give the bonding π energy band (anti-bonding π* energy band). The function $w(\vec{k})$ is given by:

$$w(\vec{k}) = \sqrt{1 + 4cos\left(\frac{\sqrt{3}k_x a}{2}\right)cos\left(\frac{k_y a}{2}\right) + 4cos^2\left(\frac{k_y a}{2}\right)} \qquad (1.10)$$

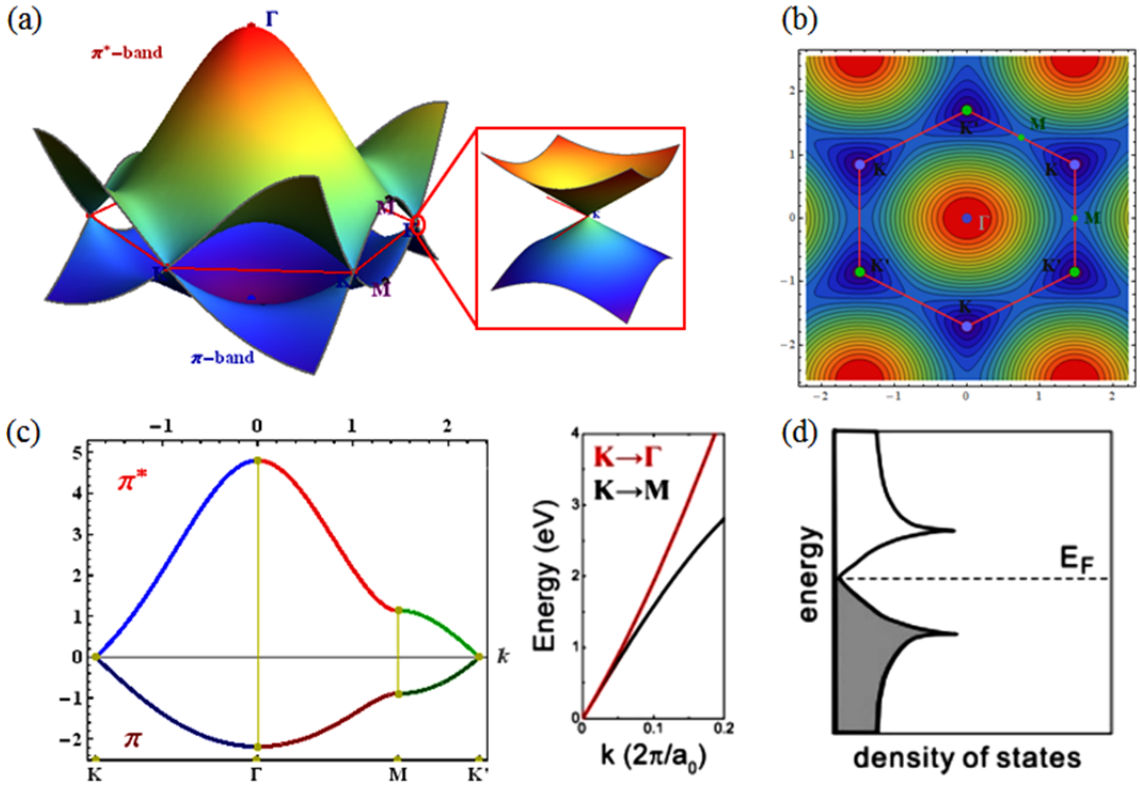

Figure 1.4*: The energy band structure of graphene. (a) A 3D view of the dispersion E(k) showing the energy of π-π* band and the linear energy dispersion at K-point (the so-called Dirac cone) . (b) The contours of energy dispersion surface for the π* electron. (c) The dispersion along high symmetry direction in the Brillouin zone and near K point, comparing the direction K → Γ and K → M (adapted from ref [14]). (d) Density of state of graphene. (adapted from ref [15]).*

As shown in Figure 1.4, the energy dispersion for the π (π*) electron is large at the zone center (Γ) and the two curves touch at the K-points. Therefore, a graphene is a semiconductor with a zero band-gap because the valence and conduction band touch at the six Dirac points of the Brillouin zone. The dispersion curves, plotted along K → Γ → M → K', are displayed on Figure 1.4c. With increasing distance from the K-point, the energy dispersion along the K → M direction deviates much faster from the linear relation than along the K → Γ direction.

When the overlap integral between wave functions centered at different atoms is ignored (s = 0), the π and π* bands become symmetrical around $E = \epsilon_{2p}$. The energy dispersion relationship of graphene in this case is given by:

$$E_g(k_x, k_y) = \pm\gamma_0\sqrt{1 + 4cos\left(\frac{\sqrt{3}k_x a}{2}\right)cos\left(\frac{k_y a}{2}\right) + 4cos^2\left(\frac{k_y a}{2}\right)} \qquad (1.11)$$

where γ_0 is the nearest neighbor hopping parameter, a is the lattice constant, k_x and k_y are the wavevectors in the Brillouin zone. The negative and positive terms correspond to the symmetrical bonding and anti-bonding energy band, respectively.

1.2.2. The electronic band structure of SWNT

The electronic band structure of SWNTs is usually calculated by using the zone-folding approximation of the π and π* electronic states obtained from a tight binding band structure of graphene. If we consider a SWNT as an infinitely long cylinder, there are two wavevectors associated with it. In Figure 1.5b, the wavevector $k_{||}$ (//) is parallel to the SWNT axis while the pseudo vector $k_{\perp}$ is along the circumference (C_h) of the SWNT. In the reciprocal space of graphene, the couple ($k_{||}, k_{\perp}$) defines 1D cutting lines corresponding to the one-dimensional energy sub-bands of a SWNT. The space between intersections is inversely proportional to the SWNT diameter while the length of the lines is inversely proportional to the length of the SWNT unit cell along the tube axis.

$$k_{\perp} = \frac{(2n+m)b_1 + (2m+n)b_2}{Nd_R}$$
$$k_{||} = \frac{mb_1 - nb_2}{N} \qquad (1.12)$$

where N is the number of hexagon in the nanotube unit cell: $N = \frac{2(n^2+nm+m^2)}{d_R}$

The 1-D energy dispersion relations of SWNT are given by:

$$E_{\mu} = E_{g2D}\left(k\frac{k_{||}}{|k_{||}|} + \mu k_{\perp}\right), (\mu = 0, ..., N-1, and -\frac{\pi}{T} < k < \frac{\pi}{T}) \qquad (1.13)$$

As mentioned in 1.2.1, graphene has a zero band-gap at K (K')-point. Thus, the position of cutting lines around Dirac points is important to identify the electronic properties of nanotubes. If one of the cutting line crosses the K (or K')-points, the SWNT will be metallic (Figure 1.5c). In this case, the chiral index of SWNT follows the relationship: mod (n-m, 3) = 0. On the other hand, if no cutting line crosses the K (or K') points, the SWNT will be semiconducting with a chiral index relationship: mod (n-m, 3) = +1 or –1. In this case, there is a band gap (E_g) between valence and conduction bands (Figure 1.5d). As a consequence, the ratio is statistically around 1/3 of metallic and 2/3 of semiconducting SWNTs.

With regards to the rule: mod (n-m, 3) =0 for metallic SWNTs and (n-m, 3) =1 or –1 for semiconducting SWNTs:

- The armchair nanotubes which correspond to the condition n = m are metallic
- The zigzag nanotubes which correspond to the condition n = 0 can be either metallic or semiconducting.
- All others SWNTs are called chiral tubes and can be either metallic or semiconducting.

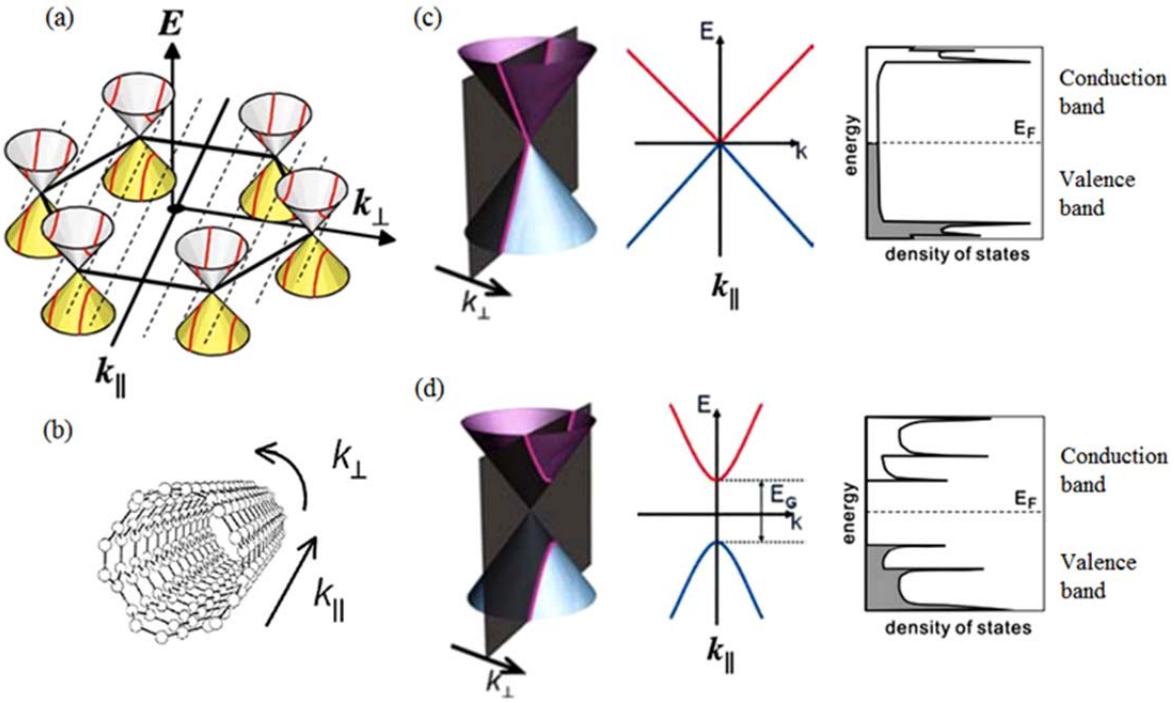

***Figure 1.5**: Construction of SWNTs band structures by using zone-folding approximation (a) The first Brillouin zone of graphene with conic energy dispersion at six K points. (b) wavevector along the circumference $k_\perp$ and nanotube axis $k_\parallel$. (c) Metallic SWNTs, and (d) Semiconducting SWNTs (adapted from ref [15, 16]).*

Since the zone-folding method neglects curvature effects, this approach is a better approximation for the large diameters (d > 1nm) than for small diameters. For the small diameters (d < 1nm), the curvature effects should be taken into account for calculation due to carbon–carbon bond length asymmetry and the σ-π orbitals overlapping and hybridization [17]. A pyramidalization angle (θ_p), (the difference between π-orbital axis vector of conjugated carbon atoms and a normal right angle), change from 0 to 19.5 degree when the carbon atoms configurations are modified from sp^2 to sp^3 (Figure 1.6a). J. Kürti *et al.* showed that the pyramidalization angles increases linearly with the reciprocal tube diameter 1/d [18] (Figure

1.6b): the smaller carbon nanotube diameter, the more mixture of the sp^2 and sp^3-configuration (in this case, the ab-initio method is more relevant to calculate the electronic band structure). Moreover, the curvature effect slightly modifies the electronic band structure by moving the K-point (Figure 1.6c). The comparison between ab-initio and tight-binding calculations of electronic band structure for the (5,0) nanotube is given in Ref. [19]. We can see that the electronic band structures are strongly affected by curvature effects (Figure 1.6d). Although the tight binding calculation predicts that the (5,0) SWNT should be semiconducting with a direct band gap of 2.3 eV, the ab-initio calculation shows that the Fermi level of this nanotube becomes populated. In other words, the (5,0) SWNT shows a metallic character rather than a semiconducting one because of curvature effect.

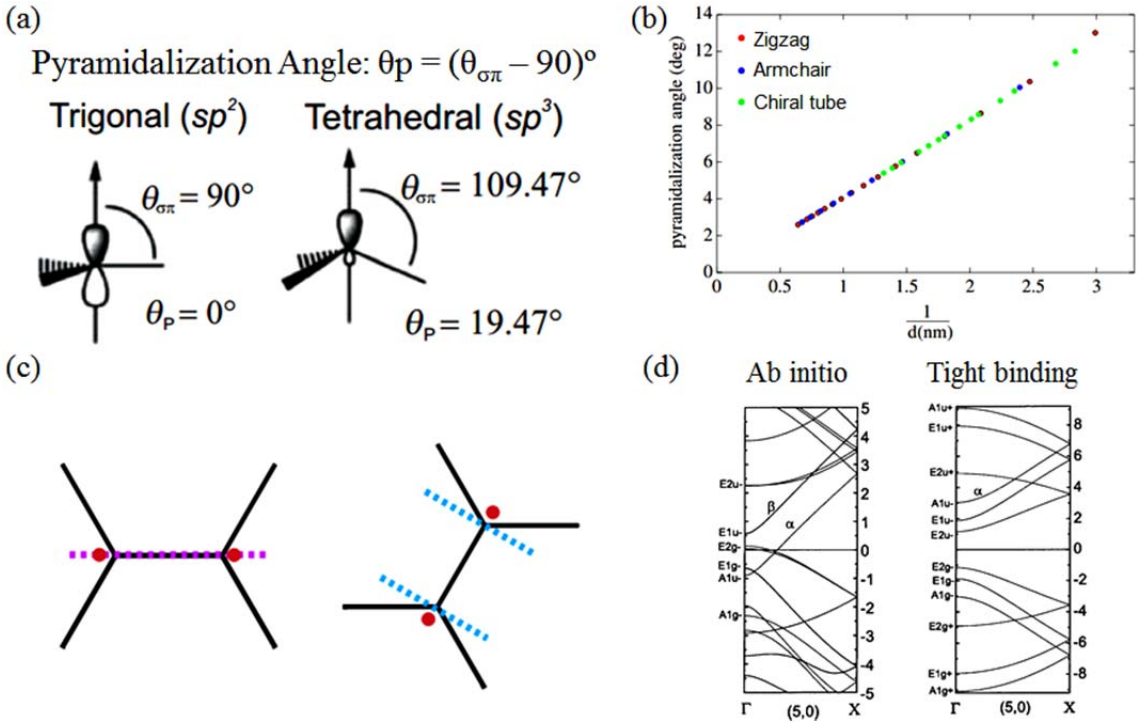

***Figure 1.6**: Pyramidization angles for (a) the trigonal sp^2 - and the tetrahedral sp^3–configuration (adapted from Ref [18]). (b) Pyramidalization angle against inverse diameter. (c) When the curvature effects are taken into account, the K-points move from the corners of the hexagon to the red dots. (d) Ab initio and tight binding calculation of the electronic band structure, E(k), of an isolated (5,0) SWNT (adapted from ref [19]).*

1.2.3. The electronic density of state (DOS) of SWNTs

Due to the 1-D structure of SWNTs, their electronic density of states (DOS) is dominated by van Hove singularities which are kinks in the DOS (Figure 1.7). The van Hove singularities correspond to conduction or valence band extrema in the dispersion relations, E(k). The DOS of 1-D sub-band is expressed as:

$$\rho(E) = \frac{2}{l}\sum_i \int dk\,\delta(k - k_i)\left|\frac{\partial E}{\partial k}\right|^{-1} \qquad (1.14)$$

Where l is the length of the first Brillouin zone, k_i are the roots of the equation $E - E(k_i) = 0$, and the term 2 in the numerator comes from the spin degeneracy of the bands.

For SWNTs, the equation (1.10) can be written as:

$$\rho(E) = \frac{4\sqrt{3}a_{C-C}}{\pi^2 d\gamma_0}\sum_\mu g(E,\varepsilon_\mu) \qquad (1.15)$$

Where $g\left(E,\varepsilon_\mu\right) = \begin{cases} \frac{|E|}{\sqrt{E^2-\varepsilon_\mu^2}}, |E| > |\varepsilon_\mu| \\ 0, |E| < |\varepsilon_\mu| \end{cases}$

γ_0 is the nearest neighbor hopping parameter, d is diameter of SNWT, ε_μ is the band-edges between conduction and valence sub-band. When $E = \varepsilon_\mu$, $g(E, \varepsilon_\mu)$ diverges leading to van Hove singularities (Figure 1.7). Basically, the DOS of semiconducting CNTs have band-gap while the merging between two bands is observed in case of metallic ones.

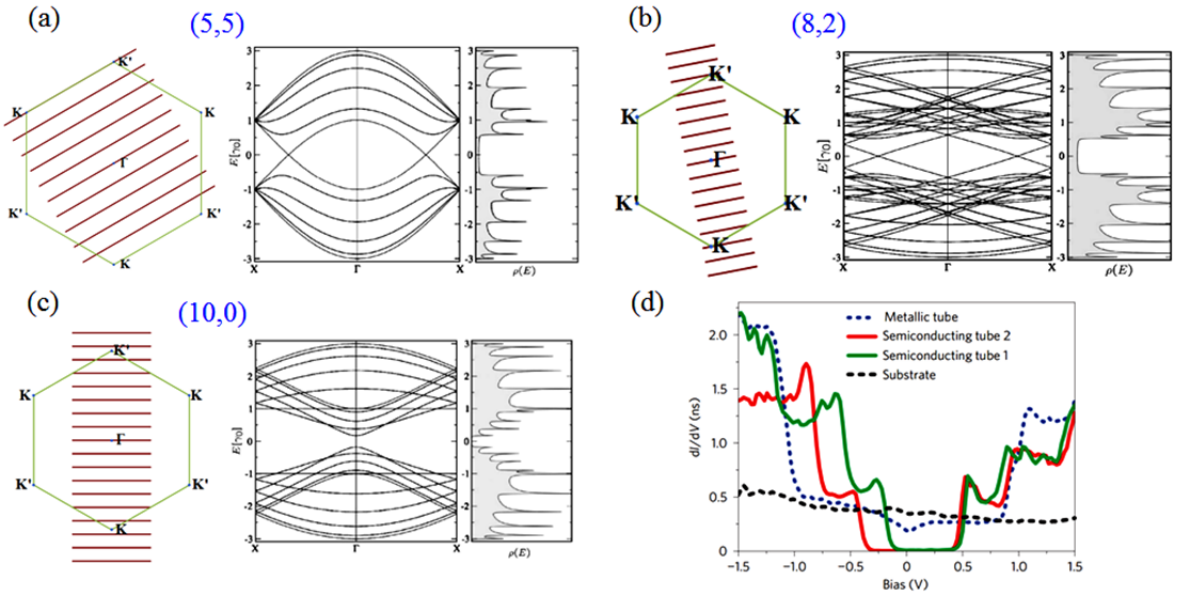

***Figure 1.7**: The electronic band structure and DOS of SWNTs by using zone-folding method of (a) armchair (5,5), (b) chiral (8,2), and (c) zigzag (10,0) (adapted from Ref [20]). (d) The scanning tunneling spectroscopy measurement DOS of single nanotubes deposited on Au (111) substrate (adapted from ref [21]).*

The electronic band structure of an armchair (5,5) SWNT is presented in Figure 1.7a. Because a cutting line crosses K point, this nanotube is metallic. The valence and conduction bands for armchair SWNTs cross at $k = k_F = \pm 2\pi/(3a)$, which is located at two-third of Γ-X. This means that the original K vertices of the original graphene hexagonal BZ are folded at two-thirds of the Γ-X line. Figure 1.7b shows the energy dispersion of the (8,2) chiral SWNT. Since the mod (n-m, 3) = 0, this nanotube also exhibits a metallic behavior with a band crossing at $k = \pm 2\pi/3T$ (T is the translational vector). An example of DOS calculation for zigzag SWNT (10,0) is presented in Figure 1.7c. This tube is semiconducting and presents a finite energy gap at Γ point. The electronic DOS of metallic and semiconducting SWNTs was successfully measured by scanning tunneling microscopy/STS in 1998 [22, 23].

1.2.4. Trigonal warping effect of SWNTs

The trigonal warping effect describes the change of energy contours in the Brillouin zone of graphene from circles around the K points to a triangular shape, when the energy increase (the summits of the triangle clock towards the K-M direction) [14]. This leads to the deviations from the linear energy dispersion around K point (see Figure 1.8a).

The trigonal warping effect on metallic SWNTs splits the singular peaks in DOS. The experiments and calculations show two distinct levels for each E_{ii} van hove singularity, denoted as E_{ii}^{M+} and E_{ii}^{M-} (Figure 1.8c) [24]. Their splitting strongly depends on the chiral angle of the SWNTs. The energy splitting $\Delta E_{ii} = E_{ii}^{M+} - E_{ii}^{M-}$ decreases with the increasing of chiral angle θ. It is maximal for zigzag nanotubes (θ = 0º) and vanished for the armchair nanotubes (θ = 30º).

The semiconducting SWNTs which have mod (n-m, 3) = – 1 (family –1) are called S-SWNTs type I. The closest intersection to a K point is at 2/(3d) (d is diameter of a SWNT) from the K point in the K → Γ direction, defines the E_{11}^{S} transition and the band gap energy [12]. The transition E_{22}^{S} is on the opposite side which is at 4/(3d) from the K point. Similar, the other E_{ii}^{S} (i > 3) are alternatively on one side or the other side of the K point.

The semiconducting SWNTs which have mod (n-m, 3) = +1 (family 1) are called S-SWNTs type II. The cutting line associating with E_{11}^{S} is at the same distance (2/(3d)) from the K than in S-SWNTs type I, except that it is on the opposite side of the K point in the K → M direction.

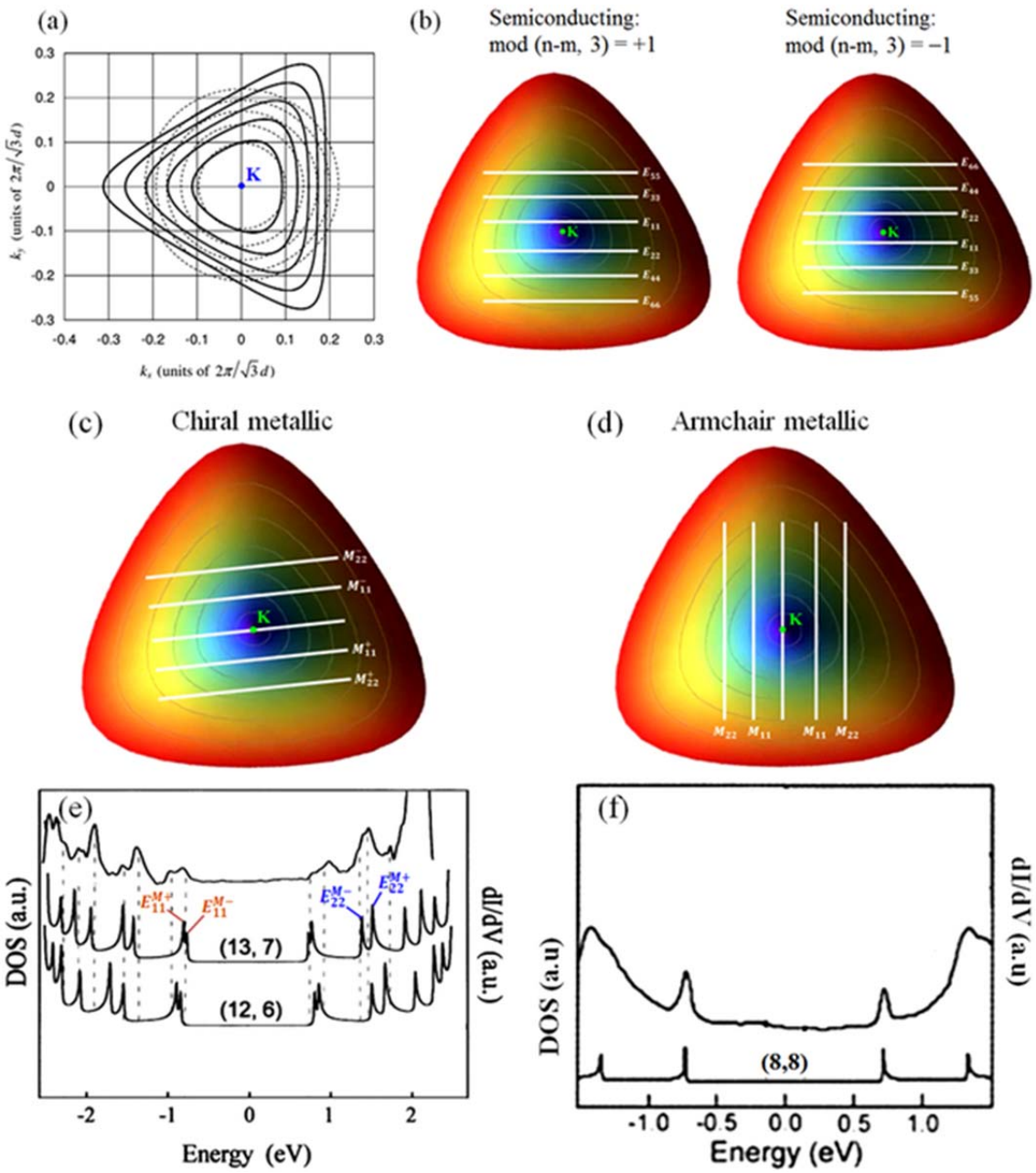

Figure 1.8: *(a) The trigonal warping effect at K point in carbon nanotubes. Equi-energy lines in the vicinity of the K-point. The circle contours dashed lines are obtained by neglecting trigonal warping effects. The trigonal warping effect, is clearly seen from the equi-energy contours shown by solid lines [25]. (b) The position of cutting lines is on opposite sides of the K point for zigzag semiconducting tube of type I or II. (c,d) The position of cutting lines for chiral and armchair metallic tubes. (e-f) The experimental DOS of chiral (armchair) metallic tubes (do not) exhibit an energy splitting due to the trigonal warping effect (adapted from ref [24, 26])*

1.2.5. The optical transitions and the "Kataura plot"

The "Kataura plot", calculated for the first time in 1999 by H. Kataura using a tight-binding model (non-interacting model), displays the energy separation between the van Hove singularities (the so-called optical band-to-band transition energies, E_{ii}) as function of diameter for a large set of (n,m) SWNTs [27]. This plot is useful to predict the resonance conditions of each (n,m) SWNT in Raman experiments. The experimental energy separations between the van Hove singularities can be measured by Raman (excitation profile), Rayleigh, photoluminescence experiments (PL) or absorption.

Figure 1.9 shows a typical "Kataura plot", revisited by V. N. Popov in the framework of a non-orthogonal tight binding model. This approach also calculates the band-to-band transitions for all nanotube in the diameter range: 0.6 – 2.4 nm. By contrast with the pioneer work of H. Kataura, this approach takes into account both curvature and trigonal warping effects. The energy covers two transitions of M-SWNTs and five transitions of S-SWNTs. The large chiral angle nanotubes are at the center of each transitions band while the small chiral angle nanotubes are located at the band extremities. The data points connected by the solid line in the Figure 1.9 belong to the same branch defined by: $2n + m = \text{constant}$. These branches display a V-shaped pattern. For metallic SWNTs, the E_{ii}^{M} transition energy splits into lower (E_{ii}^{M-}) and higher (E_{ii}^{M+}) energy transitions.

Bachilo *et al.* [28] performed PL measurements on individual semiconducting SWNTs isolated in aqueous surfactant suspensions. They observed that the energy transition ratio between the second and first van Hove singularities (E_{22}^{S} /E_{11}^{S}) of a same SWNT deviates from the average central value in the opposite directions for type I and type II semiconducting nanotubes. The SWNTs, with a chiral angle close of 30°, are close of the median line while the SWNTs close to zig-zag (chiral angle close of 0°) are the further away.

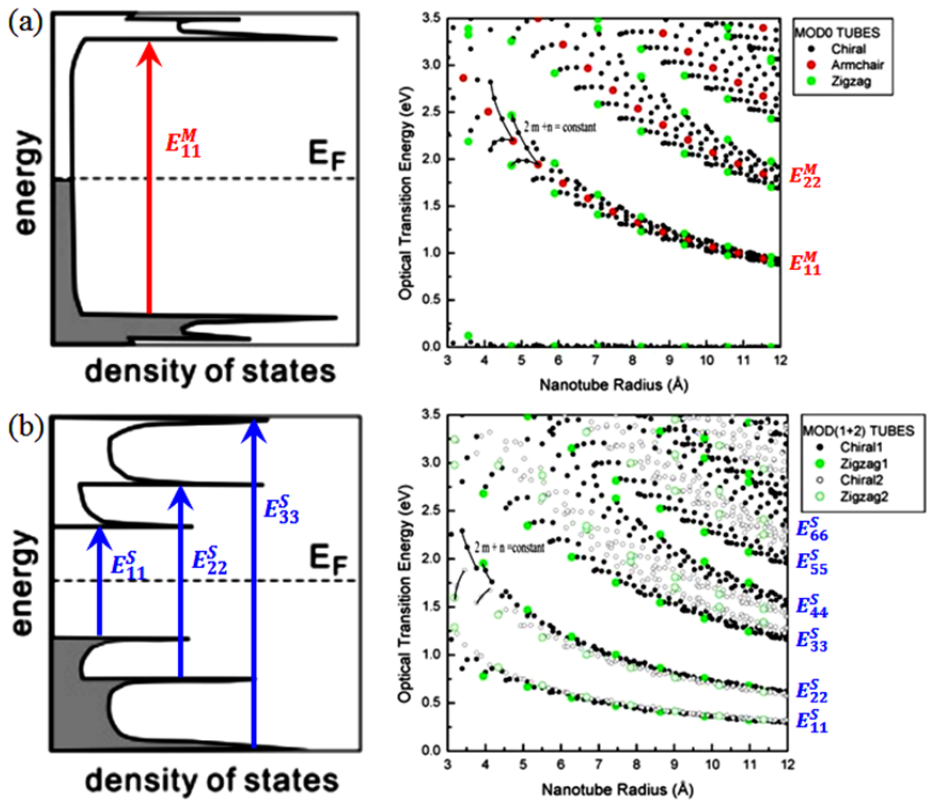

Figure 1.9: *The DOS transitions and Kataura plot calculated by using the non-orthogonal tight binding model including curvature effect for M/S-SWNTs [29]. (a) Metallic-SWNTs with mod 0. (b) Semiconducting-SWNTs with (n-m) mod3= 1 or –1 (adapted from ref [29-31]).*

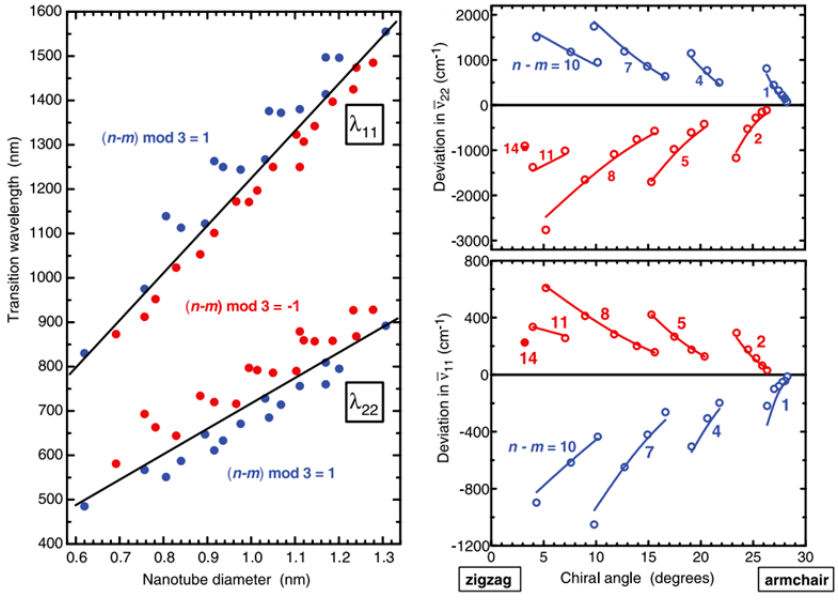

Figure 1.10: *Experimental Kataura plot obtained by PL spectroscopy for semiconducting SWNTs for λ_{ii}, i = 1, 2 (adapted from ref [28]).*

As indicated previously, V. N. Popov calculated the optical energy transitions of SWNTs with the non-orthogonal tight-binding model. However, electron-electron and electron-hole (exciton) corrections were ignored in this calculation. The comparison of the calculated optical transitions with experimental ones measured by Rayleigh and Raman experiments on suspended SWNTs shows that the calculated first and second transitions in semiconducting tubes and the first transition of metallic energy transitions have to be rigidly upshifted of about 0.3 eV [30], and the calculated third and fourth optical transitions of semiconducting nanotubes have to be rigidly upshifted of about 0.45 eV [31] in order to have a good agreement between calculations and experiments.

Other expressions have been proposed to describe the experimental dependence on diameter and chiral angle of the optical transitions in SWNTs.

Araujo *et al.* [32] performed an extended Raman study of individual carbon nanotubes wrapped in surfactant. They derived the following analytic formula for the energy transitions.

$$E_{ii}(p,d,\theta_c) = \frac{p}{d}\left(A + B log\frac{C}{\frac{p}{d}}\right) + \frac{\beta_p \cos(3\theta_c)}{d^2}$$

With A = 1.074 ($p < 4$) or 1.133 ($p \geq 4$), B = 0.502, C = 0.812, and β_p takes different values for each E_{ii} and each nanotube family.

Recently, Liu *et al.* proposed an empirical formula for the energy transitions on the basis of Rayleigh and fluorescence measurements on a large set of individual suspended SWNTs [33].

$$E_{ii}(p,d,\theta_c) = 2\hbar v_F(p)\frac{2p}{3d} + \beta\left(\frac{2p}{3d}\right)^2 + \eta(p)\cos(3\theta_c)\left(\frac{2p}{3d}\right)^2$$

where the Fermi velocity $\upsilon_F(p)$, as well as the parameters β and $\eta(p)$, are defined in ref [33]. In this expression, the different terms are associated with contributions of the linear dispersion in the K-valleys, deviations from the linear dispersion away from the center of the valleys, and trigonal warping effects.

The differences between these expressions can be ascribed to difference in the environment of the nanotubes in the two experiments. However, the three datasets by Popov, Araujo, and Liu are in good agreement within ~ 100 meV in the diameter range 1.5 – 2.5 nm.

1.3. The selection rules for optical properties in CNTs

In one-dimension nanomaterials such as CNTs, the optical properties are strongly dependent on the polarization of the electric-field vector relative to the nanotubes axis [34]. If the polarization of light is parallel to the nanotubes axis, the optical transitions in CNTs are allowed between sub-bands having the same symmetry ($E_\mu^C \rightarrow E_\mu^V$). These transitions are labeled E_{ii} (E_{11}, E_{22}, etc). On the other hand, when parallel polarization is applied, the optical transitions called E_{ij} are strongly suppressed due to the anti-symmetry ($E_\mu^C \rightarrow E_{\mu\pm1}^V$). Consequently, their intensities are negligible.

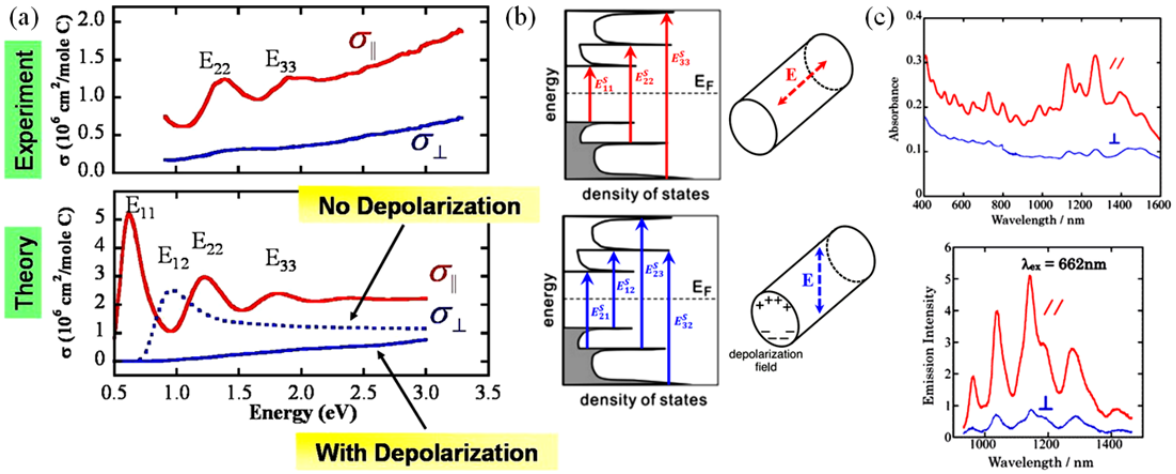

Figure 1.11*: (a) Experimental and calculated absorption cross-section for polarization parallel and perpendicular to the semiconducting CNTs (the dashed (dotted) line shows the effect of depolarization correction (adapted from ref [35]). (b) Schematic illustration of light polarized parallel and perpendicular to the tube axis. (c) Polarized absorption and photoluminescence spectra of an aligned SWNT film(adapted from ref [36]).*

M. F. Islam *el al*. [35] aligned SWNT in magnetic field and locked them in place by suspension gelation. They measured the transitions E_{12} or E_{21} for incident light preferentially polarized perpendicular to the nanotubes axis. Their signal is very weak due to the depolarizing effect arising from radial confinement. The optical responses of carbon nanotubes are highly anisotropic.

1.4. Excitons in SWNTs

1.4.1. Basic description of exciton in SWNTs

In semiconductor materials, there are two models which are used to describe the optical transitions: band-to-band transitions and transitions to excitonic levels.

Band-to-band transition consists of electrons excited from valence band to conduction band without considering any interaction between electrons and holes.

An exciton consists of photo-excited electron and hole pair bound to each other by a Coulomb interaction. Commonly in 3-D semiconductors, the binding energy is of about 10-20 meV and the optical absorption to exciton levels is usually only observed at low temperature.

In 1-D nanomaterials, such as CNTs, the optical behavior is different and Coulomb effects including electron-electron interaction and electron-hole interaction have to be considered. The electron-electron interaction ($E_{e\text{-}e}$) in SWNTs leads to band gap renormalization and accounts for a considerable blue shift of the (free-particle) Van Hove singularities. On other hand, the electron-hole (exciton) attraction causes a red-shift of the electronic transitions. A schematic view of the exciton picture in semiconducting SWNTs is depicted in Figure 1.12a.

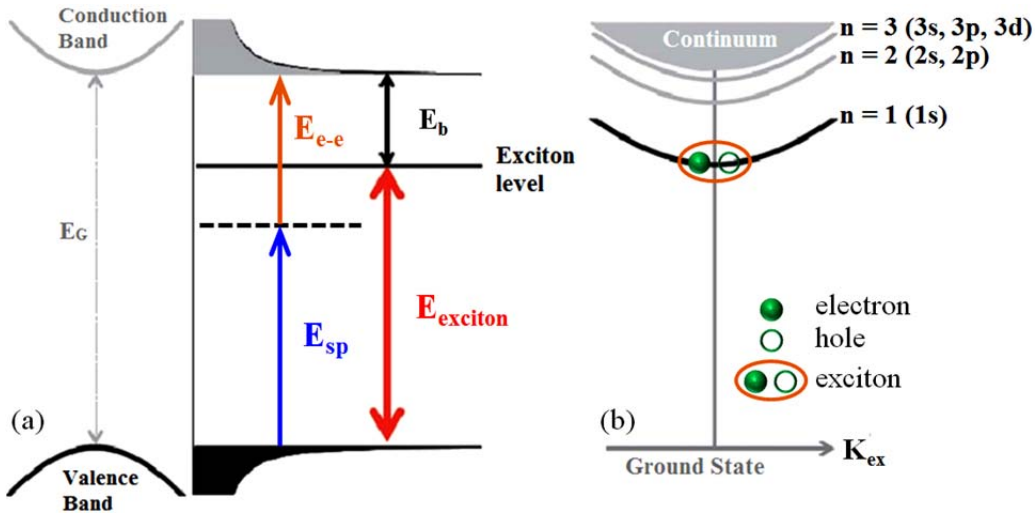

***Figure 1.12**: Coulomb interaction involving electron-electron and electron-hole interaction in CNTs. (a) Optical excitation without and with Coulomb interaction in a nanotube. (b) Schematic of an exciton dispersion relation as a function of the exciton center of mass wavenumber K_{ex} (adapted from ref [37]).*

In one dimension (1-D), excitonic states can be described by a hydrogen-like Rydberg series of levels below the single-particle bandgap. The exciton energy can be expressed by:

$$E_{exciton} = E_{sp} + E_{e\text{-}e} - E_b.$$

E_{sp} is the single-particle band-gap energy ignoring charge carrier interaction. The correction is due to "many-body effect", namely: e-e interactions ($E_{e\text{-}e}$) and e-h binding energy (E_b). In the case of CNTs, the theoretical calculations predicted that the $E_{e\text{-}e}$ is of the same order of magnitude as E_{sp} [38] and that the value of E_b varies from 0.1 eV to 1eV, depending on tube diameter, chirality, and dielectric screening.

Figure 1.12b shows a schematic of an energy dispersion relation of exciton in momentum space as a function of the exciton center of mass wavenumber K_{ex}. The exciton levels are separated in several sub-bands corresponding to hydrogenic levels of the electron-hole pair. The lowest energy exciton (n = 1) is associated with 1s level, the second level (n = 2) corresponds to 2s, 2p levels and the third one correspond to 3s, 3p, 3d levels. Although there are many excitonic levels, the exciton energy refers to the lowest active (bright) exciton level which dominates the absorption spectrum.

1.4.2. Exciton contribution to the E_{11} and E_{22} transitions

The calculations of absorption spectra with (solid lines) and without (dashed lines) excitonic effects for the first two transitions of metallic and semiconducting tubes (E_{11} and E_{22}) are shown on Figure 1.13 [39]. Generally, the influence of the excitons leads to a red shift of the peaks in the absorption spectra and this effect is considerably larger in semiconducting than in metallic nanotubes.

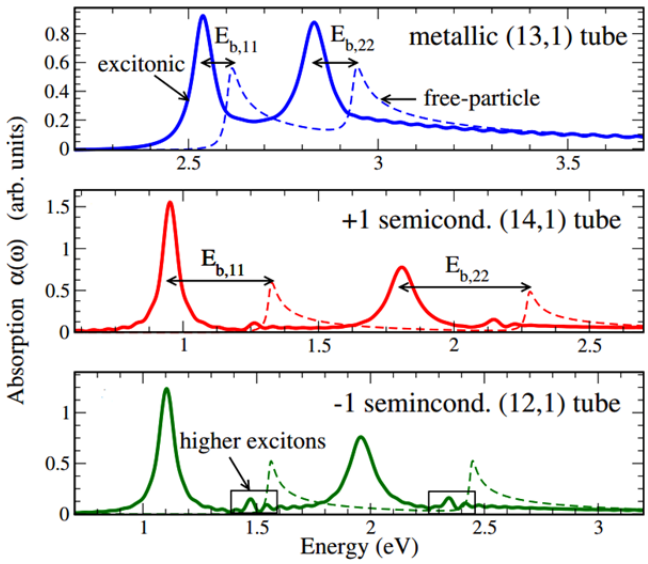

***Figure 1.13**: The theoretical absorption coefficient α(ω) as a function of the energy for metallic and semiconducting SWNTs with (solid lines) and without (dash lines) excitonic effects (adapted from ref [39]).*

In three-dimensional metallic materials, the excitons are not expected due to the strong free carrier screening of Coulomb potential which prohibits the formation of bound state of electrons and holes. The situation in SWNTs can be different because the effectiveness of screening is significantly reduced due to the quasi-one-dimensional nature of the tubes. As a result, the excitons can be observed even in the metallic SWNTs.

The excitonic signature of semiconducting and metallic SWNTs was experimental identified by Rayleigh spectra [40], two photon absorption [41, 42] and temperature-dependent resonant Raman spectroscopy [43]. The calculation and measured binding energy was estimated for metallic (semiconducting) SWNTs to be around 50 (350) meV [41-43].

1.4.3. Exciton contribution to the E_{33} and E_{44} transitions

The third and fourth energy transitions are important for optics in the visible range, since the E_{22} is in the infrared range when large diameter S-SWNTs (d > 1.3 nm) are investigated. J. Yonglei, *el al.* [44] studied the high energy optical transitions in large diameter semiconducting SWNTs, using the tight-binding (NTB) model with the long-range Coulomb interaction, which is able to include the curvature effect as well as the trigonal warping effect for interpreting the large family spread in the optical transitions. The calculation showed that the exciton's binding energies of E_{33} and E_{44} are in the range of 400 – 600 meV, which is generally larger than that of lower E_{11} and E_{22} transitions (Figure 1.14). Their calculation results are in good agreement with transition energies evaluated from Raman resonance data obtained in the diameter range 0.7–2.3 nm of suspended individual SWNTs [32].

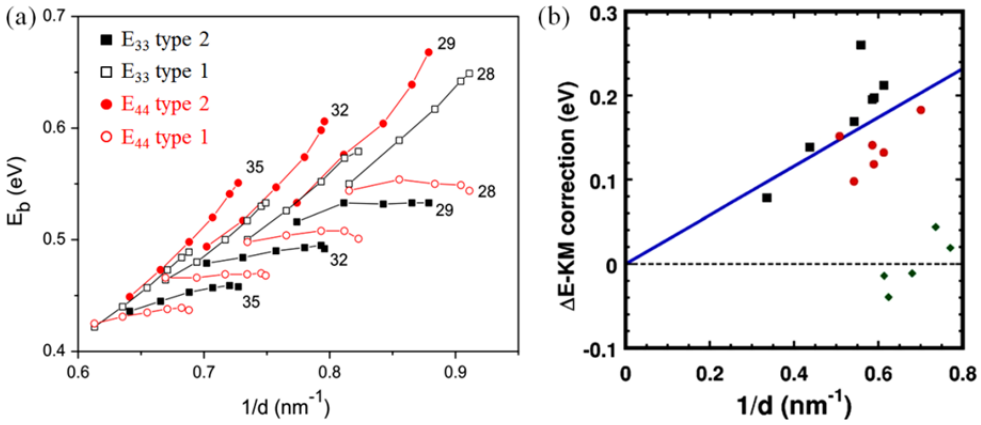

***Figure 1.14**: (a) The calculated exciton binding energy of high transitions (E_{33} and E_{44}) for SWNTs versus their inverse diameter (adapted from Ref [44]). (b) Experimental deviation of ΔE from the KM correction vs. 1/d for the third semiconducting (red dots), fourth semiconducting (black squares), and first metallic transitions (green diamonds). The blue solid line (black dotted line) is the linear fit of the average deviation vs. 1/d for the third and fourth semiconducting transitions (first metallic transition) (adapted from ref [45]).*

The quantum-chemistry [32] or solid-state physics [46, 47] were used to calculate the energy of high transitions. The quantum-chemistry model predicts a weakly bound excitonic state for the E_{33}^{S} and E_{44}^{S} levels as compared to the lower-energy ones. However, the solid-state physics method gives the information that the third and fourth transitions, are in excitonic nature. The excitonic nature of the high energy transitions was confirmed experimentally [40].

1.4.4. The screening effect

The screening effect, which refers to the dielectric constant ε of the surrounding medium, can reduce both band gap renormalization ($E_{e\text{-}e}$) and binding energy (E_b). As a result, the transition energies of individually suspended SWNTs in various dielectric media are usually red-shifted related to those of suspended SWNTs in air or in vacuum. This change has been observed experimentally by PL measurement of SWNTs in different environment such as in air, and in aqueous suspensions in surfactants [48-51]. Moreover, the results also show that the energy shifts of E_{11} and E_{22} strongly depend on chiral angle, the diameter and the type of SWNTs. For higher transitions, the measured E_{33} and E_{44} of semiconducting SWNTs showed that they are almost independent of sample environment [52].

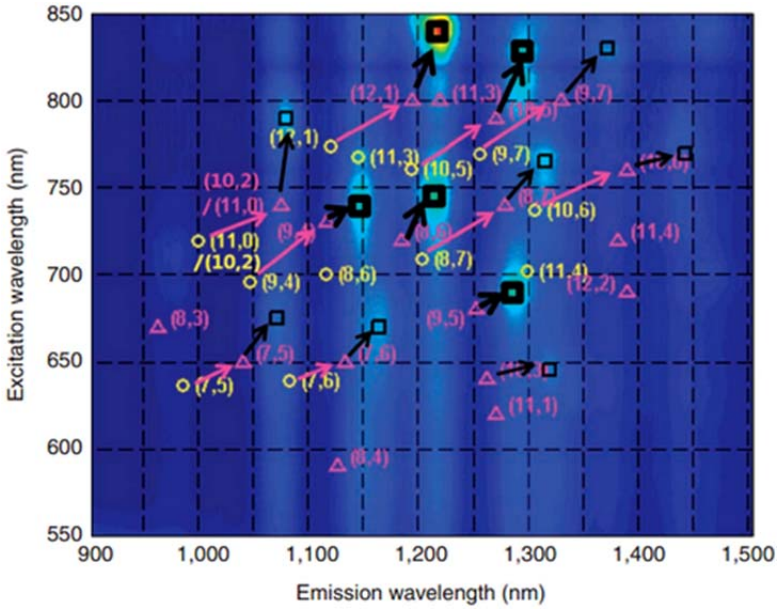

Figure 1.15*: PLE of SWNTs in different media. Yellow dots: air-suspended SWNTs; purple triangles: SWNTs wrapped with SDS and dispersed in water; black squares: SWNTs dispersed with rr-P3DDT in toluene, and bold black squares: SWNTs dispersed in rr-P3DDT in relatively higher concentrations (adapted from ref [51]).*

1.4.5. Bright and dark excitons

Due to the symmetry between K and K' region and the mixing of two electrons and two holes between two valleys, there exist four singlet excitons corresponding to direct and indirect band-gap transitions as shown in Figure 1.16a.

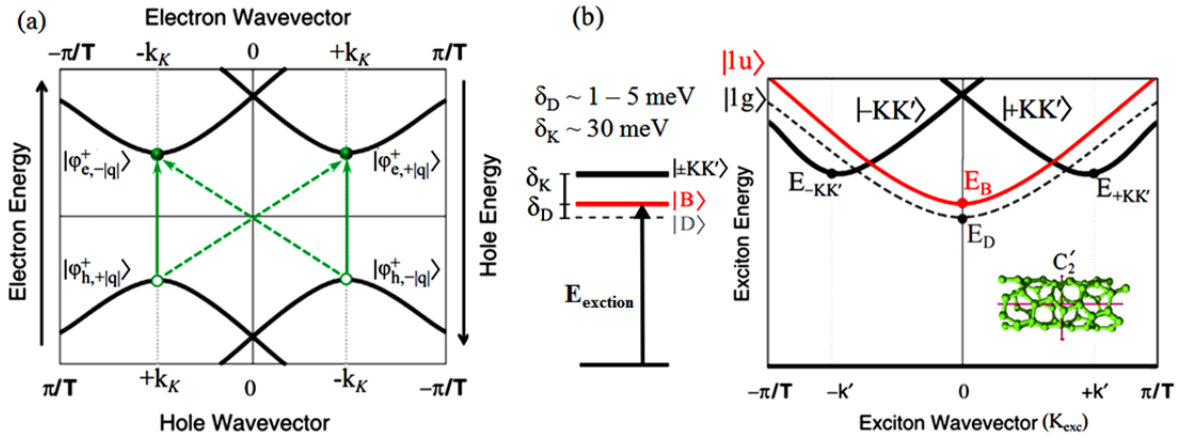

***Figure 1.16**: (a) Schematic energy diagram for singlet excitons in SWNTs, four possible electron-hole configurations, direct (solid lines) and indirect (dashed lines). (b) Four singled states of exciton dispersion, $|1u\rangle$ is bright state $|B\rangle$; $|1g\rangle$ is dark state $|D\rangle$. $|-KK'\rangle$ and $|+KK'\rangle$ are the K-momentum dark states. (adapted from ref [53])*

Theory predicts that three of excitonic states do not interact with light due to selection rules and are therefore called "dark" excitons. Only one is optically allowed, namely "bright" exciton [53] (Figure 1.16b). If both the electron and the hole are located at the same K (or K') region, the center of the momentum of excitons are located near Γ point and have zero angular momentum along the nanotube axis. The singlet excitons $|KK\rangle$ and $|K'K'\rangle$ are coupled into bonding and anti-bonding states. As a result, the mixing of the electron and hole states with opposite quantum number k (solid lines) with zero angular momentum will give rise to bright $|1u\rangle$ excitonic states (antisymmetric) and dark $|1g\rangle$ excitonic state (symmetric). The dark exciton has a slightly lower energy than the bright exciton (Figure 1.16b). The bright exciton absorption comes from the dipolar transition when the light is polarized parallel to the nanotube axis and it dominates the optically absorption spectrum.

1.5. Phonon dispersion in graphene and single-walled carbon nanotubes

1.5.1. Phonon dispersion in graphene

In crystals, with n atoms in the primitive cell, there are 3n degrees of freedom and then, for each wave vector of propagation q, 3n possible lattice vibrations. The lattice vibrations, the so-called phonons, decompose into three acoustic phonons (A) and 3n-3 optical phonons (O).

In the limit of long wavelengths (phonon wavevector, q, close to 0), acoustic phonons correspond to a simple displacement of the whole crystal. Consequently, acoustic phonons exhibit a linear relationship between its frequency and the phonon wavevector, and the frequencies of acoustic phonons tend to zero at q =0. Longitudinal and transverse acoustic phonons are usually abbreviated as LA and TA phonons, respectively. The atom displacements for LA phonon are parallel to the direction of propagation, q, while they are normal to the q direction for TA phonon.

Optical phonons involve out-of-phase displacements of the atoms in the lattice. In the limit of long wavelengths, optical phonons have a non-zero frequency at the center of the Brillouin zone and, opposite to acoustic modes, show, in general, no dispersion. As for acoustic modes the same convention are used to distinguish between longitudinal (LO) and transverse (TO) phonons.

The dependence of the phonon energy with q displays the so-called phonon dispersion curves.

Applying these general definitions to graphene leads to the following description of its dispersion curves:

In graphene, there are two distinct carbon atoms, A and B, in the primitive cell. Consequently they are six degrees of freedom by primitive cell leading to six dispersion curves for each direction of q (Figure 1.17). The three phonon dispersion curves at low frequency, with energy close of 0 near the Γ point of BZ, are the acoustic modes. We distinguish the longitudinal acoustic phonon (iLA), the in-plane transverse acoustic phonon (iTA), and the out-of-plane transverse acoustic phonon (oTA). The three dispersion curves at higher energy correspond to optical phonons. We distinguish the in-plane longitudinal optical phonon (iLO), the out-of-plane transverse optical phonon (oTO), and the in-plane transverse optical phonon (iTO).

In Figure 1.17a, the solid lines result from calculations of the dispersion curves (including force constants up to 14th nearest neighbors) and the symbols represent experimental data measured by inelastic X-ray scattering experiments [54].

The optical phonons in the zone-center (Γ) and zone edge (K and K') region are of particular interest because they can be accessible by Raman spectroscopy. In-plane transverse optical phonon (iTO) and in-plane longitudinal optical phonon (iLO) are degenerated at Γ point. The resulting mode is called: G-mode, its symmetry is E_{2g} and it is Raman-active.

The out-of-plane phonon mode (oTO), around 860 cm^{-1} at the Γ point, (symmetry A_{2u}), is an infrared-active phonon mode.

Another mode of interest is the D-band (D for defect). It corresponds at the iTO mode at the K point of the BZ. It is Raman-active by a process of double resonance implying an in-plane defect. It must be emphasized that Raman D-mode is dispersive in the sense that its experimental frequency varies with the photon excitation energy. Note that the overtone of this mode, the so-called 2D-band (or G'-band) is of a great interest to evaluate the number of graphene layers and to study electron-phonon coupling in graphene. It is always observed in Raman of graphene, including defect-free graphene, *via* a double-resonance process.

The mode displacement vectors involved in the iLO, iTO modes and D mode are shown schematically in Figure 1.17b.

The strong electron-phonon coupling leads to an anomalous dispersion, of the G-mode and D-band near the high symmetry points Γ and K respectively, the so-called Kohn-anomalies.

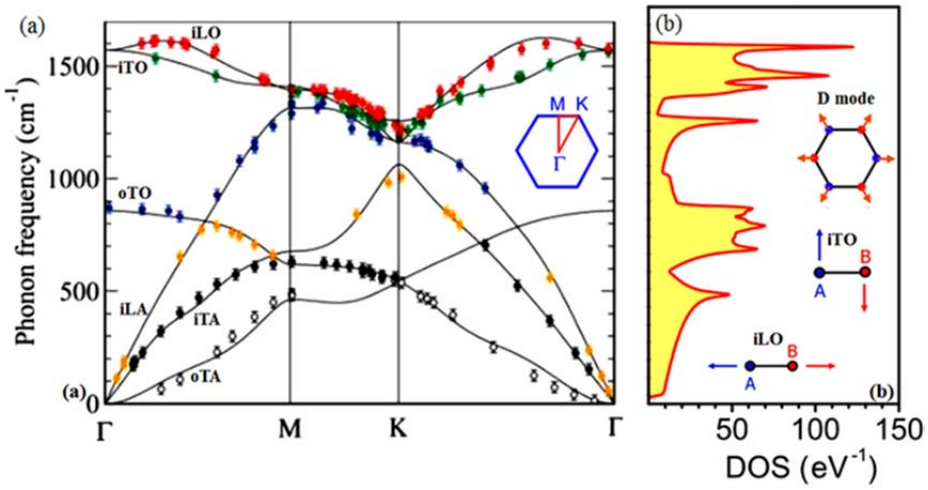

***Figure 1.17**: (a) Phonon dispersion of graphene in the 2D Brillouin zone. The symbols are experimental data obtained by inelastic X-ray scattering and the lines are fitted to experimental phonon data using up to 14th nearest-neighbor interactions. The high symmetry lines are shown schematically in the inset where the Brillouin zone has been rotated clockwise by 30°. (b) Phonon density of states in units of phonon modes per hexagonal unit cell. The mode displacement vectors for the q = 0 in-plane LO and TO phonons are shown schematically. (adapted from ref [54]).*

1.5.2. Phonon dispersion in SWNTs

In a first approximation, the phonon dispersion of SWNT can be determined by zone folding the graphene phonon dispersion curves. One applies the same procedure as the one used for the electronic structure. The rolling of graphene leads to the dispersion curves of SWNTs. The zone folding method consists to project the 2D dispersion curve of graphene on the 1D SWNT. The one-dimensional phonon energy dispersion curves for a SWNT are related to those of graphene by:

$$\omega_{1D}^{m\mu}(k) = \omega_{2D}^{m}\left(k\frac{K_2}{|K_2|} + \mu K_1\right), \begin{pmatrix} m = 1, \dots, 6 \\ \mu = 0, \dots, N-1 \end{pmatrix} and \; -\frac{\pi}{T} < k \leq \frac{\pi}{T}$$

k is the one-dimensional wavevector along the axis of the tube. K_2 is the reciprocal lattice vector along the nanotube axis, K_1 is the reciprocal lattice vector in the circumferential direction, N is the number of hexagons per unit cell, and T is defined in expression 1.8 and Figure 1.3a.

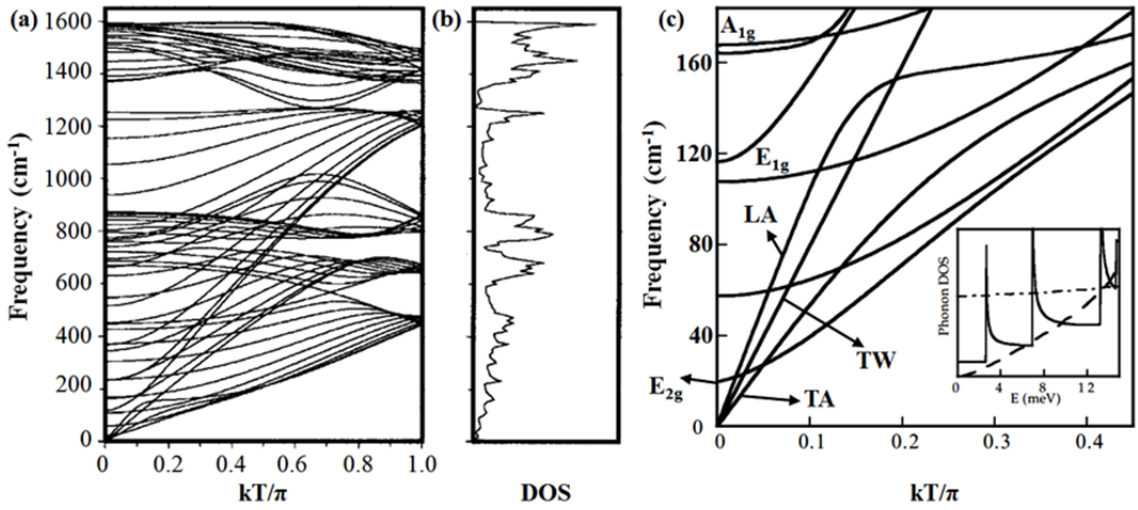

***Figure 1.18**: (a) The calculated phonon dispersion relations of a (10,10) SWNT. (b) The corresponding phonon DOS in units of state per C atom per cm^{-1} (adapted from [55]). (c) Low-energy phonon dispersion relation for this nanotube; the inset in Figure 1.13c shows the low-energy phonon DOS of nanotubes (solid line), and that of graphite (dashed line) and graphene (dot-dashed line) (adapted from ref [55]).*

The previous expression means that, for a SWNT with an extended unit cell including 2N atoms, 6N phonon dispersion relations are folded into the one-dimensional Brillouin zone of a CNT along the K_2 direction. For instance, because the extended unit cell of a (10,10) nanotube includes 40 atoms, we have 120 vibrational degrees of freedom. However, due to mode degeneracies, there are only 66 explicit phonon branches (12 modes are non-degenerate and 54 are doubly degenerate). In Figure 1.18, an example of the phonon dispersion for (10,10), calculated by using zone-folding approach, is displayed.

However, the zone folding method has two main limitations.

First, it does not predict the presence of the low-frequency radial breathing mode (RBM) which is a specific mode of nanotube. Also, it does not predict that the Raman-active G-mode is composed of two modes, namely: the LO and TO G-modes that arises from the lifting of the degeneracy due to curvature effects of the iLO and iTO branch of graphene.

Among the large number of the phonon modes in carbon nanotubes, only few of them are Raman-active. The displacements associated to the Raman active modes are shown in Figure 1.19. As it will be discussed in the following (chapter 2), the main important modes are modes with A_{1g} symmetry, namely: the radial breathing mode (RBM), predicted around 165 cm^{-1}, and the G-modes (or tangential modes) located around 1587 cm^{-1} in (10,10) SWNT (Figure 1.19).

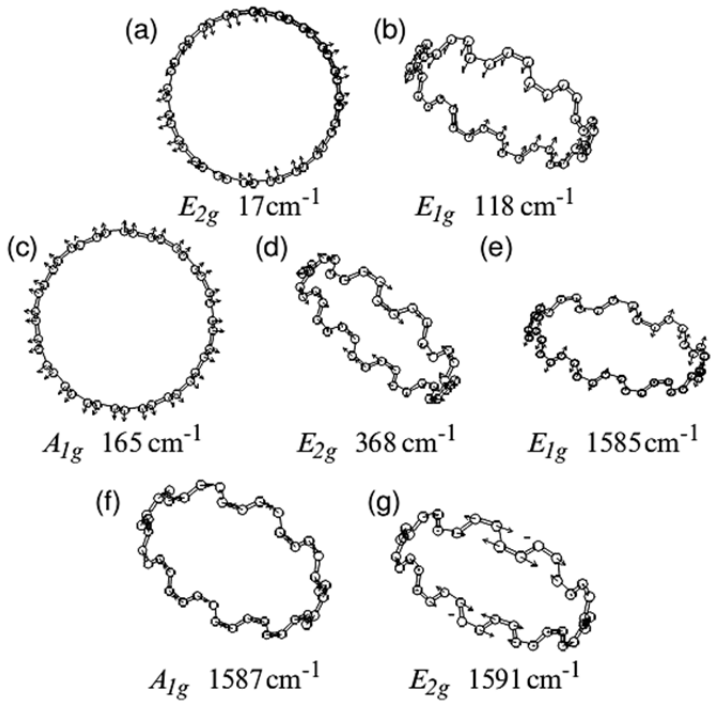

Figure 1.19*: The Raman-active modes of the (10, 10) SWNT: symmetries, frequencies, and atomic displacements (adapted from ref [55]).*

PART B: structure and electronic properties of DWNTs

1.6. Double-walled carbon nanotubes: an overview

In this part, we briefly summarize the structure and electronic properties of DWNTs. The features of phonons in these nanostructures, which are at the center of my thesis, will be detailed in another chapter.

1.6.1. Structure

A double-wall carbon nanotube (DWNT) is the simplest system of multi-walled carbon nanotubes (MWNT). A DWNT consists of two concentric and weakly van der Waals coupled SWNTs and is uniquely characterized by the chiral indices (n_i,m_i) and (n_o,m_o) of the constituent inner and outer SWNTs respectively. Usually, the structure of a DWNT is identified as: $(n_i,m_i)@(n_o,m_o)$.

The distance between the inner and outer tubes: $\Delta=(d_o-d_i)/2$, (d_o (d_i) is the diameter of the outer (inner) tube), depends on the composition of the DWNT. It was found that Δ ranges from 0.3 nm to 0.4 nm, with an average distance around 0.34 nm, which is close to the inter-layer distance in graphite.

A DWNT can be either commensurate, when inner and outer walls have commensurate carbon lattices, or incommensurate when inner and outer walls have incommensurate carbon lattices. It is almost impossible to observe experimentally a commensurate DWNT because the probability is very low to find two commensurate SWNTs with the radius difference matching the tube-tube separation.

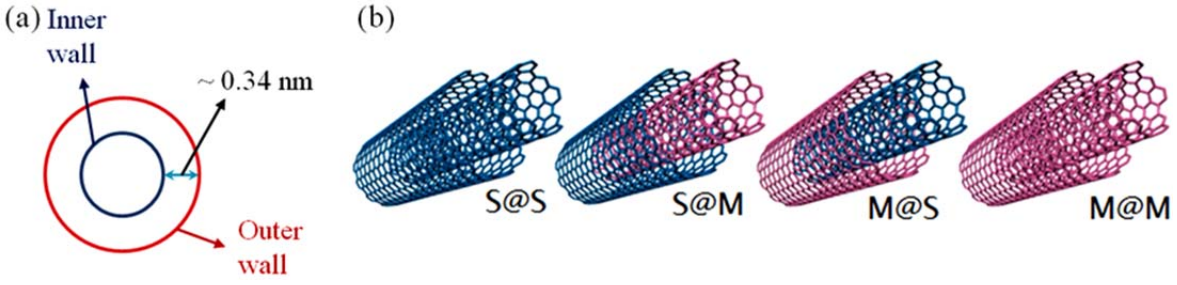

***Figure 1.20**: (a) An illustration of the DWNTs structure and (b) the four possible DWNT configurations.*

The inner and outer tubes (from now, also called 'layer') can be either semiconducting (SC) or metallic (M). Consequently, DWNTs display four different configurations, namely SC@SC,

SC@M, M@SC and M@M (inner@outer tubes), which possess distinct electronic properties. All the properties of DWNTs are related to the individual nature of each layer and their interactions [56]. The various wall-to-wall distances can affect the behavior of DWNT by changing the strength of the intertube interactions [57, 58].

DWNTs appear as a prototypal nanomaterial for studying coupling, layers interactions and screening effects at the nanoscale [59-63]. Moreover, the small diameters of inner walls enable to study more deeply high-curvature effects.

1.6.2. Electronic structure

The electronic structure of DWNT depends not only of the electronic bands of the constituent SWNTs but also on their inter-wall interactions.

It is generally believed that the inter-tube coupling does not strongly modify the energy bands of the SWNTs which form the DWNT (Figure 1.21a). This is more or less true when the two SWNTS have a common periodicity along the tubes (commensurate structure) [52]. However, very few DWNTs have commensurate structure and the rest of them do not have the well-defined periodicity (incommensurate structure). Even in commensurate DWNT, the effect of the curvature can lead to specific changes of the electronic features. For instance, the band structures of commensurate (7,0)@(15,0) DWNT were calculated and compared to those of constituent zigzag SWNTs (Figure 1.21b) [64]. Notice that the gap exhibited by the (15,0) SWNT is already due to the curvature effect. The result shows that, in the DWNT, the electronic band of the inner wall (7,0) is much more strongly downshifted than that of the outer wall (15,0). Due to the strong downshift of the conduction band of the inner tube, the valence band and conduction band of the inner tube overlaps, the crossing of two bands defining the Fermi level in this DWNT, and the combination of two zigzag semiconducting SWNTs leads to a metallic DWNT.

The situation is different and more complex for incommensurate DWNTs. It was shown recently that the combinations of SWNTs with almost the same physical properties such as diameter and energy gap can end up with very different DWNTs depending on the interlayer Moiré interferences (Figure 1.21d) [65]. The new and specific electronic bands of incommensurate DWNTs can dramatically influence its optical absorption, photoluminescence, electronic transport, and Raman scattering.

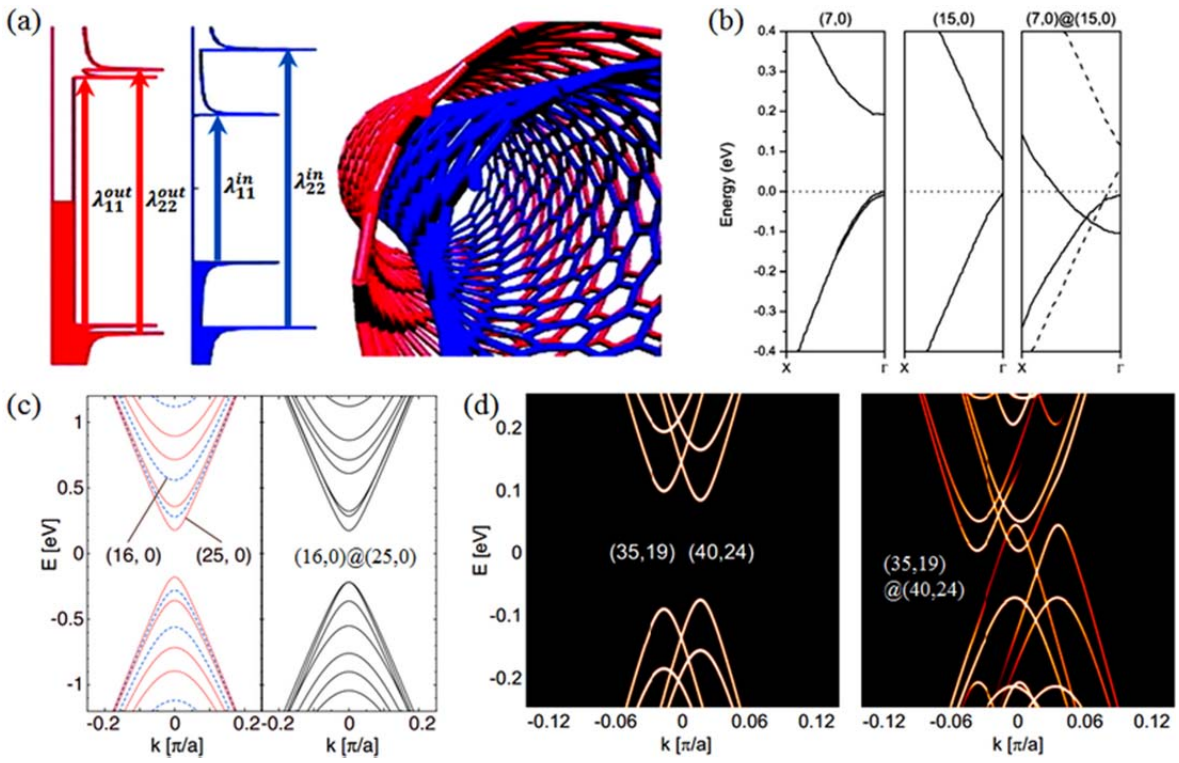

Figure 1.21*: (a) Schematic of two electronic structure DWNTs (adapted from [65]). (b-d) Band structure calculations of different DWNTs: (b) The band structures of commensurate zig-zag (7,0)@(15,0) DWNT. (adapted from ref [64]). (c) The band structures of commensurate zig-zag (16,0)@(25,0) DWNT without and with inter tube coupling (adapted from ref [65]). (d) The band structures of the incommensurate (35,19)@(40,24) DWNT without and with inter tube coupling (adapted from ref [65]).*

Summary

Because the basic building-block of all the DWNTs is a single-walled carbon nanotube, the fundamental physics including structural, electronic, optical and vibrational properties of SWNTs have been reviewed in detail.

The structure and electronic bands of DWNTs have also been introduced. It has been emphasized that the electronic properties of incommensurate DWNTs can be far beyond a simple sum of electronic bands of the two constituent SWNTs. This result can have important consequences for the understanding of the resonant Raman spectra of DWNTs.

CHAPTER 2 : PHONONS IN INDIVIDUAL SINGLE- AND DOUBLE-WALLED CARBON NANOTUBES: A STATE-OF-ART

2.1. The Raman scattering process

Raman spectroscopy is based on the analysis of inelastic scattered light. Historically, Raman scattering occurs from optical modes of vibrations of atoms or molecules of a gas, liquid, or solid. However, other excitations such as magnons, plasmons or even electronic excitations provide sources for the Raman process. My work focused on Raman scattering occurring by phonons in carbon nanotubes

From a classical approach, Raman scattering originates from the modulation by the vibrations of systems of the electronic polarizability of molecules, (susceptibility in crystals), induced by the excitation light. For a complete description of the first-order Raman process, and especially the so-called resonant Raman process, it is necessary to use the quantum approach. In this approach, the excitation of an electron by an incident photon is anticipated. This excitation is followed by a recombination with the simultaneous emission of a photon with an energy different than the incident one. Since energy and momentum must be conserved, the generation (Stokes process) or absorption (anti-Stokes process) of a quantum of vibration (phonon in crystals) is required during these two processes. The first-order of Stokes Raman process is illustrated in Figure 2.1.

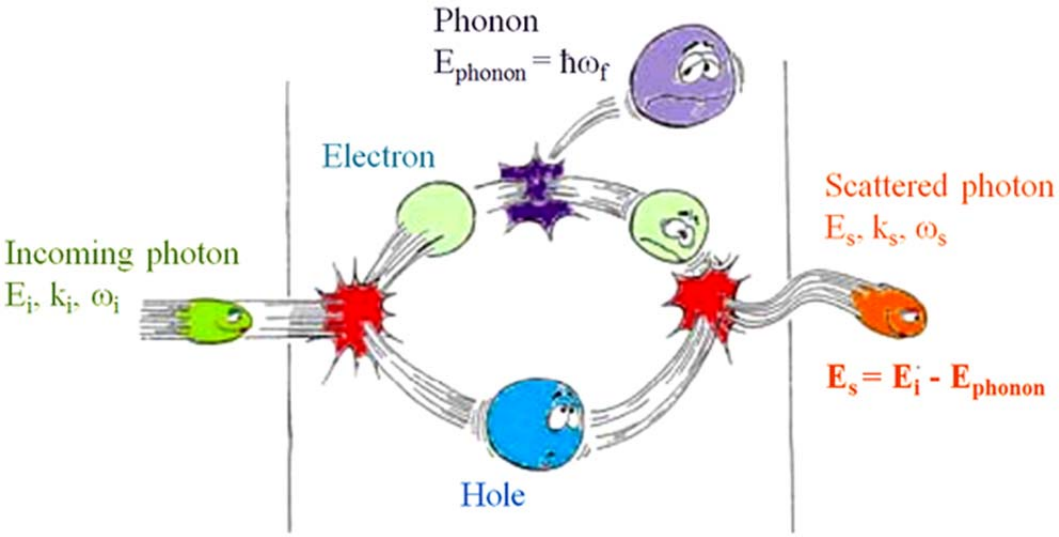

Figure 2.1*: Schematic picture of first-order Raman process (Stokes process) [66].*

Raman spectroscopy is used to measure the scattered photon intensity as a function of the Raman shift, which is the difference of energy (usually expressed in cm^{-1}) between the incident photon and the scattered photon [54, 67-69]. The Raman shift is a direct measure of the energy (frequency) of the Raman-active vibration modes of the system under investigation.

In terms of transitions, the final state of the system, f, is reached from the initial, state, i, via an intermediate state, z. The final state differs from the initial state by the generation (Stokes process) or absorption (anti-Stokes process) of a quantum of vibration, $\hbar\omega_{phonon}$. Usually the intermediate state, z, is a virtual state because the energy of the incident photon is smaller than the energy of the gap in insulating crystals or in large gap semiconducting (or smaller than the HOMO-LUMO difference in molecules). When the energy of the incident (or scattered) photon matches the energy of the intermediate state, the Raman process is resonant. For incident photon in the visible range, the Resonant Raman scattering (RRS) process arises in metallic systems or small gap semi-conductors.

The main consequence of the resonance is a significant dependence of the intensity of the spectra with the energy of the excitation, with a large enhancement of the intensity of the Raman modes when the excitation energy matches the energy of one of the optical transitions of the system. Notice that, at the resonance, the vibration modes which have a strong electron-phonon coupling are especially enhanced. An enhancement factor as high as 10^3 has been measured [68].

2.2. The resonant Raman scattering process in SWNTs

Raman spectroscopy is a powerful tool to characterize semiconducting or metallic SWNTs. In addition, the resonance process allows measurement either on an ensemble of SWNTs or on individual SWNTs.

Beyond the first order Raman scattering (Figure 2.2), the specificity of the Raman spectra of graphene, and SWNTs is to contain second-order Raman peaks with a relative strong intensity. Second order processes involve: (i) one phonon and a defect or (ii) two phonons. Intra-valley or inter-valley scattering processes are allowed. The intra-valley scattering connects different k states around the same K (or K') points. The inter-valley scattering involves different k states of K and K' together. The details of these two processes for a metallic SWNT (or graphene) are illustrated in Figure 2.2 for both incident and scattered resonance.

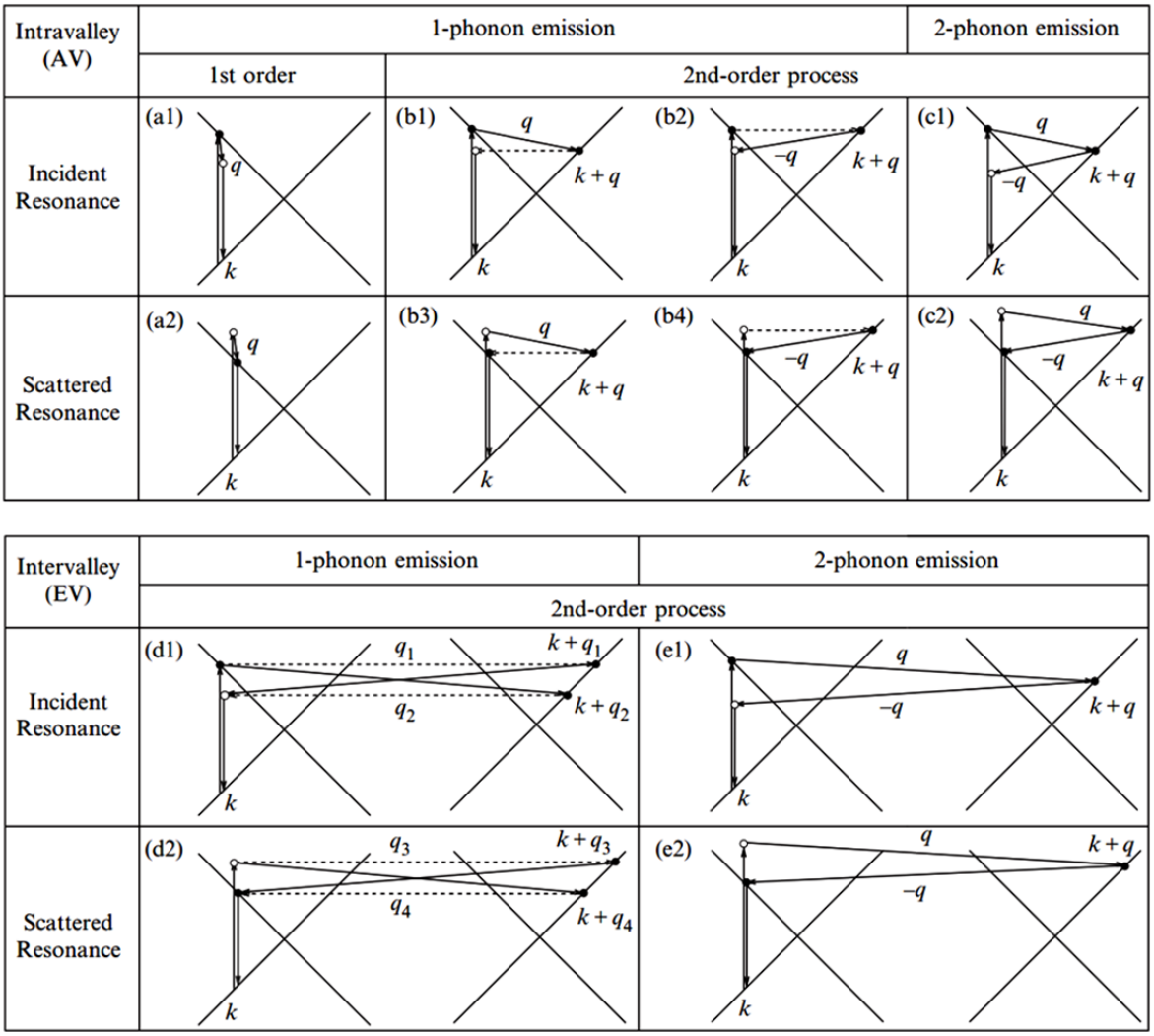

***Figure 2.2**: Intra valley scattering (AV, top) [70]: (a1, a2) First-order process, and (b1, b2) second-order process involving one-phonon and a defect, (c1, c2) two-phonon second-order process. Resonance on the incident light (top) and resonance of the scattered light (bottom). In the second order process, the scattering by the defect is an elastic scattering (dashed lines). Resonance points are shown as solid circles. Inter valley scattering (EV, bottom) [71]: (d1,d2) second-order process involving one-phonon and a defect, (e1,e2) two-phonon second-order. The upper (lower) row corresponds to incident (scattered) resonance conditions.*

2.3. Phonon modes of SWNTs

The first order Raman spectroscopy gives information of the phonons at the center of the Brillouin zone, Γ. Second-order Raman processes can give access to phonons at other points of the Brillouin zone. Process involving a defect can active silent Raman modes. A specificity of the Raman spectrum of graphene and SWNTs is that the second-order spectra can be intense. This is in particular the case of the 2D band (or G' band) in graphene which is usually more intense than the G-mode.

In SWNTs, the RBM and G-band are phonon of the center of the Brillouin zone, Γ; the D mode (activated by the scattering via a defect) involves phonons near of the K point; these phonons contribute to the 2D band.

2.3.1. The radial breathing modes

In SWNTs, a low frequency mode of A_{1g} symmetry, the so-called radial breathing mode (RBM), appears typically in the range 100-400 cm^{-1}. This vibrational mode corresponds to an in-phase displacement of the carbon atom in the radial direction at the surface of the nanotube, *i.e.* it is an oscillation of the diameter. An important feature of this mode is that its frequency varies as the inverse of the tube diameter. In a lot of SWNTs, it was found experimentally that the RBM frequency follows the relation (see Figure 2.3):

$$\omega_{RBM} = A/d_t + B$$

The parameters A and B strongly depend on the environment of the SWNTs. The Table 2.1 lists the various relationships RBM frequencies as function of nanotubes diameter for SWNTs prepared in different conditions with various environments. Recent experimental and theoretical works suggest using the "universal" expression to describe the dependence of the RBM frequency on diameter:

$$\omega_{RBM} = \frac{227}{d}\sqrt{1 + C_e \cdot d_t^2}$$

The C_e parameter is related to environmental conditions. C_e is equal to 0 for environment-free SWNTs.

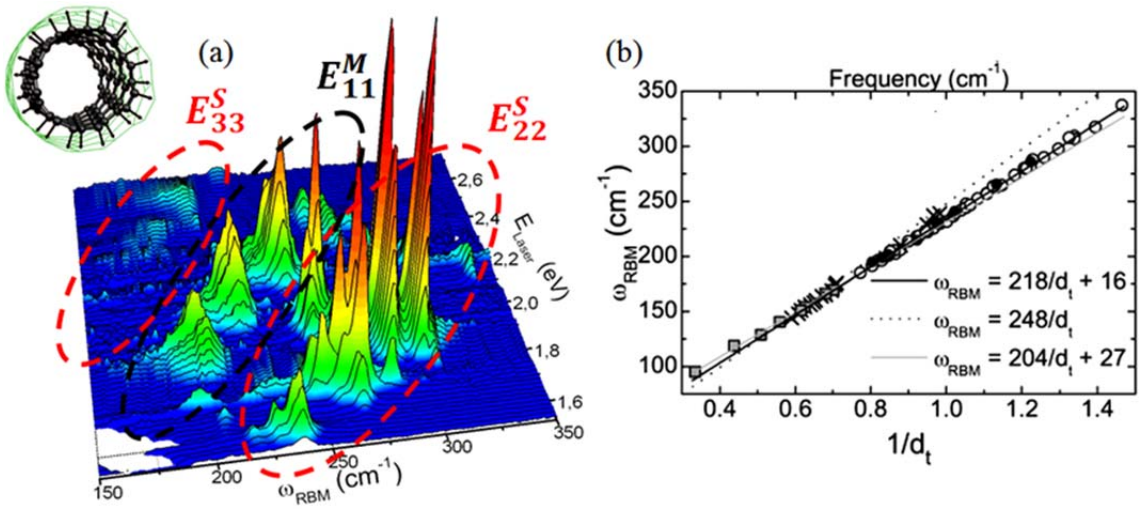

***Figure 2.3**: The Radial breathing modes of CNTs (a) the arrows show the phonon eigenvector (upper) and RBM Raman mapping of HiPCO-SWNTs dispersed in SDS aqueous solution (lower) [72]. (b) The RBM frequencies versus diameter with different environment and their fit by the $\omega_{RBM} = A/d_t + B$ relation: CVD SWNTs on SiO_2 (crosses) (adapted from ref [73]), HiPCO SWNTs on SiO_2 (solid circles), HiPCO SWNTs in SDS (open circles) (adapted from ref [28]), free-standing SWNTs (gray squares) (adapted from ref [74]).*

Sample	A	B
Alcohol-assisted CVD SWNTs [32]	217	15
Water-assisted CVD SWNTs [75]	227	0
Laser ablation bundled SWNT [76]	232	0
SWNTs on silicon substrate [73]	248	0
HiPCO SWNTs SDS-dispersed [28]	223.5	12.5
HiPCO SWNTs SDS-dispersed [77]	214.4	18.7
HiPCO SWNTs SDS-dispersed [72]	218	17
HiPCO SWNTs SDS-dispersed [78]	227	7.3/11.8
Free-standing SWNTs (d = 1.3 -3 nm) [74]	204	27
Suspended SWNTs (d > 2nm) [79]	228	0

***Table 2.1:** A and B values found in literature.*

2.3.2. The G modes

While in graphene, the longitudinal and transverse optical modes, located around 1580 cm^{-1}, are degenerated at the Γ point, and give rise to a single peak in the Raman spectrum; in a SWNT this mode is splitted into two G^+ and G^- modes. The dominant reason of this splitting is the curvature which leads to a rehybridization of the valence orbitals from sp^2 to sp^3-like [12, 54, 80]. In experiments performed on an ensemble of SWNTs containing nanotubes with different

diameters and chiralities, a bunch of G-modes is observed at high frequency in the 1530-1600 cm^{-1} range [80-83].

From experiments performed on individual index-identified SWNTs, it was established that only two G-modes (G^+ and G^- components) are present in the polarized (// //) Raman spectrum of a chiral SWNT (// means that the incident (scattered) polarization is along the tube axis), and only one G-mode (G^+ or G^- component) appears in the Raman spectrum of an achiral SWNT [84]. More precisely, each G component corresponds to the so-called LO or TO phonon [54]. The LO phonon in SWNTs is associated with C=C stretching vibration along the nanotubes axis. On the other hand, the TO phonon describes C=C stretching vibration along the circumference. Due to the large phonon energies of G band (around ≈ 0.2 eV), distinct resonances by incoming and outgoing photons can be observed [31, 85].

On the basis of symmetry arguments, the experiment performed on index-identified individual SWNT have definitively permitted to assign the intrinsic response of the chiral and achiral, metallic and semiconducting SWNTs, in the G-mode range:

- In chiral semiconducting SWNTs, the G^+ and G^- components, corresponding to LO and TO phonons respectively, are sharp and symmetric and each peak is described by a Lorentzian (Figure 2.4). In addition, the LO intensity is much higher than TO intensity due to the larger electron-phonon coupling for the LO mode than for the TO mode. It was predicted that the TO intensity increases with increasing the chiral angle from 0º to 30º [86]. For achiral semiconducting zigzag SWNT, a single component, assigned to the LO mode, is present in the spectrum [84].

- In chiral metallic SWNTs, only the higher frequency G^+ assigned to the TO mode is narrow while the G^- component assigned to the LO mode is broad. Notice that the assignment of the G^+ and G^- components is inversed in metallic and semiconducting SWNTs. Usually the profile of the LO mode is described by using a Breit-Wigner-Fano line shape [87]. This specific line shape arises from interference between the LO phonon and a continuum of the electronic states [88]. The softening of LO mode in metallic SWNTs with respect to the position of the LO mode in semiconducting SWNT, as well as the broadening of the mode, are the consequences of the electron-phonon coupling between the LO phonon and electrons close of the Fermi level leading to a Kohn anomaly in the dispersion curve of the LO mode near the Γ point [89]. From a general point of view, in a metal, it has been demonstrated that for certain phonons, $\omega(q)$, having a wavevector, q, connecting to point of the Fermi surface, one can observe an abrupt change of the electronic screening of the vibrations resulting in a sudden softening of the phonons frequencies, which is called Kohn anomaly. Increasing the chiral angle increases the TO mode intensity with respect to that of the LO mode [84]. For armchair metallic SWNT, the LO mode is

non-Raman active and only a narrow component assigned to the TO mode is observed [84]. Conversely, only the LO phonon mode is observed for zigzag metallic SWNTs. A summary about the features of G^+ and G^- components in metallic and semiconducting SWNTs are shown in the Table 2.2.

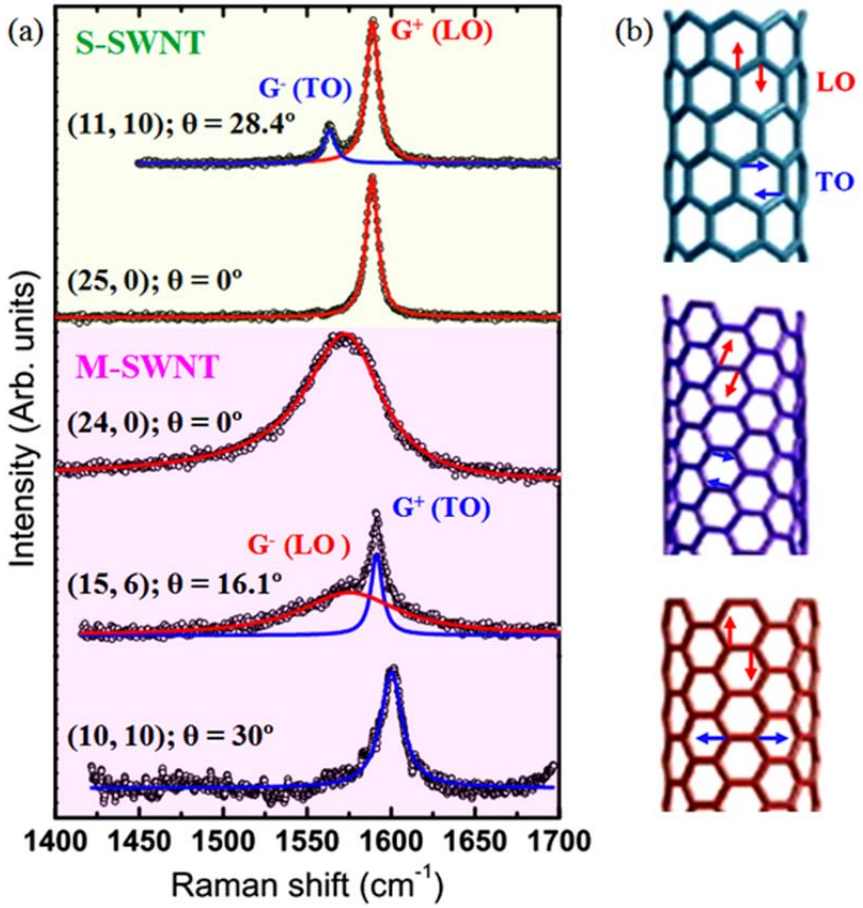

***Figure 2.4**: (a) G-mode part of the Raman spectrum of chiral and achiral semiconducting SWNTs (S-SWNT) and metallic SWNT (M-SWNT) (adapted from ref [84]). (b) The atomic displacements corresponding to LO (red arrows) and TO (blue arrows) modes in zig-zag (top), chiral (middle) and armchair (bottom) nanotubes.*

	Type nanotube	G^+	G^-
Phonon mode	Semiconducting	LO	TO
	Metallic	TO	LO
Frequency	Semiconducting	~ 1590 cm^{-1}	$\omega_{G^-} = \omega_{G^+} - C/d_t^2$ with C = 47.7 $cm^{-1}nm^2$ [81]
	Metallic	~ 1590 cm^{-1}	$\omega_{G^-} = \omega_{G^+} - C/d_t^2$ with C = 79.5 $cm^{-1}nm^2$ [81]
Line-shape	Semiconducting	Lorentzian	Lorentzian
	Metallic	Lorentzian	Breit-Wigner-Fano
Zig-zag ($\theta = 0^o$)	Semiconducting	Active	Not active
	Metallic	Not active	Active
Armchair ($\theta = 30^o$)	Metallic	Active	Not active

***Table 2.2**: The G^+ and G^- components in metallic and semiconducting SWNT.*

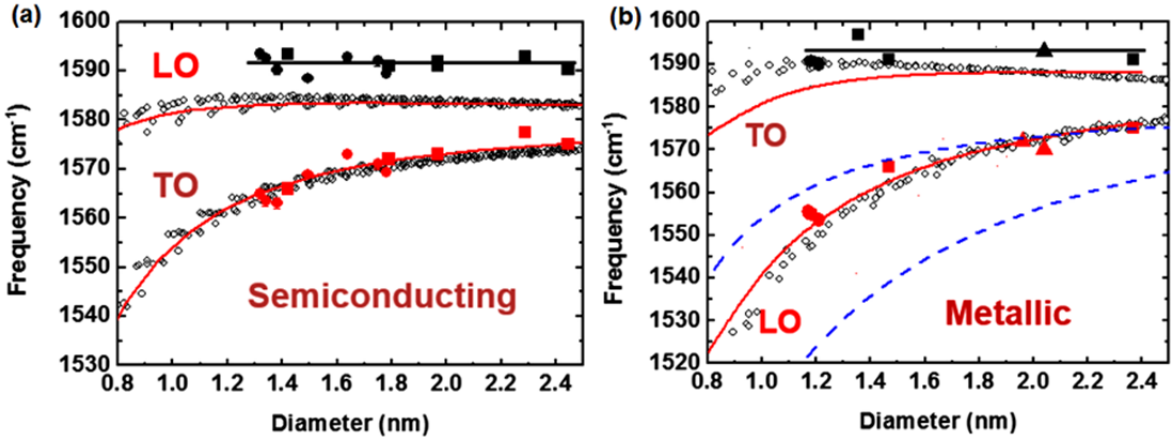

***Figure 2.5**: Diameter dependence of the frequencies of the LO and TO modes. (a) Semiconducting SWNTs: red dotted lines and white open symbols, calculated frequency using adiabatic calculation; black and red solid dots, experimental frequencies measured on identified individual SWNTs. (b) Metallic SWNTs: red dotted lines and white open symbols, calculated frequencies using non-adiabatic approach; dashed blue lines calculated frequencies using adiabatic approach; black and red solid dots, experimental frequencies measured on identified individual SWNTs. (adapted from ref [90]).*

Concerning the frequency, the G^+ peak of SWNTs slightly depends on diameter (for diameters larger than 1.3 nm) while the G^- peak is shown to decrease with decreasing nanotube diameter (Figure 2.5).

For semiconducting SWNTs, as mentioned above, the G^- component is assigned to the TO mode (atomic vibrations along the circumference). As shown in Figure 2.5a, its frequency decreases with the diameter in relation with the increasing of the curvature of the tube. Therefore, the curvature effects bend down the TO mode much more than LO one. The good agreement

between experimental frequencies, measured on individual semiconducting SWNTs, and theoretical frequencies calculated by using the adiabatic approximation must be emphasized.

For metallic SWNTs, the G^- component is assigned the LO mode. As shown in Figure 2.5b, the LO frequency significantly depends on diameter. Notice the strong disagreement between the experimental frequencies and the theoretical ones calculated by using the adiabatic approximation. One has to consider both non-adiabatic and curvature effects in order to obtain a reasonable agreement between experimental and theoretical LO frequencies [91] (Figure 2.5b).

2.3.3. The D-band and the 2D-band

A feature around 1340 cm^{-1}, the so-called D mode, originates from a double resonant Raman process which involves a phonon near of the K point and a defect (such as impurity, missing atoms, finite size effects and grafted molecules to the nanotubes side walls) [54, 92, 93]. The D mode is assigned to the breathing motion of six-fold rings (chapter 1 – Figure 1.17) near the K zone boundary. The D mode intensity increases with increasing the number of defects in the carbon wall [93]. The ratio of the D/G intensity is used to quantify the structural quality of CNTs [92].

The second order harmonic of the D band appears around 2700 cm^{-1} [69]. It is the result of a double resonance process which involves two D-phonons near of the zone boundary. This band is often called 2D mode (or G') and it is always Raman active independently of the in-plane disorder.

2.4. Phonon modes of DWNTs

2.4.1. The radial breathing like modes (RBLMs)

As previously reminded, it is well known that the RBM frequency of SWNT depends on the inverse of the nanotube diameter. Because a DWNT is formed by two concentric SWNTs of different diameters two RBM are expected at distinct frequencies. In DWNT, because the RBM can differ from the RBM of constituent SWNTs, they are called RBLM. In Figure 2.6, the region of RBLMs of the Raman spectra measured on an ensemble of DWNTs in suspensions (Figure 2.6a) and on a free-standing individual DWNT (Figure 2.6b) are presented. The spectra for the DWNTs in suspension were excited at 1.77 eV (Figure 2.6a). As expected, the RBLMs divide into low- (< 220 cm^{-1}) and high-frequency (> 220 cm^{-1}) ranges which are assigned, in a first approximation, to the RBLM of the outer and inner tubes, respectively. In Figure 2.6b, the RBLM parts of the Raman spectra measured on an individual (12,8)@(16,14) DWNT are shown. As expected, only two RBLMs are observed.

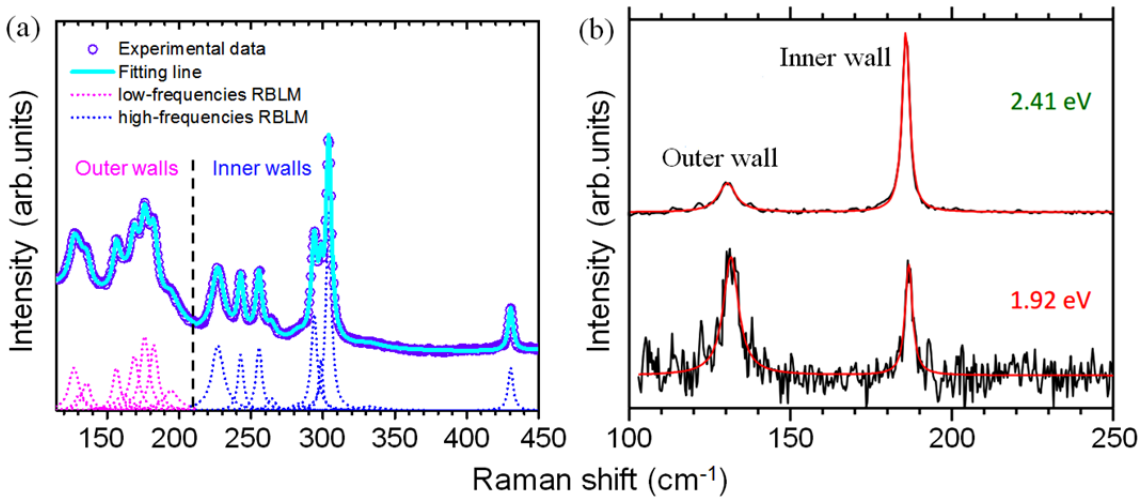

Figure 2.6*: The RBLM region of the Raman spectrum of DWNTs. (a) measured on an ensemble of DWNTs* E_{laser} *=1.77 eV. The vertical dashed line separates the RBLM of the inner and outer tube (solid lines are the results of the fit of the different peaks). (b) Free-standing individual (12,8)@(16,14) DWNT,* E_{laser} *=2.41eV (top) and 1.92eV (bottom) (adapted from ref [60]).*

V. N. Popov *et al.* [59] calculated the RBLM of individual DWNTs. Due to the van der Waals coupling between inner and outer tubes, different behaviors than the ones found in individual SWNTs are predicted. Two types of model, namely atomistic model, and a continuum model, are used [21]: (i) an atomistic model, based on a lattice-dynamical model, DWNTs are seen as two coaxial cylindrical carbon layers. The dynamical matrix is calculated thanks to the combination of valence- force field type (intra tube interaction) and Lennard-Jones type (inter tube interaction). (ii) a continuum model which considers the nanotube layers as homogeneous

cylindrical surfaces with constant surface mass density. Both calculations predict that the coupled RBLM frequencies are always higher than the uncoupled ones as shown in Figure 2.7c. The eigenmodes of inner and outer tubes combine into a counter-phase RBLM and in-phase RBLM, respectively (Figure 2.7a and b).

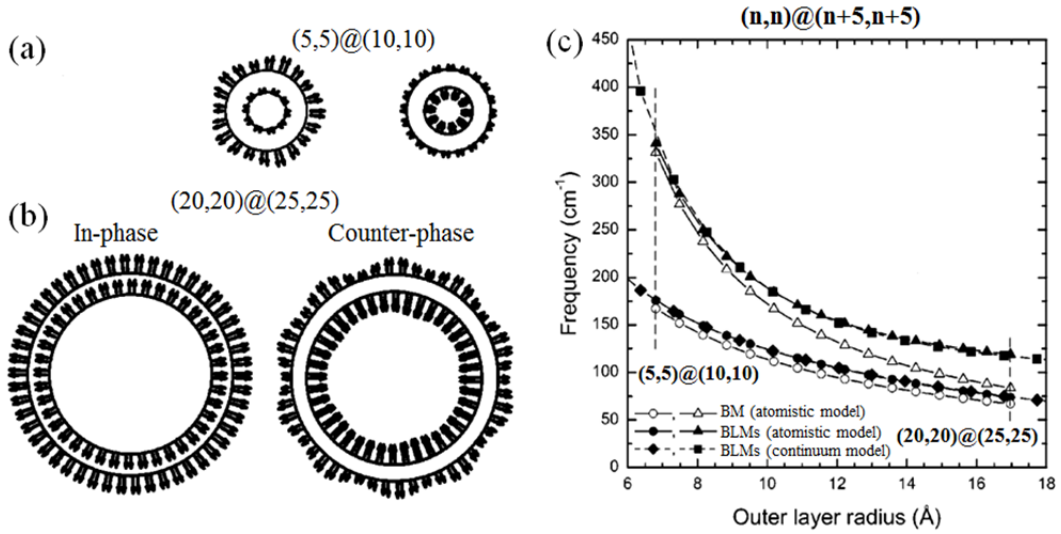

Figure 2.7*: (a) In-phase and out-of-phase RBLM for tubes of small diameters. (b) In-phase and out-of-phase RBLM for tubes of large diameters (c) Open symbols, RBM frequencies of corresponding inner and outer SWNTs as a function of the outer tube diameter; solid symbols, frequencies of the in-phase and out-of-phase RBLM as a function of the outer tube diameter in DWNTs. (adapted from ref [59])*

The calculations also state that for small diameter below 2 nm, for example (5,5)@(10,10), the interlayer interaction is small and the RBLM of DWNTs is dominated by either outer or inner wall. For the larger nanotube, for instant (20,20)@(25,25), the RBLM of DWNTs is a collective motion of both layers. This phenomenon leads to the strong upshift of RBLM in DWNTs as compared to the RBM of corresponding SWNTs. Furthermore, the author also suggested that the mechanical coupling vanishes when the interlayer distance is larger than 0.4 nm.

The first observation of RBLMs in individual index-identified DWNT was reported by D. Levshov *et al.* [60] thanks to the combination of Raman spectroscopy and electron diffraction [60]. The authors observed that both coupled RBLMs will be resonantly excited if an electronic transition of either wall matches the excitation energy. In addition, the measured RBLM values were compared with two expressions of individual SWNTs: $\omega_{RBM} = 228/d$ [79] or $\omega_{RBM} = 204/d + 27$ [74]. As expected, the results show a significant upshift of these RBLMs as compared to those RBMs of corresponding SWNTs.

Recently, Liu *et al.* [62] measured the RBLMs of 13 individual index-identified DWNTs The low and high-frequency RBLM are called ω_L and ω_H respectively. Notice that the values of the inter-tube separation range from 0.34 to 0.37 nm. They calculate the RBLM vibration in the

framework of two coupled harmonic oscillators. The van der Waals force constant, k_c, between the two layers are obtained for each tube by adjustment to find the best agreement between experimental and calculated frequencies of both RBLMs. From the values of k_c, the authors derive the average unit-area force constant owing to the tube-tube interaction for the different inter-tube separation. These force constants are compared with the van des Waals interaction between graphene sheets under pressure obtained from compressibility measurements. By this way, these authors have been able to connect the interlayer distance with an internal effective pressure. They found that for interlayer distance larger (smaller) than 0.34 nm a negative (positive) pressure occurs between the tubes. Negative (positive) pressure means that the inner-outer interaction causes a slight contraction (expansion) of the outer tube concomitant with the expansion (contraction) of the inner tube [60].

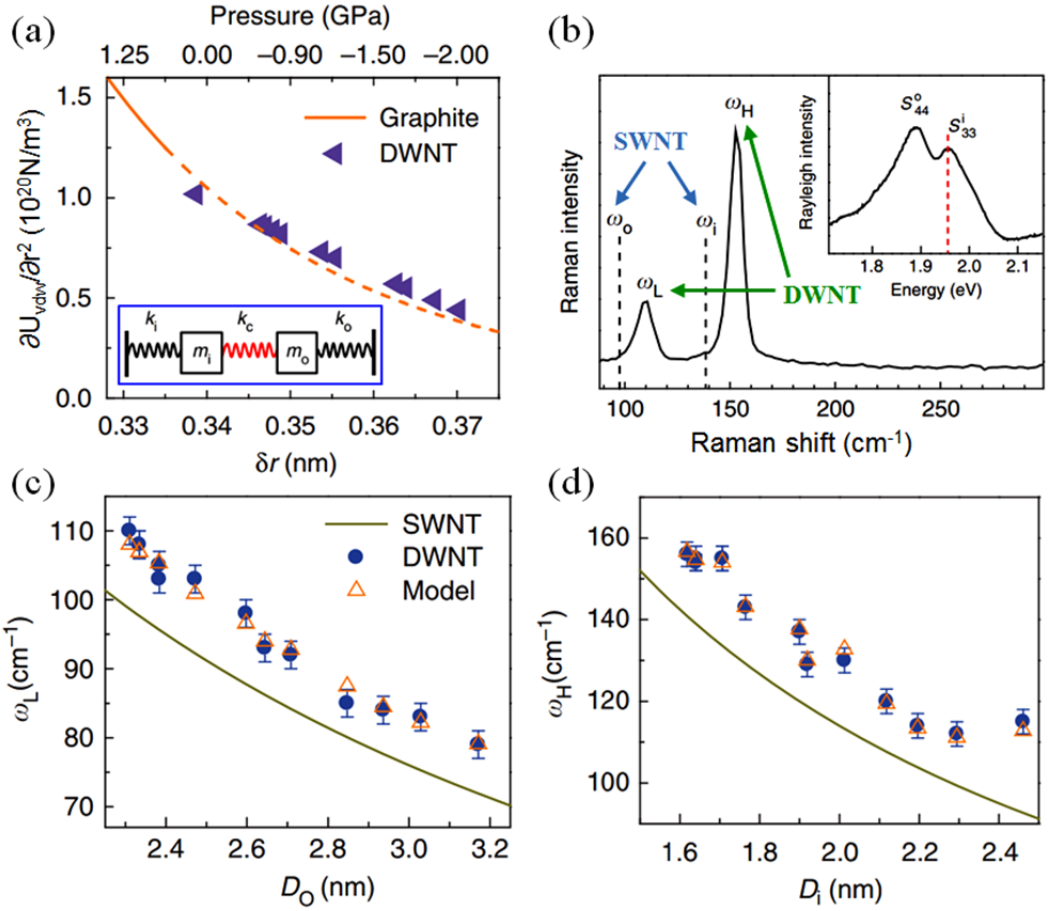

Figure 2.8*: RBLMs in DWNTs (adapted from [62]). (a) Derived unit-area force constant owing to tube–tube van der Waals interaction, $\partial^2 U_{vdw}/\partial r^2$, for different inter-tube separation (triangles), and the comparison to results from high-pressure graphite measurements (line), inset: the coupled oscillator model, (b) RBLMs spectrum for a DWNT as compared to the corresponding positions in SWNTs, (c) ω_L versus outer nanotube diameters (dots), (d) ω_H versus inner nanotube diameter.*

2.4.2. The G modes of DWNTs

Figure 2.9 presents the G-modes part of the Raman spectra measured on ensemble of DWNTs in suspensions and on a free-standing individual DWNT. In Figure 2.9a, we see that the G-band of DWNTs suspensions contain a sum of overlapped pairs of G^+ and G^- modes which correspond to the G-modes of outer and inner tubes present in the sample. For the individual free-standing DWNT (12,8)@(16,4), two G^- components are clearly observed in the spectrum excited at 2.41 eV and assigned to the TO G-modes of each tube. For this (12,8)@(16,4) DWNT, it must be emphasized the two G^- components have frequencies close to the ones of the TO G-mode of the corresponding outer and inner SWNTs. This example underlines that detailed information concerning G-modes can only be obtained from Raman experiments on individual DWNT.

To precise the dependence of the G-modes as a function of the inter-tube distance was one of the objectives of my PhD work. Consequently, new additional results concerning the G-modes of DWNTs will be presented and deeply discussed in the chapter 4.

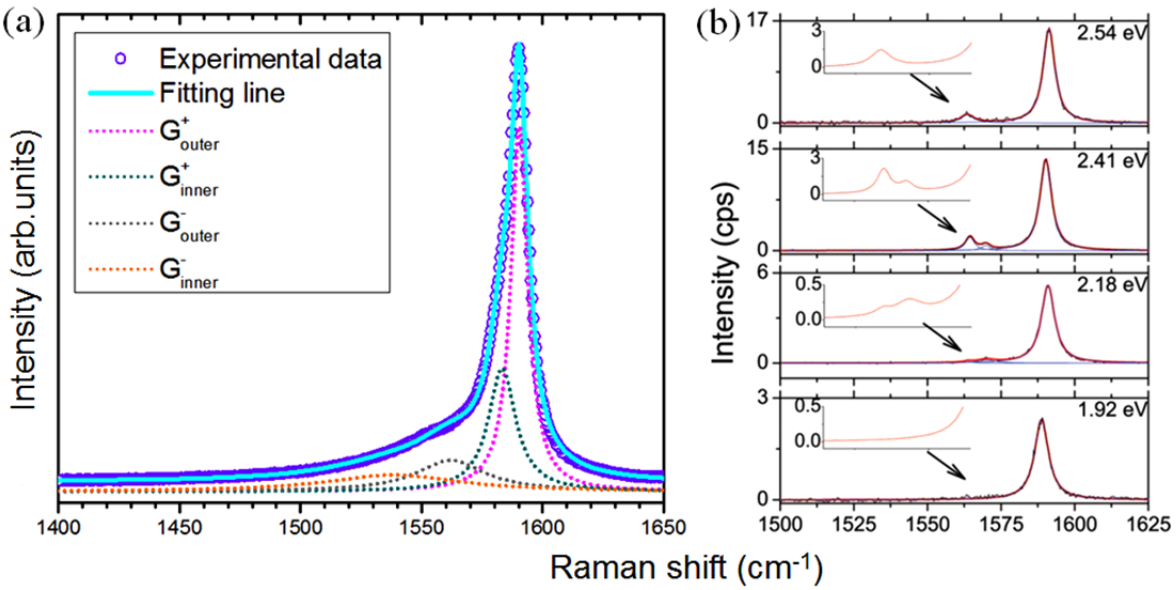

***Figure 2.9**: Raman spectra of DWNTs G modes. (a) G modes pristine DWNTs suspension at 1.77 eV. The fit frequencies of G modes of inner and outer walls for p-DWNTs. (b) The G modes of free-standing individual DWNT (12,8)@(16,4) at several excitation energies (adapted from ref [60]). Inset: zoom of the G^- band in the 1550 – 1585 cm^{-1} frequency range.*

Summary

In this chapter, information on phonons in SWNTs and DWNTs were reviewed.

For SWNTs, we remind: (i) the frequency of RBMs depend not only on nanotubes diameter but also on the surrounding medium. (ii) In semiconducting SWNTs, the frequency of TO G-mode significantly increases with increasing of nanotube diameter. In metallic SWNTs, a non-adiabatic approach has to be used to describe the main features of the G-modes: softening and broadening of the LO G-mode.

For DWNTs, we remind: (i) the measured frequency of RBLMs breaks down the conventional relationship between the frequency and the diameter established in SWNTs. The RBLM frequencies depend either on the diameters and inter-tube separation. Due to the coupling, both RBLMs can appear for the same excitation energy despite that only one tube is in resonance condition. (ii) Precise information on the G-modes can only be obtained from measurements on individual DWNT.

PART A: THE INTRINSIC OPTICAL AND PHONON PROPERTIES OF INDIVIDUAL CARBON NANOTUBES

CHAPTER 3 : INTRINSIC PROPERTIES OF INDIVIDUAL SINGLE-WALLED CARBON NANOTUBES

One important part of my PhD concerns the understanding of the intrinsic properties of single-walled carbon nanotubes (SWNTs), with a peculiar attention on the intrinsic properties of semiconducting SWNTs (S-SWNTs). In the first part of this chapter, we will assign the chiral indices (n,m) of S-SWNTs by combining the information derived from Raman and electron diffraction measurements (section 3.1). These assignments are used to understand the absorption data reported in section 3.2. In the following of this chapter, we will present and discuss some results obtained by Raman spectroscopy on individual SWNTs. The following items shall be covered:

- Band-to-band vs. excitonic transitions to describe the shape of Raman excitation profiles (REPs) (section 3.3).
- The effects of the quantum interferences on the Raman intensity of the LO and TO G-modes (section 3.4).
- The change of TO/LO intensity ratio with the order of the optical transition (section 3.5).

3.1. Assignment of SWNTs by combining electronic diffraction and Raman spectroscopy

In this section, we derive the structural characteristics of individual free-standing SWNTs by combining the information obtained from electron diffraction and Raman spectroscopy experiments. In order to illustrate our approach, we discuss two opposite situations. A first example illustrates the possibility to extract unambiguously the (n,m) indices of a SWNT by this way. By contrast, in a second example, we can only propose a few possible assignments for another investigated SWNT.

Electron Diffraction (ED) is considered to be the most accurate technique to assign the structure of nanotubes. However, in some cases such as high tilt angle (the angle between the normal to the e-beam and the nanotube axis), low-quality of the electron diffraction patterns (EDPs), due for example to vibrations of the nanotube under the electron beam, or nanotubes with large diameters, ED can fail to give unambiguous index-assignments. In such cases, Raman spectroscopy gives additional information which can allow to precise the assignment of the nanotubes.

3.3.1. First example of the structural assignment of an individual suspended SWNT

In the Figure 3.1, we show the low and high-resolution TEM images and the electron diffraction pattern (EDP) measured on an individual suspended SWNT, the so-called: SWNT1. The analysis of the EDP provides the following values of the chiral angle with a relatively good accuracy: 12.85 ± 0.2°. However, this chiral angle cannot be assigned specifically to one tube only. On the other hand, from the TEM image and the analysis of the EDP pattern, the tube diameter is estimated as 2.28 ± 0.45 nm.

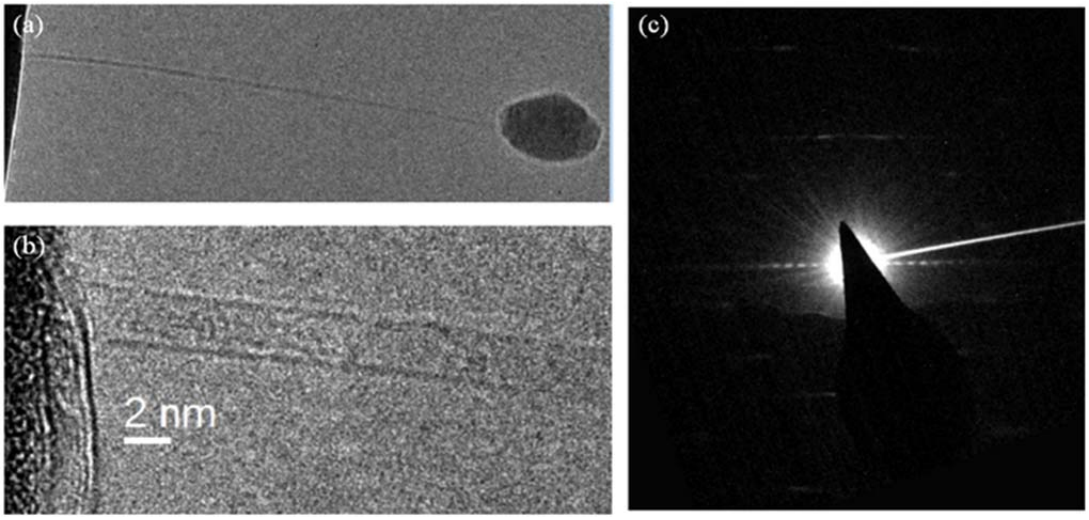

Figure 3.1: *(a) Low- (b) high-resolution TEM image measured on the individual SWNT1. (c) the corresponding electron diffraction pattern.*

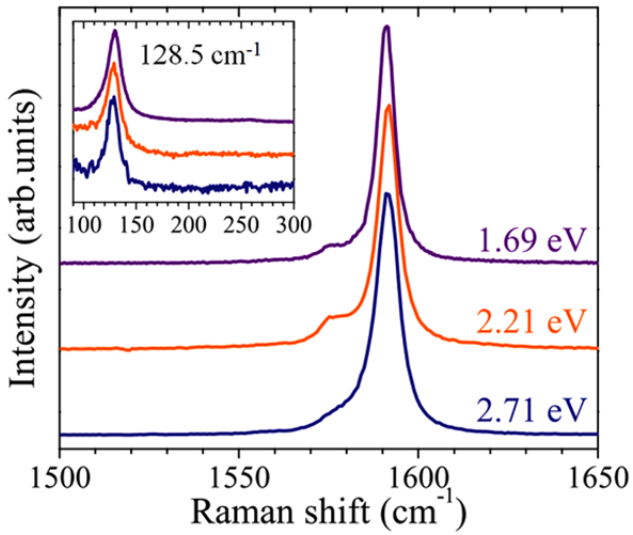

Figure 3.2: *RBM (inset) and G-modes regions of the Raman spectra of SWNT1 for three excitation energies: 1.69 eV, 2.21 eV and 2.71 eV.*

Raman measurements were performed at different excitation wavelengths; some representative spectra are shown on Figure 3.2. From the G-bands line-shape, we can infer that SWNT1 is semiconducting and chiral. The RBM is located at 128.5 ± 3 cm^{-1} (inset of Figure 3.2). The relationship between the RBM frequency and the tube diameter is:

$$\omega_{RBM}[cm^{-1}] = 204/d[nm] + 27 \qquad (3.1)$$

By applying the relation 3.1, the diameter of SWNT1 is estimated as 2.01 ± 0.04 nm. Note that the error bar is underestimated since we only take into account the experimental error (± 2 cm^{-1}) and do not consider the own uncertainty of the relation 3.1.

In order to assign the (n,m) indices of SWNT1, we gather the TEM-ED and Raman information in the graph shown on Figure 3.3.

On this graph:

- The chiral angle is set from the value measured by electron diffraction with an error bar of ± 0.2° corresponding to the yellow area in the Figure 3.3.
- The brown dashed line indicates the diameter of nanotube derived from electron diffraction (in Figure 3.3). Due to the poor accuracy in the evaluation of diameter by ED, we consider a broad range of error bar, namely: ± 0.45 nm. The blue dashed line indicates the diameter obtained from the RBM frequency.
- We only consider the possible nanotubes which are inside the yellow area.

The presence of two narrow and symmetric peaks in the G-mode range states that SWNT1 is a chiral semiconducting SWNT (S-SWNT). Consequently, four possible S-SWNTs are compatible with the TEM and EDP information, namely: (20,6), (23,7), (27,8), and (29,9) SWNTs. However, as summarized on the table 3.1, we show that the calculated RBM frequency (the theoretical diameter of each (n,m) SWNT is considered in the 3.1 equation), and the theoretical value of the chiral angle of the (23,7), show the best agreement with the RBM frequency measured by Raman, and the chiral angle derived from EDP. Therefore, we conclude that the most probable assignment for the SWNT1 is **(23,7).**

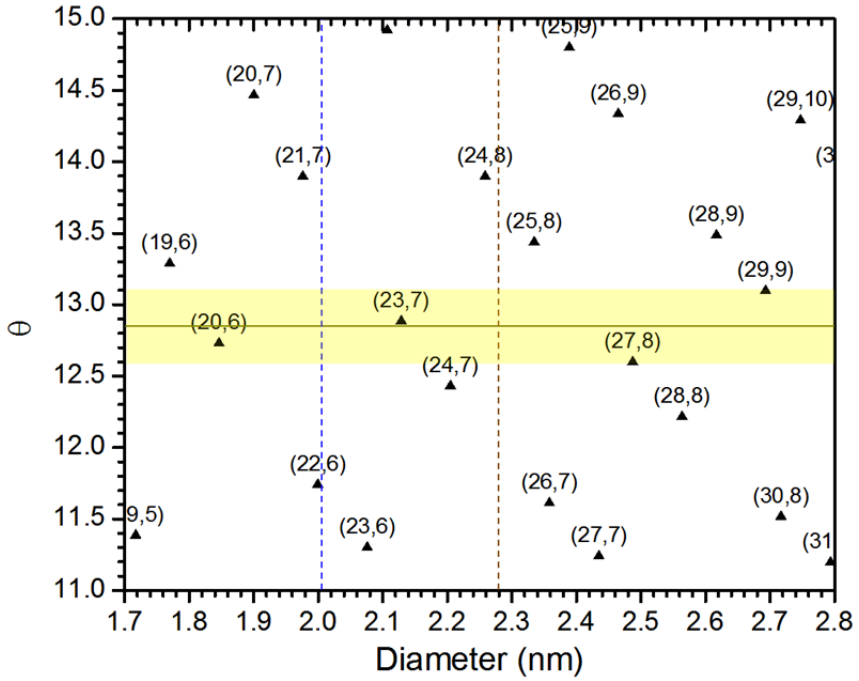

Figure 3.3: *The chiral angle as function of diameters for semiconducting nanotubes (black triangles with each (n,m) labeled). The horizontal dark solid line indicates the 12.85° chiral angle (derived from EDP). The yellow area represents the diameter/angle region derived from TEM, and EDP, and Raman data. The vertical yellow (blue) dash line corresponds to the diameter of SWNT1 obtained by TEM/ED (RBM).*

	Raman	EDP	(20,6)	(23,7)	(27,8)	(29,9)
Diameter (nm)		2.28 ± 0.45	1.846	2.129	2.487	2.693
Chiral angle (°)		12.85 ± 0.2	12.73	12.89	12.6	13.1
ω_{RBM} (cm^{-1})	128.5		137.5	122.8	109	102.7

Table 3.1*: The diameters, chiral angles and RBM frequencies of the four possible candidates as compared to the experimental diameter, chiral angle and RBM frequency.*

3.3.2. Second example of the structural assignment of an individual suspended SWNT

In the Figure 3.4, we show two high-resolution images and the EDP measured on the SWNT called: SWNT2. Due to the vibration of the suspended nanotube under the electron beam during the experiment, the quality of the HRTEM images and EDP is relatively poor and does not permit to determine the chiral angle and the diameter of this tube with a good accuracy. From the analysis of the EDP patter, the chiral angle is estimated as 1.24±1°. From the TEM images, and the EDP pattern, the diameter is estimated as 2.5±0.5 nm.

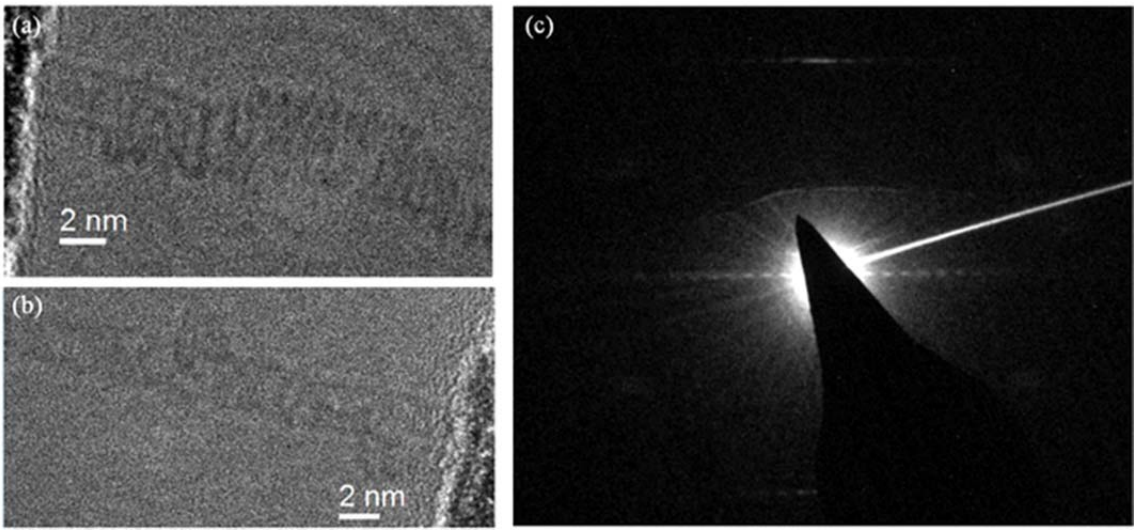

Figure 3.4: *(a,b) High-resolution TEM images of two part of the individual SWNT2. (c) The corresponding electron diffraction pattern.*

The Raman spectra of SWNT2, recorded at different excitation energies, are displayed on Figure 3.5. From the G-band profile, we state that the SWNT2 is a chiral semiconducting SWNT. Its RBM is located at 118 ± 2 cm^{-1} (inset of Figure 3.5). By applying the equation (3.1), the diameter is evaluated as 2.24 ± 0.05 nm. Note that the error here is underestimated since we only take into account the experimental error (± 2 cm^{-1}) and do not consider the uncertainty of the relation 3.1.

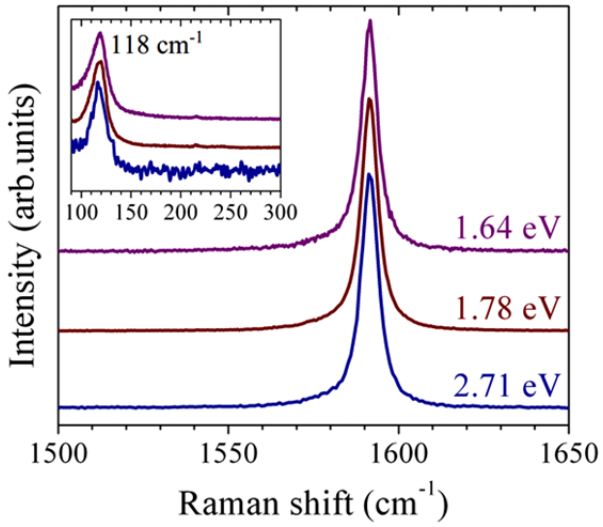

Figure 3.5: *RBM (inset) and G-modes regions of the Raman spectra of SWNT2 for three excitation energies: 1.64 eV, 1.78 eV and 2.71 eV.*

Using the same procedure as the one used previously for SWNT1, and by combining the high-resolution TEM, ED and Raman information, we find six possible (n,m) assignments, namely: (26,1), (27,1), (29,1), (30,1), (32,1), (33,1), (35,1), (36,1).

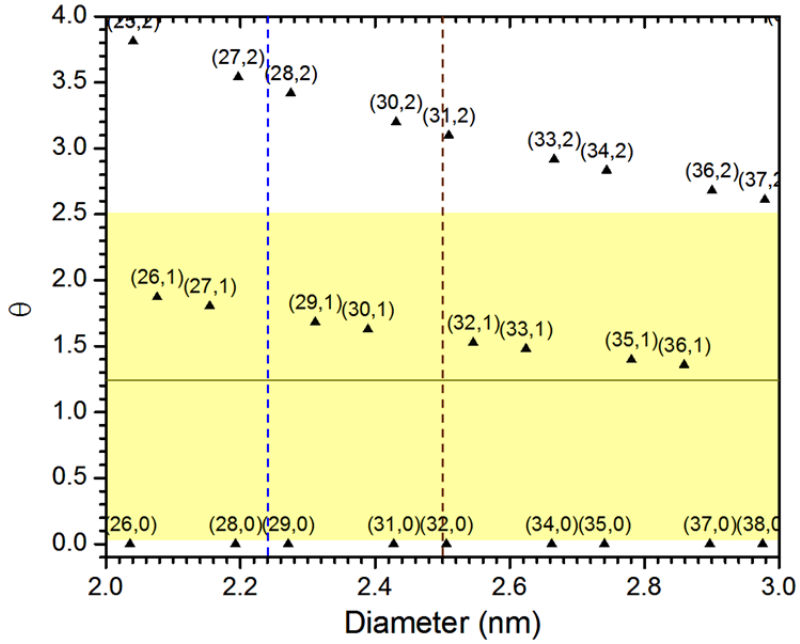

Figure 3.6: *The chiral angles as function of diameters for semiconducting nanotubes (black triangles with each (n,m) labelled). The horizontal dark solid line indicates the 1.24° chiral angle (derived from EDP). The yellow area represents the diameter/angle region derived from TEM, and EDP. The vertical yellow (blue) dash line corresponds to the diameter of SWNT1 obtained by TEM/ED (RBM).*

	Raman	EDP	(26,1)	(27,1)	(29,1)	(30,1)	(32,1)	(33,1)	(35,1)	(36,1)
Diameter (nm)		2.5 ± 0.5	2.076	2.154	2.311	2.389	2.546	2.624	2.781	2.859
Chiral angle (°)		1.24 ± 1	1.872	1.804	1.682	1.626	1.526	1.481	1.397	1.359
ω_{RBM} (cm^{-1})	118		125.3	121.7	115.3	112.4	107.1	104.7	100.3	98.4

Table 3.2*: The diameters, chiral angles and RBM frequencies of the eight possible candidates for SWNT2 as compared to the experimental diameter, chiral angle and RBM frequency.*

In the Table 3.2, we summarized the calculated RBM frequencies and chiral angles for all candidates. Four of them, namely: (26,1), (27,1), (29,1), and (30,1) lead to the best agreement with the experimental data. Due to the proximity of diameters, angles and RBM frequencies for these four SWNTs, no single assignment emerges for the SWNT2. In the next section, we will compare the optical transition energies measured on SWNT2 by absorption spectroscopy with those found in literature for the four possible candidates. From this comparison, the (n,m) assignment of SWNT2 will be achieved.

3.2. Absorption spectroscopy on individual suspended SWNTs

The spectral absolute absorption cross-section of individual semi-conducting SWNTs has been determined by using spatial modulation spectroscopy. These experiments were carried out by J.-C. Blancon and collaborators of the Institut Lumière Matière in Lyon (for detail see, ref. [94, 95]). In the presentation of our results, for simplicity, we write absorption spectroscopy instead of spatial modulation spectroscopy.

3.2.1. Absorption spectroscopy of SWNT1

The absorption cross-section per unit length of the (23,7) SWNT (SWNT1), measured by absorption spectroscopy, and for the incident light polarized along the nanotube axis, is shown on Figure 3.7. Three absorption peaks are observed at 1.66, 2.21 and 2.61 eV.

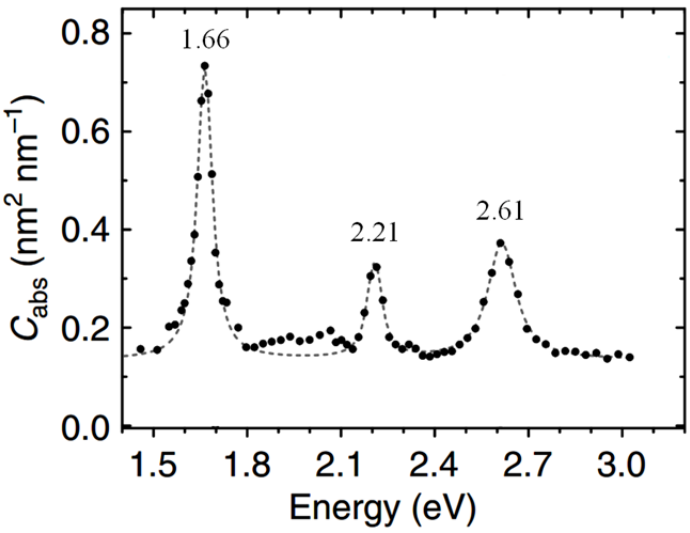

Figure 3.7: *Absorption spectroscopy of the individual free-standing SWNT1. The dash line is the result of a fit (for details, see Ref. [94, 95]).*

In the Table 3.3, the energies of the optical transitions calculated by V. N. Popov [31, 96] and measured/extrapolated by F. Wang's group [33] for the (23,7) SWNT are listed and compared to our experimental data. The experimental half-width at half-maximum (HWHM) of each peak is also given (it was derived by the fit of the absorption peak (see Ref. [94, 95]). A good agreement between calculated and experimental energies (within 60 meV) is found.

	(23,7)		Absorption measurement	
			Energy	HWHM (meV)
	V. Popov	F.Wang		
E_{33}^{S} (eV)	1.72	1.69	1.66	27.5
E_{44}^{S} (eV)	2.21	2.23	2.21	25.5
E_{55}^{S} (eV)	2.58	2.57	2.61	51

Table 3.3*: Energies, (and widths) of the optical transitions of (23,7) SWNT1 measured by absorption spectroscopy, and calculated in ref. [31, 33, 96].*

3.2.2. Absorption spectroscopy of SWNT2

Figure 3.8 presents the absorption cross-section per unit length of the SWNT2, measured by absorption spectroscopy for incident light polarized along the nanotube. Four absorption peaks are observed at 1.64, 1.79, 2.5 and 2.62 eV.

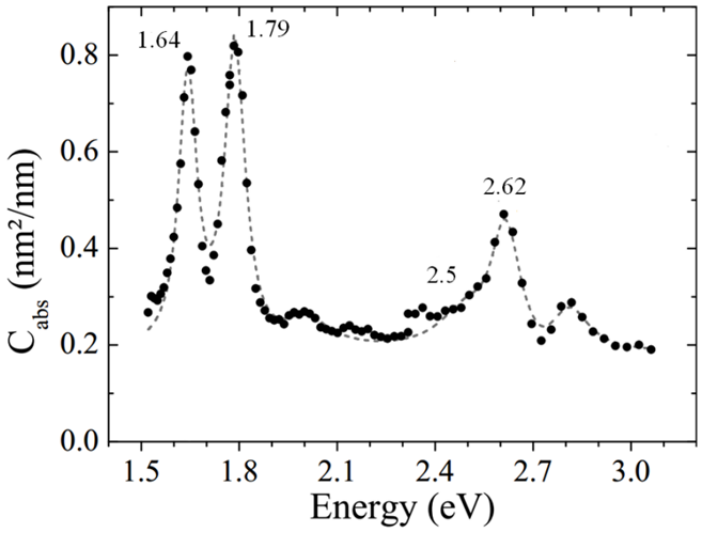

***Figure 3.8**: Absorption spectroscopy of the individual free-standing SWNT2. The dash line is the result of a fit (for details, see Ref. [94, 95]).*

In the Table 3.4, we list the optical transitions calculated by V. N. Popov and measured (or extrapolated) by F.Wang's group for the four (n,m) SWNTs proposed from the analysis of the EDP and Raman data. These energies are compared to the experimental transition energies measured by absorption spectroscopy on SWNT2. Clearly, the calculated transition energies of the (30,1) SWNT are closer to the ones measured by absorption than the calculated energies of the (26,1), (27,1) and (29,1) SWNTs. Consequently, the most probable assignment of ***SWNT2 is (30,1).***

	(26,1)		(27,1)		(29,1)		(30,1)		Absorption measurement	
									Energy	HWHM (meV)
	Popov	F.Wang	Popov	F.Wang	Popov	F.Wang	Popov	F.Wang		
E^S_{33} (eV)	1.744	1.70	1.852	1.81	1.622	1.55	1.716	1.67	1.64	30.5
E^S_{44} (eV)	2.28	2.33	1.976	1.94	2.084	2.09	1.834	1.81	1.79	35.5
E^S_{55} (eV)	2.606	2.56	2.78	2.95	2.418	2.40	2.584	2.71	2.50	97
E^S_{66} (eV)	3.354	3.41	2.986	2.68	3.126	3.13	2.732	2.54	2.62	40

***Table 3.4**: Energies, and widths of the optical transitions of SWNT2 measured by absorption spectroscopy. The experimental energies are compared with the calculated energies of the (26,1), (27,1), (29,1) and (30,1) SWNTs, reported in Ref. [31, 33, 96]).*

It has to be noticed that in the paper concerning the absorption spectroscopy of individual SWNTs [94, 95], the assignment of a few tubes slightly differs with the ones reported in the present work: for example (22,6) instead of (23,7) for SWNT1. For the study concerning the first evaluation of the absolute absorption cross-section of individual SWNTs [94, 95], no ED information of the investigated nanotubes was available and the assignment was only derived by combining Raman and adsorption spectroscopy. It must be emphasized that the slight difference between present and previous assignments does not change the conclusions of the preceding paper about the values of the absorption cross-section of individual SWNTs.

3.3. Band-to-band vs. excitonic transitions

3.3.1. The single Raman resonant process

In the Figure 3.9, the level transition diagrams for non-resonant and resonant first-order Raman processes are reminded.

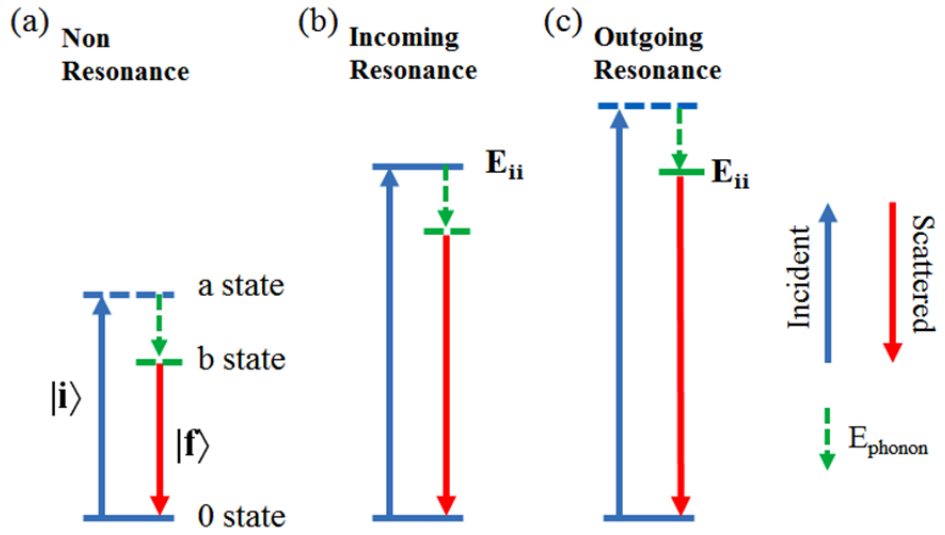

Figure 3.9: *Scheme of Raman processes for (a) non-resonant process, (b) incoming and (c) outgoing resonance process. 0, a and b refer the ground state, excited and scattering states (adapted from ref. [12]).*

In chapter 2, the Raman scattering process in SWNTs and DWNTs was discussed with their corresponding phonon modes. Basically, in a first-order Raman process, the Raman shift of the mode (RBM, RBLM and G-modes) is independent on the excitation energy but its intensity strongly depends on the excitation energy. In Stokes process, resonant Raman scattering (RRS) occurs if either the incident excitation energy matches a real state of the CNT (incoming resonance) or the energy of scattered photon matches a such CNT state (outgoing resonance) (see Figure 3.9b and c respectively).

To follow the changes of the Raman intensity with the excitation energy, the experimental Raman signal has to be calibrated versus the signal of a reference sample (here, we chose silicon) for each incident laser wavelength, and corrected from the response of the spectrometer.

The Raman efficiency of a bulk material for Stokes scattering, *i.e.* the number of photons emitted per incident photons per unit length and solid angle dΩ is given by [12]:

$$\frac{dS}{d\Omega} = \frac{1}{V}\frac{d\sigma}{d\Omega} = \frac{\omega_1\omega_2^3}{4\pi^2}\frac{\eta_1\eta_2^3}{c^4}\frac{V_c N}{(\hbar\omega_1)^2}\sum_f \left|K_{2f,10}\right|^2 [N(\omega)+1] \qquad (3.2)$$

This Raman cross section is proportional to $\left|K_{2f,10}\right|^2$.

$K_{2f,10}$ is the Raman matrix element which is expressed as [12]:

$$K_{2f,10} = \sum_{a,b} \frac{\langle \omega_2,f,i|H_{eR,\rho}|0,f,b\rangle\langle 0,f,b|H_{ep}|0,0,a\rangle\langle 0,0,a|H_{eR,\sigma}|\omega_1,0,i\rangle}{(E_l - E^e_{ai} - i\gamma)(E_l - \hbar\omega - E^e_{bi} - i\gamma)} \qquad (3.3)$$

where |ω, p, c> means: |photon state, phonon state, electronic state>

For instance:

- $|\omega_1, 0, i\rangle$ indicates that the present state is defined as: photon of energy $E_l = \hbar\omega_1$, no phonon, electronic state i.
- The final phonon state is denoted by f. It corresponds to the creation of a phonon in the exited state b.
- Initial and final electronic states are assumed to be the same. The sum is over all possible intermediate electronic states a and b.
- E_l is the excitation energy of the incident laser.
- γ is the resonance window which is related to the inverse lifetime of excited electronic state (the photoexcited carriers). The lifetime of the photoexcited carrier is calculated by the transitions probability for emitting phonon through the electron-phonon (or exciton-phonon) interaction. The calculation of γ value for S-SWNTs suspension as a function of (n,m) showed that they are dependent on nanotubes types and inversely proportional to the diameter [97]. Usually, the lifetimes, γ, of the various excited states are taken to be the same in expression 3.2.
- E^e_{ai} is the energy differences between the electronic states a and i (excited and ground state respectively).
- ħω is the phonon energy.

There 3 terms in the numerator can be described as follows:

- $\langle 0,0,a|H_{eR,\sigma}|\omega_1,0,i\rangle$ is the matrix element for the coupling between electrons (e) and the incoming radiation R (with polarization σ). A photon ω_1 is absorbed, and an electron-hole pair is created.
- $\langle 0,f,b|H_{ep}|0,0,a\rangle$ is the matrix element for the coupling between electron (e) and phonon (p). This step corresponds to the scattering of the electron from state a to

b, and the creation of a phonon. After interaction, the electronic state is b and the phonon state is f.

- $<\omega_2, f, i|H_{eR,\rho}|0, f, b>$ is the matrix element for the coupling between electrons (e) and outgoing radiation R (with polarization ρ). It describes the recombination of the electron-hole pair and the emission of a scattered photon, ω_2.

There 2 terms in the denominator:

- The first one gets small if the incoming photon energy matches the energy of the real excited electronic state E_{ii}. This corresponds to the incoming resonance.
- The second one gets small if the outgoing photon energy matches the energy of the real excited electronic state E_{ii}. This corresponds to the outgoing resonance.

In SWNTs, two processes can be considered to describe the Raman resonance scattering and then to calculate the element of the Raman matrix $K_{2f,10}$: (a) band-to-band transition and (b) excitonic transition. The first approach is based on the photoexcitation of an electron from valence band to conduction band. Whereas, the second involves the bound electron-hole pairs created by the excitation.

3.3.2. Band-to-band transition vs. excitonic transition

All the previous RRS studies devoted to the dependence of the Raman mode intensity on the incident excitation, the so-called resonance excitation profile (REP), evoke two models in order to explain the shape of REP measured on RBM and G-modes of SWNTs: band-to-band transitions and excitonic transitions. The difference between these two models is illustrated in Figure 3.10.

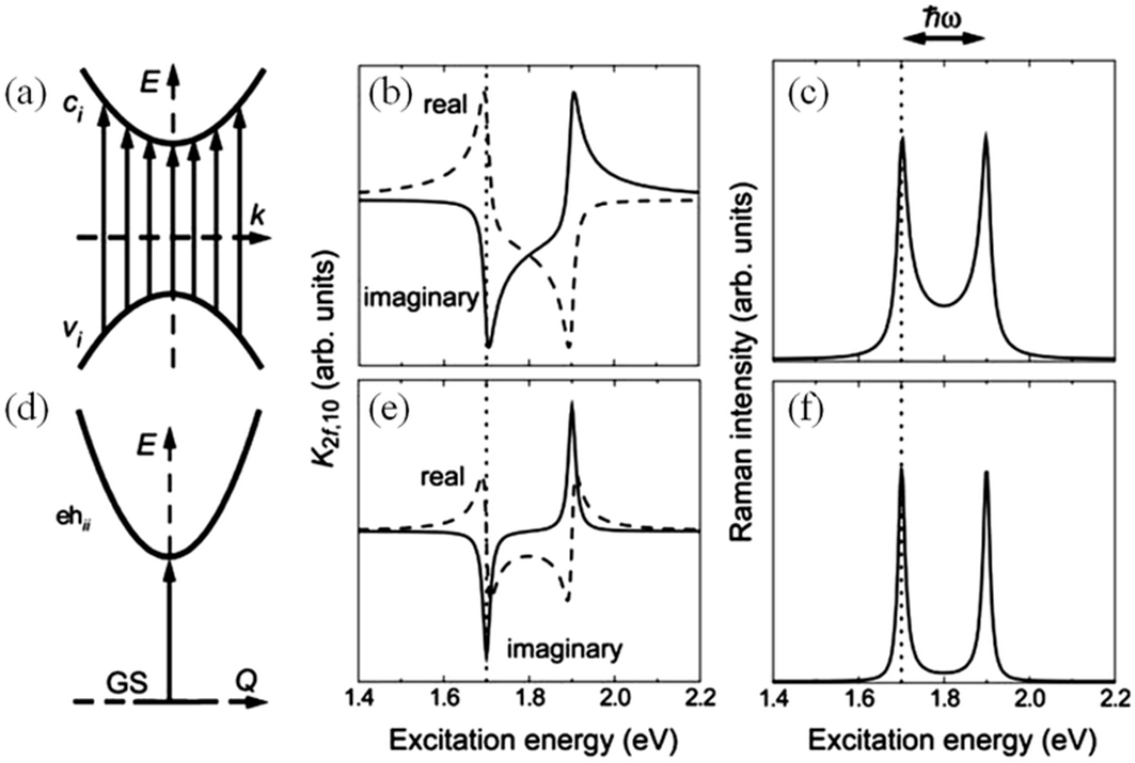

Figure 3.10: *(adapted from ref [12]). Band-to-band model: (a) Parabolic valence (v_i) and conduction (c_i) band with a gap E_{ii}. Optical excitations (arrows) are nearly vertical to conserve momentum. (b) Real (dashed line) and imaginary (solid line) part of the Raman matrix element $K_{2f,10}$ for band-to-band transitions with E_{ii} = 1.7 eV, ħω = 0.2 eV (1600 cm^{-1}), and γ = 0.01 eV. (c) Raman intensity* $\propto \left|\boldsymbol{K_{2f,10}}\right|^2$ *calculated from Band-to-band model: (d) Parabolic exciton dispersion eh_{ii} around Q = k_e + k_h. Optical excitations (arrow) occur at Q ≈ 0 only. (e) Real (dashed line) and imaginary (solid line) part of the Raman matrix element $K_{2f,10}$ for exciton, (f) Raman intensity calculated from Excitonic model.*

- Band-to-band model

The band-to-band transitions consider all the possible electronic transitions between valence and conduction bands. In a first approximation both bands have a parabolic shape. In the band-to-band model, there is more than a single transition which is involved. More precisely, all the band-to-band vertical transitions associated to different wave vectors, k, of the photo-excited electrons participate at the process (Figure 3.10a). Usually, the electronic bands are described by:

$$E^e_{ai}(k) = E^e_{bi}(k) = E_{ii} + \hbar^2 k^2 / 2\mu \qquad (3.4)$$

Where k is the magnitude of the electron wave vector and $1/\mu = 1/m_e + 1/m_h$ is the reduced effective mass.

For a one set of valence and conduction bands, the sum in 3.3 can be converted into an integral over k, in other words, over all possible vertical transitions. Abbreviating the numerator in 3.3 by M, this expression becomes [12]:

$$K_{2f,10} = \frac{L\sqrt{\mu/2}}{i\hbar^2\omega}\left(\frac{M}{\sqrt{E_l - E_{ii} - i\gamma}} - \frac{M}{\sqrt{E_l - \hbar\omega - E_{ii} - i\gamma}}\right) \qquad (3.5)$$

The resulting incident excitation dependence of the Raman intensity (proportional to $|K_{2f,10}|^2$), for a mode located at 1600 cm^{-1}, is shown in Figure 3.10c. The two maxima arise from the incoming resonance at E_{ii} (low-energy peak) and from the outgoing resonance at $E_{ii} + \hbar\omega$ (high-energy peak).

- Excitonic model

We now consider excitonic states as the intermediate states a, b in the Raman process. The evaluation of 3.3 is slightly different from the band-to-band model. For an excitonic model, the energies in 3.3 are exciton levels, called eh_{ii}:

$$E^e_{ai} = E^e_{bi} = eh_{ii}\ (Q \approx 0) \qquad (3.6)$$

In excitonic picture, there is only one transition at center, and no integration over the wave vector is needed because the exciton momentum Q is ≈ 0 for optical transitions (Q is the wave vector of the exciton $Q = k_e + k_h$). Considering excitonic transitions, the expression (3.3) has the following form [12]:

$$K_{2f,10} = -\frac{1}{\hbar\omega}\left(\frac{M}{E_l - eh_{ii} - i\gamma} - \frac{M}{E_l - \hbar\omega - eh_{ii} - i\gamma}\right) \qquad (3.7)$$

The Raman intensity shows two-peaks assigned to the incoming resonance and outgoing resonance (Figure 3.10f). However, the shape of REP is different of that predicted in band-to-band model.

To distinguish between these models, the γ parameter is a very important factor for two reasons:

- Resolving incoming or outgoing resonances depends on the width of the excited electronic state. If the resonance width is too broad compared to the energy of the phonon the two resonances cannot be resolved.
- By using the same value for γ=0.01 eV in the two models, we see that the shape of REP is sharper in excitonic model than that in band-to-band model. However, if

we reduce the γ value in band-to-band calculation, we can obtain a profile similar to the one found with excitonic model.

In general, γ is unknown, and it is rather difficult (impossible) to discriminate between the two models from the measurement of the resonance excitation profile of a mode by Raman spectroscopy. Therefore, we will show that combining Raman and absorption measurements on the same individual index-identified SWNTs, allows to distinguish between band-to-band and excitonic models. Indeed, γ is directly estimated from absorption measurement and this value is directly injected in the calculations of the Raman intensity (expressions 3.5 and 3.7).

3.3.3. Raman excitation profiles in SWNTs: a state-of-art

As reminded previously, in resonant Raman spectroscopy, the intensity of each Raman mode is strongly dependent on the excitation energy. In SWNTs, as illustrated in Figure 3.11, for each Raman active mode (here for RBM), there are two resonances corresponding to the incoming and outgoing resonance. These resonances are separated by the phonon energy. The so-called Raman excitation profile (REP) is the dependence of the intensity of a given mode on the laser excitation energy.

RBM

The REPs of low frequency RBM was reported in many publications [72, 77, 98-102]. Generally, the splitting between the incoming and outgoing resonance for Stokes Raman measurement is not observed because the width of the resonance is of the same order of magnitude than the RBM energy (~20 meV). The calculation of the REP for RBM suggests that the RBM resonance can only be resolved if the resonance window, γ, is extremely narrow [103].

Depending of the kind of SWNT and its environment, different values of the resonance width was found.

C. Fantini *et al.* [72] measured the both anti-Stokes and Stokes REPs of several RBM in aqueous suspension of individual SWNTs wrapped by SDS and in SWNT bundles. By using, the excitonic model, they derived a width of the resonance window, γ = 120 meV, significantly broader in SWNT bundle than in individual SWNTs (γ = 60 meV). Moreover, these measurement have also permitted to determine with a good accuracy the transition energy which is defined by the intersect point between anti-Stokes and Stokes REPs (Figure 3.11). Notice the redshift of the transition energy for SWNT in bundle.

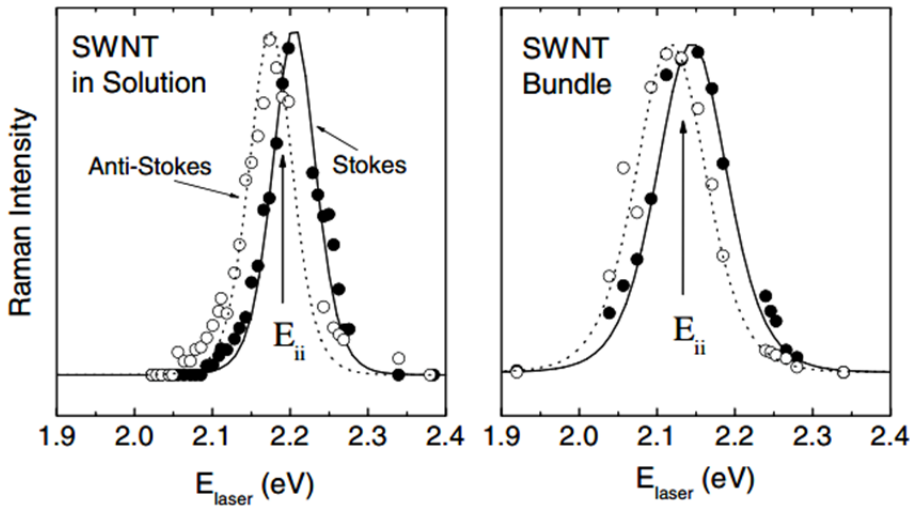

Figure 3.11: *Stokes (solid symbols) and anti-Stokes (open symbols) experimental resonance windows obtained for the same (n,m) nanotube (ω_{RBM} = 244 cm^{-1}) dispersed in aqueous solution and wrapped with SDS (left), and in a bundle (right) (from ref. [72]).*

G-modes

The large phonon energy of the G-modes (~200 meV) permits to resolve easily the two resonances in REP. Few years ago, the group of S. K. Doorn [104, 105] has measured the REPs of the G-modes of highly enriched in single-chiralities semiconducting SWNTs (Figure 3.12). They state that the scattered resonance response is always weaker than the incident resonance response for E_{22} transition. In the framework of a semiclassical second-order model [106], and by using a four-level model commonly used for describing Raman scattering in molecular systems, the authors proposed that the strong asymmetry in the REPs between incoming and outgoing resonance results from non-Condon effects. In the framework of this approach, the experimental REPs are well-fitted by the expression below, in which M_1 and M_2 represent matrix elements for resonance with incident and scattered photons respectively. Within this model an asymmetric response occurs when M_1 and M_2 are not equal.

$$I_{RRS} \propto \left| \left[\frac{M_1}{E_L - E_{ii} - i\gamma} - \frac{M_2}{E_L - E_{ii} - E_{ph} - i\gamma} \right] \right|^2 \qquad (3.8)$$

The non-Condon parameter C is directed related to the matrix elements:

$$M_2/M_1 = (1-C) / (1+C)$$

Furthermore, the results of the fit indicated that the values of γ depend on the chirality of SWNTs and they are in the range: 26-38 meV. On the basis of the agreement between experiment

and model, these authors claim that non-Condon effects are intrinsic of the nanotube photophysics.

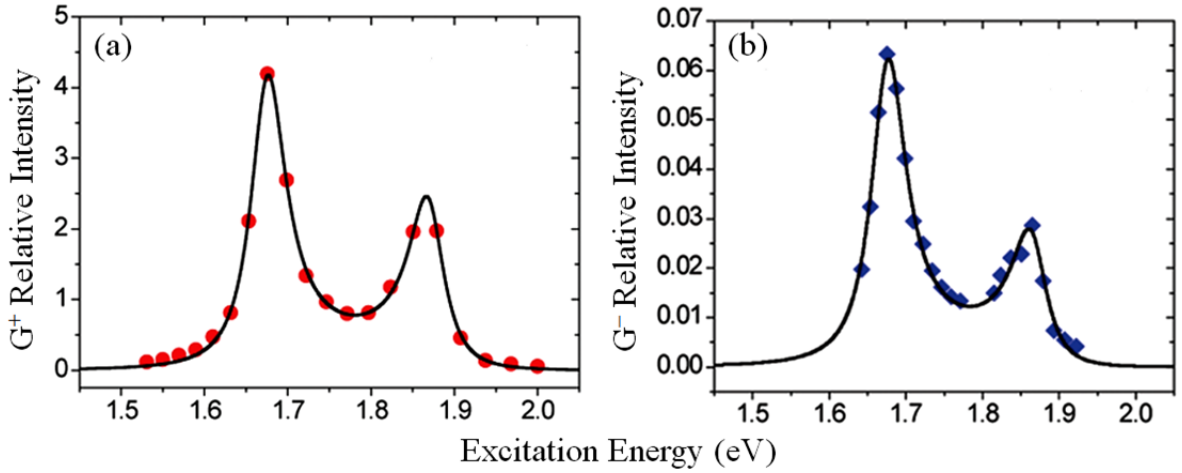

Figure 3.12: *REPs of the LO-mode. (a) and TO-mode of (10,2) SWNT. The scattered resonance peak around 1.86 eV is seen to be significantly weaker than the incident resonance around 1.67 eV (from ref [104, 105]).*

Recently, L. G. Moura *et al.* [107] reported measurements of the REPs of the G band of the (6,5) and (7,5) SWNTs in suspension (Figure 3.13). The authors also observed an asymmetry of REPs. However, opposite to the conclusion of Doorn and collaborators [104, 105], they suggested that the asymmetry of REPs can be described by the third-order quantum model instead of a semi classical second-order model within non-Condon approximation. In the framework of the third-order quantum model, they show that the asymmetry of REPs mainly occurs when the electronic band structure of a carbon nanotube and the k dependence of the electron-photon and electron-phonon matrix elements are taken into account. These authors also conclude that REP asymmetry is an intrinsic feature in SWNTs.

To state definitively the nature of the transitions (band-to-band vs excitonic transitions), additional investigations have to be done. In this aim, we have combined absorption and Raman experiments on individual free-standing index-identified SWNTs.

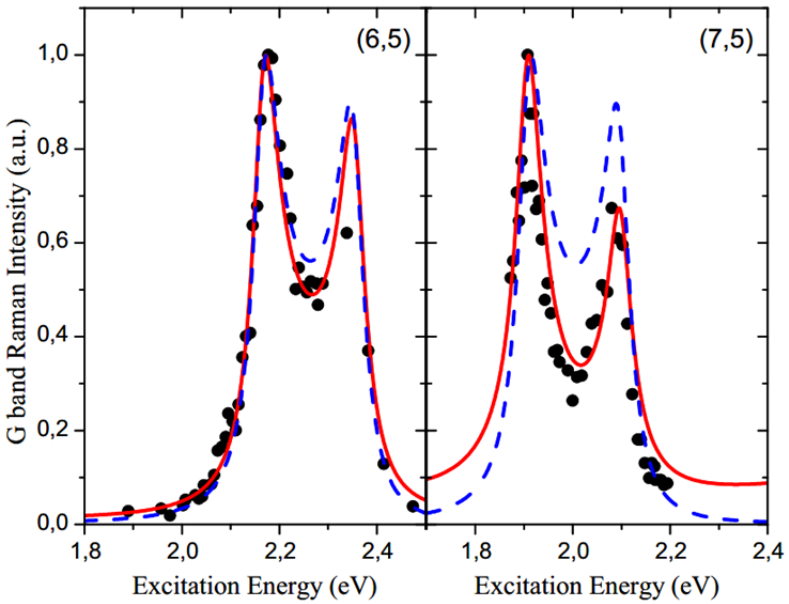

Figure 3.13: *The REP of G-mode for (6,5) and (7,5) SWNTs [107]. The black circles are experimental data. The solid red lines are the result of a calculation with all matrix elements, while the dashed blue line is the result of a calculation with constant matrix elements (γ = 25 meV in both calculations) (from ref [107]).*

3.3.4. Our experimental approach and results

In this section, we discuss the models which are used to fit the REPs of semiconducting SWNTs. On this basis, we try to determine between the nature of the involved transitions by fitting the REPs of the RBM and G-modes, measured on the well-identified (23,7) SWNT, by using band-to-band or excitonic models. It must be emphasized that, in the excitation range investigated: 1.55 - 1.80 eV, only the E_{33} transition of the (23,7) SWNT is present. The other transitions E_{44} (2.21 eV) and E_{55} (2.61 eV) are far from the investigated energy range. The Raman spectra excited at 1.66 eV (746 nm) and 1.85 eV (670 nm) correspond to the incoming and outgoing resonance (for G mode), respectively (Figure 3.14). As expected, RBM does not appear in the Raman spectrum excited at 1.85 eV.

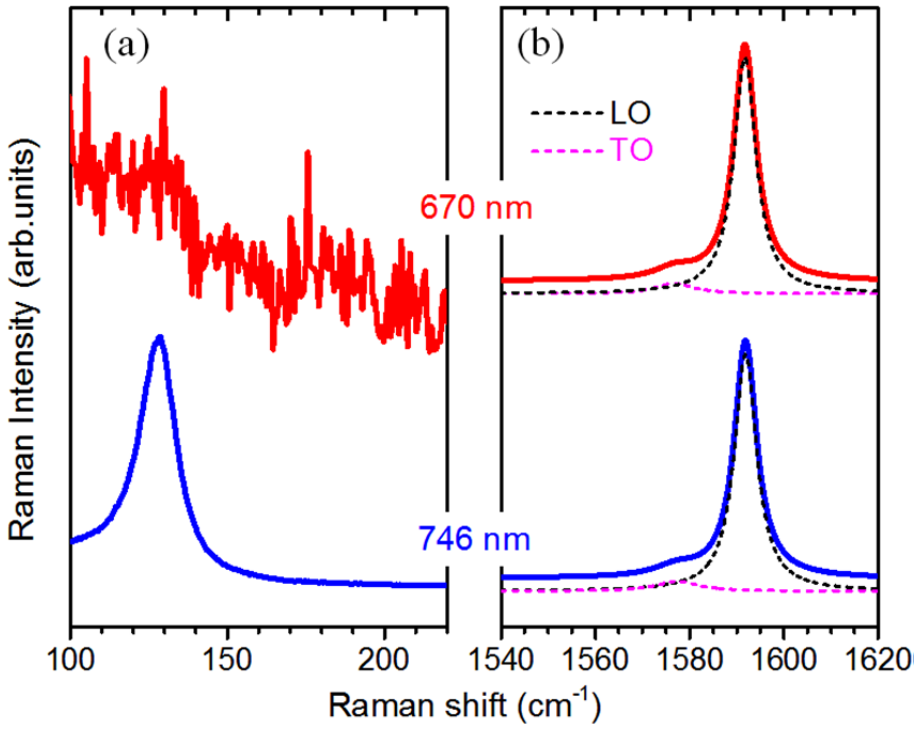

Figure 3.14: *Raman spectra correspond to imcoming and outgoing resonance (blue and red full line, respectively). (a) RBM, (b) G-modes, the black (pink) dash lines is fitting of LO (TO) mode.*

The expressions of the Raman intensity, I_{RRS}, that we will use to fit the REPs are reminded below.

Band-to-band model	Excitonic model
$I_{RRS} \propto \left\| \left[\frac{M}{\sqrt{E_L - E_{ii} - i\gamma}} - \frac{M}{\sqrt{E_L - E_{ii} - E_{ph} - i\gamma}} \right] \right\|^2$ (3.9)	$I_{RRS} \propto \left\| \left[\frac{M}{E_L - E_{ii} - i\gamma} - \frac{M}{E_L - E_{ii} - E_{ph} - i\gamma} \right] \right\|^2$ (3.10)

In the Table 3.5, we listed the frequencies of RBM and G modes of the (23,7) SWNT, with their corresponding phonon energies.

	RBM	LO	TO
Frequency (cm^{-1})	128.2	1591.2	1576.5
Phonon energy (meV)	15.9	197.3	195.5

Table 3.5. *Experimental frequencies/energies of RBM, LO- and TO G modes of (23,7) SWNT.*

The experimental REPs of the RBM, LO and TO G-modes are displayed on Figure 3.15 (open dots). The raw data have been corrected by the total transmission of our optical system and normalized by the intensity measured on silicon (see Annex for the details).

In the first step, we let the transition energy (E_{ii}), resonance window (γ), and matrix element M_{33} as free parameters for both models. The fit of REPs was performed independently for RBM, LO G-mode, and TO G-mode. In Figure 3.15a, black solid line (violet solid line) is the fit of the experimental REP for excitonic (band-to-band) model. For both RBM and G-modes, the two models fit very well the experimental data.

For RBM, we did not observe two separated peaks for incident and scattered resonance in the REP. This observation is in good agreement with many previous reports [72, 77, 98-102]. For RBM, the incident and outgoing resonances cannot be resolved because the resonance width (γ) is too broad compared to the energy of the phonon (~20 meV).

For G-modes, the LO mode has a 10 times larger intensity than the TO mode (Figure 3.15a). For both G-modes, the two resonances are well resolved.

The positions of the E_{33} derived from the fit of the REPs for either band-to-band or excitonic models are very close of the one measured by absorption spectroscopy (see Table 3.6).

Concerning the γ parameter, the values obtained in the framework of excitonic model by the fit of all three REPs are: (i) close one to another, and (ii) close of the one measured by absorption (Table 3.6). By contrast, in the framework of band-to-band model, the γ values, obtained by the fit of the REPs of the RBM, LO and TO G-modes, are (i) different one from another, and (ii) are different of the one measured by absorption (Table 3.6).

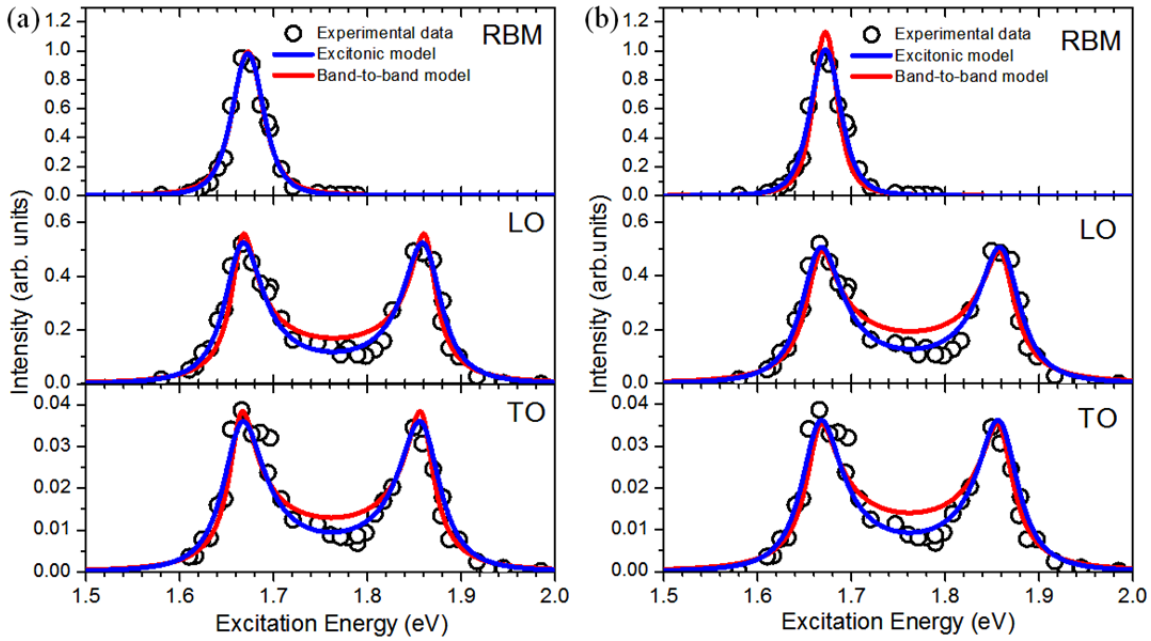

Figure 3.15: *Raman excitation profiles of the RBM and G-modes measured on the (23,7)SWNT. From top to bottom: REP of RBM, LO G-mode, and TO G-mode. The black dots are experimental data; the blue (red) solid line is the result of a fit by considering the nature of the transition as excitonic (band-to-band). (a) The fit was performed independently for the three experimental REPs. (b) The fit was performed at the same time for three experimental REPs.* E_{33}^{S}, γ_{33}, M_{33} *are free parameters.*

	Absorption	Excitonic model			Band-to-band model		
		RBM	LO	TO	RBM	LO	TO
E_{33}^{S} (eV)	1.66	1.664	1.665	1.664	1.665	1.665	1.664
γ_{33} (meV)	27.5	28.3	25.1	27.1	22.7	12.4	13.6
M_{33}		$3x10^{-3}$	$3.3x10^{-4}$	$2.6x10^{-5}$	0.211	0.010	$7x10^{-4}$
R^2		0.980	0.957	0.915	0.977	0.886	0.871

Table 3.6*: Summary of the transition energy and width derived from optical absorption and fitting of REPs using excitonic and band-to-band models. The fit was performed independently for the experimental data of RBM, LO G-mode, and TO G-mode.* E_{33}^{S}, γ_{33}, *and* M_{33} *as free parameters.*

In the previous step, the E_{33} and γ_{33} parameters derived from the fit of the REPs for either band-to-band or excitonic models are not equivalent for RBM, LO, and TO modes. In the further step of analysis, we performed another kind of fit, namely: the measured REPs of RBM, LO, and TO modes are fitted together at the same time instead of one by one. In this case, the E_{33}, γ_{33}, and M_{33} are adjustable parameters for both models but E_{33} and γ_{33} are set to be the same for all the modes. In Figure 3.15b, blue solid line (pink solid line) is the fit of the experimental REP for excitonic (band-to-band) model. The excitonic model shows a slightly better fit of the REPs. However, the values of γ, obtained by the fit of the REPs of the RBM, LO and TO G-modes, in the framework of excitonic (band-to-band) model are close of (different of) the one measured by absorption (Table 3.7).

	Absorption	Excitonic model			Band-to-band model		
		RBM	LO	TO	RBM	LO	TO
E_{33}^{S} (eV)	1.66	1.664	1.664	1.664	1.664	1.664	1.664
γ_{33} (meV)	27.5	26.7	26.7	26.7	16.1	16.1	16.1
M_{33}		$24x10^{-4}$	$7x10^{-4}$	$6x10^{-4}$	0.0984	0.0214	0.0207
R^2		0.954	0.954	0.954	0.895	0.895	0.895

Table 3.7*: Summary of the transition energy and width derived from optical absorption and fitting of REPs using excitonic and band-to-band models. The fitting was performed at the same time for three experimental data of RBM, LO G-mode, and TO G-mode. Fit of the REP of RBM and G-modes.* E_{33}^{S}*,* γ*, and* M_{33} *as free parameters.*

In a final step, we used the γ value obtained by absorption measurements (γ =27.5 meV) for both excitonic (Figure 3.16, black dashed line) and band-to-band models (Figure 3.16, violet dashed line) to fit the experimental REPs of RBM and G-modes (Figure 3.16, dots). E_{33} and M_{33} are let as free parameters. The results of the fit are shown in Table 3.8. We unambiguously state that the excitonic model provides excellent agreement with experimental data while the band-to-band model does not work.

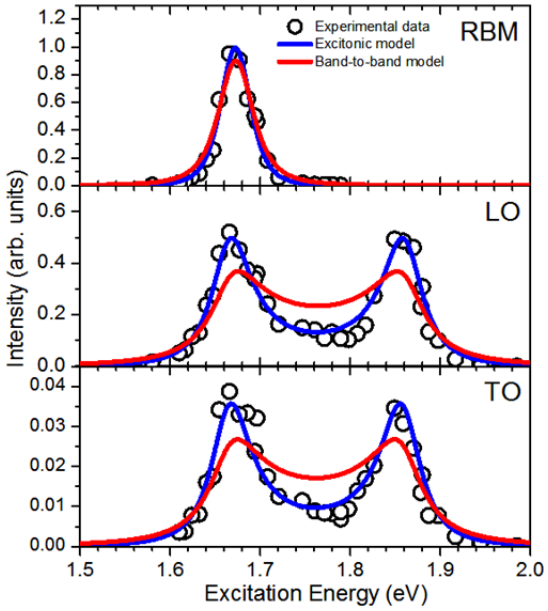

Figure 3.16: *Raman excitation profiles of the RBM and G-modes measured on the (23,7)SWNT. From top to bottom: REP of RBM, LO G-mode, and TO G-mode. The black dots are experimental data; the blue (red) solid line is the result of a fit by considering the nature of the transition as excitonic (band-to-band). In the fit, γ_{33} is kept fixed at the value determined from absorption spectroscopy: γ_{33} = 27.5 meV. E_{33}^{S}, M_{33} are free parameters.*

	Absorption	Excitonic model			Band-to-band model		
		RBM	LO	TO	RBM	LO	TO
E_{33}^{S} (eV)	1.66	1.664	1.664	1.664	1.665	1.665	1.664
γ_{33} (meV)	27.5	27.5	27.5	27.5	27.5	27.5	27.5
M_{33}		2.6×10^{-3}	3.8×10^{-4}	2.7×10^{-5}	0.328	0.016	1.1×10^{-3}
R^2		0.979	0.959	0.916	0.972	0.673	0.702

Table 3.8: *Summary of the transition energy and width derived from optical absorption and fitting of REPs using excitonic and band-to-band models. Fit of the REP of RBM and G-modes. γ_{33} = 27.5 meV for all the modes. E_{33}^{S}, M_{33} are free parameters.*

In summary, although both band-to-band and excitonic models can describe the REPs of the RBM and G-modes of individual SWNT, the values of the resonance window, γ, obtained in the framework of band-to-band model gives significant different values for RBM and G-modes, and are non-consistent with the value of γ derived from absorption measurement. On the other hand, by combining absorption and Raman spectroscopy on the same index-identified individual SWNT, we have unambiguously confirmed that the nature of optical transitions in SWNTs is excitonic.

3.4. Quantum interferences effects in the Raman response of individual SWNTs

3.4.1. Quantum interferences on REPs and Raman intensity: state-of-art

The presence of two closely spaced optical transitions can lead to quantum interference in the resonant Raman response of a CNT. In this situation, different Raman matrix elements related to different excited states, *i.e.,* different optical transitions, contribute to the Raman response. Quantum interferences can significantly affect the lineshape of the REP and consequently complicate the extraction of the transition energies derived from it.

Usually, quantum interference effects arise in the resonant excitation profiles of the RBM of metallic nanotubes due to the proximity of the lower (E_{ii}^{M-}) and upper (E_{ii}^{M+}) transitions, (or the close values of $E_{ii}^{M-}+\hbar\omega$ and E_{ii}^{M+}). Such quantum interference effects were investigated by Bussi *et al.* from the measurements of the excitation profile of the RBM of an individual metallic SWNTs deposited on Si/SiO_2 substrate [108]. In the framework of single-resonance expression based on band-to-band transition, the excitation dependence of RBM intensity, (around the $E_{11}^{M-,+}$) was calculated from the following expression of $K_{2f,10}$.

$$K_{2f,10} = \frac{L}{i\sqrt{2}\hbar^2\omega}\left[\begin{array}{l}\dfrac{M_1}{\sqrt{E_L - E_{11}^{M+} - i\gamma}} - \dfrac{M_1}{\sqrt{E_L - \hbar\omega - E_{11}^{M+} - i\gamma}} \\ + \dfrac{M_2}{\sqrt{E_L - E_{11}^{M-} - i\gamma}} - \dfrac{M_2}{\sqrt{E_L - \hbar\omega - E_{11}^{M-} - i\gamma}}\end{array}\right] \quad (3.11)$$

The authors showed that the relative sign of $M_1 = E_{ii}^{M+}$ and $M_2 = E_{ii}^{M-}$ strongly affects the transition energies extracted from the excitation resonance profile (Figure 3.17a). Constructive ($M_1/M_2 > 0$) and destructive ($M_1/M_2 < 0$) interferences correspond to dashed and full line respectively in Figure 3.17a. On Figure 3.17b, the fit of the experimental REP measured on the (12,6) metallic SWNT (ω_{RBM} = 188 cm^{-1}) leads to two resonances located at 1.79 eV and 1.91 eV and permits to derive a value of the M_1/M_2 ratio equal to -2.22.

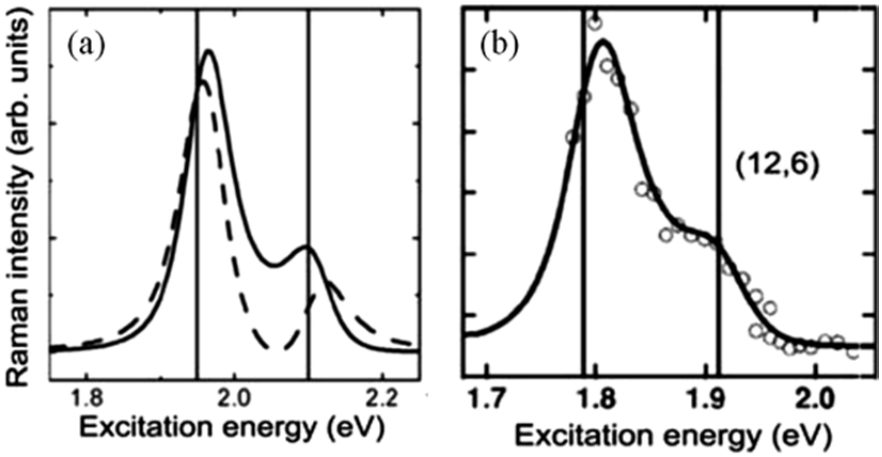

Figure 3.17: *Effects of quantum interferences on the Raman intensity of the RBM in metallic nanotubes (a) calculated resonance profile for two close transitions energies E_{ii}^{M-} = 1.94 eV and E_{ii}^{M+} = 2.1 eV. Full line M_1/M_2 = –2, dash line M_1/M_2 = +2. (b) dots: Experimental REP for (12,6) nanotube; solid line: fit using equation 3.8 with γ = 45 meV (adapted from ref [12, 108]).*

In individual semiconducting SWNTs (S-SWNTs), quantum interferences effects are usually not observed in the excitation profile of the RBM and G-modes measured around the first and second transitions. That is due to the large separation between these two consecutive optical transitions in S-SWNTs. However, the decreasing of the gap between two successive optical transitions of high-order can give the opportunity to observe quantum interference effects in the REP of any modes of S-SWNTs. On the other hand, in S-SWNTs, the proximity of the E_{i+1i+1} and $E_{ii}+\hbar\omega_G$ energies ($\hbar\omega_G$ close of 200 meV) can offer the possibility to observe quantum interference effects in the excitation profile of the G^+ and G^- modes.

In all the cases, the sign of matrix elements, M_{ii}, related to the involved optical transition, is a key parameter to describe the quantum interference effects on the excitation profile of any modes.

V. N. Popov *et al.* [109] calculated the elements of the so called J_{ii} matrix, which determines the tube-dependent height or amplitude of the REP, for the RBM and G-modes of M-SWNTs and S-SWNTs for the six first optical transitions. It must be emphasized that J_{ii} is directly related to matrix elements M_{ii}, especially the optical transition dependence and the sign of J_{ii} and M_{ii} are the same.

The dependence of J_{ii} of the LO and TO G-modes with the order of the optical transition is shown on Figure 3.18 for S-SWNTs. For a given (n,m) S-SWNT, the calculations state that the signs of J_{ii} of the LO G-mode for two consecutive transitions are opposite. In other words, J_{ii}/J_{i+1i+1} is always negative (Figure 3.18a). By contrast, the ratio J_{ii}/J_{i+1i+1} of TO modes is always positive (Figure 3.18b).

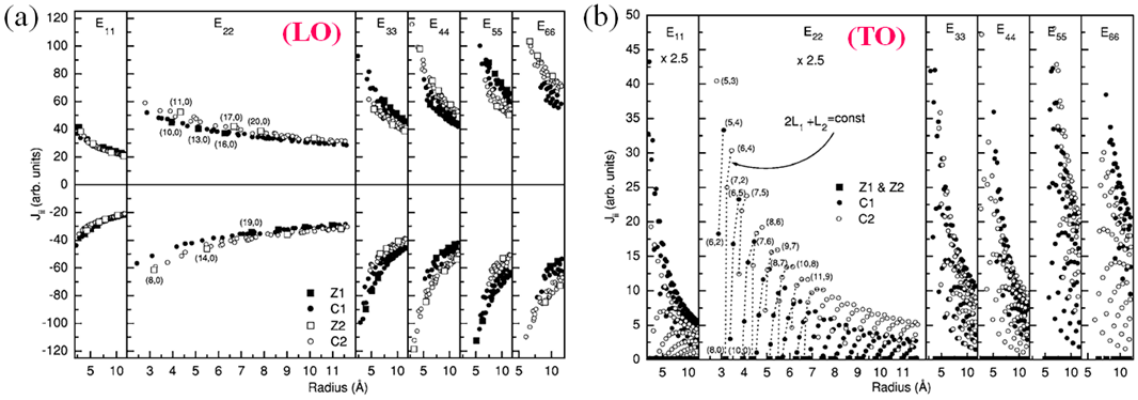

Figure 3.18: *The calculated J_{ii} of the (a) LO G-mode and (b) TO G-mode of semiconducting SWNTs (adapted from ref [109]).*

Recently, the group of S. K. Doorn [110] measured the REPs of the G-modes of samples highly enriched in single semiconducting chirality, namely: (8,6), (9,4), and (10,5) SWNTs. They observed quantum interference effects in the REP measured in the E_{33} and E_{44} optical transitions range.

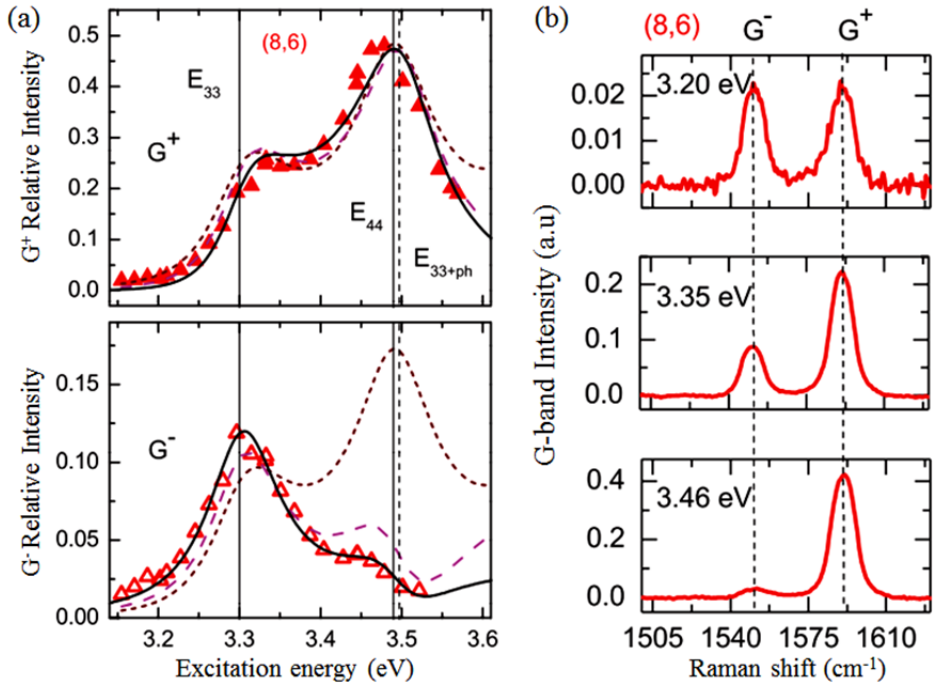

Figure 3.19*: (a) G-modes REPs of (8,6) SWNT. Symbols: experimental data. Red dotted line: model excluding interference and non-Condon effects ($C \neq 0$). Magenta dashed line: fit including interference effects, with $C = 0$. Black line: fit including interference and non-Condon effects. (b) (8,6) G-modes part of the Raman spectra excited at 3.20 eV, 3.35 eV, and 3.46 eV. (from ref [110]).*

We comment here the results obtained in (8,6) S-SWNT. For this tube, the absorption measurements determined that the third and fourth optical transitions were close and located at

3.31 eV and 3.50 eV respectively. The energy difference between the outgoing resonance (for the G-mode) corresponding to the lower transition, (E_{33}), and the incoming resonance corresponding to the higher transition, (E_{44}), is weak (~10 meV). When the outgoing resonance of the lower energy transition overlaps with the incoming resonance of the higher state (around 3.50 eV in (8,6) SWNT), the LO mode shows an enhancement of intensity while the TO mode intensity is strongly reduced (Figure 3.19). This contrasting interference effect can lead to an anomalous LO\TO intensity depending on the excitation energy. Notice that these dependencies are qualitatively well explained in the framework of the J_{ii} predictions of V. N. Popov *et al.* [109]. The change of sign between J_{ii} and J_{i+1i+1} for LO mode leads to constructive interference for this mode. By contrast, the same sign of J_{ii} and J_{i+1i+1} for TO mode leads to destructive interference for the TO mode. The Raman spectra shown on Figure 3.19b clearly illustrates the constructive and destructive interferences effects on the LO and TO G-mode intensity, respectively (see Figure 2 of ref. [110]).

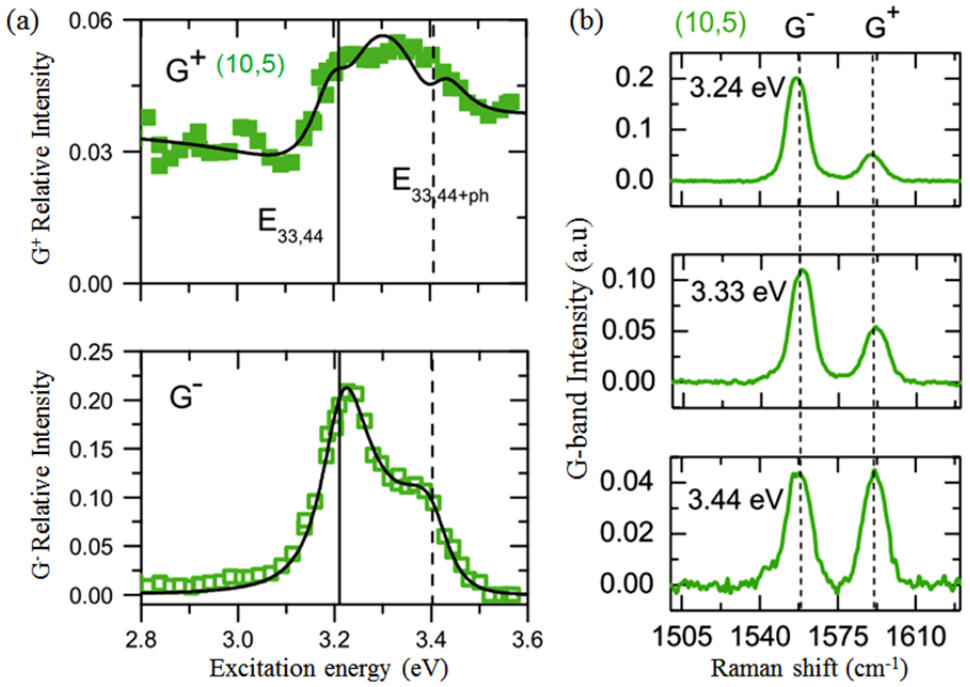

Figure 3.20: *(a) The G-modes REPs of (10,5) SWNT. Symbols: experimental data. Black line: fit including interference and non-Condon effects. (b) (10,5) G-modes part of the Raman spectra excited at 3.24 eV, 3.33 eV, and 3.44 eV. (adapted from [110]).*

Results obtained on the (10,5) SWNT provides another example of the importance of interference effects to explain the dependence of the LO and TO G-mode intensity on the incident excitation. The absorption measurement, performed on this tube, have permitted to state that the third (E_{33}) and fourth (E_{44}) optical transitions were located close to each other ($E_{33,44}$ = 3.22 eV). Obviously, both outgoing resonances ($E_{33,44} + \hbar\omega_G$) also occur at the same energy. The authors

observed that the REP of LO G-mode has a weak intensity and a featureless shape. This is the result of destructive interference effect as predicted by V. N. Popov *et al.* [109]. By contrast, the REP of TO G-mode displays a strong intensity related to constructive interference effect (Figure 3.20a). The excitation dependence of the Raman spectra, from 3.24 eV to 3.44 eV, provides an illustration of the changes in the shape of the Raman spectra due to the destructive and constructive interference effects on the intensity of LO and TO modes, respectively (Figure 3.20b).

In summary, these previous investigations emphasize the importance to take into account possible quantum interferences effects in order to describe correctly the dependence of the intensity of the RBM and G-modes on the incident excitation and to reproduce the resonance excitation profile of any mode. The key parameters are: (i) the proximity of the E_{ii} and E_{i+1i+1} transitions or that of the E_{ii} +$\hbar\omega_p$ and E_{i+1i+1} transitions ($\hbar\omega_p$ is the energy of the phonon involved in the Raman process) (ii) the sign of the exciton-phonon matrix elements for each incoming and outgoing transitions involved in the Raman process.

3.4.2. Quantum interference effects: our results

In this section, we discuss the quantum interference effects measured on individual suspended S-SWNTs. Our approach consists to combine absorption and Raman measurement on the same individual SWNTs. We illustrate our experimental approach from the measurements performed on an individual S-SWNT, the (30,1) SWNT (see sections 3.1.2 and 3.2.2). Its energies and widths (γ) are given in Figure 3.8 and Table 3.4.

As discuss in the section 3.3.4, the excitonic model well describes the optical transitions of S-SWNTs. Thus, in this section, we only used excitonic model to discuss the effect of quantum interference on the REPs of S-SWNTs. In this assumption, the expressions of the Raman intensity, with and without interference effects, are reminded below (E_L: the excitation energy of the laser; E_1: the lower transition energy; E_2: the higher transition energy, γ_1: the resonance window width corresponding to the lower transition; γ_2: the resonance window width corresponding to the higher transition; M_1: the Raman matrix element corresponding to the lower transition; M_2: the Raman matrix element corresponding to the higher transition.

Interference	$I_{Raman} \propto \left\| \frac{M_1}{E_L - E_1 - i\gamma_1} - \frac{M_1}{E_L - E_1 - E_{ph} - i\gamma_1} + \frac{M_2}{E_L - E_2 - i\gamma_2} - \frac{M_2}{E_L - E_2 - E_{ph} - i\gamma_2} \right\|^2$ (3.12)
No-interference	$I_{Raman} \propto \left[\left\| \frac{M_1}{E_L - E_1 - i\gamma_1} - \frac{M_1}{E_L - E_1 - E_{ph} - i\gamma_1} \right\|^2 + \left\| \frac{M_2}{E_L - E_2 - i\gamma_2} - \frac{M_2}{E_L - E_2 - E_{ph} - i\gamma_2} \right\|^2 \right]$ (3.13)

For the (30,1) SWNT, the resonance Raman spectra excited at 1.64 eV (756 nm) and 1.84 eV (674 nm) correspond to the incoming and outgoing resonance of the E_{33}, respectively. Similarly, the Raman spectra excited at 1.79 eV (693nm) and 1.99 eV (623 nm) correspond to the incoming and outgoing resonance of the E_{44}, respectively. Due to the energy difference between E_{33} and E_{44} as well as between E_{55} and E_{66} near of 150 meV (close of the G-modes energy) we expect that quantum interference effects can be observed on the G-modes REPs of this S-SWNT.

In the Table 3.9, we listed the frequencies of RBM and G modes of the (30,1) SWNT, with their corresponding phonon energies.

	RBM	LO	TO
Frequency (cm^{-1})	118	1591	1578
Phonon energy (meV)	14.6	197.3	195.7

Table 3.9: *Frequencies/energies of RBM and LO- and TO modes of (30,1) SWNT*

In order to discuss the experimental data, we first simulate the dependence of intensity of the Raman G-mode (expression 3.12 and 3.13), with and without interference effects, as a function of the incident excitation and for a difference between two consecutive optical transitions ranging from 0 to 400 meV (Figure 3.21). In the calculations, $|M_1|=|M_2|$ and the relative sign of the M_1 and M_2 matrix-elements are derived from the calculations of V. N. Popov *et al.* [3] (see Table 3.10), and the resonance window (γ) values are kept at 25 meV.

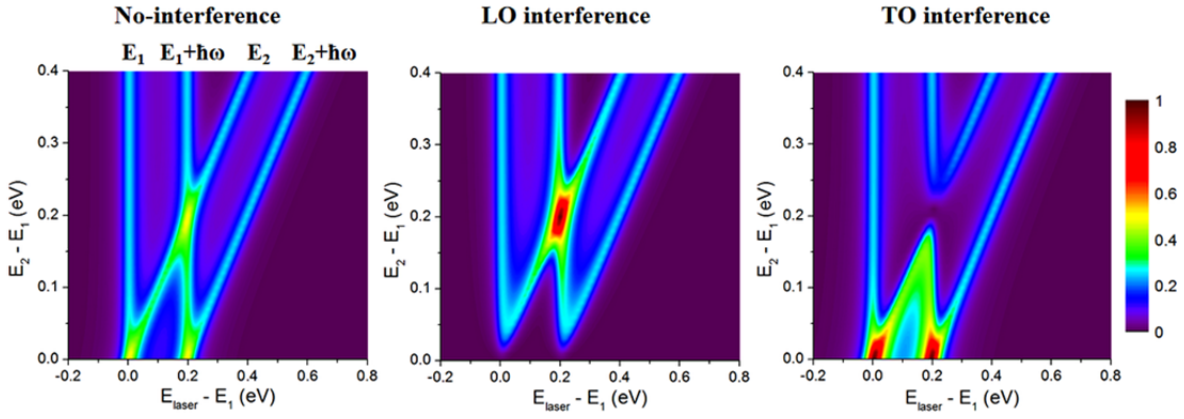

Figure 3.21: *Calculated dependence of the resonant intensity of the LO G-mode and TO G-mode as a function of the incident energy and for different values of the gap between two consecutive transitions, (a) without interference effect, (b) and (c) with interference effect. In these calculations E_{ph} = 0.2 eV; γ_1 = γ_2 = 25 meV; M_1/M_2 = -1 for LO mode and M_1/M_2 = 1 for TO mode (see text).*

The plots of Figure 3.21 illustrate the interference effects on the Raman intensity of the LO and TO G-modes. When the energy spacing between two consecutive transitions is

approximately equal to the G-mode energy ($E_1 - E_2 = 0.2$ eV), the interference leads to (i) a high intensity of the LO mode, and (ii) the vanishing of the TO mode. By contrast, when the two consecutive transitions are close, a high intensity of the TO mode and the vanishing of the LO mode are predicted. Table 3.10 summarizes the result for two specific cases: (i) when two consecutive transitions, E_1 and E_2, are close in energies; (ii) when E_2 and $E_1+\hbar\omega_G$ are in coincidence. For each G-mode, destructive or constructive interference effects are indicated. As expected, when no quantum interference effects are taking into account, the LO mode and TO mode show the same dependence on the excitation energy. In this latter assumption, an illustration of dependence of the intensity of the LO (or TO) G-mode is displayed on Figure 3.21a.

	G^+(LO)	G^-(TO)
Sign(M_1/M_2)	–	+
$E_2 = E_1$	Destructive	Constructive
$E_2 = E_1 + \hbar\omega_G$	Constructive	Destructive

***Table 3.10**: Depiction how the sign of the M_1/M_2 ratio for G^+ and G^- modes influences the constructive or destructive nature of quantum interferences for different E_1 and E_2 energy spacing.*

We can now discuss the dependence of the Raman intensity on incident excitation of the (30,1) SWNT by fitting the experimental REPs of the RBM and G-modes with and without quantum interferences effect. We will focus on the REPs of the RBM and G modes measured in the range of the E_{33} and E_{44} transitions of the (30,1) SWNT with excitation laser energies ranging from 1.55 eV to 2.1 eV.

In the fit of the REPs, we consider two simple approximations: (a) the Raman matrix elements corresponding to incoming (M_{ia}) and outgoing (M_{ib}) resonances are the same ($M_{ia}=M_{ib}$, expressions 3.12 and 3.13). In the framework of the so-called four-level model, this assumption corresponds to the Condon approximation; [104, 105, 110]); (b) the Raman matrix elements corresponding to incoming and outgoing resonances are different ($M_{ia}\neq M_{ib}$, expressions 3.14 and 3.15). In the framework of the four-level model, this assumption consists to take into account non-Condon contributions (see ref [104, 105, 110]).

Concerning the analysis of the data, for each approximation, the fit of the REPs of the RBM, LO G-mode, and TO G-modes was: (a) first performed independently for the three experimental data sets, and (b) in a second step, the three groups of data are considered together in the fit.

- $M_{ia} = M_{ib}$.

The experimental REPs of the RBM, and LO and TO G-modes measured on (30,1) SWNT are displayed in Figure 3.22 (symbols).

On the Figure 3.22a, black (violet) solid line is the fit of the experimental REPs, with (without) interference effect, performed in the framework of the semi-classical second-order model (expressions 3.12 and 3.13). In a first step, we let the energy transition (E_i), resonance window (γ_i), and matrix elements (M_i) as free parameters (see expressions 3.12, 3.13). The REPs of RBM, and LO, and TO G-modes were fitted independently. Clearly, a better fit of the profile of the REP of the LO mode occurs when interference effect are taken into account, especially the shoulder around 1.85 eV, which is observed in the REP of the LO G-modes, is better described in this assumption (Figure 3.22a).

We detail hereafter the results mode by mode.

- For RBM: taking into account, or not, of interference effects reproduces the experimental data. We observe in the REP, two separated peaks corresponding to the resonance involving the third and the fourth optical transitions respectively. The peaks corresponding to incoming and outgoing resonance cannot be resolved due to the small energy of the RBM (~0.015 eV). Exciton-phonon coupling is expected to be stronger for transitions originating in the K-M valley and weaker for those from the K-Γ valley [12]. This predicted that the Raman intensity of E_{44} has to be stronger than the ones of E_{33} for S-SWNTs type I. This prediction is in agreement with our measurements.

- For G-modes: the LO mode is 10 times larger in intensity than the TO mode (Figure 3.22a). That is mainly due to the strong difference in the value of the matrix-element for the two modes [109]. On the other hand, because the $\Delta E_{33\text{-}44}$ is close to the phonon energy of G-modes, a partial overlap between E_{44} and $E_{33}+\hbar\omega_G$ occurs around 1.8 eV. In this situation, quantum interference effects can occur. Especially, in agreement with theory which predicts, in this case, constructive interference effects for LO G-mode, an enhancement of the intensity of the LO mode is observed for an incident excitation around 1.8 eV.

The positions of the E_{33} and E_{44} transition energies derived from the fit of the REPs, with or without interferences, are very close of the E_{33} and E_{44} transition energies measured in absorption spectroscopy (see Table 3.11).

Concerning the γ parameters, in the both models, the γ values, obtained by the fit of the REPs of the RBM and TO, are rather close of the ones measured in absorption although some discrepancies can be noted. The maximum gap between the two determinations is less than 10 meV. By contrast, the γ values, obtained by the fit of the REPs of the LO G-mode are

significantly different with the one measured by absorption. Overall, the agreement with the absorption data seems better when interference effects are taken into account although none approach looks fully satisfactory.

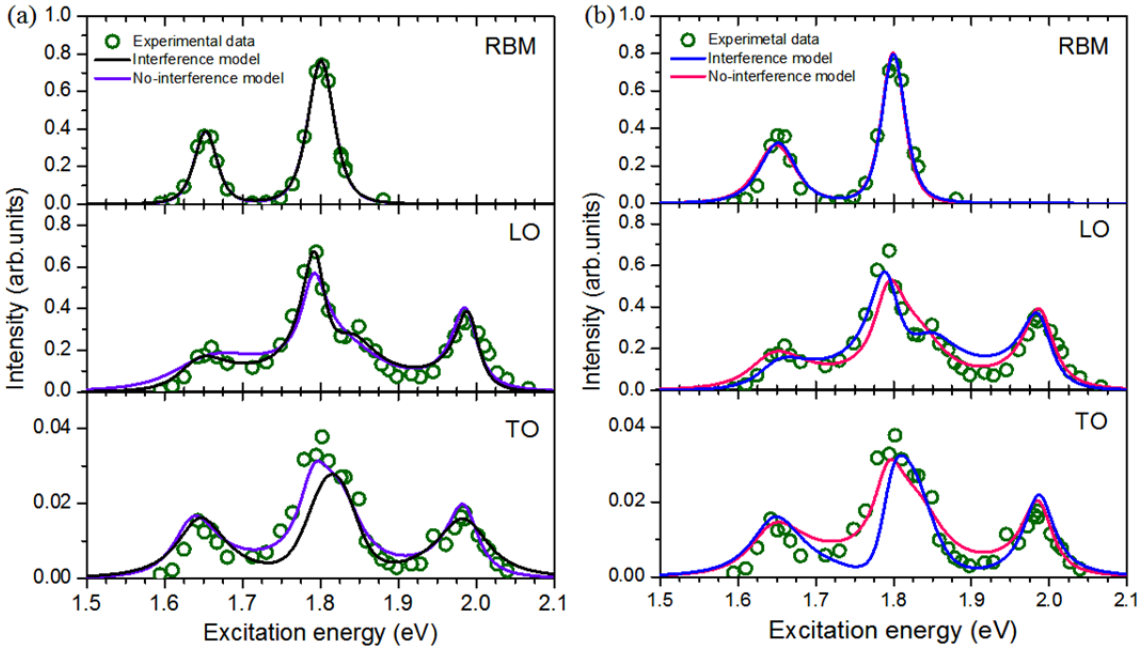

Figure 3.22: *(30,1) S-SWNT: Raman excitation profiles of RBM, LO and TO G-modes. The equation 3.12 and 3.13 ($M_{ia} = M_{ib}$) are used to fit the data. E_{ii}, γ_{ii}, and M_{ii} are free parameters in the fit. (a) The fit of the experimental REP of RBM, LO G-mode, and TO G-mode was performed independently. The green dots are experimental data; the black (violet) line is the result of the fit with (without) interference effects. (b) The fit of the experimental REP of RBM, LO G-mode, and TO G-mode was performed at the same time. The green dots are experimental data; the blue (pink) line is the result of the fit with (without) interference effects.*

	Absorption	Interference model			No-interference model		
		RBM	LO	TO	RBM	LO	TO
E_{33}^{S} (eV)	1.64	1.644	1.640	1.644	1.645	1.645	1.633
E_{44}^{S} (eV)	1.79	1.794	1.795	1.790	1.793	1.790	1.790
γ_{33} (meV)	30.5	25.2	38.9	39.1	24.3	69.5	34.4
γ_{44} (meV)	35.5	28.9	18.8	41.5	28.5	20.2	25
M_{33}		0.027	0.0155	0.0049	0.027	0.030	0.0044
M_{44}		0.051	-0.012	0.0052	0.051	-0.013	0.0035
R^2		0.997	0.928	0.759	0.997	0.876	0.894

***Table 3.11**: Comparison between the transition energies (E_{ii}) and widths (γ_{ii}) measured by absorption spectroscopy with the transition energies and widths derived from the fit of the REPs, by considering $M_{ia} = M_{ib}$, with or without interference effects. E_{ii}, γ_{ii} and M_{ii} are free parameters in the fit. The fit was performed independently for the RBM, LO G-mode, and TO G-mode.*

One of the discrepancies stands in the fact that E_{33} and, more significantly, γ_{33} values obtained by the fit of the REPs, with or without interferences, are significantly different for RBM, LO, and TO G-modes (Table 3.11). In a second step, we performed the fit of the REPs of RBM, LO, and TO G-modes at the same time. In this case, the E_{33}, E_{44}, γ_{33}, γ_{44}, M_{33} and M_{44} are adjustable parameters for both models but E_{33}, E_{44}, γ_{33}, and γ_{44} are set to be the same for all REPs. In Figure 3.22b, blue (pink) solid line is the result of the fit of the experimental REPs using this procedure and by taking into account (or not) interference effects. The values of the parameters are shown in Table 3.12. With or without interference effects, the values of E_{44} and γ_{44} derived from the fit of the experimental data are equivalent in both models while E_{33} and γ_{33} are slightly different. Concerning the γ parameter, with or without interference effects, the γ values obtained by the fit of the REPs are significantly different of the ones measured in absorption; especially γ_{33} is found significantly larger than γ_{44} in disagreement with absorption results (Table 3.12).

	Absorption	Interference model			No-interference model		
		RBM	LO	TO	RBM	LO	TO
E_{33}^{S} (eV)	1.64	1.645	1.645	1.645	1.616	1.616	1.616
E_{44}^{S} (eV)	1.79	1.791	1.791	1.791	1.792	1.792	1.792
γ_{33} (meV)	30.5	40.6	40.6	40.6	44.0	44.0	44.0
γ_{44} (meV)	35.5	24.4	24.4	24.4	24.2	24.2	24.2
M_{33}		0.069	0.0196	0.025	0.076	0.024	0.025
M_{44}		0.041	-0.0192	0.017	0.039	-0.019	0.016
R^2		0.843	0.843	0.843	0.893	0.893	0.893

Table 3.12: *Comparison between the transition energies (E_{ii}) and widths (γ_{ii}) measured by absorption spectroscopy with the transition energies and widths derived from the fit of the REPs, by considering $M_{ia} = M_{ib}$, with or without interference effects. E_{ii}, γ_{ii} and M_{ii} are free parameters in the fit. The fit was performed at the same time for the RBM, LO G-mode and TO G-mode.*

- $M_{ia} \neq M_{ib}$.

We have seen that the width of the resonance window, γ_{ii}, derived from the fit of the REP of G-modes, by assuming $M_{ia} = M_{ib}$, are, in general, in poor agreement with the experimental optical absorption data. We propose to use different Raman matrix elements for incoming and outgoing resonances, namely $M_{ia} \neq M_{ib}$ [104, 105, 110]. With $M_{ia} \neq M_{ib}$, the Raman intensities are written as: expressions 3.14 and 3.15. $M_{1a(b)}$ is the Raman matrix element corresponding to the lower transition at incoming (outgoing) resonance, and $M_{2a(b)}$ is the Raman matrix element corresponding to the higher transition at incoming (outgoing) resonance.

Interference	$I_{Raman} \propto \left\| \frac{M_{1a}}{E_L - E_1 - i\gamma_1} - \frac{M_{1b}}{E_L - E_1 - E_{ph} - i\gamma_1} + \frac{M_{2a}}{E_L - E_2 - i\gamma_2} - \frac{M_{2b}}{E_L - E_2 - E_{ph} - i\gamma_2} \right\|^2$ (3.14)
No-interference	$I_{Raman} \propto \left[\left\| \frac{M_{1a}}{E_L - E_1 - i\gamma_1} - \frac{M_{1b}}{E_L - E_1 - E_{ph} - i\gamma_1} \right\|^2 + \left\| \frac{M_{2a}}{E_L - E_2 - i\gamma_2} - \frac{M_{2b}}{E_L - E_2 - E_{ph} - i\gamma_2} \right\|^2 \right]$ (3.15)

In the Figure 3.23a, red (green) solid line is the fit of the experimental REP with (without) interference effect. Similar to the first approach, we first let the energy transition (E_{ii}) and resonance window (γ_{ii}) as free parameters. The REPs of RBM, LO, and TO G-modes were first fitted independently. Clearly, taking into account, or not, interference effects fit very well the experimental REP of the RBM, LO and TO G-modes (Figure 3.23a).

The positions of the E_{33} and E_{44} energy transition derived from the fit of the REPs, with or without interference, are very close of the E_{33} and E_{44} transition energies measured by absorption spectroscopy (see Table 3.13).

Concerning the γ_{ii} parameters, the values derived from the fit of the REPs of the RBM, LO and TO do not agree with the absorption data, even when the interference effects are taken into account.

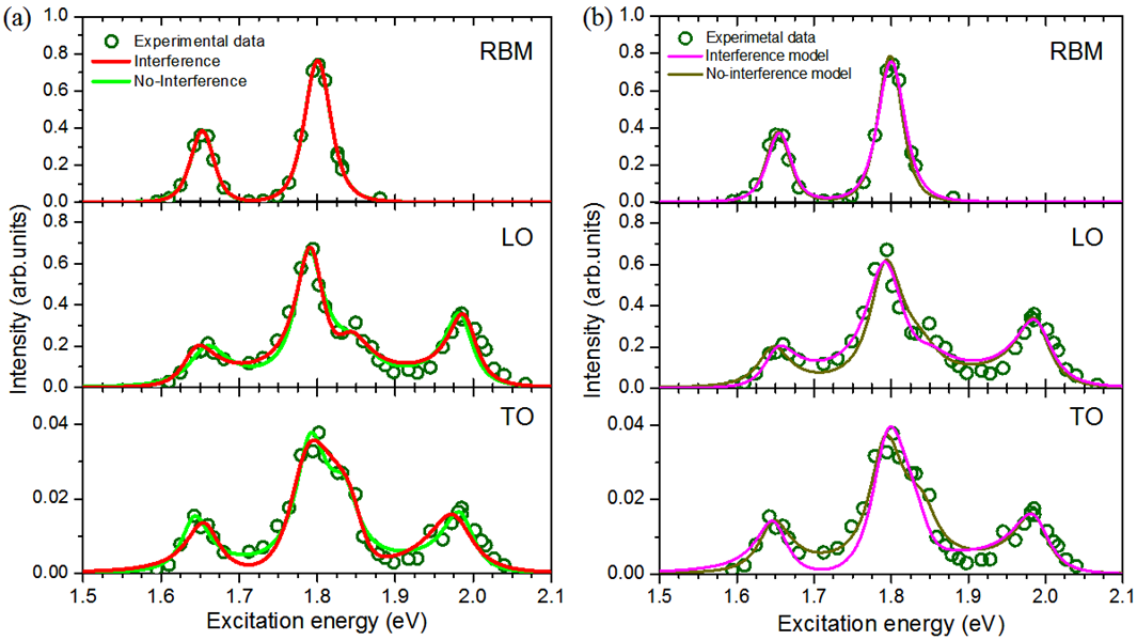

Figure 3.23: *(30,1) S-SWNT: Raman excitation profiles of RBM, LO and TO G-modes. The equations 3.14 and 3.15 ($M_{ia} \neq M_{ib}$) are used to fit the data. E_{ii}, γ_{ii}, and M_{ii} are free parameters in the fit. (a) The fit of the experimental REP of RBM, LO G-mode, and TO G-mode was performed independently. The green dots are measured data; the red (green) line is the result of the fit with (without) interference effects. (b) The fit of the experimental REP of RBM, LO G-mode, and TO G-mode is performed at the same time. The green dots are experimental data; the magenta (brown) line is the result of a fit with (without) interference effects.*

	Absorption	Interference model			No-interference model		
		RBM	LO	TO	RBM	LO	TO
E_{33}^{S} (eV)	1.64	1.646	1.642	1.656	1.647	1.656	1.641
E_{44}^{S} (eV)	1.79	1.793	1.793	1.781	1.792	1.787	1.790
γ_{33} (meV)	30.5	24.8	25.6	26.8	24.1	30.1	21.9
γ_{44} (meV)	35.5	28.5	22.5	33.7	28.5	22.0	24.5
M_{33a}		0.027	0.011	0.0028	0.027	0.013	0.0027
M_{33b}		0.027	0.007	0.0024	0.027	0.011	0.0027
M_{44a}		0.051	-0.017	0.006	0.051	-0.017	0.0045
M_{44b}		0.051	-0.013	0.004	0.051	-0.013	0.0031
R^2		0.996	0.947	0.938	0.997	0.917	0.941

Table 3.13: *Comparison between the transition energies (E_{ii}) and widths (γ_{ii}) measured by absorption spectroscopy with the transition energies and widths derived from the fit of the REP, by considering $M_{ia} \neq M_{ib}$, with or without interference effects. E_{ii}, $\gamma_{ii,}$ and $M_{ii,a(b)}$ are free parameters in the fit. The fits of the REPs of the RBM, LO G-mode, and TO G-mode were performed independently.*

In a second step (see section 3.3.4), we perform the fit of the experimental REPs (RBM, LO, and TO G-modes) at the same time. The E_{33}, E_{44}, γ_{33}, γ_{44}, M_{33} and M_{44} are always adjustable parameters but E_{33}, E_{44}, γ_{33}, and γ_{44} are the same for all REPs. In Figure 3.23b, magenta (brown) solid line is the fit of the experimental REPs with (without) interference effects. In the Table 3.14, the positions of the E_{33} and E_{44} energy transition derived from the fit of the REPs, with (without) interference effects, are very close of the ones measured by absorption spectroscopy. On the other hand, the γ values obtained by the fit of the REPs are in relative good agreement with the ones measured by absorption, especially when interference effects are taking into account (they are 5 meV smaller). However, the ratio of 4.4 between M_{33a} and M_{33b} for the LO G-modes REP (Table 3.14) seems not consistent and higher than expected since a maximum value of 3 was reported by Duque *et al.* [110].

	Absorption	Interference model			No-interference model		
		RBM	LO	TO	RBM	LO	TO
E_{33}^{S} (eV)	1.64	1.649	1.649	1.649	1.646	1.646	1.646
E_{44}^{S} (eV)	1.79	1.792	1.792	1.792	1.791	1.791	1.791
γ_{33} (meV)	30.5	25.1	25.1	25.1	25.3	25.3	25.3
γ_{44} (meV)	35.5	29.5	29.5	29.5	26.4	26.4	26.4
M_{33a}		0.030	0.0145	0.0133	0.029	0.0143	0.0143
M_{33b}		0.030	0.0033	0.0055	0.029	0.0090	0.0130
M_{44a}		0.056	-0.030	0.0274	0.046	-0.0261	0.0231
M_{44b}		0.056	-0.022	0.0175	0.046	-0.0196	0.0159
R^2		0.935	0.935	0.935	0.932	0.932	0.932

***Table 3.14:**. Comparison between the transition energies (E_{ii}) and widths (γ_{ii}) measured by absorption spectroscopy with the transition energies and widths derived from the fit of the REP, by considering $M_{ia} \neq M_{ib}$, with or without interference effects. E_{ii}, γ_{ii} and $M_{ii,a(b)}$ are free parameters in the fit). The fit of the REPs of RBM, LO G-mode, and TO G-mode was performed simultaneously.*

Finally, we calculated the REP of the LO and TO G-modes by using the values of E_{ii} and γ_{ii} previously derived from the fit of the REP of the RBM. Indeed, the values derived through the fit of RBM are found to be rather independent of the model used, and the slight difference with the values measured by absorption are attributed to uncontrolled change of the nanotube environment in the meaning time between the two kind of experiments. The line-shapes of REPs derived from calculations are analyzed to distinguish between the "interference" and "no-interference" models. The incoming Raman resonance at 1.64 eV (E_{33}) and outgoing Raman resonance at 2 eV (E_{44}+ $\hbar\omega_G$) are not affected by interference effects. Consequently, in these ranges, the values of the corresponding optical matrix elements (M_{33a} and M_{44b}) are adjusted in order to give the best agreement with the experimental data. In the 1.7 – 1.92 eV range, a ratio of 0.8 for M_{33b}/M_{33a} and M_{44b}/M_{44a} was found to give the closest agreement with the experimental data.

The REP of the LO and TO G-modes are displayed in Figure 3.24a. Figure 3.24b (resp. 3.24c) shows the line-shape of REPs of LO and TO G-modes, calculated with (without) interference effects. On the Figure 3.24b, the line-shape of REPs of LO and TO G-modes are strongly different from each other when the quantum interferences are taken into account. Especially, a strong shoulder peak is observed at 1.85 eV in case of LO G-mode. In addition, the

energy position of the maximum of intensity around 1.64 eV on the REP of the LO G-mode is slightly up-shifted as compared to the one of the REP of the TO G-mode. By contrast, without considering interferences effect, the line shape of either REPs of the LO and TO G-mode are very similar and no energy shift is observed around 1.64 eV (Figure 3.24c).

On Figure 3.24a, are reminded the experimental REPs of the LO and TO G-mode. These profiles display different shapes (Figure 3.24a). These differences are only reproduced by considering the interferences effects. Especially, in agreement with the theoretical predictions, the energy shift between the maximum of the REPs of the TO and LO, around 1.64 eV, is only well reproduced if interference effects are considered Figure 3.24b. However, a less good agreement is found at intermediate energies: (a) around 1.72 eV (1.92 eV), concerning the shape of the REP of the TO (LO) G-mode; (b) around 1.8 eV, concerning the width of the REP of the TO G-mode.

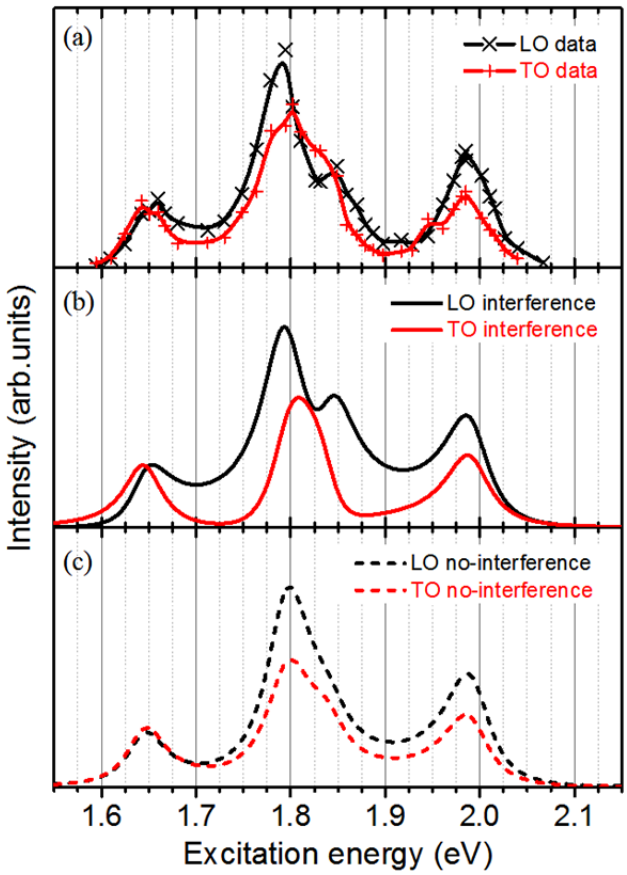

Figure 3.24: *The calculated REPs of LO and TO G-modes of (30,1) S-SWNT by considering $M_{ia} \neq M_{ib}$ (equation 3.14 and 3.15); (a) Experimental REPs: black (red) crosses are data for LO (TO) G-mode; (b) with interference effects; (c) without interference effects. E_{ii} and γ_{ii} are derived from the fit of the REP of the RBM.*

	Absorption	Interference model			No-interference model		
		RBM	LO	TO	RBM	LO	TO
E_{33}^{S} (eV)	1.64	1.646	1.645	1.645	1.647	1.645	1.645
E_{44}^{S} (eV)	1.79	1.793	1.795	1.795	1.792	1.795	1.795
γ_{33} (meV)	30.5	24.8	25	25	24.1	25	25
γ_{44} (meV)	35.5	28.5	29	29	28.5	29	29
M_{33a}		0.027	0.53	0.53	0.027	0.5	0.53
M_{33b}		0.027	0.424	0.424	0.027	0.4	0.424
M_{44a}		0.051	-1.05	0.85	0.051	-1.1	0.85
M_{44b}		0.051	-0.84	0.68	0.051	-0.85	0.68

Table 3.15*: The parameters derived from the calculation of the REP by considering $M_{ia} \neq M_{ib}$ model, with or without interference effects. E_{ii} and γ_{ii} are derived from the fit of the REP of the RBM.*

In conclusion, the fit of the REPs of the modes of the (30,1) SWNT, by considering $M_{ia} \neq M_{ib}$, provides a better agreement with the experimental data, including the absorption data, than those performed by considering $M_{ia} = M_{ib}$, especially if the interference effects are taking into account. The comparison between the calculations and measurements of the REPs of the LO and TO G-modes gives strong indications about the occurrence of quantum interference effects. However, we were not able to reproduce in a fully satisfactory way the experimental data using the rather simple models within our grasp. Different reasons for that can be found: the models used are too simple; the interference effects are rather small because the separation between the two optical transitions does not match perfectly the phonon energy; difficulties in the normalization of the experimental data measured in a relatively broad excitation range.

We are however convinced that interference effects have to be taken into account to reproduce the REP of the (30,1) SWNT. Additional clearer evidence of the importance of interference effects to describe correctly the intensity of the Raman active mode in carbon nanotubes will be presented in the case of a DWNT in the section 4.4 of chapter 4.

3.5. The TO/LO intensity ratio of individual semiconducting SWNTs

3.5.1. Introduction and state-of-art

It was found theoretically that, for close diameters, the A_{TO}/A_{LO} intensity ratio decreases when the chiral angle decreases [86, 111] (Figure 3.25). However, as shown previously, interference effects can lead to an enhancement or a vanishing of the TO or LO mode intensity. The interference effects can lead to significantly disperse A_{TO}/A_{LO} experimental ratio. We remind that interference effects on the intensity of the TO and LO modes depend on the gap between the energies of the different transitions and of the incoming and outgoing resonance energies.

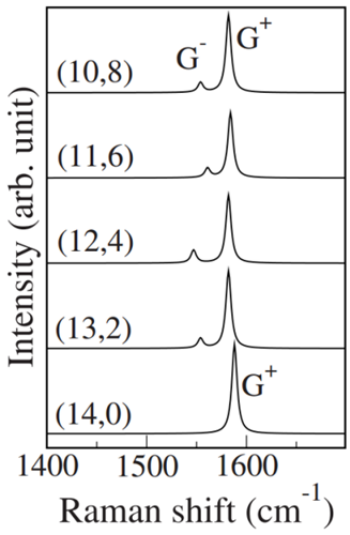

Figure 3.25*: The calculated G-mode part of the Raman spectra of the 28 family SWNTs (from ref [86]).*

Few years ago, H. Telg *et al.* [80] measured the A_{TO}/A_{LO} intensity ratio of several S-SWNTs (diameters range: 0.6-1 nm) by using laser excitation energies located around the E_{22} transition of these S-SWNTs. Their results confirmed that the intensity ratio A_{TO}/A_{LO} generally increases with increasing the chiral angles of S-SWNTs. However the values of the A_{TO}/A_{LO} ratio also display a significant dispersion (Figure 3.26). These authors claimed that their result displays the intrinsic behavior of A_{TO}/A_{LO} ratio with chiral angle rather than the results presented in ref [31, 74, 84, 85]. The authors suggested that the Raman intensities in ref [31, 74, 84, 85] were strongly affected due to the etching process for sample preparation.

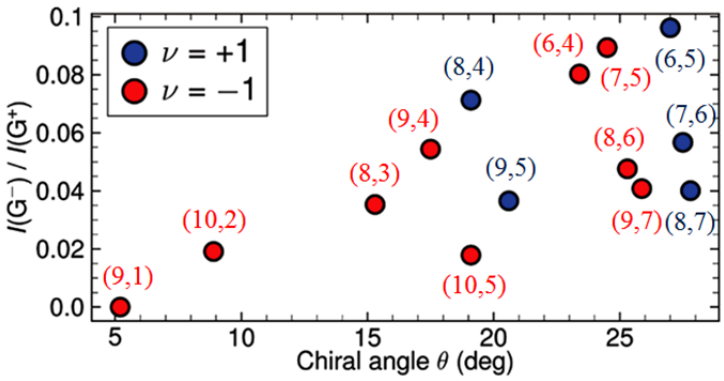

Figure 3.26: *Intensity ratio of G^-(TO) and G^+(LO) as function of chiral angle θ in several S-SWNTs (adapted from the ref [80]).*

Although the intensity of TO and LO modes were investigated by numbers of groups, there is no publication in which the behavior of TO and LO modes was investigated around different optical transitions. In this section, we will present the intensity ratio of TO and LO G-modes measured around three high-order energy transitions, namely E_{33}, E_{44}, and E_{55}.

3.5.2. Our results and discussion

A series of free-standing SWNTs suspended through a wide trench was prepared by CVD (without using etching process). The Raman measurements were performed in air and at room temperature. A peculiar attention was devoted to the investigation of the TO/LO intensity ratio (A_{TO}/A_{LO}) measured on several suspended individual SWNTs. In the analysis of the A_{TO}/A_{LO} ratio, we combine the present results with those of D. Levshov (PhD, Montpellier, 2013 [90]), and those of the ref. [31, 74, 84, 85].

Two examples of the A_{TO}/A_{LO} intensity ratios measured on S-SWNTs around various optical transitions are shown (Figures 3.27 and 3.28). In the first example, the difference between two consecutive optical transitions is significantly larger than the G-mode phonon energy (no interference effects are expected) (Figure 3.27). In the second one, the gap between two consecutive optical transitions is close to the G-modes phonon energy (interference effects are expected) (Figure 3.28).

- *Individual S-SWNT (23,7).*

For this tube, the difference between two consecutive optical transitions is larger than the energy of G-mode.

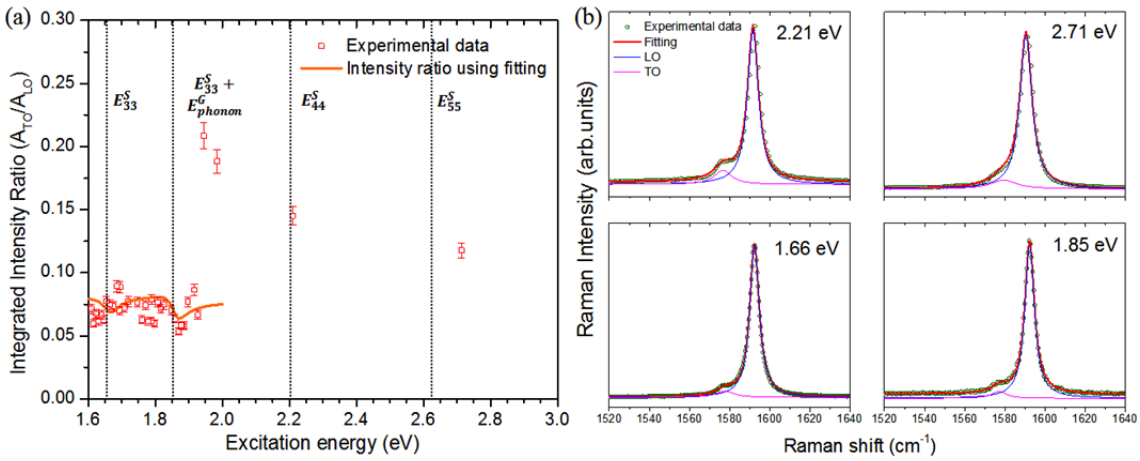

Figure 3.27: *(a) Excitation energy dependence of the A_{TO}/A_{LO} measured on the (23,7) SWNT. (b) Examples of Raman spectra corresponding to incoming or outgoing resonances.*

On Figure 3.27a (symbols), the A_{TO}/A_{LO} intensity ratio of (23,7) SWNT (SWNT1), measured for various excitation energies, are displayed (see for detail the Table 3.18 in the annex of this section). We remind that the diameter of this SWNT is 2.13 nm and its chiral angle is 12.89º. We clearly observe that the integrated intensity ratio A_{TO}/A_{LO} (red dots in Figure 3.27a) depends on the excitation energy. The A_{TO}/A_{LO} ratio derived from the REP of TO and LO mode (see Figure 3.15, black solid line) is also plotted (Figure 3.27a orange line). For the measurements in the E_{33} range, the intensity ratio corresponding to incoming resonance is the same as that of outgoing resonance. The average value is about 0.075 which is close to the ratio of optical matrix elements M_{33}^{TO}/M_{33}^{LO} (0.08) obtained by the fit of the REP. Notice that, due to the absence of resonance condition for laser excitation close of 2 eV, with as first consequence a low-signal-to-noise ratio of the Raman spectrum, the values of the A_{TO}/A_{LO} ratio around 2 eV have to be considered as not reliable. At high-order energy transitions, only few data have been measured. The values of the ratio are 0.145 and 0.118 around the E_{44} and E_{55} transitions, respectively.

In his PhD thesis, D. Levshov reports the excitation dependence of the A_{TO}/A_{LO} ratio in two other index-identified SWNTs, namely: (19,15) and (24,8) [90]. For these tubes, with regards to the gap between the transition energies, no interference effects are expected. Figure 3.28a and 3.28 b show the behavior of the A_{TO}/A_{LO} ratio of the (19,15) and (24,8) SWNTs respectively as a function of the excitation energy. Around E_{33} transition, an average values of 0.08 for the (19,15) SWNT and 0.1 for the (24,8) SWNT were found.

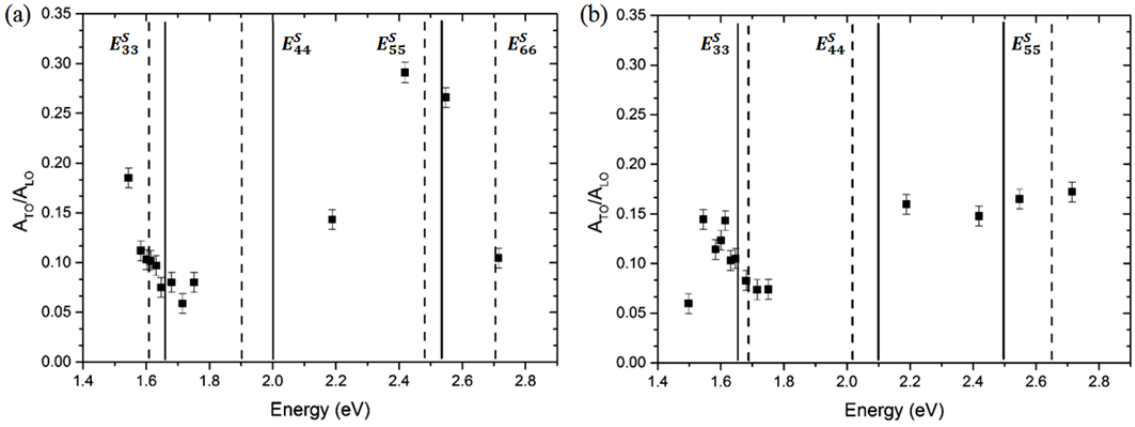

Figure 3.28: *Excitation energy dependence of the A_{TO}/A_{LO} measured on the (a) (19,15) SWNT, (b) (24,8) SWNT. Solid and dashed lines correspond to the optical transitions calculated by Popov et al. [96] and Liu et al. [33], respectively. (adapted from [90]).*

Clearly, as in the S-SWNT1, the few integrated intensity ratios measured around E_{44}, and E_{55} are higher than the ones measured around E_{33}.

In order to have additional information about intensity ratio of TO and LO, we also look the Raman spectra performed on S-SWNTs of the ref [31, 74, 84, 85]. Table 3.16 summarizes the A_{TO}/A_{LO} intensity ratio (as well as the FWHM of TO and LO modes) of all these S-SWNTs.

SWNTs	Excitation Wavelength (nm)	Excitation Energy (eV)	A_{TO}	$FWHM_{TO}$	A_{LO}	$FHWM_{LO}$	A_{TO}/A_{LO}
(19,2)	514.5	2.41	10.87	10.8	249.4	6.8	0.044
(27,4)	647.1	1.92	3.6	12	16.3	7	0.22
(17,9)	514.5	2.41	34.6	15.6	126.7	10.2	0.27
(12,8)	514.5	2.41	26.7	10.6	119.2	7.8	0.22
(20,16)	514.5	2.41	17.7	13.2	67.2	9.2	0.26
(11,10)	514.5	2.41	32.5	9.8	115.2	11.2	0.28
(15,14)	647.1	1.92	23	9.3	106.8	7	0.22
(15,14)	514.5	2.41	15	12.4	92.4	9.1	0.16

Table 3.16*: The integrated intensity A_{TO}/A_{LO} and FWHM of S-SWNTs measured in several SWNTs in ref [31, 74, 84, 85].*

- Individual S-SWNT (30,1).

For this tube, the gap between E_{33} + $\hbar\omega_p$ and E_{44} is close and interference effects are expected.

In the Figure 3.29, we presented the intensity ratio of (30,1) S-SWNT for different excitation energies (see for detail the Table 3.19 in the annex of this section). The diameter of this SWNT is 2.24 nm and its chiral angle is 1.63°. The small chiral angle of the (30,1) SWNT can explain the very weak intensity of the TO mode (as shown in Figure 3.5).

In this S-SWNT, we observe that the average values of integrated intensity ratio A_{TO}/A_{LO} around the E_{33} and E_{44} transitions are near of 0.1 and 0.07, respectively. These intensity ratios measured around the E_{33} and E_{44} are rather close of the corresponding ones measured on the (23,7). However, the ratios of optical matrix elements M_{33}^{TO}/M_{33}^{LO} and M_{44}^{TO}/M_{44}^{LO}, derived by the fit of the REPs are 0.3 and 0.375, respectively. These latter values are significantly different than those obtained by experiments.

On Figure 3.29a, we plotted together the ratio derived from the fit of the spectra (red symbols in Figure 3.29a) and the intensity ratio derived from the fits of the REPs of TO and LO G-modes (see orange and blue lines in Figure 3.29a). The two sets of data are consistent and display strong fluctuations in the E_{33} – E_{44} range. This observation can be explained by the occurrence of interference effects. The value of intensity ratio is 0.036 for E_{66}.

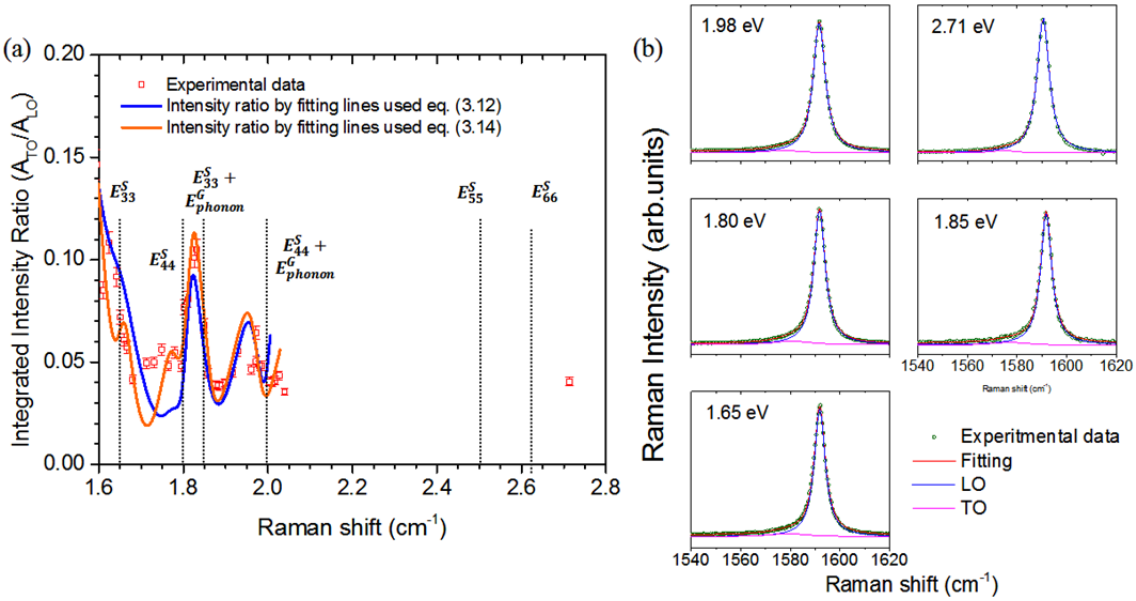

Figure 3.29: *(a) Excitation energy dependence of the A_{TO}/A_{LO} measured on the (30,1) SWNT. (b) Some examples of Raman spectra corresponding to the incoming and outgoing resonances.*

- *Discussion*

The values of ratios at various excitation energies and for different S-SWNTs are presented in tables 3.16, 3.18, and 3.19 and on the Figures 3.27-3.29. Table 3.17 summarizes the main information related to the A_{TO}/A_{LO} ratio obtained in different works performed on index-identified SWNTs.

Nanotube	Chiral angle (degree)	1-cos(6θ)	Diameter (nm)	Type	A_{TO}/A_{LO}		
					E_{33}	E_{44}	E_{55}
(30,1)	1.63	0.0145	2.24	I ($\nu = -1$)	0.1	0.07	0.037
(19,15)	26.11	1.918	2.31	II ($\nu = +1$)	0.1	0.14	0.27
(23,7)	12.89	0.781	2.13	II ($\nu = +1$)	0.075	0.14	0.118
(24,8)	13.9	0.885	2.26	II ($\nu = +1$)	0.105	0.16	0.17
(19,2)	4.95	0.131	1.57	I ($\nu = -1$)	0.044	0.044	-
(27,4)	6.81	0.244	2.29	I ($\nu = -1$)	0.22	0.22	-
(17,9)	19.93	1.494	1.79	I ($\nu = -1$)	-	0.27	-
(12,8)	23.41	1.771	1.37	II ($\nu = +1$)	0.224	-	-
(20,16)	26.33	1.927	2.45	II ($\nu = +1$)	-	-	0.264
(11,10)	28.43	1.987	1.42	II ($\nu = +1$)	0.28	-	-
(15,14)	28.86	1.993	1.97	II ($\nu = +1$)	0.215	0.164	-

Table 3.17*: Summary of the excitation dependence of integrated area ratio (A_{TO}/A_{LO}) for chiral semiconducting SWNTs. The values of SWNTs (19,15) and (24,8) are results presented in D. Levshov's PhD thesis [90]. Other values are adapted from ref [31, 74, 84, 85].*

In the Figure 3.30a, the dependence of integrated Raman intensity ratio (A_{TO}/A_{LO}), measured around three different high-order energy transitions, are plotted as function of chiral angle. In agreement with H. Telg *et al.* [80], the plot displays a general trend, namely an increase of the intensity ratio with increasing the chiral angles. This general trend seems to be independent of the involved optical transitions.

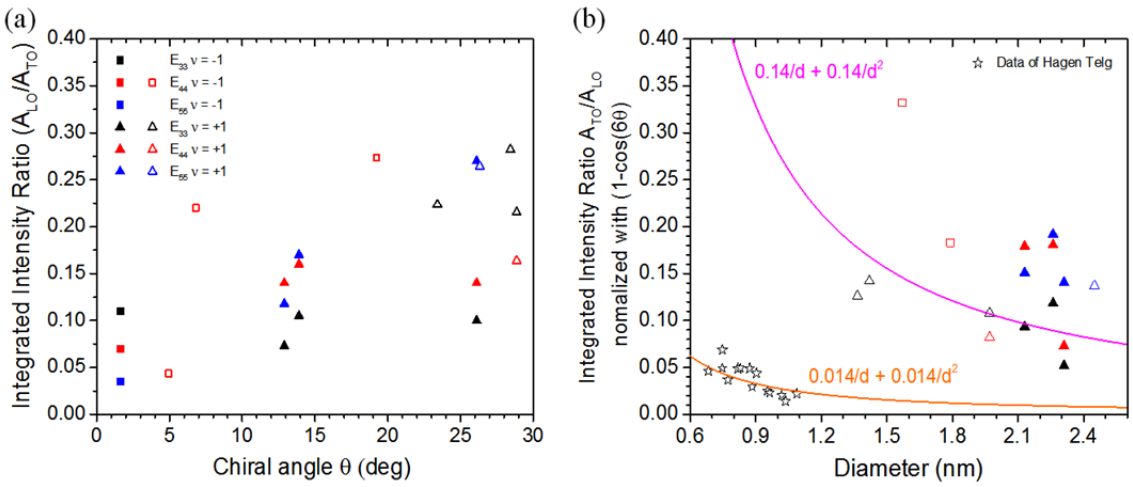

Figure 3.30: *(a) Integrated Raman intensity ratio, A_{TO}/A_{LO}, as a function of chiral angle θ, (b) Normalized A_{TO}/A_{LO} as a function of diameter. The solid dots are data obtained in the present work, the open dots are data from [31, 74, 84, 85], stars are data from Telg et al [80].*

In order to describe the intensity ratio as function of diameter, H. Telg *et al* [80] suggested the following expression:

$$\frac{A_{TO}}{A_{LO}} = \left(\frac{b_1}{d} + \frac{b_2}{d^2}\right)(1 - \cos(6\theta)) \qquad (3.16)$$

On the Figure 3.30b, the A_{TO}/A_{LO} ratios, normalized to the chiral angle dependence by the term (1 – cos(6θ)), are plotted as a function of the diameter. The fit of the data using the equation (3.16) gives: b_1 = 0.14 nm and b_2 = 0.14 nm^2. Both our experimental data and their fit are strongly different of the one's of Telg *et al.* [80]. At this time, we have no explanation to understand such a result. The differences suggest that the order of the transition plays a role in the values of this ratio. We remind that measurements have been performed with excitation around the E_{22} transition in Ref [80], and around higher-order transitions in the present work.

3.6. Summary

In this chapter, we focused on the study of the intrinsic properties of individual semiconducting SWNTs. First, we propose an approach to assign SWNTs when the information derived from electron diffraction does not lead an unambiguous assignment of the nanotube. This method, which combines Raman spectroscopy and electron diffraction, is illustrated on two examples: the (23,7) and the (30,1) SWNTs. The assignments of these SWNTs allow to precise the attribution of the transition energy measured by absorption spectroscopy.

In the following, we focus on the information that can be derived from the measurements of the resonant excitation profile (REP) of (23,7) and (30,1) SWNTs. By combining this information with the knowledge of the energy transition, E_{ii}, and resonance window, γ_{ii}, directly measured by absorption spectroscopy, important conclusions have been drawn:

-The REPs of RBM and G-modes of the (23,7) SWNT can be described by either band-to-band or excitonic models. However, only the values of energies, E_{ii}, and widths, γ_{ii}, derived by the fit of the REPs, in the framework of excitonic model, are in good agreement with the values derived from absorption spectroscopy. Consequently, our approach confirms the excitonic nature of the optical transitions in SWNTs.

-The measurement of the REPs of the (30,1) SWNT, in a broad excitation range, has permitted to evidence the role of the quantum interference effects on the intensity of the LO and TO G-modes. The results clearly establish that interference effects have to be considered to describe correctly the REPs of RBM and G-modes of the (30,1) SWNT.

-Finally, the dependence of the integrated Raman intensity ratio, A_{TO}/A_{LO}, has been measured on several index-identified SWNTs. These measurements have been performed with excitation energy around high-order transitions (E_{33}, E_{44}, E_{55}). The values of this ratio are significantly higher than those found in Ref [80]. In this latter study, the measurements were performed with excitation energies around the E_{22} transition. The differences suggest that the order of the transition could play a role in the values of this ratio. However, this suggestion about the role of the energy transition on the values of A_{TO}/A_{LO} ratio is not sufficient to explain the strong discrepancies with the results of ref. [80]. The role of the quantum interferences in the evaluation of the A_{TO}/A_{LO} ratio of the (30,1) SWNT was also discussed.

Annex

Excitation wavelength (nm)	Excitation energy (eV)	A_{TO}	$FWHM_{TO}$	A_{LO}	$FHWM_{LO}$	A_{TO}/ A_{LO}
457.0	2.71	212.0	14.9	1798.60	7.3	0.1179
561.0	2.21	94.3	10.5	649.60	6.6	0.1452
624.7	1.99	1.22	3.6	6.48	7.2	0.1883
637.6	1.94	1.48	9.3	7.10	6.0	0.2085
643.1	1.93	1.45	5.2	21.80	6.0	0.0665
646.9	1.92	5.0	8.3	57.90	5.8	0.0864
653.4	1.90	11.14	9.3	144.75	6.5	0.0770
657.1	1.89	14.70	7.9	253.60	5.7	0.0580
659.5	1.88	90.84	8.6	1571.9	5.6	0.0578
660.1	1.88	24.4	7.8	420.00	5.6	0.0581
663.1	1.87	33.4	7.9	625.70	5.9	0.0534
667.1	1.86	24.1	9.2	380.13	6.5	0.0634
670.6	1.85	41.6	10.7	593.70	5.8	0.0701
678.9	1.83	42.0	9.8	562.00	5.7	0.0747
682.5	1.82	27.8	11.0	388.28	5.7	0.0716
682.4	1.82	19.5	6.9	367.20	5.6	0.0531
685.9	1.81	23.3	10.6	304.40	6.1	0.0765
689.6	1.80	16.9	10.4	282.50	5.9	0.0598
693.0	1.79	24.0	13.0	304.00	5.9	0.0789
693.0	1.79	29.6	10.6	480.70	5.5	0.0616
696.9	1.78	35.11	10.3	571.86	5.6	0.0614
700.1	1.77	20.7	11.3	278.30	5.9	0.0744
704.3	1.76	37.57	10.4	599.13	5.6	0.0627
709.9	1.75	30.24	11.0	394.43	5.4	0.0767
720.8	1.72	29.47	11.8	382.06	5.8	0.0771
725.9	1.71	35.62	9.9	492.88	5.4	0.0723
731.0	1.70	50.56	11.1	571.01	5.5	0.0886
732.0	1.69	65.74	9.3	941.22	5.6	0.0698
735.6	1.69	42.16	12.2	472.57	5.5	0.0892
739.5	1.68	42.15	10.4	573.92	5.7	0.0734
744.4	1.67	49.66	10.4	666.14	5.7	0.0746
749.5	1.65	53.11	10.5	686.12	5.6	0.0774
752.6	1.65	21.8	8.0	348.09	5.5	0.0626
756.0	1.64	18.9	8.1	283.56	5.7	0.0667
759.8	1.63	9.34	7.8	151.71	5.5	0.0615
763.5	1.62	25	9.6	369.40	6.0	0.0676

767.1	1.62	11.82	7.4	197.2	5.5	0.0600
770.2	1.61	11.2	8.28	156.8	5.63	0.0713

***Table 3.18**: The excitation energy dependence of the A_{TO}/A_{LO} ratio measured on the (23,7) SWNT.*

Excitation wavelength (nm)	Excitation energy (eV)	A_{TO}	$FWHM_{TO}$	A_{LO}	$FHWM_{LO}$	A_{TO}/ A_{LO}
457.0	2.71	31	15.0	767	5.9	0.0404
608.0	2.04	5	15.0	142	5.7	0.0355
611.9	2.03	4	15.5	95	5.4	0.0435
615.1	2.02	15	15.0	359	5.6	0.0409
616.7	2.01	21	15.0	519	5.6	0.0400
617.6	2.01	3	15.0	88	5.6	0.0330
619.4	2.00	32	15.0	787	5.6	0.0404
624.7	1.99	95	15.1	1919	5.8	0.0493
624.7	1.99	50	15.0	1043	5.7	0.0482
626.0	1.98	103	15.0	2138	5.9	0.0481
628.7	1.97	25	15.5	393	5.6	0.0642
628.7	1.97	84	14.7	1661	5.8	0.0505
632.4	1.96	49	15.0	1064	5.8	0.0465
632.4	1.96	36	15.3	796	5.8	0.0452
637.6	1.94	21	15.0	180	6.3	0.1174
643.1	1.93	7	15.0	125	5.8	0.0555
646.9	1.92	8	15.0	172	5.7	0.0449
653.4	1.90	5	15.0	115	5.7	0.0399
657.1	1.89	8	15.0	201	5.6	0.0383
660.1	1.88	9	15.0	238	5.5	0.0387
663.1	1.87	10	15.0	261	5.7	0.0391
667.1	1.86	8	15.8	185	6.0	0.0444
670.6	1.85	25	15.0	373	5.4	0.0678
677.0	1.83	122	15.0	1160	5.4	0.1049
677.0	1.83	111	15.0	1080	5.4	0.1026
679.0	1.83	108	15.0	930	5.3	0.1164
679.0	1.83	97	15.0	955	5.4	0.1011
685.0	1.81	84	15.0	1041	5.5	0.0807
688.1	1.80	139	15.0	1812	5.6	0.0768
691.1	1.79	101	15.0	2100	6.1	0.0479
697.0	1.78	107	15.0	1951	5.6	0.0547
703.0	1.76	52	14.5	1072	5.5	0.0482
709.1	1.75	37	15.0	652	5.3	0.0562
716.6	1.73	20	15.0	392	5.4	0.0499

724.1	1.71	16	15.0	323	5.4	0.0495
737.9	1.68	15	15.0	365	5.5	0.0414
743.9	1.67	26	15.2	459	5.5	0.0573
747.1	1.66	24	15.0	402	5.5	0.0608
751.2	1.65	22	15.0	300	5.4	0.0719
755.1	1.64	37	15.0	398	5.7	0.0918
763.3	1.62	18	15.0	171	5.5	0.1084
770.3	1.61	6	15.2	71	5.4	0.0851
777.8	1.59	3	15.1	17	5.2	0.1466
678.9	1.83	65	15.0	637	5.5	0.1024
682.4	1.82	78	15.0	885	5.5	0.0885
685.9	1.81	120	15.0	1017	6.1	0.1183
689.6	1.80	84	15.0	1326	5.6	0.0630
693.0	1.79	112	15.0	1680	5.8	0.0668
700.1	1.77	50	15.0	1037	5.6	0.0481

***Table 3.19**: The excitation energy dependence of the A_{TO}/A_{LO} ratio measured on the (30,1) SWNT.*

CHAPTER 4 : INTRINSIC PROPERTIES OF INDIVIDUAL DOUBLE-WALLED CARBON NANOTUBES

This chapter concerns the understanding of the properties of individual DWNTs. In a first part (section 4.1), we will remind the model used to derive the diameter of the inner and outer tubes from the knowledge of the experimental in-phase and out-of-phase RBLMs. On the other hand, the profile of the G-modes allows us to identify, the achiral or chiral type, and the semiconducting or metallic character of the inner (outer) tube. Finally, the information derived from combined Raman and electron diffraction measurements allows to propose the identification of the structure of a $(n_i,m_i)@(n_o,m_o)$ DWNT (section 4.2). These assignments and Raman data are used to understand the optical absorption spectrum (section 4.3). Afterward, some new results obtained by Raman spectroscopy on individual DWNTs will be reported and discussed. They concern:

- The quantum interference effects which play a significant role on the relative intensity of the TO and LO modes of inner and outer tubes (section 4.4).
- The frequencies dependence of G-modes of inner tubes on the inter-tube distance (section 4.5)

4.1. Modeling of the RBLMs frequencies in DWNTs

To define the structure of a DWNT, one has to know the diameter of inner and outer tubes. Based on a model presented by Liu *et al.* [62], we develop a numerical method to evaluate the diameters of inner and outer tubes from the RBLM frequencies measured by Raman spectroscopy.

It must be reminded that all the individual suspended (free-standing) SWNTs, studied at L2C, follow the relationship $\omega_{RBM} = 204/d + 27$, which relates the nanotube diameter and the RBM frequency [74]. However, in DWNTs, the breathing-like mode (RBLM) frequencies are modified due to the mechanical coupling between the inner and outer tubes [62, 112]. This coupling causes a significant upshift of the RBLM frequencies as compared to the RBM frequencies of the corresponding individual inner and outer SWNTs. Very importantly, it was found that this shift also depends on the inter-layer distance between nanotubes. Thus, the conventional relationship between RBM frequencies and diameters in SWNTs does not work for RBLMs in DWNTs.

Kaihui Liu *et al.* [62] investigated the role of the inter-tube coupling on the RBLMs by combining Raman spectroscopy, Rayleigh scattering and electron diffraction experiments on

individual suspended DWNTs. These authors observed the up-shift for both the in-phase and out-of-phase RBLM frequencies in comparison with RBM frequencies of related individual SWNTs. Based on these experimental results, these authors developed a simple model, namely coupled harmonic oscillators including the van der Waals force constant between inner and outer tubes (Figure 4.1), to predict the relationship between the RBLMs frequencies and the diameters of the inner and outer tubes.

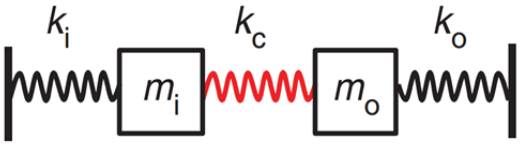

Figure 4.1*: Illustration of the coupled harmonic oscillators' model for DWNTs [62].*

As shown in the Figure 4.1, k_i and k_o are the unit-length intrinsic force constant of the corresponding inner and outer SWNTs. Values of k_i and k_o can be experimentally derived from the knowledge of the RBM frequency, $\omega_{i(o)}$, of the corresponding inner (i), and outer (o) SWNTs, by the expression:

$$k_{i(o)} = m_{i(o)}\, \omega^2_{i(o)} \qquad (4.1)$$

where $m_{i(o)}$ is the linear mass of inner (outer) SWNT; it is given by:

$$m_{i(o)} = c_1 D_{i(o)} \text{ (kg/m) with } c_1 = 2.4\times10^{-6} \text{ kg/m}^2 \qquad (4.2)$$

where $D_{i(o)}$ is the diameter of inner (outer) SWNT. Notice that in the case where $\omega_{i(o)}$ =228 (cm^{-1} nm) /$d_{i(o)}$. (as established for the individual free-standing SWNTs studied by Liu *et al.* [62]), one shows that:

$$k_{i(o)} = c_2/D_{i(o)} \text{ with } c_2 = 4.4\times10^3 \text{ N/m} . \qquad (4.3)$$

The unit-length coupling force constant, k_c, is a coupling force constant that characterizes the inter-layer interaction, defined by van der Waals interaction between the two concentric nanotubes. This parameter contains information how the van der Waals interaction varies with the separation between the inner and outer tubes. Obviously, k_c is expected to be different for different DWNTs. For given DWNT, with known (n_i,m_i)@(n_o,m_o), k_c can be derived as the single adjustable parameter to reproduce simultaneously the in-phase and out-of-phase RBLM frequencies.

The elementary spring geometry of coupled oscillators determines the RBLMs frequencies. The equations of motion for two coupled oscillators are given by:

$$\begin{aligned} m_i \ddot{x}_i &= -(k_i + k_c)x_i + k_c x_o \\ m_o \ddot{x}_o &= -(k_o + k_c)x_o + k_c x_i \end{aligned} \tag{4.4}$$

The system of equations (4.4) can be written in matrix form after introducing the weighted coordinates: $X = \sqrt{m}x$:

$$\begin{pmatrix} \ddot{X}_i \\ \ddot{X}_o \end{pmatrix} = K \begin{pmatrix} X_i \\ X_o \end{pmatrix} \text{ with } K = \begin{pmatrix} -\dfrac{k_i + k_c}{m_i} & \dfrac{k_c}{\sqrt{m_i m_o}} \\ \dfrac{k_c}{\sqrt{m_i m_o}} & -\dfrac{k_o + k_c}{m_o} \end{pmatrix} \tag{4.5}$$

K is the so-called dynamical matrix.

Let consider the following definitions and abbreviations [62]:

$$\omega_i^2 = \frac{k_i}{m_i},\ \omega_o^2 = \frac{k_o}{m_o},\ \omega_c^2 = \frac{k_c}{\sqrt{m_i m_o}},\ z_1 = \frac{\omega_i^2}{\omega_c^2} + \sqrt{\frac{m_o}{m_i}} \text{ and } \quad z_2 = \frac{\omega_o^2}{\omega_c^2} + \sqrt{\frac{m_i}{m_o}} \tag{4.6}$$

Then, dynamical matrix K can be written as:

$$K = \begin{pmatrix} -\omega_c^2 z_1 & \omega_c^2 \\ \omega_c^2 & -\omega_c^2 z_2 \end{pmatrix} \tag{4.7}$$

Let consider the most general real symmetric 2 x 2 matrix

$$A = \begin{pmatrix} a & c \\ c & b \end{pmatrix} \tag{4.8}$$

The eigenvalues are the roots of the characteristic equation:

$$\det \begin{vmatrix} a-\lambda & c \\ c & b-\lambda \end{vmatrix} = (a-\lambda)(b-\lambda) - c^2 = \lambda^2 - \lambda(a+b) + (ab - c^2) = 0 \tag{4.9}$$

The two eigenvalues λ_1 and λ_2, can be written as:

$$\lambda_{1,2} = \frac{1}{2}\left[a + b \pm \sqrt{(a-b)^2 + 4c^2} \right] \tag{4.10}$$

The frequencies of the RBLMs are the square roots of the eigenvalues.

By applying equation (4.10) and by using the definitions (4.6), the frequencies of the RBLMs of a DWNT are given by:

$$\omega_L = \sqrt{\lambda_1} = \frac{1}{2\pi c} \times \omega_c \times \sqrt{\frac{1}{2}\left[(z_1 + z_2) - \sqrt{(z_1 - z_2)^2 + 4} \right]} \tag{4.11}$$

$$\omega_H = \sqrt{\lambda_2} = \frac{1}{2\pi c} \times \omega_c \times \sqrt{\frac{1}{2}\left[(z_1 + z_2) + \sqrt{(z_1 - z_2)^2 + 4} \right]} \tag{4.12}$$

Where; c is speed of light, ω_L is the low-frequency RBLM *i.e.* the in-phase breathing modes of the tubes, and ω_H is the high-frequency RBLM *i.e.* the out-of-phase breathing modes of the tubes.

As discussed in chapter 3, the distance between inner and outer walls, δr, defined by the expression 4.13, ranges from 0.32 nm to 0.38 nm, with an average around 0.34 nm.

$$\delta r = \frac{\Delta D}{2} = \frac{D_o - D_i}{2} \tag{4.13}$$

Using this previous expression, the RBLM frequencies for each DWNT defined by the diameter of its inner and outer tubes, and then by the inter-tube distance, can be calculated and the best agreement between the calculated and experimental RBLMs provides the value of k_c for each DWNT investigated.

In must be emphasized that the unit-length coupling force constant k_c can be approximated by using the average unit-area inter-tube van der Waals potential U_{vdw} by (ref. [62]):

$$k_c = \left(\frac{\partial^2 U_{vdw}}{\partial r^2} \right) \cdot \pi \cdot \left(\frac{D_i + D_0}{2} \right) \tag{4.14}$$

where $(\partial^2 U_{vdw}/\partial r^2)$ is the unit-area force constant. Then, the knowledge of k_c permits to plot $(\partial^2 U_{vdw}/\partial r^2)$ as a function of the inter-tube distance. Figure 4.2 displays the dependence for the unit-area force constant $(\partial^2 U_{vdw}/\partial r^2)$ on the inter-walls distance (δr). This "exact" dependence is established from measurements on index-identified DWNTs performed by F. Wang group [62] and D. Levshov [90][1]. The red line is the van der Waals interaction between unit-area graphene sheets under pressure obtained from the measured compressibility of graphite [113]. The prediction well agrees with the ensemble of data measured on individual index-identified free-standing DWNTs. This plot can be used to derive the value of $(\partial^2 U_{vdw}/\partial r^2)$, and then k_c, for any individual DWNT with known δr.

[1] Here $\omega_i = 228/d$ and $\omega_o = 204/d + 27$.

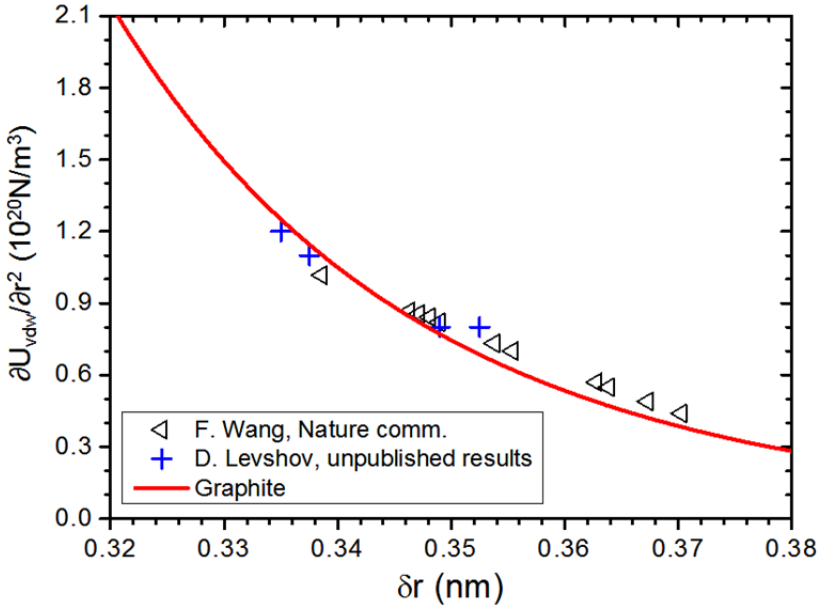

***Figure 4.2**: Unit-area force constant owing to tube–tube van der Waals interaction, ($\partial^2 Uvdw/\partial r^2$), triangles are experimental data from Feng Wang's group [62]; crosses are experimental data from the PhD thesis of D. Levshov [90]. The red line is the Van der Walls interaction between unit-area graphene sheet under pressure adapted from measurements on graphite (from ref. [113]).*

Usually, the inner walls diameters (D_i) range from 0.7 nm to 3 nm and the δr distance between inter-tubes from 0.32 nm to 0.38 nm. Then, for any given D_i, we can calculate the outer walls diameters by using expression (4.13). The values $m_{i(o)}$ and $k_{i(o)}$ are calculated by using expression (4.2) and (4.3), respectively. From the Figure 4.2, we can evaluate the value $\partial^2 U_{vdw}/\partial r^2$ for any given inter-tube distance and then derive the value of k_c by using expression (4.14). By applying expressions (4.6), we calculated the values of ω_i, ω_o, ω_c, z_1, and z_2. For the calculations, we use the relationship ω_i =228 (cm^{-1} nm)/D_i (ω_o =204 (cm^{-1} nm) /D_o+27) between the RBM frequency and the diameter of inner (outer) SWNT [90]. Using the equation (4.11) and (4.12), we can calculate the diameter dependence of the in-phase, (ω_L), and out-of-phase, (ω_H), RBLM frequencies as a function of the distances between the tubes. We plot in Figure 4.3a and 4.3c (Figure 4.3b and 4.3d) the calculated RBLM frequencies as a function of the diameter of inner (outer) nanotubes for various diameter differences (ΔD). As expected, the RBLM frequencies decrease with increasing diameter of inner (outer) tubes.

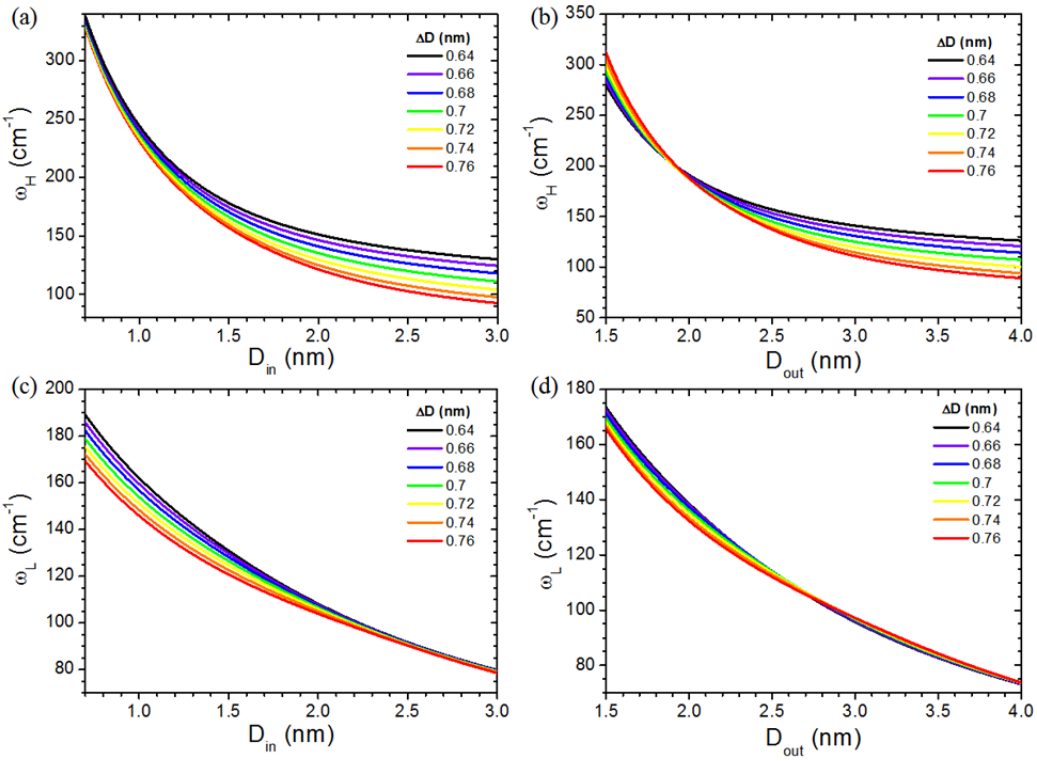

***Figure 4.3**: Frequencies of the in-phase (low-frequency, ω_L) and out-of-phase (high-frequency, ω_H) RBLMs as function of the diameter of the inner tube (a,c) and outer tube (b,d) for different ΔD.*

In order to derive the diameter of the inner and outer tubes from the knowledge of the experimental RBLMs, we developed the following method. The experimental RBLMs (ω_H and ω_L) are recorded by Raman spectroscopy. We plot in Figure 4.4 the calculated iso-frequency curves corresponding to the experimental ω_L and ω_H as a function of nanotubes diameter and diameter differences. Notice that in this calculation we used values of k_i and k_o adapted to the experimental situation. In our case, the frequencies of the RBM of the inner tube is given by ω_i =228 (cm^{-1} nm) /D_i and that of the outer tube by ω_o =204 (cm^{-1} nm)/D_o + 27(cm^{-1}) (see ref. [90]).

$$\omega_{RBM}^{i} = \frac{1}{2\pi c}\sqrt{\frac{k_i}{m}} = \frac{228}{D_i} \Rightarrow k_i = \frac{228^2 \times m \times (2\pi c)^2}{D_i^2} = \frac{4.4\times 10^3 (\mathrm{N/m})}{D_i}$$

$$\omega_{RBM}^{o} = \frac{1}{2\pi c}\sqrt{\frac{k_o}{m}} = \frac{204}{D_o} + 27 \Rightarrow k_o = \left(\frac{204}{D_o} + 27\right)^2 \times m \times (2\pi c)^2$$

The intersection point between ω_H and ω_L iso-frequency curves in Figure 4.4 determines the predicted inner (outer) tube diameter and diameter difference. In order to take into account the different error sources in the measurements of ω_H and ω_L, we consider that the experimental values of ω_L and ω_H are determined at ± 3 cm^{-1}. The green zone (of the Figure 4.4) called

"predicted range" corresponds to the estimated range for the couple (D_{out}, ΔD) within these hypotheses. The estimated maximum and minimum values in the predicted range allow us to evaluate the error bars on the predicted nanotubes diameter and diameter difference.

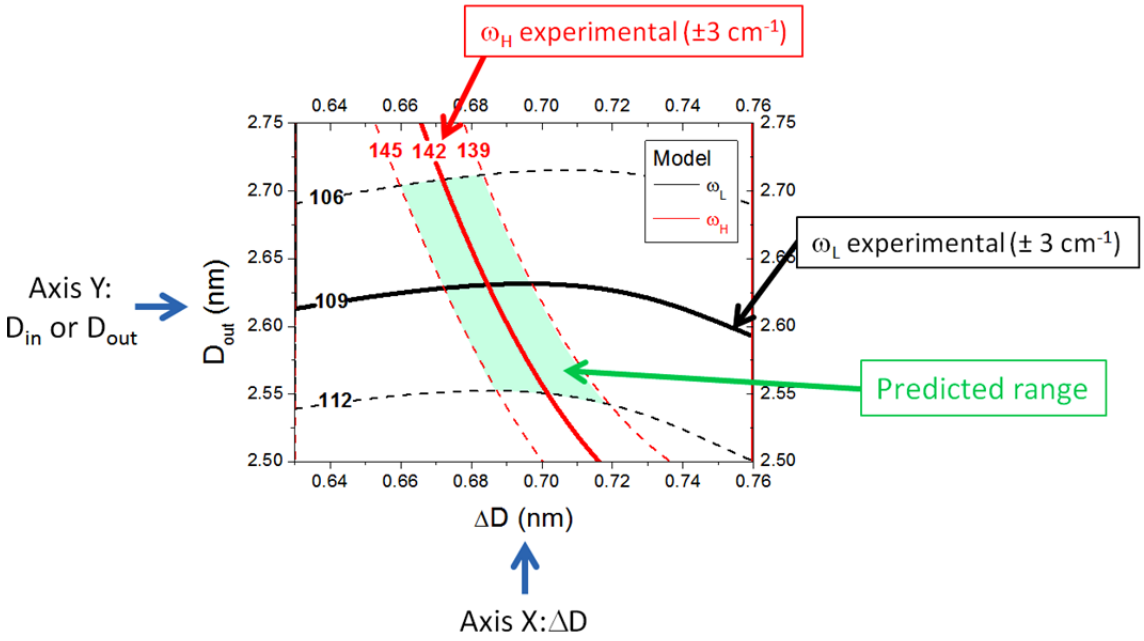

***Figure 4.4**: Iso-frequencies RBLM curves as a function of nanotube diameter and diameter differences.*

After the evaluation of each tube's diameter by Raman, the structure assignment of inner and outer tubes is only possible by taking into account information (especially the chiral angles) derived from electron diffraction.

4.2. Combined electron diffraction and Raman spectroscopy for structural assignment of individual $(n_i,m_i)@(n_o,m_o)$ DWNTs

In this section, we use the same procedure as the one developed for SWNTs (see chapter 3) to assign the chiral structure of the inner and outer tubes of individual free-standing DWNTs. The method combines information derived from electron diffraction (ED) and Raman spectroscopy. It must be emphasized that usually ED is sufficient to extract the structure of any DWNT. However, in our experiments, if the chiral angles are defined with a good precision from ED, a lack of a precise calibration of the distance due to possible tilt of the nanotube do not permit to define the diameters of the tubes with a sufficient precision. Consequently, Raman information are necessary to precise the structure of the investigated DWNTs. As indicated in the chapter 2, since the inner and outer tubes can be either semiconducting (SC) or metallic (M), a DWNT can display four configurations, namely SC@SC, SC@M, M@SC and M@M (inner@outer tubes).

All the TEM and ED analysis have been carried out by R. Arenal (University of Zaragoza, Spain). The method is first detailed for the assignment of the DWNT1 and, it is applied afterward to other DWNTs.

4.2.1. DWNT1

The high-resolution TEM (HRTEM) image and the EDP of the DWNT1 obtained by R. Arenal (University of Zaragoza, Spain) are shown on Figure 4.5. The analysis of the EDP provides the following values for the chiral angles: 15.3 ± 0.2° and 25.45 ± 0.20°. Notice that, at this stage, these angles cannot be specifically assigned to the inner or to the outer tube. From the TEM image and EDP the diameters of inner and outer tubes are also estimated as 2.07 ± 0.50 nm and 2.78 ± 0.50 nm, respectively.

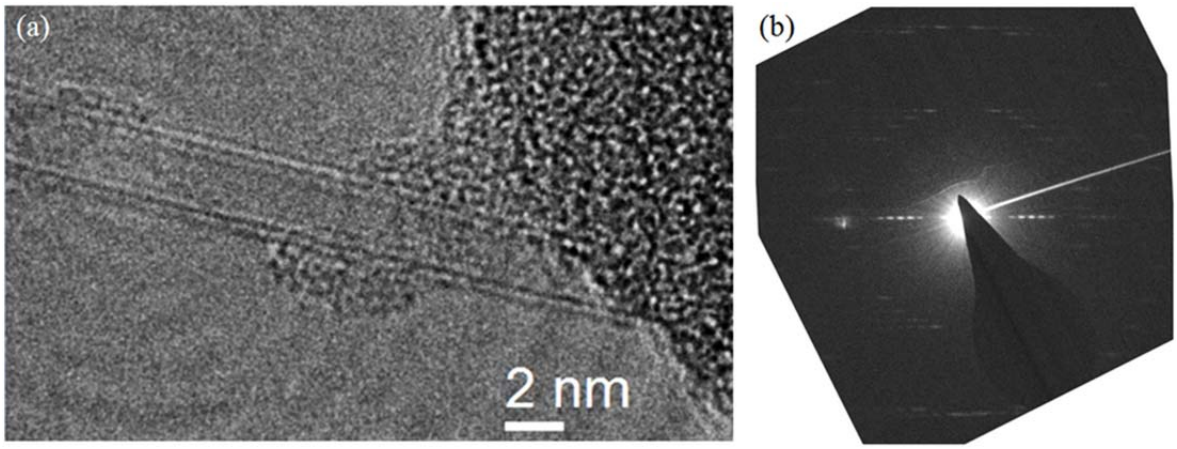

Figure 4.5*: (a) High-resolution TEM image of the DWNT1. (b) The corresponding electron diffraction pattern.*

Raman measurements were performed at different excitation wavelengths and representative spectra are shown on Figure 4.6a. From the G-bands line-shape, we can infer that both inner and outer tubes of this DWNT are semiconducting and chiral. The in-phase and out-of-phase RBLM are observed at 109 cm^{-1} and 142 cm^{-1}, respectively. Using the procedure presented in section 4.1, we can derive: i) the diameters of the inner and outer tubes which are: 1.945±0.100 nm and 2.63±0.10 nm respectively, and ii) the diameter difference: 0.685±0.030 nm (see Figure 4.6b and c). In order to assign the $(n_i,m_i)@(n_o,m_o)$, we plot together the TEM/ED and Raman information in the graph shown on Figure 4.7.

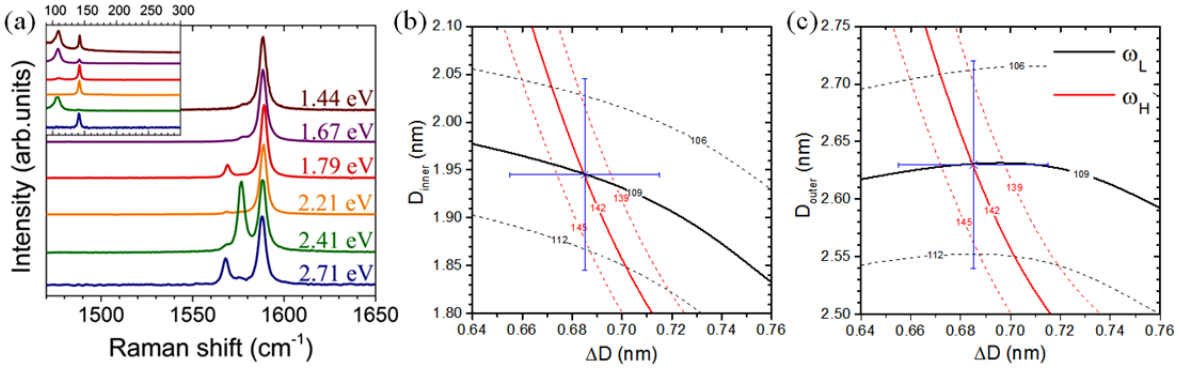

Figure 4.6: *(a) The G-modes part and RBLM part (inset) of Raman spectra of DWNT1 measured at different excitation energies. (b) Iso-frequencies RBLM curves as a function of the diameter of the inner tube and the diameter difference. (c) Iso-frequencies RBLM curves as a function of the diameter of the outer tube and the diameter difference.*

On this Figure 4.7:

-The two average chiral angles are derived from the electron diffraction with an uncertainly of 0.2° (the blue and yellow area in the Figure 4.7).

-The inner (bottom) and outer (top) diameter scale are aligned in order to have a difference of 0.685 nm between the diameters.

-The vertical dash yellow line puts in correspondence the diameter of inner and outer tubes derived from electron diffraction.

-The vertical dash blue line puts in correspondence the diameter of inner and outer tubes evaluated from the RBLM frequencies (Figure 4.6b, c)

Due to the poor accuracy of measured diameters, we consider a broader diameter range around the average diameter evaluated by Raman and ED (for each diameter, a range of about ± 0.5 nm is taken into account).

To determine all the possible assignments, we consider all SC@SC DWNTs which fall inside the yellow and blue areas and which have diameters in agreement with the ones derived from ED and Raman. On the plot, in order to take into account the error of 0.03 nm on the diameter difference, we affect an error bar of ±0.03 nm to the predicted diameter of the inner tube. For DWNT1, the possible assignments can be visually determined by looking for a couple of (n,m) (one in the bottom and one in the top part of the graph) which are vertically aligned and falls within the range defined above (Figure 4.7). We find only two possibilities, namely: (16,12)@(27,10) or (20,15)@(32,12), even for an unrealistically broad diameter range. The experimental and calculated data are compared on Table 4.1. We remind that the RBLM frequencies are calculated by using the model discussed in section 4.1 [62]. We clearly observe

that the calculated RBLM frequencies of (16,12)@(27,10) are close to the ones obtained from Raman experiments. On the other hand, the calculated RBLM frequencies of (20,15)@(32,12) are far away from the experimental ones. In conclusion, the most probable assignment for the DWNT1 nanotubes is: ***(16,12)@(27,10)***.

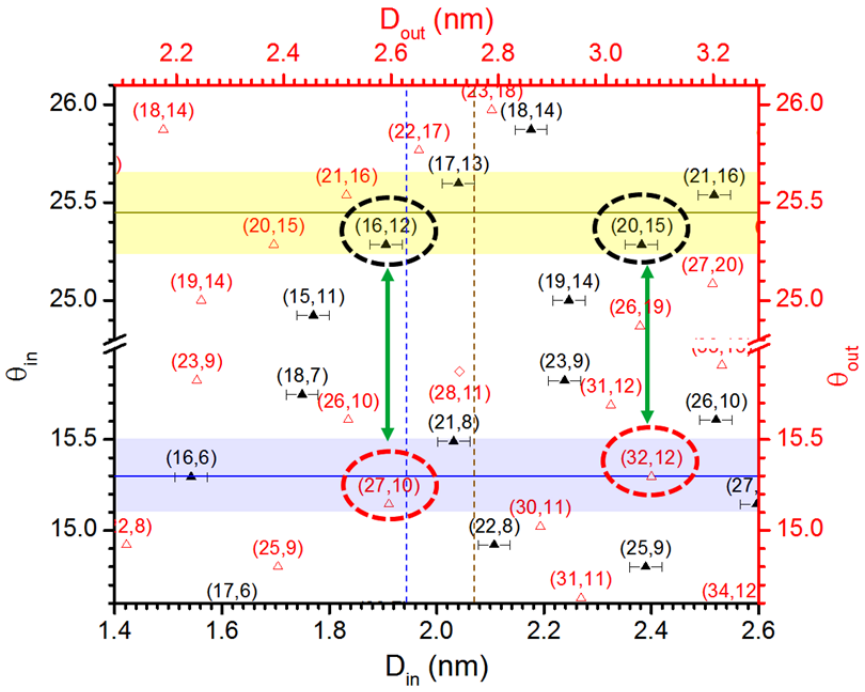

Figure 4.7: *Plot of the chiral angles as function of diameters for chiral semiconducting inner (bottom-left scale) and outer tubes (top-right scale). The solid black (open red) symbols correspond to inner (outer) tubes with (n,m) in labels. The blue (yellow) area corresponds to chiral angles of 15.3°± 0.2° (25.45°± 0.2°). The blue (yellow) dash line corresponds to the diameter of inner and outer tubes evaluated by Raman (electron diffraction). Error bars, correspondence of top and bottom scale (± 0.03 nm).*

	Raman	EDP	(16,12)@(27,10)	(20,15)@(32,12)
D_{in} (nm)	1.945 ± 0.100	2.07 ± 0.50	1.905	2.38
θ_{in}		25.45 ± 0.2°	25.285	25.285
D_{out} (nm)	2.63 ± 0.10	2.78 ± 0.50	2.595	3.08
θ_{out}		15.3 ± 0.2°	15.143	15.3
ΔD (nm)	0.685 ± 0.030	0.71	0.6905	0.703
ω_L / ω_H (cm^{-1})	109 / 142		97 / 139 (model from ref [62])	81 / 116
			110 / 141 (our approach)	94 / 120

Table 4.1*: The experimental diameters of inner/outer tubes, chiral angles, and diameter differences obtained by Raman measurements and EDP as compared to the theoretical values for the two possible assignments of DWNT1.*

4.2.2. DWNT2

On the Figure 4.8, we show the high-resolution and the EDP of the DWNT2. The analysis of the EDP provides the following values for the chiral angles: 20.28 ± 0.20° and 21.63 ± 0.20°. From the TEM image and the EDP the diameters of inner and outer tubes are estimated as 1.65 ± 0.50 nm and 2.33 ± 0.50 nm, respectively.

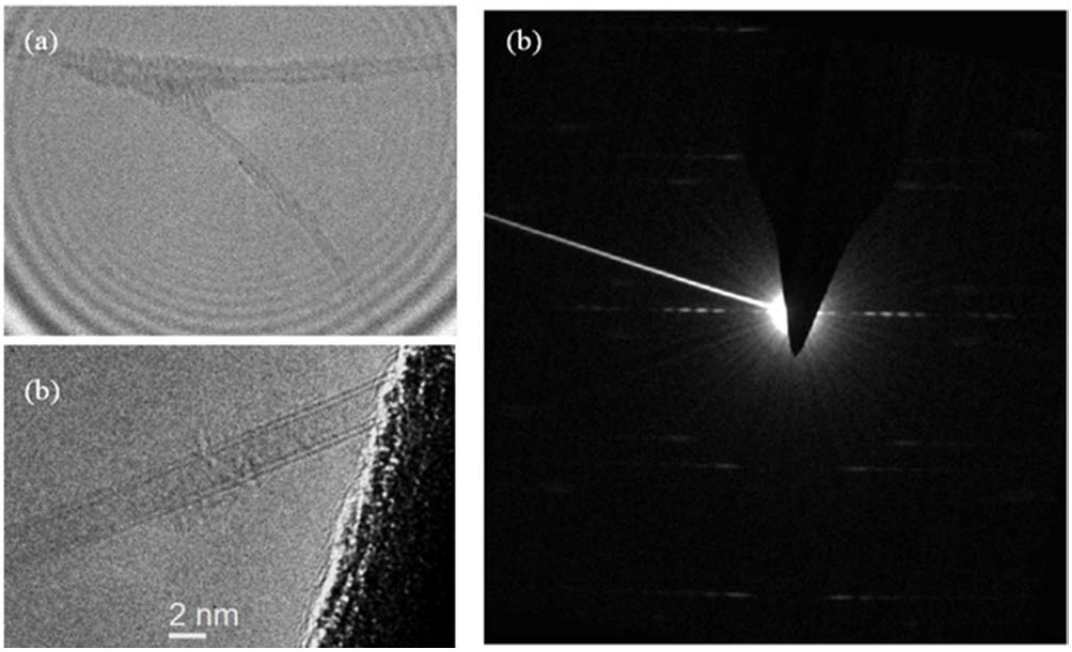

Figure 4.8*: (a) Low- (b) high-resolution TEM image of individual DWNT2. (c) The corresponding electron diffraction pattern.*

Raman measurements were performed at different excitation wavelengths and representative spectra are shown on Figure 4.9a. From the RBLM location and G-bands line-shapes, we can infer that the inner-tube and outer-tube of this DWNT are chiral metallic and semiconducting, respectively. The in-phase and out-of-phase RBLM are observed at 120 cm^{-1} and 157 cm^{-1}, respectively. Using the procedure presented in section 4.1, we can derive: i) the diameters of the inner and outer tubes which are, respectively, 1.675±0.125 nm and 2.358±0.100 nm and ii) the diameter difference: 0.683±0.050 nm (see Figure 4.9b and c). By considering all the possibilities of $(n_i,m_i)@(n_o,m_o)$ reported on Figure 4.10, we propose to assign the DWNT2 ***as (15,9)@(22,12).***

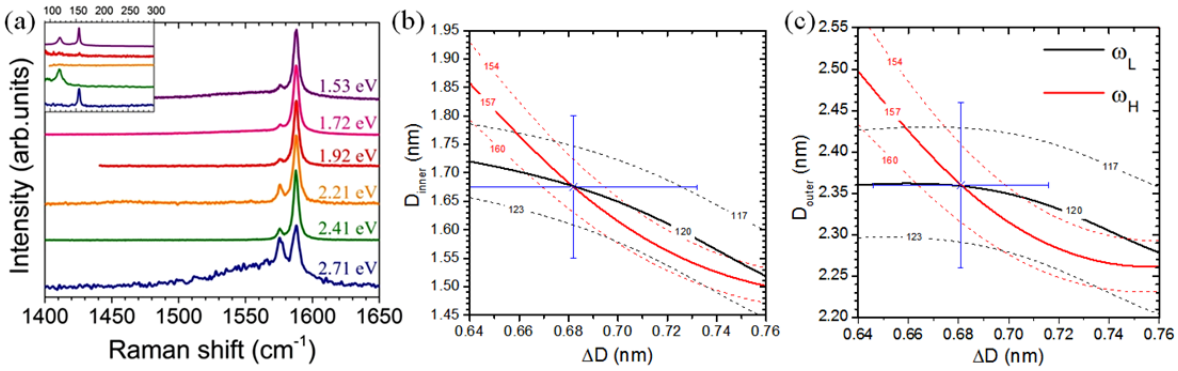

Figure 4.9: *(a) The G-modes part and RBLM part (inset) of Raman spectra of the DWNT2 measured at different excitation energies. (b) Iso-frequencies RBLM curves as a function of the diameter of the inner tube and the diameter difference. (c) Iso-frequencies RBLM curves as a function of the diameter of the outer tube and the diameter difference.*

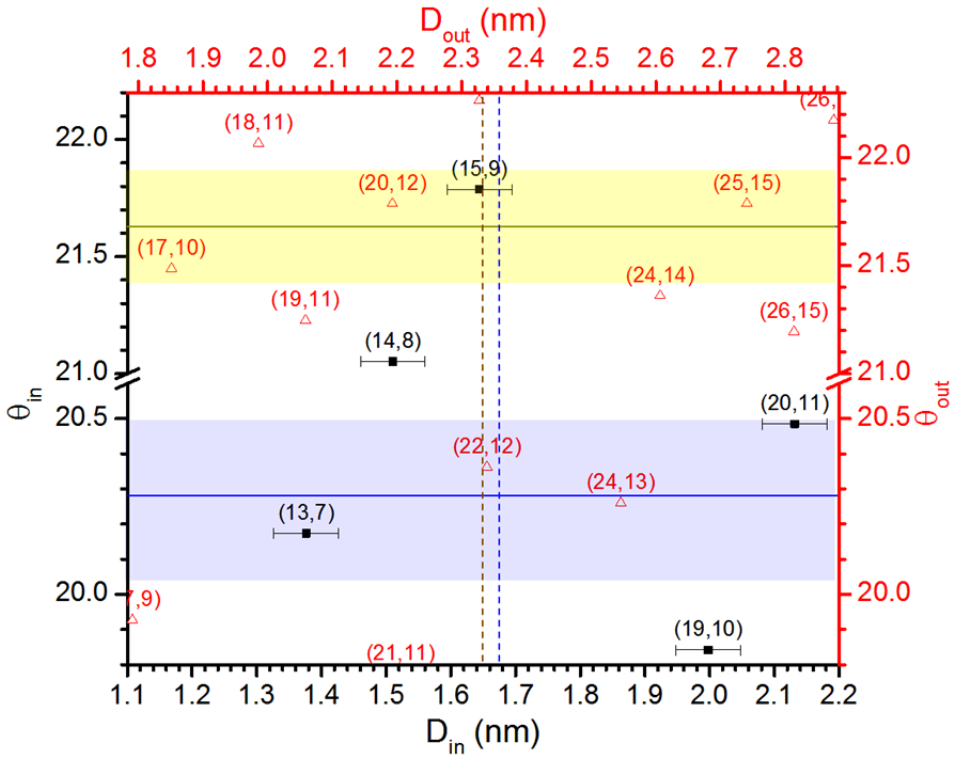

Figure 4.10: *Plot of the chiral angles as function of diameters for metallic inner (bottom-left scale) and semiconducting outer tubes (top-right scale). The solid black (open red) symbols correspond to inner (outer) walls with (n,m) in labels. The blue (yellow) area corresponds to chiral angles of 20.28°± 0.2° (21.63°± 0.2°). The blue (yellow) dash line corresponds to the diameter of inner and outer tube evaluated by Raman (electron diffraction). Error bars, correspondence of top and bottom scale (±0.05 nm).*

As summarized in the Table 4.2, we clearly observe that the calculated values of (15,9)@(22,12) are in good agreement with the ones obtained from Raman/ED experiments.

	RBLM	EDP	(15,9)@(22,12)
D_{in} (nm)	1.675 ± 0.125	1.65 ± 0.50	1.644
θ_{in}		21.63 ± 0.20°	21.79
D_{out} (nm)	2.358 ± 0.100	2.33 ± 0.50	2.34
θ_{out}		20.28 ± 0.20°	20.36
ΔD (nm)	0.683 ± 0.050	0.68	0.696
ω_L / ω_H (cm^{-1})	120/157		106/154 (model from ref [62])
			120.5/155 (our approach)

Table 4.2: *The experimental diameters of inner/outer tubes, chiral angles, and diameter differences obtained by Raman measurements and EDP as compared to the theoretical values for the (15,9)@(22,12) DWNT2.*

4.2.3. DWNT3

On Figure 4.11, we show the EDP of the DWNT3. The analysis of the EDP provides the following values for the chiral angles: 22.3 ± 0.5° and 27.56 ± 1°. Unfortunately, due to the breaking of the DWNT during TEM analysis and to the impossibility to derive the period of the equatorial line, we have not been able to evaluate the diameters of the inner and outer tubes by TEM.

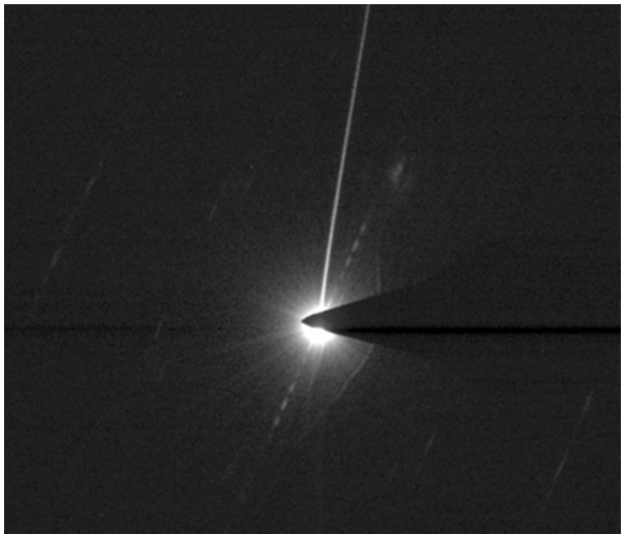

Figure 4.11: *The electron diffraction pattern on DWNT3.*

Raman measurements were performed at different excitations and representative spectra are shown on Figure 4.12a. From the G-bands line-shape we can infer that both inner and outer tubes are semiconducting and chiral. The in-phase and out-of-phase RBLM are observed at 135 cm^{-1} and 193 cm^{-1}, respectively. Consequently, we state that: (i) the diameters of the inner and outer

tubes are, respectively, 1.215±0.125 nm and 1.96±0.10 nm, and (ii) the diameter difference is 0.7465±0.0700 nm (see Figure 4.12b and c).

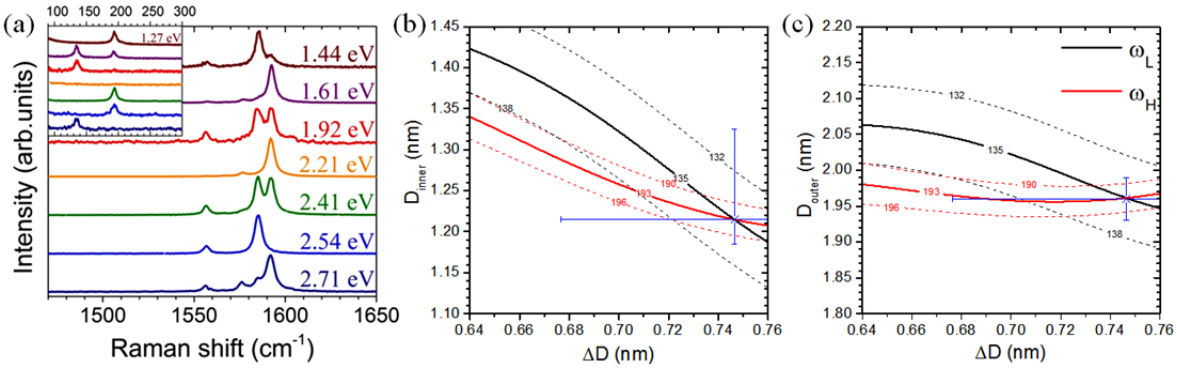

***Figure 4.12**: The G-modes part and RBLM part (inset) of Raman spectra of DWNT3 measured at different excitation energies. (b) Iso-frequencies RBLM curves as a function of the diameter of the inner tube and the diameter difference. (c) Iso-frequencies RBLM curves as a function of the diameter of the outer tube and the diameter difference.*

From the analysis of the Figure 4.13, we show that eight possible assignments can be proposed, namely: (10,6)@(15,13), (11,7)@(15,13), (11,7)@(16,14), (13,8)@(17,15), (10,9)@(18,11), (11,9)@(19,12), (11,10)@(19,12), (11,10)@(20,12), and (13,11)@(21,13).

We calculated the low-/high-frequency RBLM for all possible DWNTs. Only one, the (10,9)@(18,11), gives values which are compatible with the experimental ones (as summarized on the Table 4.3). The details of calculation for all possible assignments are shown in the Table 4.16 (in annex of this chapter). The calculated RBLM frequencies for the other possible DWNTs are incompatible with from the experimental frequencies. Therefore, we assign the DWNT3 as ***(10,9)@(18,11).***

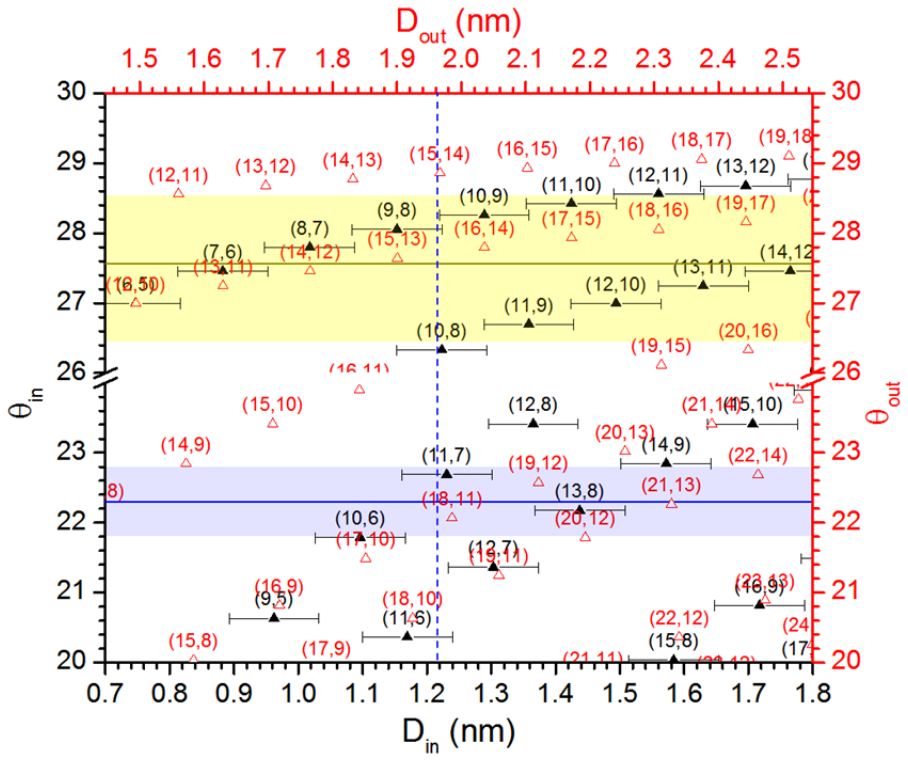

Figure 4.13: *Plot of the chiral angles as function of diameters for both semiconducting inner (bottom-left scale) and outer (top-right scale) tubes. The solid black (open red) symbols correspond to inner (outer) walls with (n,m) in labels. The blue (yellow) area corresponds to chiral angles of 22.3°±0.5° (27.56°±1°). The blue dash line corresponds to the diameter of inner and outer tube obtained by RBLM. Error bars, correspondence of top and bottom scale (±0.07 nm).*

	Raman	EDP	(10,9)@(18,11)
D_{in} (nm)	1.215±0.125		1.289
θ_{in}		27.56 ± 1°	28.26
D_{out} (nm)	1.96±0.1		1.986
θ_{out}		22.3 ± 0.5°	22.07
ΔD (nm)	0.7465±0.0700		0.697
ω_L / ω_H (cm^{-1})	135/193		123/188 (model from ref [62])
			137/189 (our approach)

Table 4.3*: The experimental diameters of inner/outer walls, chiral angles, and diameter differences obtained by Raman measurements and EDP as compared to the theoretical values for the (10,9)@(18,11) DWNT.*

4.2.4. DWNT4

Figure 4.14 shows the high-resolution image and the EDP of the DWNT4. The analysis of the EDP permits only to estimate one chiral angle at 19.1 ± 0.2°. From the TEM image, the diameters of inner and outer tubes are estimated close of 1.34 ± 0.50 nm and 2.07 ± 0.50 nm, respectively.

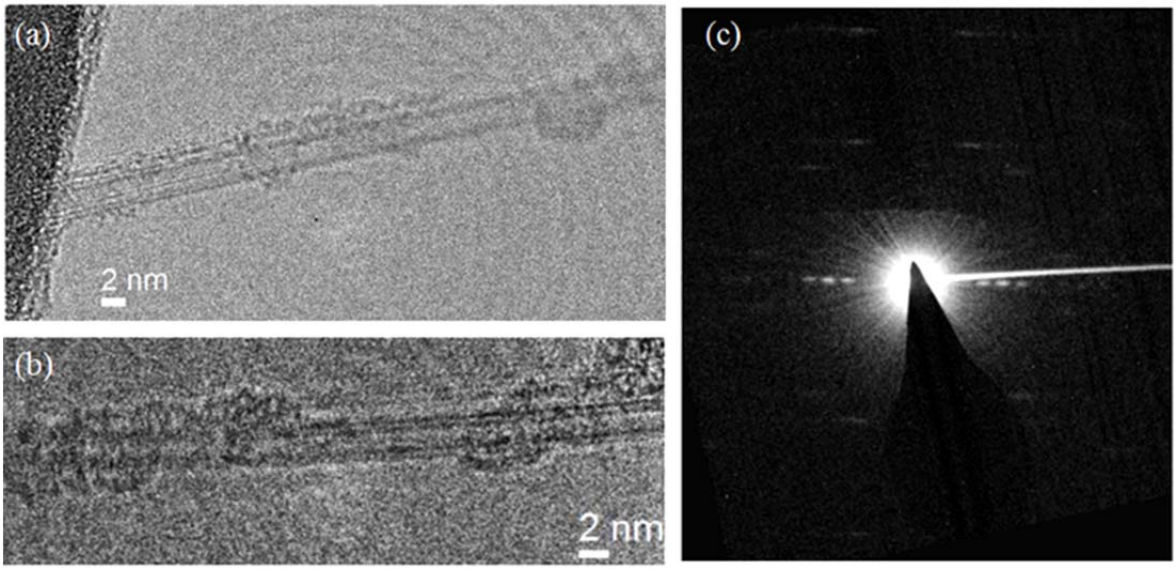

Figure 4.14: *(a) Low- (b) high-resolution TEM image of individual DWNT4. (c) The corresponding electron diffraction pattern.*

Raman measurements were performed in the 1.37 – 1.7 eV range. Representative spectra are shown on Figure 4.15. From the RBLM location and G-bands line-shape, we can infer that the inner (outer) tube of this DWNT is chiral semiconducting (chiral metallic) tube. The in-phase and out-of-phase RBLM are observed at 141 cm^{-1} and 206 cm^{-1}, respectively. Using the procedure reported previously, we can derive that: i) the diameters of the inner and outer tubes are, respectively, 1.146±0.075/0.040 nm and 1.874±0.030 nm, and ii) the diameter difference is 0.728±0.060 nm (see Figure 4.15b and c).

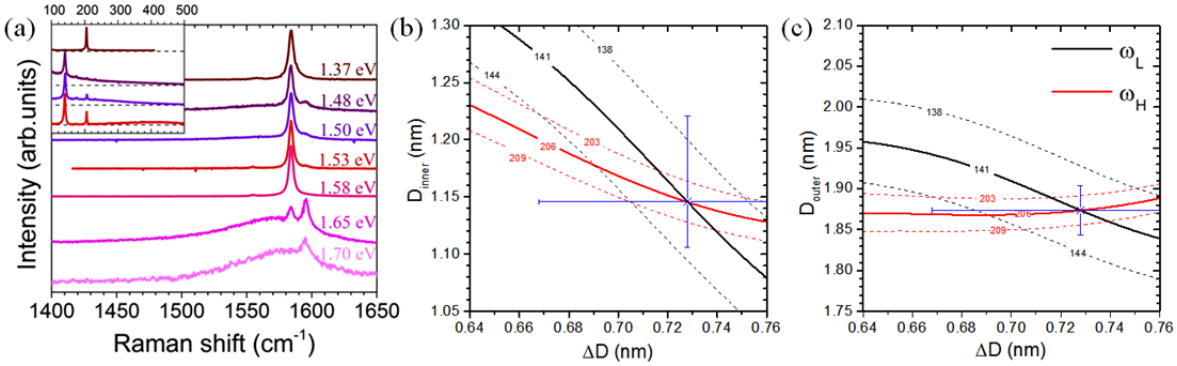

Figure 4.15: *(a) The G-modes part and RBLM part (inset) of Raman spectra of DWNT4 measured at different excitation energies. (b) Iso-frequencies RBLM curves as a function of the diameter of the inner tube and the diameter difference. (c) Iso-frequencies RBLM curves as a function of the diameter of the outer tube and the diameter difference.*

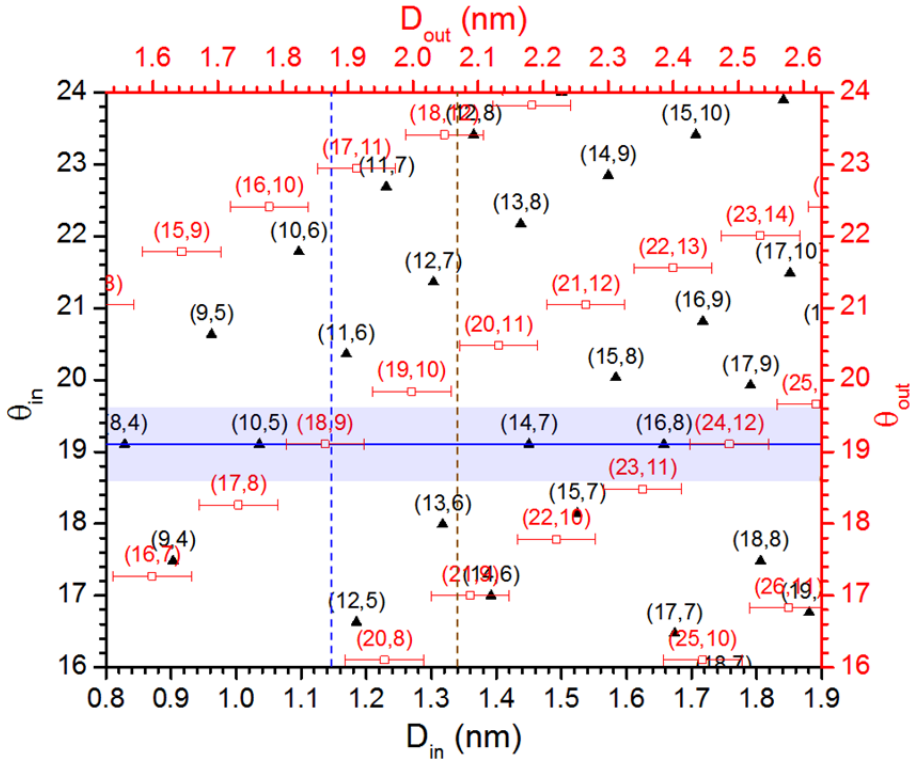

Figure 4.16: *Plot of the chiral angles as function of diameters for semiconducting inner (bottom-left scale) and metallic outer (top-right scale) tubes. The black (red) dots correspond to inner (outer) walls with (n,m) in labels. The blue solid line corresponds to chiral angles of 19.1°± 0.2°. The blue (yellow) dash line corresponds to the diameter of inner and outer tube obtained by RBLM (electron diffraction). Error bars, correspondence of top and bottom scale (±0.06 nm).*

The Figure 4.16 shows that it is not possible to find a corresponding inner and outer tubes with the same chiral angle although only one is observed experimentally. Since the intensity of the diffraction pattern is related to the number of carbon atoms interacting with the electron

beam, it seems reasonable to assume that the observed pattern corresponds to the outer tube. From the Figure 4.16, the best candidate for the metallic outer wall is (18,9).

We consider all possible inner tubes which have the diameters and diameter differences in the predicted range (Figure 4.17). Consequently, five pairs of indices for DWNT4, namely: (11,6)@(18,9), (9,8)@(18,9), (13,3)@(18,9), (14,1)@(18,9), (12,4)@(18,9), can be considered.

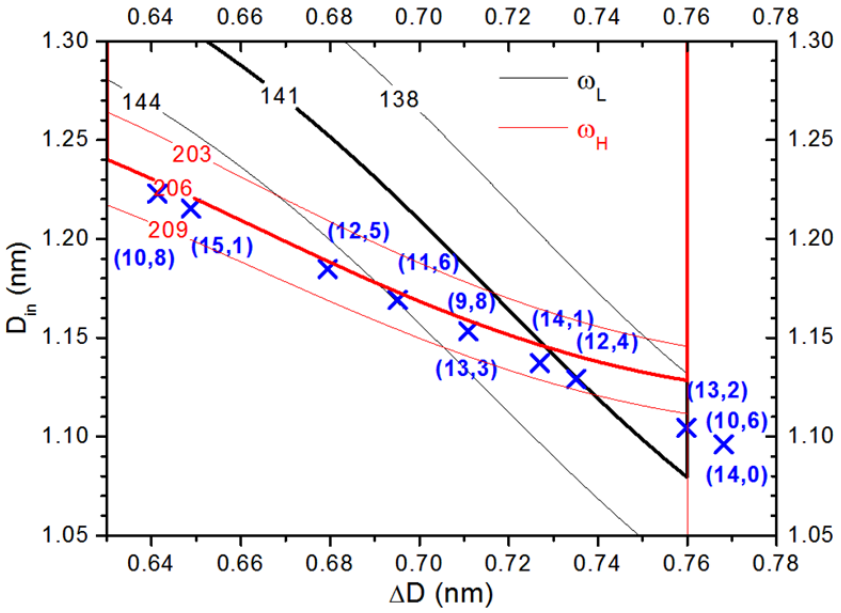

Figure 4.17: *Iso-frequencies RBLM curves as function of the diameter of inner tubes and diameter difference. The green cross symbols are possibilities of inner tubes associated with (18,9) metallic outer wall for DWNT4.*

4.2.5. Summary of DWNTs structure assignments

In the Table 4.4, we summarize the structure assignments of DWNTs derived by combining EDP and Raman spectroscopy.

DWNT	$(n_i,m_i)@(n_o,m_o)$	Type	ω_L (cm^{-1}) (data/calculation)	ω_H (cm^{-1}) (data/calculation)	D_{in} (nm)	D_{out} (nm)	ΔD (nm)	θ_{in}	θ_{out}
1	(16,12)@(27,10)	SC@SC	109/110	139/141	1.905	2.595	0.691	25.28	15.14
2	(15,9)@(22,12)	M@SC	120/120.5	157/155	1.644	2.34	0.696	21.79	20.36
3	(10,9)@(18,11)	SC@SC	135/137	193/189	1.289	1.986	0.697	28.26	22.07
4	Not assigned	SC@M	141/	206/	1.169	1.865	0.696		19.1

Table 4.4*: Characteristics of the five DWNTs investigated in the present work. The RBLMs frequencies are obtained by Raman measurements. Diameter of inner tubes and outer tubes are evaluated from the procedure described in section 4.1, (see text). For DWNT1-3, the diameter and diameter differences are calculated from the (n,m) indices of each tube. For DWNT4, the diameters and diameter difference are only estimated from the RBLM positions.*

4.3. Assignments of the transition energies of DWNTs from combined optical absorption and Raman spectra

By using spatial modulation spectroscopy (see chapter 3 and details in annex), absorption spectra have been measured on five index-identified DWNTs for incident light polarized along the nanotube. These results, obtained in collaboration with J.-C. Blancon (Université de Lyon), are detailed below. The transition energies of inner and outer tubes in DWNTs can be derived by combining the positions of absorbance bands and the measured Raman spectra at corresponding energies.

4.3.1. DWNT1: (16,12)@(27,10)

The absorption of the (16,12)@(27,10) DWNT is shown on Figure 4.18a. Six absorption peaks associated to optical transitions are observed at 1.44, 1.67, 1.81, 2.15, 2.44, and 2.75 eV (see Table 4.6).

The Raman spectra were recorded at excitation energies corresponding to the absorption peaks (Figure 4.18b). All the Raman spectra excited at these energies clearly show RBLMs and G-modes. The G-band profile is composed of three phonon components: one of them at ~1589 cm^{-1} is assigned to LO-mode of outer and inner tubes; the two others at 1577 cm^{-1} and 1568 cm^{-1} are assigned to TO-modes of outer and inner tubes, respectively.

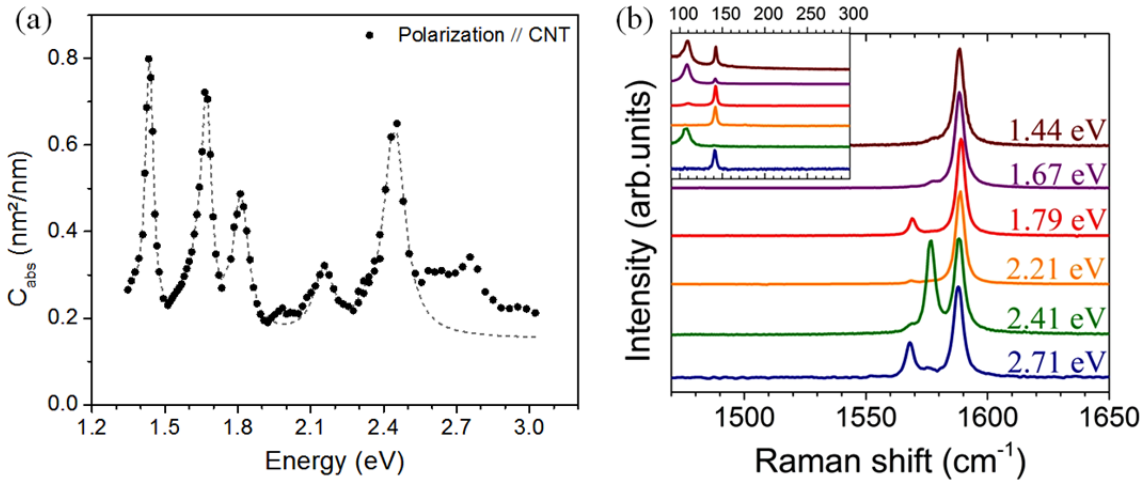

***Figure 4.18**: (a) Absorption spectrum and fitting dash line with Voigt functions, (b) Raman spectra of individual free-standing (16,12)@(27,10) DWNT.*

From the experimental absorption and Raman spectra, we propose that:

- The peaks at 1.44 and 1.67 eV are associated with optical transitions of the outer tube because we observe a stronger intensity for the in-phase RBLMs and the TO mode of outer tube

only at these energies. From the diameter of outer tube (2.595 nm), we infer that the transitions at 1.44 and 1.67 eV are identified as $E^S_{33,out}$, $E^S_{44,out}$, respectively.

-The peak at 2.44 eV is associated with optical transitions of the outer tube because of the resonance of the in-phase RBLM on the Raman spectra. In addition, we clearly observe that the TO mode of the outer tube displays an unusual strong intensity ascribed to constructive quantum interferences. Therefore, we suggest that the peak at 2.44 eV is a mix of $E^S_{55,out} + E^S_{66,out}$. Further discussions about interference effects on the Raman of this nanotube are detailed in section 4.4.2.

- The peaks at 1.81, 2.15, and 2.75 eV are associated with optical transitions of the inner tube since the out-of-phase RBLM dominate the Raman spectra recorded at these energies. From the inner tube diameter (1.905 nm), these energies are identified as $E^S_{33,in}$, $E^S_{44,in}$, and $E^S_{55,in}$.

In order to infer the transitions energy shifts for the (16,12)@(27,10), we compare the experimental values to the ones of the corresponding SWNTs. The optical transitions of SWNTs are calculated by V. Popov [31, 96] and measured/interpolated by F. Wang's group [33]. The results are summarized in the Table 4.5.

	Absorption energy (eV)	HWHM (meV)	Popov calculation [31, 96] (eV)				F. Wang calculation [33] (eV)			
			(16,12)	Δ_{inner}	(27,10)	Δ_{outer}	(16,12)	Δ_{inner}	(27,10)	Δ_{outer}
$E^S_{33,out}$	1.44	17.5			1.58	-0.14			1.53	-0.09
$E^S_{44,out}$	1.67	21.5			1.817	-0.147			1.74	-0.07
$E^S_{33,in}$	1.81	35	1.916	-0.106			1.88	-0.07		
$E^S_{44,in}$	2.15	97	2.32	-0.17			2.34	-0.19		
$E^S_{55,out}$ $+E^S_{66,out}$	2.44±0.05	48.5			E_{55}: 2.455 E_{66}: 2.485				E_{55}:2.5 E_{66}:2.48	
$E^S_{55,in}$	2.75	-	2.912	-0.162			2.896	-0.145		

Table 4.5*: Absorption characteristics of (16,12)@(27,10) (SC@SC) and the transitions energy shifts as compare to the corresponding SWNTs.*

Recently, the absorption spectrum of the (12,5)@(16,12) DWNT has been reported. It has been shown that the E_{33} and E_{44} transition energies of the (16,12) outer tube are 1.84 and 2.28 eV, respectively [112]. In this case, the authors noted that the E_{33} and E_{44} are downshifted by -0.04 eV and -0.06 eV as compared to the corresponding transitions of the (16,12) SWNT. In our case (16,12)@(27,10), the E_{33} and E_{44} transitions of the (16,12) inner tube are downshifted by -0.07 eV and -0.19 eV, respectively.

4.3.2. DWNT2: (15,9)@(22,12)

The absorption spectrum of the (15,9)@(22,12) is shown on Figure 4.19a, and b. Six absorption peaks are observed and located at 1.53, 1.57, 1.91, 2.38, 2.64, and 2.93 eV (see Table 4.6) [53].

The Raman spectra excited in range of 1.53 – 2.71 eV show three components for G-modes: a sharp G^+ peaks at 1588 cm^{-1}, a narrow and a broad G^- peak at 1576 cm^{-1} and 1558 cm^{-1}, respectively (Figure 4.19c and d).

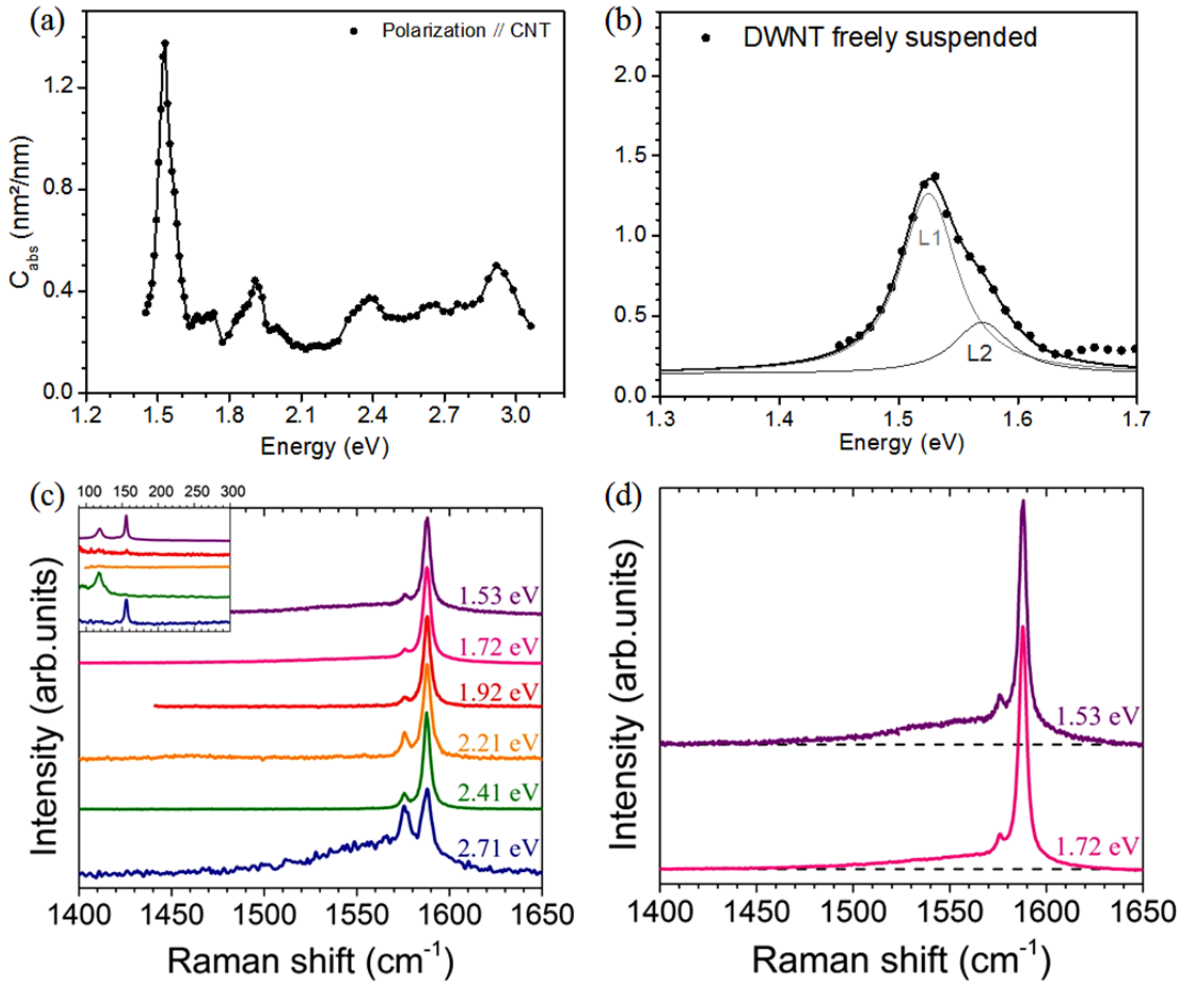

***Figure 4.19**: (15,9)@(22,12) DWNT. (a) Absorption spectrum; (b) zoom on the region around 1.55 eV in which two components are identified (L1 and L2). (c,d) RBLM (inset) and G-modes parts of the Raman spectra. The corresponding excitation laser energies are labeled on the graphs.*

From the experimental absorption and Raman spectroscopy data, we propose that:

- The peak at 2.38 eV is unambiguously assigned to $E^{S}_{55,out}$ because only the in-phase RBLM and a narrow and symmetric profile of TO and LO G-modes are observed in the Raman spectra excited at 2.41 eV.

- The peak at 1.91 eV is assigned to $E^{S}_{44,out}$ in agreement with three arguments: (i) the narrow and symmetric profile of the LO and TO G-modes in the Raman spectrum excited at 1.92 eV which identify G-mode of the semiconducting outer tube. (ii) No RBM was observed in the spectrum excited at 1.92eV in agreement with the calculations of V. N. Popov [109] which predict a zero amplitude of the RBM of the (22,12) tube in the Raman spectrum excited around its E_{44} transition. (iii) The G-mode spectra corresponding to the outgoing resonance at 2.21 eV confirms that an optical transition of the semiconducting outer tube is close of 1.91 eV.

- The peak at 2.64 eV is assigned to $E^{M}_{22(-),in}$ transitions because we observe only the out-of-phase RBLM and a broad profile of G^{-}-modes on the spectrum recorded at 2.71 eV.

- The peak at 2.93 eV can be assigned to $E^{M}_{22(+),in} + E^{S}_{66,out}$ transitions. However, no Raman spectrum was recorded to confirm this hypothesis.

The G-band line-shape of Raman spectra, excited at 1.53 and 1.72 eV, indicate that the peak at 1.53 eV should contain transitions of both metallic inner and semiconducting outer tubes (Figure 4.19d). From the diameter of inner (1.644 nm) and outer (2.34 nm) tubes, we infer that the absorption band at 1.53 eV relates to $E^{M}_{11,in}$ and $E^{S}_{33,out}$. Figure 4.20 presents the experimental REPs of RBLM, G-modes of the (15,9)@(22,12) in the 1.5-1.7 eV range. The fitting of REPs were performed independently for RBLM, LO and TO G-modes and they are needed here to assign the transition energies of inner and outer tubes.

From the results of the fit, we propose that the resonances peak at 1.53 eV corresponds to $E^{M}_{11(-),in} + E^{S}_{33,out}$ transition and the one at 1.57 eV to $E^{M}_{11(+),in}$ transition. Indeed, the transition energies of inner and outer tubes seem to be overlapped at 1.53 eV since the RBLM REPs for both tubes are observed to show a resonance at this energy (Figure 4.20a). This is consistent with the large absorption cross section of this DWNT at 1.53 eV (Figure 4.19a). The REPs of the G-modes also confirm this assignment (Figure 4.20b-d). Furthermore, the REP of the G^{-}-mode of the metallic inner tube (Figure 4.20c) can only be conveniently fitted if two interfering transitions at 1.53 and 1.57 eV are taken into account. This implies that the transition energies of 1.53 and 1.57 eV are the $E^{M}_{11(-),in}$ and $E^{M}_{11(+),in}$, respectively. Moreover, the absence of signal around $E^{M}_{11(+),in}$ in the REP of the out-of-phase RBLM is in agreement with the theoretical prediction of V. N. Popov [109].

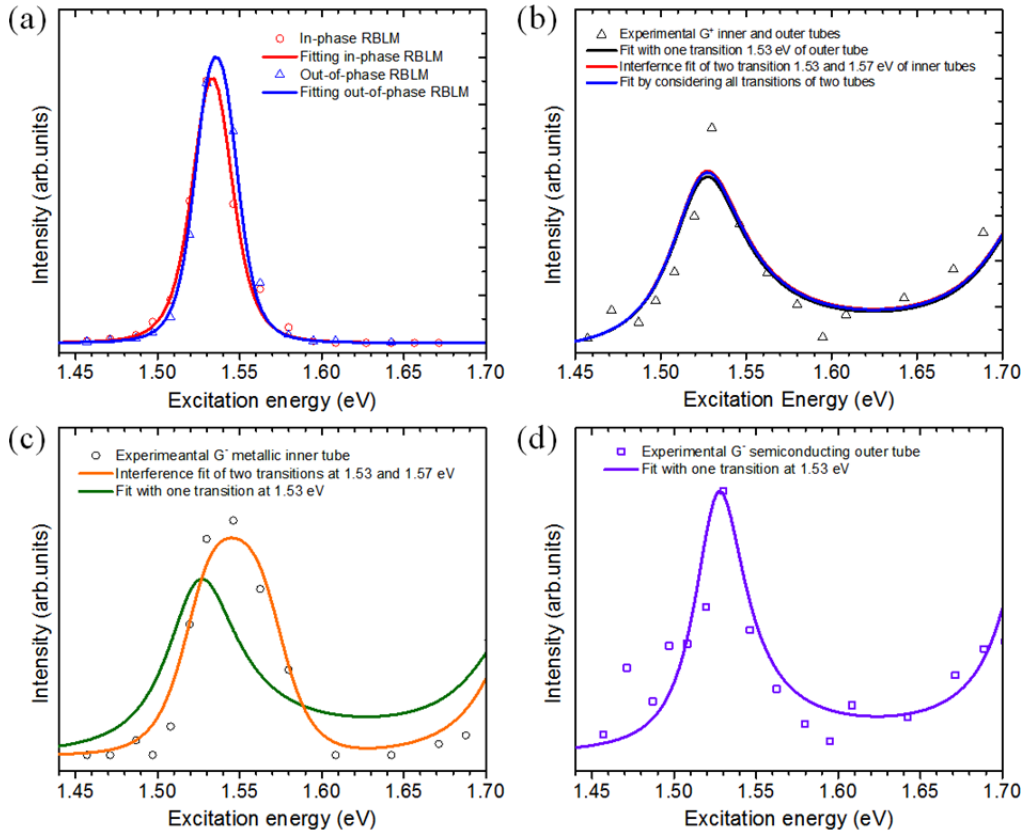

Figure 4.20: *(15,9)@(22,12) DWNT. (a) Experimental (symbols) and fit (solid lines) of the REPs of (a) RBLMs, and (b) G^+-mode of inner and outer tubes. (c) Experimental (symbols) and fit (solid lines) of the REP of the LO G-mode of the metallic inner tubes. The solid lines correspond to the fit of the REP with (orange line) and without (green line) interferences. (d) Experimental (symbols) and fit (violet solid lines) of the REP of the G^--mode of semiconducting outer tube. The values of E_{ii} and γ_{ii} obtained from absorption experiments are used in the fit of the REPs.*

By comparing the expected values for the corresponding SWNTs [31, 33, 96], we evaluated the related shifts for inner and outer tubes transitions as shown in Table 4.6. As in the case of DWNT1, we found an overall redshift of the transitions of the order of 100 meV. Our results compare well with the ones measured on the (15,9)@(25,8) DWNT for which the energies of the $E^{M}_{11(-)}$ and $E^{M}_{11(+)}$ transitions of the (15,9) inner tube were reported at 1.49 eV and 1.61eV respectively [112].

	Absorption energy (eV)	HWHM (meV)	Popov calculation [31, 96]				F. Wang calculation [33]			
			(15,9)	Δ_{inner}	(22,12)	Δ_{outer}	(15,9)	Δ_{inner}	(22,12)	Δ_{outer}
$E^{M}_{11(-),in}$ $+E^{S}_{33,out}$	1.53	26.5	1.59	-0.06	1.64	-0.07	1.59	-0.06	1.57	-0.04
$E^{M}_{11(+),in}$	1.57	27	1.67	-0.1			1.67	-0.1		
$E^{S}_{44,out}$	1.91	31.5			2.00	-0.09			2.01	-0.1
$E^{S}_{55,out}$	2.38	76			2.46	-0.08			2.48	-0.1
$E^{M}_{22(-),in}$	2.64	137	2.84	-0.2			2.79	-0.15		
$E^{M}_{22(+),in}$ $+ E^{S}_{66,out}$	2.93±0.1	93	3.06		2.92		3.08		2.97	

Table 4.6: *Absorption characteristics of (15,9)@(22,12) (M@SC).*

4.3.3. DWNT3: (10,9)@(18,11)

The absorption spectrum of the DWNT3 (the most probable assignment is (10,9)@(18,11)) is shown on Figure 4.21. Five absorption peaks are observed at 1.59, 1.9, 2.2, 2.42, and 2.8 eV. Additionally, a transition at 1.26 eV is identified by Raman resonance scattering (Figure 4.21b and 4.22).

The Raman spectra were recorded at excitation energies corresponding to the absorption peaks. The G-band profile is composed of four phonon components assigned as: LO_o at ~1592 cm^{-1}, LO_i at 1586 cm^{-1}, TO_o at 1577 cm^{-1} and TO_i at 1557 cm^{-1}.

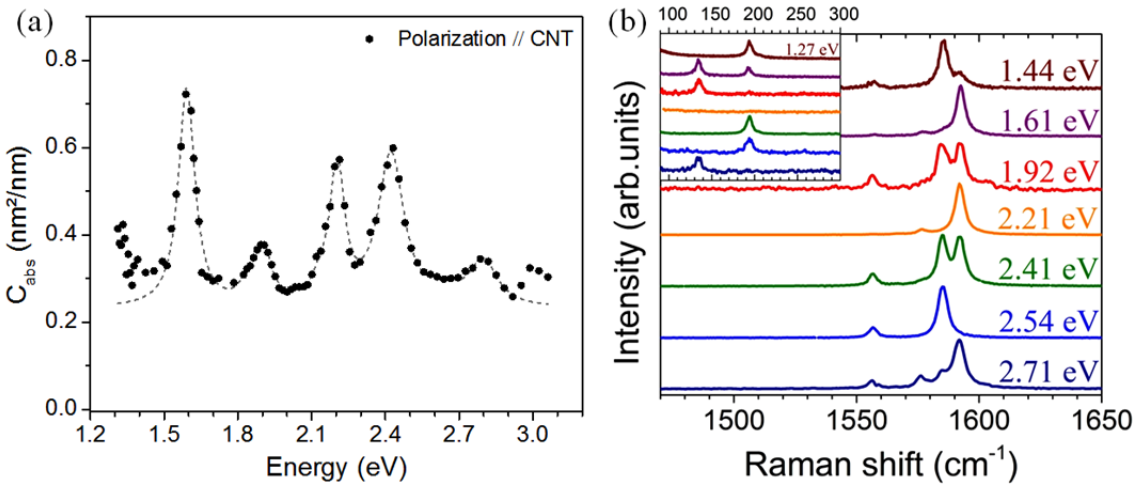

Figure 4.21*: (10,9)@(18,11) DWNT. (a) Absorption spectrum (black dots) and fit (dashed line) [53], (b) Raman spectra of the individual free-standing (10,9)@(18,11) DWNT.*

From the absorption spectra and Raman measurements, we propose the following assignments:

- The peaks at 1.26, and 2.42 eV are associated with optical transitions of the inner tube (diameter: 1.289 nm), namely: $E^S_{22,in}$ and $E^S_{33,in}$ respectively because i) only out-of-phase RBLM is observed on the Raman spectra at 1.27 and 2.41 eV eV and ii) the LO_i+TO_i dominate the spectra at 1.44 and 2.54 eV.

- The peaks at 1.9, and 2.8 eV are associated with optical transitions of the outer tube (diameter: 1.986 nm), namely: $E^S_{33,out}$, and $E^S_{55,out}$, respectively because only the in-phase RBLM is observed on the Raman spectra excited at 1.92 and 2.71 eV.

- The Raman spectrum, excited at 2.21 eV, shows no RBM but the resonance of G-modes was observed. This observation is consistent with the theoretical calculations by V. N. Popov which predicts a low intensity for the (18,11) RBM excited close of the E_{44}. Moreover, the G-band spectrum at 2.41 eV (as well as the one at 2.33 eV (not shown)) confirms that a transition of the outer tube is present at 2.21 eV. Therefore, the absorption peak at 2.2 eV is assigned to $E^S_{44,out}$.

Within the framework of these attributions, the absorption peak located at 1.59 eV cannot be assigned to any optical transition of the constituting SWNTs. The first question to address is then if another assignment could be possible. If we try to assign the measured transitions by just ordering them with regards to their energies in SWNTs, two options can be found as shown in Table 4.7. However, in both cases, inconstancies with the Raman data are present and the resulting shifts of the measured transitions with respect to the ones of SWNTs are unreasonable. Consequently, these alternative attributions have to be ruled out. We thus conclude that a new transition which doesn't exist in the corresponding SWNTs is present on the absorption spectrum of DWNT3. From our first analysis, the transition at 1.59 eV would be this new transition (E_{mix}) involving possibly a mixing of inner and outer tube electronic states. This hypothesis is supported by the striking behavior of the Raman features in the excitation range 1.5-1.8 eV. Indeed, as shown on Figure 4.21b and 4.22, i) both RBLM are only present with comparable intensities on the spectra measured near E_{mix} and ii) on the G modes REP near E_{mix}, for the resonance with incoming light, the G-modes of the outer tube dominate the spectra while for the resonance with outgoing light, the ones of the inner tube dominate. Looking back at the absorption spectrum presented on Figure 4.21a, this transition assignment rises some questions. Indeed, the high absorption cross-section at 1.59 eV could be found surprising for a mixed state. Furthermore, the low absorption cross-section at 1.9 eV as compared to the one at 2.21 eV questions its assignment as $E^S_{33,out}$. We can therefore not fully rule out the possibility that the transition at 1.59 eV corresponds to $E^S_{33,out}$ and the one at 1.9 eV corresponds to the new transition. Calculations as the ones recently reported [65, 112] would be certainly helpful to fully address this point. In the framework of this manuscript and without such additional information, we will consider that our first hypothesis is valid in the following.

	$E^S_{22,out}$	$E^S_{22,in}$	$E^S_{33,out}$	$E^S_{44,out}$	$E^S_{33,in}$	$E^S_{55,out}$	$E^S_{44,in}$
Popov	1.06	1.44	1.84	2.27	2.59	2.79	3.1
Wang	0.96	1.4	1.79	2.28	2.563	2.78	3.052
Option 1	1.26	1.59	1.9	2.2	2.42	2.8	
Option 2		1.26	1.59	1.9	2.2	2.42	2.8

Table 4.7: *Two possible assignments of transitions of (10,9)@(18,11) DWNT.*

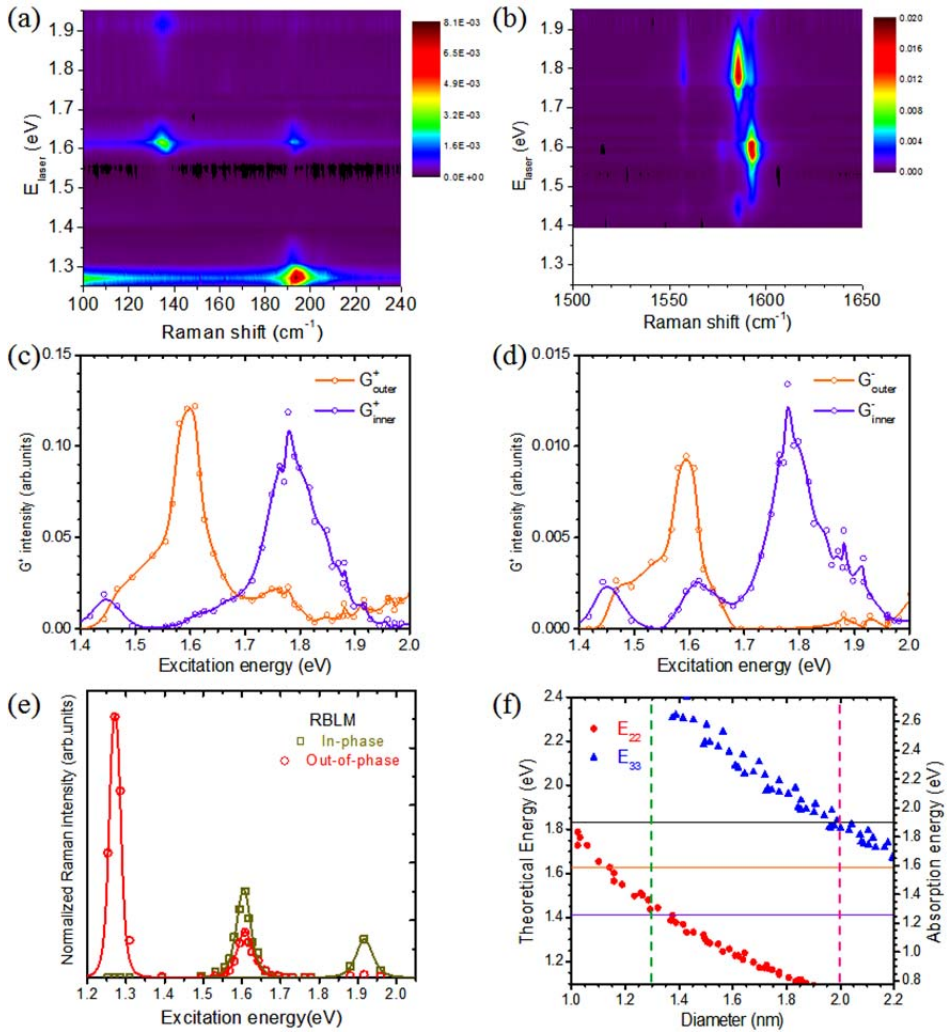

Figure 4.22: *(a) Raman map of (a) RBLM and (b) G-modes of (10,9)@(18,11) as function of excitation energy, in the range of 1.2 – 1.95 eV. (c,d) REPs of G-modes of outer and inner tubes. (e) Raman excitation profiles of (10,9)@(18,11) for in-phase and out-of-phase RBLMs. The transition energy (E_{ii}), and the width (γ) are free parameters in the fit. (f) The Kataura plot. Right scale corresponds to the theoretical calculation, (from ref. [29]), red (blue) dots: calculated energy of SNWTs type II (v = +1). Left scale corresponds to the measured absorption energies (violet, orange, black horizontal lines correspond to 1.26, 1.59, 1,9 eV). The dash green (pink) vertical line is diameter of inner (outer) tube.*

The comparison between the measured values of the transition energies of (10,9)@(18,11) to the one of corresponding SWNTs is shown on Table 4.8. Liu *et al.* observed the E_{44} of outer tube (18,11) in (12,7)@(18,11) DWNT at 2.21 eV and it is downshifted -0.07 eV as compare to the corresponding one in (18,11) SWNT [112]. Clearly, our data measured at 2.2 eV is close of the one of this previous report.

	Absorption energy (eV)	HWHM (meV)	Popov calculation [31, 96]				F. Wang calculation [33]			
			(10,9)	Δ_{inner}	(18,11)	Δ_{outer}	(10,9)	Δ_{inner}	(18,11)	Δ_{outer}
$E^{S}_{22,in}$	1.26		1.44	-0.18			1.40	-0.14		
New E^{S}_{mix}	1.59	38.5			(1.84)	(-0.25)			(1.79)	(-0.2)
$E^{S}_{33,out}$	1.9	38			1.84	+0.06			1.79	+0.11
$E^{S}_{44,out}$	2.2	33.5			2.27	-0.07			2.28	-0.08
$E^{S}_{33,in}$	2.42	61.5	2.59	-0.17			2.56	-0.14		
$E^{S}_{55,out}$	2.8	51			2.79	+0.01			2.78	-0.02

Table 4.8*: Absorption characteristics of DWNT3: (10,9)@(18,11) (SC@SC).*

4.3.4. DWNT 4: inner@(18,9)

The absorption spectrum of the DWNT4 is shown on Figure 4.23a. The main absorption features, derived by fitting the spectrum, are located at 1.36, 1.46, 1.52, 2.60, 2.77, and 2.88 eV.

The Raman spectra excited in range 1.37 – 1.7 eV showed two G^+-modes at 1585 cm^{-1} and 1596 cm^{-1} (linewidths ~ 5 cm^{-1}) and two G^--modes are located at 1555 cm^{-1} (linewidths ~ 4 cm^{-1}) and 1565 cm^{-1} (linewidths ~ 80 cm^{-1}) (Figure 4.23b).

Based on absorption and Raman measurements, we propose that:

- The peak at 1.36eV corresponds to the $E^{S}_{22,in}$ because we observed only the out-of-phase RBLM and a narrow profile of G-modes on the Raman spectra at 1.37 eV.

- The peaks at 1.46, 1.52 eV is assigned to the transitions of the metallic outer tube, namely: $E^{M}_{11(-),out}$, $E^{M}_{11(+),out}$ because we observed a strong in-phase RBLM in this laser energy range and an electronic Raman scattering (ERS) band at ~1.46 eV associated to the E^{M}_{-} in metallic tubes [114, 115]. Additionally, the outgoing resonances of the metallic outer tube G-modes at 1.65 and 1.7 eV confirm this assignment.

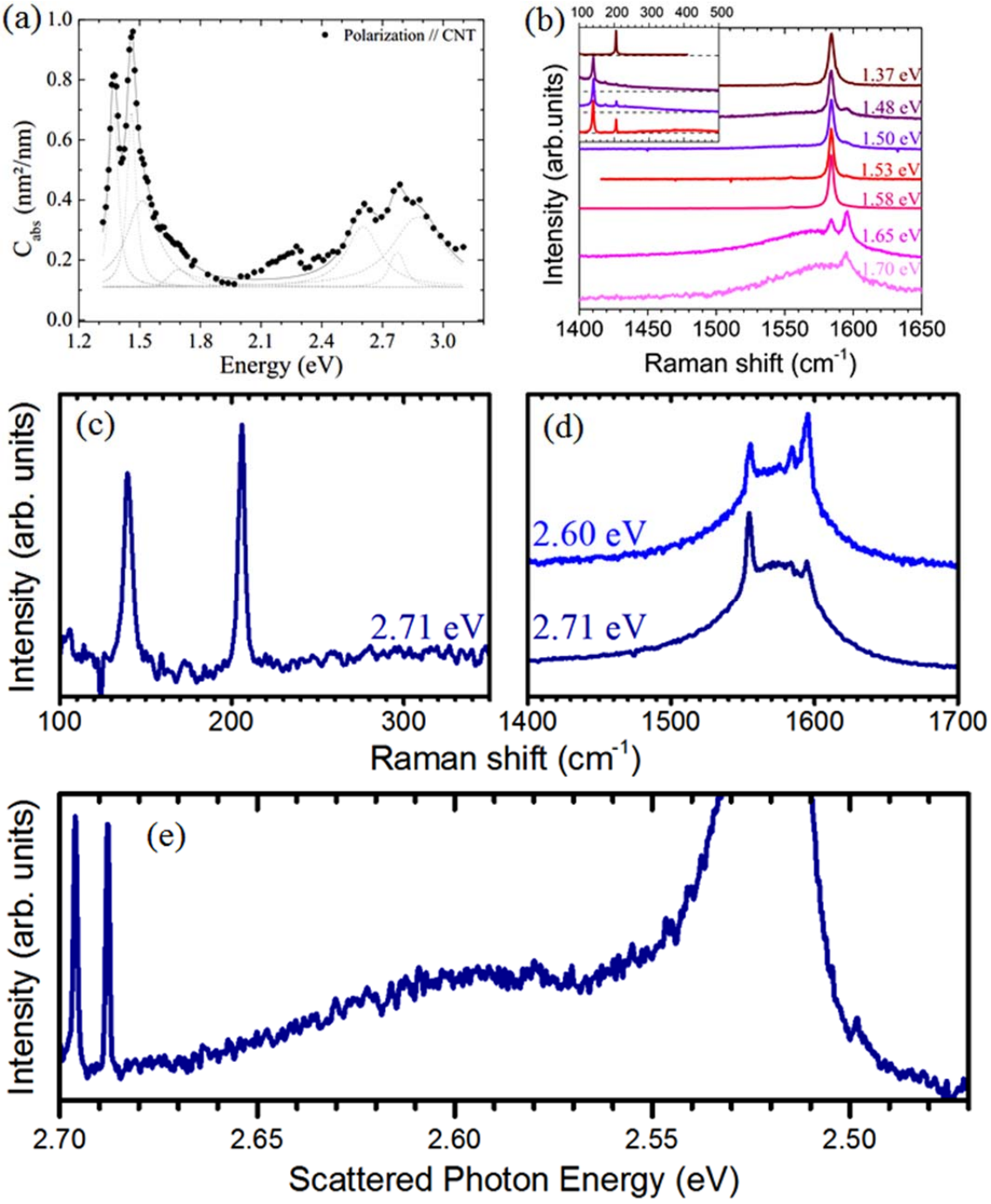

Figure 4.23: *(a) Absorption spectrum and fit [53], (b) Raman spectra of individual free-standing DWNT4. Raman spectra excited at 2.6 and 2.71 eV, (c) RBLM, (b) G-modes part. (e) Electronic Raman scattering exited at 2.71 eV.*

- The peaks at 2.6 eV is assigned to $E^{M}_{22(-),out}$ because of the incoming resonance of G^--modes at 1564 cm^{-1} (Figure 4.23d) and the observation of an ERS band at 2.6 eV. On Figure 4.23e, the Raman spectrum, excited at 2.71 eV, of the suspended DWNT4 is plotted as a function of scattered photon energy ($\hbar\omega_s$). The Raman spectrum shows a broad peak located between RBLM and G-modes. The scattered photon energy of the ERS peak is observed around 2.6 eV which corresponds to the $E^{M}_{22(-)}$ transition of the metallic outer tube.

- The peaks at 2.77 eV is assigned to a mix of $E^{S}_{33,in} + E^{S}_{44,in}$ because the Raman spectra, excited at 2.71 eV, shows a dominant (absent) signal of TO (LO) G-mode of semiconducting inner tube (Figure 4.23d). This is the result of interference effects arising in the case of two merged transitions which is further discussed in the following section 4.4.1.

- The resonances peaks at 2.88 eV could be assigned to $E^{M}_{22(-),out}$. However, no Raman data are available to confirm this prediction.

The assignments of transition energies allow us to identify the chiral index of inner tube of DWNT4. We remind that five candidates for inner tube are remaining after the analysis of the TEM/ED in section 4.2.4, namely the (11,6), (9,8), (13,3), (14,1) and (12,4). In order to assign the chirality, we compare the calculated transition energies of all candidates with the corresponding ones measured by absorption. In the recent publication of Liu *et al.* [112], it is reported that the optical transition energy shifts are varying from a downshift of 190 meV to an upshift of 50 meV. In Figure 4.24, we plotted the energy shifts of E_{33}, E_{44}, and E_{55} that will imply each of the five possible assignments for DWNT4's inner tubes. The only inner tube for which all the energy shifts are falling in range –200 meV – +50 meV is the (11,6). We thus assign **DWNT4** as the **(11,6)@(18,9)**.

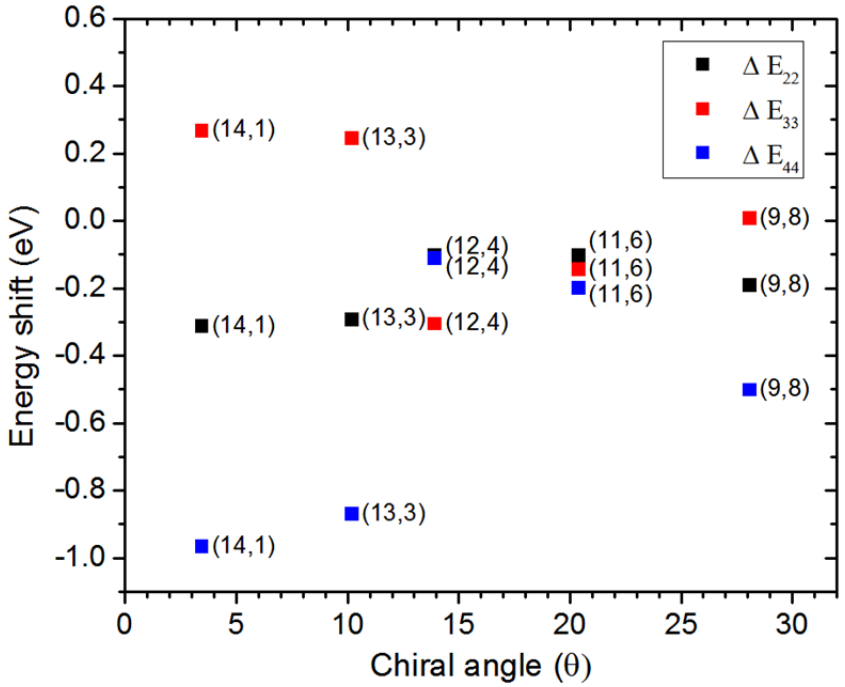

Figure 4.24: *The chiral angle dependence of the energy shifts between the experimental energies and the calculated ones for the five possible candidates for inner tube of the inner@(18,9) DWNT.*

We summarize the calculated values of (11,6)@(18,9) as compared to the ones obtained by Raman/ED experiments (Table 4.9). The comparison between the measured energies of the (11,6)@(18,9) and the calculated ones of corresponding (11,6) and (18,9) SWNTs is shown on Table 4.10.

	RBLM	EDP	(11,6)@(18,9)
D_{in} (nm)	1.146±0.075/0.04		1.169
θ_{in}			20.36
D_{out} (nm)	1.874±0.03		1.865
θ_{out}		19.1 ± 0.2°	19.1
ΔD (nm)	0.728±0.06		0.696
ω_L / ω_H (cm^{-1})	141/206		130.5/206.7 (model from ref [62])
			143.5/206 (our approach)

Table 4.9: *The diameter of inner/outer tubes, and the diameter differences evalutated by combined Raman and EDP data as compared to the theoretical values for the (11,6)@(18,9) DWNT.*

	Absorption energy (eV)	HWHM (meV)	Popov calculation [31, 96]				F. Wang calculation [33]			
			(11,6)	Δ_{inner}	(18,9)	Δ_{outer}	(11,6)	Δ_{inner}	(18,9)	Δ_{outer}
$E^{S}_{22,in}$	1.36	27.5	1.5	-0.14			1.46	-0.1		
$E^{M}_{11(-),out}$	1.46	28			1.45	+0.01			1.42	+0.04
$E^{M}_{11(+),out}$	1.52	52			1.51	+0.01			1.51	+0.01
$E^{M}_{22(-),out}$	2.60	96			2.58	+0.02			2.55	+0.05
$E^{S}_{33,in} + E^{S}_{44,in}$	2.77±0.04	34	2.93 3.13				2.91 2.97			
$E^{M}_{22(+),out}$	2.88	146			2.8	+0.08			2.84	+0.04

***Table 4.10**: Absorption characteristics of DWNT4: (11,6)@(18,9) (SC@M).*

In summary, the absorption energies measured on four index-identified individual DWNTs by spatial modulation spectroscopy were compared to the calculated ones of related SWNTs. The results displayed in Figure 4.25 show that the average downshift of inner tubes is of about 150 meV for most of the transition energies. By contrast, the shifts of the transition energies of outer tubes range from -100 meV (red-shift) to100 meV (blue-shift). Our results are in agreements with previous data obtained by absorption measurements [112] and by the fit of the experimental REPs [116].

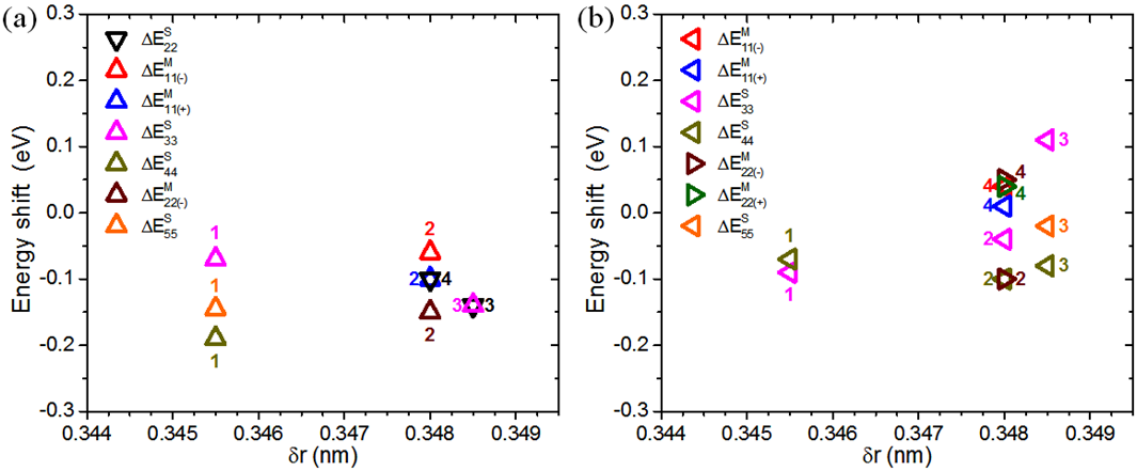

***Figure 4.25:** The energy shift of the optical transitions of (a) inner tubes and (b) outer tube, with regards to the optical transitions energies of the corresponding SWNTs, of four index-identified DWNT as function of inter-tube distances. 1-(16,12)@(27,10); 2-(15,9)@(22,12); 3-(10,9)@(18,11); 4-(11,6)@(18,9).*

4.4. Quantum interference in double-walled carbon nanotubes

As in SWNTs (see chapter 3), with regards to the values on one hand of the energies of the incoming and outgoing resonances (especially those involving the G-modes), and on the other hand the values of the energies of the optical transitions, quantum interferences can be observed in DWNTs. Especially, interference effects can produce striking behaviors on the dependence of the intensity of G-modes of the inner and outer tubes with the excitation energy.

4.4.1. Quantum interference effect on the response of G-modes

Case 1: $E_{jj} = E_{ii} + E^{G}_{phonon}$.

Individual (16,12)@(27,10) DWNT (SC@SC): As shown in the Figure 4.18, the third and fourth optical transitions of outer tube are located at 1.44 eV and 1.67 eV. The energy difference, $\Delta E = 0.23$ eV, is close to the phonon energy of G-modes (~200 meV). This situation can give the opportunity to observe the effects of quantum interferences on the intensity of the G-modes of the outer tube.

In Figure 4.26, the Raman spectrum of (16,12)@(27,10) DWNT, excited at 1.55 eV, is shown. An intense LO mode, located at 1589 cm^{-1}, is observed while the TO mode is completely absent. Although the energy difference between the excitation energy and the E_{33} transition is 0.11 eV, the intensity of the LO (TO) mode is significantly affected by constructive (destructive) interference in the Raman spectrum excited at 1.55 eV. Indeed, as shown in Figure 4.26b and c, an enhancement is expected for the LO mode and a concomitant significant decreasing of the intensity of the TO mode is predicted. The experimental results are in good agreement with the predictions.

It can be emphasized that a fast analysis of the profile of the Raman spectrum would lead at the conclusion that a zigzag tube is present in the structure of this DWNT [84]. The assignment of the tubes from ED rules out such assignment. As a consequence, combining Raman and ED allows us to precise the role of the interference effects and to explain the dominant LO contribution measured in the Raman spectrum of the (16,12)@(27,10) DWNT excited at 1.55 eV.

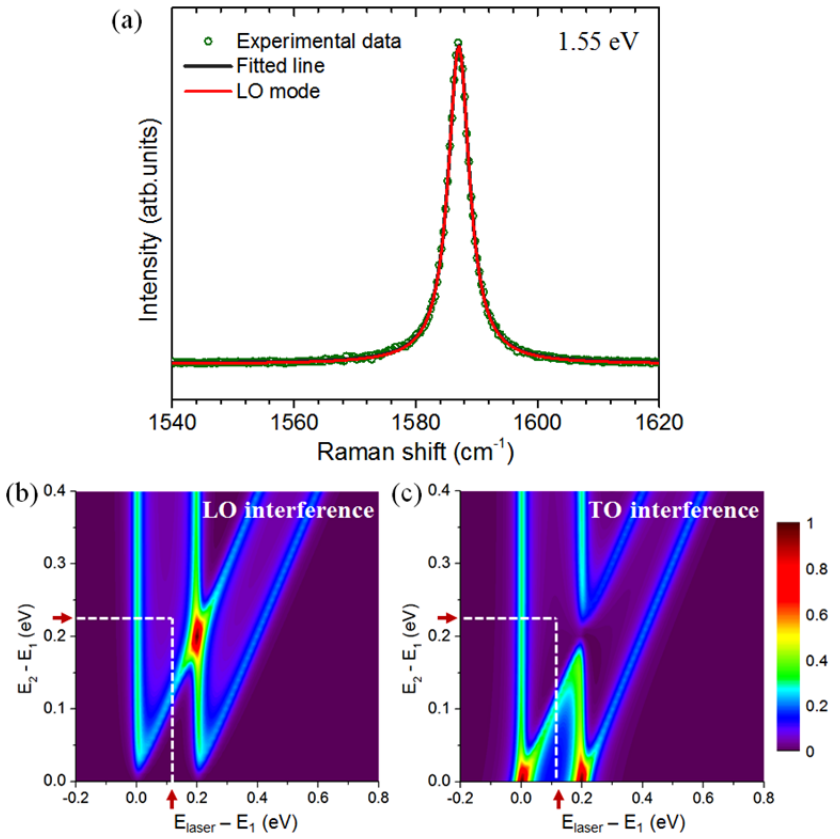

Figure 4.26*: (16,12)@(27,10) DWNT. (a) G-modes region of the Raman spectrum excited at 1.55 eV. Dark dots: experimental data, red solid line: fit by using a single Lorentzian. (b) The corresponding prediction of the LO and TO intensity. Parameter for calculations* E_{ph} *= 0.2 eV;* γ_1 *= 17.5 meV;* γ_2 *= 21.5 meV;* M_1/M_2 *= -1 for LO and* M_1/M_2 *= 1 for TO.*

Case 2: $E_{jj} = E_{ii}$.

Interference effects have also a strong influence when two optical transitions are located at the same energy. We present in the following two examples of interference effects observed in suspended index-identified DWNTs.

Individual (16,12)@(27,10) DWNT (SC@SC): In this part, we present the interference effects on the Raman spectrum measured on (16,12)@(27,10) DWNT (SC@SC). On Figure 4.27a, a series of the normalized Raman spectra in the excitation range: 2.33 – 2.71 eV, show the effect of quantum interference on the intensities of LO and TO modes. The Raman spectra show three intense peaks located at 1568 cm^{-1}, 1577 cm^{-1} and 1589 cm^{-1}. The peak at 1568 cm^{-1} (1577 cm^{-1}) is assigned to the TO mode of the inner (outer) tube. The 1589 cm^{-1} peak is assigned to the overlap of the LO modes of the inner and outer tubes ($LO=LO_o+LO_i$). The Raman spectra excited at 2.41 and 2.47 eV, close of the E_{55} and E_{66} optical transitions of the (27,10) outer tube located around 2.44 eV (Table 4.5) is dominated by the LO and TO modes of the outer tube. Figure 4.27b

presents the intensity ratio TO_i/LO and TO_o/LO in the investigated range. Clearly, the high TO_o/LO intensity around 2.5 eV is due to an interference effect (Figure 4.27b, blue dots). The relative strong intensity of the TO_o mode is due to a constructive interference effect as expected from simple calculations (see the Figure 4.27c). The intensity TO/LO ratio, derived by Raman experiments suggest that energy difference $\Delta E_{66\text{-}55}$ should be less than +/- 25 meV even if the contributions from the inner tube circumvents a full analysis of the data.

Because the signal of LO_o excited at 2.41 eV is expected to be small, we state that the majority of the signal at 1589 cm^{-1} can be assigned to the contribution of the LO_i mode of the inner tube. Indeed, the 2.41 eV excitation energy is close of $E_{44,in}+\hbar\omega_G$ transition (2.15 eV+ $\hbar\omega_G$ outgoing resonance) and the TO_i mode is clearly observed in this spectrum. On the other hand, at 2.47 eV, only the TO_o and LO_o are observed. For the 2.71 eV excitation energy, close of the $E_{55,in}$ transition (2.75 eV), the TO_i mode is observed and the main part of the signal at 1589 cm^{-1} comes probably from the LO mode of the inner tube (LO_i).

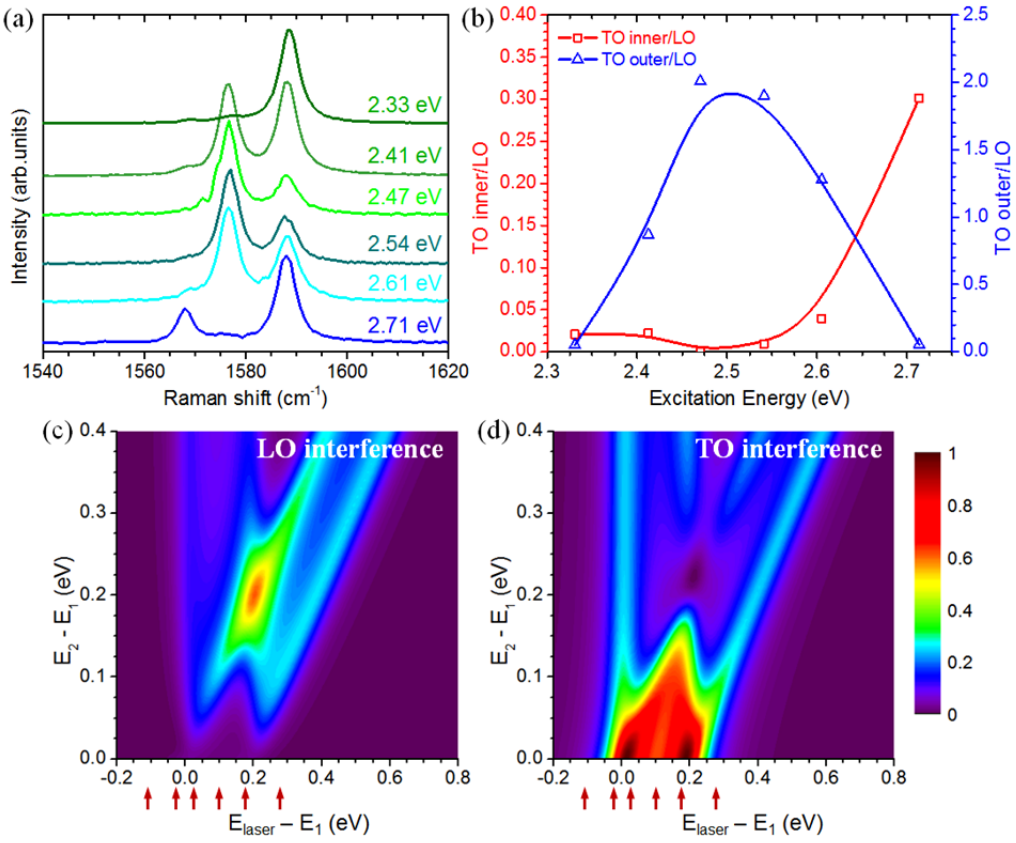

***Figure 4.27**: (16,12)@(27,10) DWNT. (a) G-modes region of the Raman spectrum excited in range 2.33 – 2.71 eV. (b) The ratio intensity of TO and LO corresponding to inner or outer tube. (c,d) The corresponding prediction of the LO and TO intensity. Parameter for calculations E_{ph} = 0.2 eV; $\gamma_1 = \gamma_2$ = 48.5 meV; M_1/M_2 = -0.65 for LO and M_1/M_2 = 1 for TO.*

Individual (11,6)@(18,9) DWNT (SC@M): On Figure 4.28, are shown the Raman spectra excited at 2.6 eV and 2.71 eV of the (11,6)@(18,9) DWNT. By contrast to the previous case (SC@SC DWNT), the outer (inner) tube is metallic (semiconducting) here.

The low-frequency Raman spectrum excited at 2.71 eV shows two modes at 141 cm^{-1} and 206 cm^{-1} which are assigned to the in-phase and out-of-phase RBLMs, respectively.

In the G-modes region of the Raman spectrum excited at 2.60 eV, four peaks are observed and correspond to the G-modes of the M outer tube and SC inner tube, namely TO_o at 1596 cm^{-1}, LO_o around 1570 cm^{-1}, LO_i at 1585 cm^{-1} and TO_i at 1555 cm^{-1}.

On the spectrum exited at 2.60 eV, the intensity of the TO_i is slightly higher than the one of the LO_i. By contrast, on the Raman spectrum excited at 2.71 eV, the intensity of the TO_i at 1555 cm^{-1} is significantly higher than the intensity of the LO_i at 1585 cm^{-1}. This behavior is in agreement with the predictions if we consider that the feature measured at 2.77eV on the optical absorption spectrum of this tube corresponds to the $E_{33,in}$ + $E_{44,in}$ transitions. As in the previous case, an enhancement of the TO mode concomitant with a reduction of the LO mode is expected in this situation.

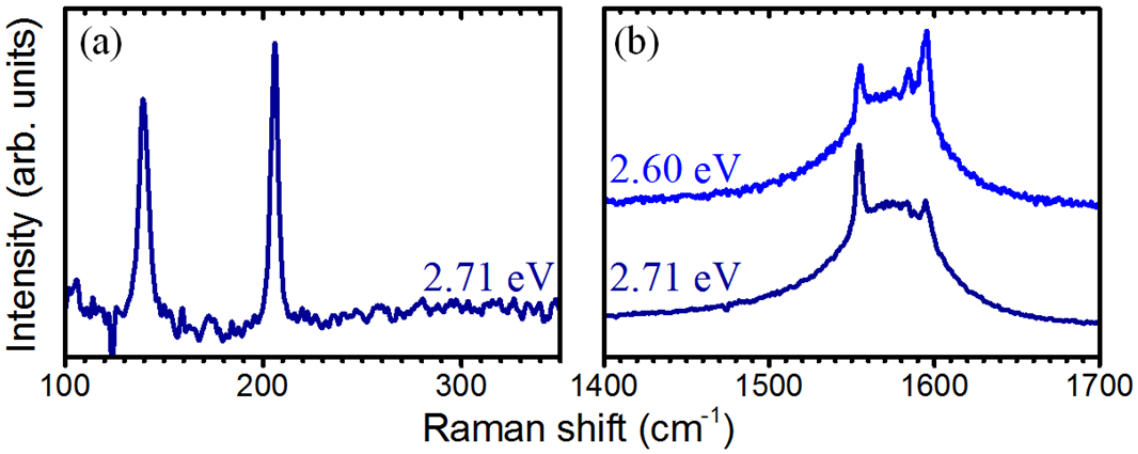

***Figure 4.28**: Raman spectra of the (11,6)@(18,9) DWNT: (a) RBLM region for an excitation at 2.71 eV, (b) G-modes region for excitations at 2.6 and 2.71 eV.*

In summary, the Raman spectra excited at some specific energies corresponding to high-order optical transitions show striking behaviors of the LO and TO of inner or outer tubes. These behaviors are well understood by considering quantum interference effects. These effects explain the observed changes of the TO/LO intensity ratios with the excitation energy.

4.4.2. Evidence of quantum interference in REPs of (16,12)@(27,10) (DWNT2)

In this section, we will discuss the quantum interference effects on the REPs of the individual (16,12)@(27,10) (SC@SC) in the 1.3-2.3 eV range. We remind that, in this range, because the energy differences between E_{33} and E_{44} of outer tube is close of the energy of G-mode, quantum interference effects are expected to play a role on the REPs of the different G-modes of this DWNT.

As discuss in the chapter 3-section 3.2.3, the excitonic model well describes the optical transitions of S-SWNTs. Thus, in this section, we used excitonic model in the framework of "M_{ia}=M_{ib} model" to discuss the effect of quantum interference on the REPs of S-SWNTs. In this assumption, the expressions of the Raman intensity, with and without interference effects, are reminded below with E_L: the excitation energy of the laser; E_1 (E_2): the lower (higher) transition energy of outer wall; E_3 (E_4): the lower (higher) transition energy of inner wall; γ_1 (γ_2): the resonance window width corresponding to the lower (higher) transition of outer wall;: γ_3 (γ_4): the resonance window width corresponding to the lower (higher) transition of inner wall; M_1 (M_2): the Raman matrix element corresponding to the lower (higher) transition of outer wall; M_3 (M_4): the Raman matrix element corresponding to the lower (higher) transition of inner wall.

Interference	$I_{Raman} \propto \left[\left\| \frac{M_1}{E_L - E_1 - i\gamma_1} - \frac{M_1}{E_L - E_1 - E_{ph} - i\gamma_1} + \frac{M_2}{E_L - E_2 - i\gamma_2} - \frac{M_2}{E_L - E_2 - E_{ph} - i\gamma_2} \right\|^2 + \left\| \frac{M_3}{E_L - E_3 - i\gamma_3} - \frac{M_3}{E_L - E_3 - E_{ph} - i\gamma_3} + \frac{M_4}{E_L - E_4 - i\gamma_4} - \frac{M_4}{E_L - E_4 - E_{ph} - i\gamma_4} \right\|^2 \right]$	(4.9)
Non-interference	$I_{Raman} \propto \left[\left\| \frac{M_1}{E_L - E_1 - i\gamma_1} - \frac{M_1}{E_L - E_1 - E_{ph} - i\gamma_1} \right\|^2 + \left\| \frac{M_2}{E_L - E_2 - i\gamma_2} - \frac{M_2}{E_L - E_2 - E_{ph} - i\gamma_2} \right\|^2 + \left\| \frac{M_3}{E_L - E_3 - i\gamma_3} - \frac{M_3}{E_L - E_3 - E_{ph} - i\gamma_3} \right\|^2 + \left\| \frac{M_4}{E_L - E_4 - i\gamma_4} - \frac{M_4}{E_L - E_4 - E_{ph} - i\gamma_4} \right\|^2 \right]$	(4.10)

The experimental REPs of the RBLMs, and those of the LO and TO G-modes for both inner and outer walls, are displayed in Figure 4.29 and 4.30 (symbols). On the same figure, the black (resp. orange) solid line is the fit of the experimental REP with (resp. without) taking into account interference effects. It must be emphasized that the transition energies (E_{ii}), and the widths of the excited electronic state (γ) are let as free parameters in the fit.

REPs of the RBLMs

For RBLMs, the interference and no-interference models fit very well the experimental REPs. Well resolved peaks are observed and corresponds to the resonance with the E^{S}_{33-out}, E^{S}_{44-out}, E^{S}_{33-in} and E^{S}_{44-in} optical transitions of outer and inner walls, respectively (Figure 4.29).

These results also provide a clear illustration that RBLMs can be resonantly excited if an electronic transition of either wall matches the excitation energy. For instance, at 1.44 eV and 1.67 eV, only the outer tube is in resonance and a significant intensity is observed for both in-phase and out-of-phase RBLMs. At 1.81 eV, only the inner tube is in resonance and intensity is also observed for both in-phase and out-of-phase RBLMs. However, when a resonance condition of the outer (inner) tube is achieved, the RBLM intensity of the in-phase (out-of-phase) RBLM is always stronger than that of out-of phase (in-phase).

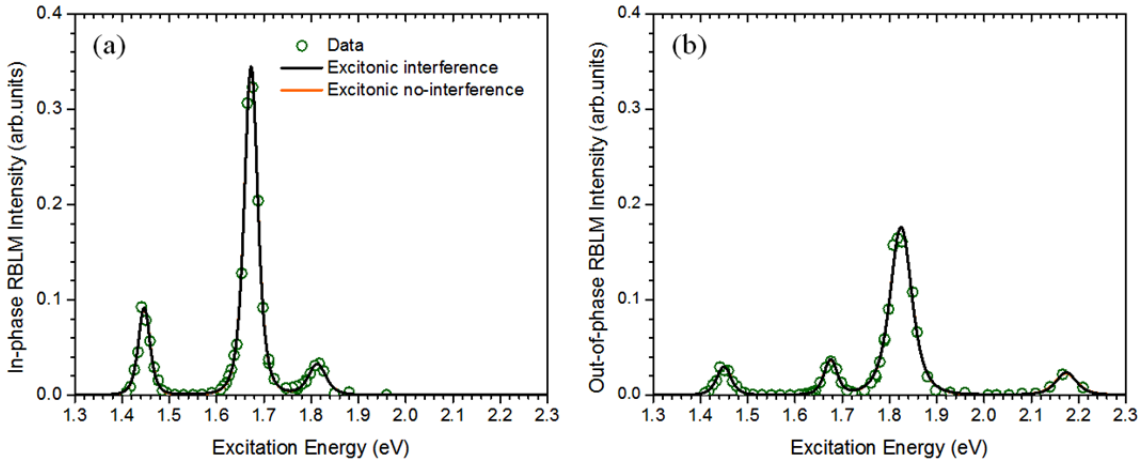

Figure 4.29*: Raman excitation profiles of (16,12)@(27,10) for RBLM at (a) low- and (b) high-frequencies. The black (orange) line corresponds to excitonic interference (no-interference) model.*

REPs of the LO and TO G-modes

We remind that for this DWNT, with regards to the interlayer distance close of 0.34 nm, the G-modes are expected to be slightly shifted with respect to their positions in the corresponding SWNTs (weak internal pressure). Especially, the LO G-mode of the inner and outer tubes, located near of 1589 cm^{-1}, are degenerated.

For the outer tube, the difference E_{44}-E_{33} is close to the phonon energy of G-modes. Consequently, there is an overlapping between the incoming resonance of the higher energy state (E_{44}) and the outgoing resonance of the lower energy state (E_{33}) around 1.67 eV. In this situation, a strong (weak) intensity of LO (TO) G-mode of the outer tube is expected due to constructive

(destructive) interference effect (Figure 4.30). This effect explain the strong intensity of the LO G-mode around 1.67 eV and the very weak intensity of the TO mode of the outer tube in the same energy range.

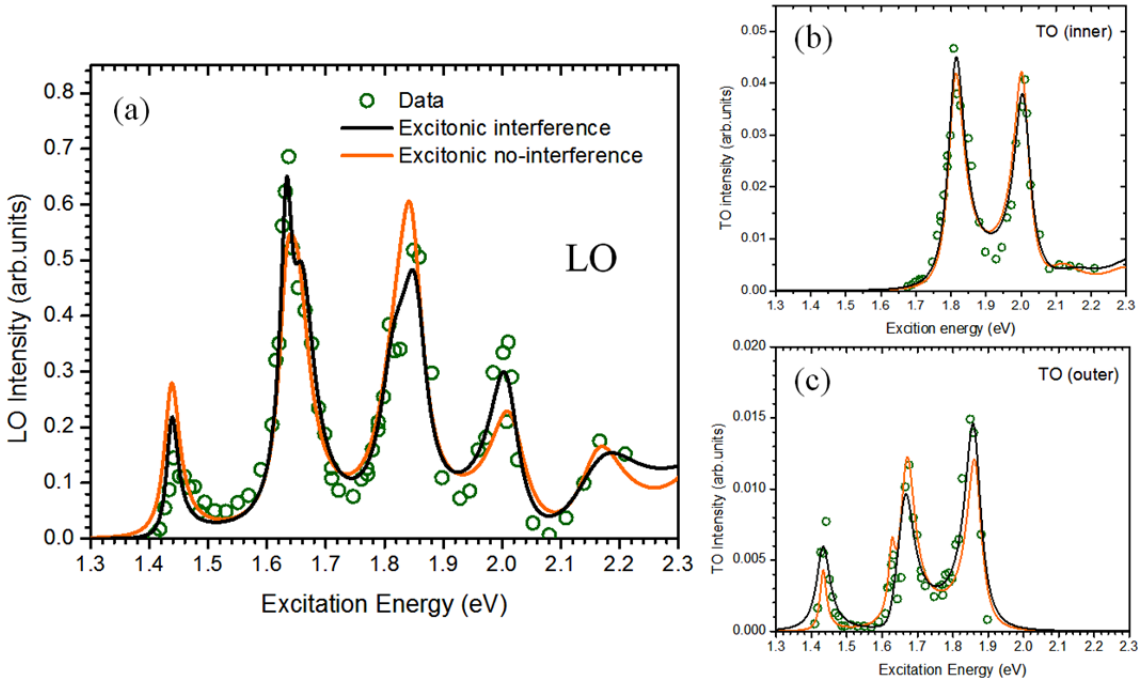

Figure 4.30: *Raman excitation profiles of (16,12)@(27,10) for (a) degenerated LO G-mode of inner and outer wall, and the TO G-modes of (b) inner and (c) outer walls. The black (orange) line corresponds to excitonic interference (no-interference) model.*

On the other side, since the $\Delta E_{33\text{-}44}$ is 0.34 eV for the inner tube (*i.e.* larger than the phonon energy), no interference effects are expected. Then, two maxima are predicted to appear in the REPs of the LO and TO modes of the inner tube in the 1.75-2.1 eV range, corresponding to the incoming and outgoing resonance involving the E_{33} transition of the inner tube. In agreement with this prediction, two well defined maxima in REPs of the LO and TO modes are measured at 1.81 eV and ~ 2.01 eV. Due to the separation of the TO G-modes of the inner and outer tubes, this result is especially clear in the REP of the TO G-mode of the inner tube. Notice another maximum around 2.15 eV in the REP of the LO mode which is assigned, in agreement with the absorption data, to the E_{44} transition of the inner tube.

The parameters derived by the fit of the experimental data, by using interference and no-interference models, are shown in Table 4.11 and Table 4.12, respectively.

It must be emphasized that the positions of the E_{33} and E_{44} energy transition of outer and inner tubes, derived from the fit of the REPs for either interference model or no-interference model, are very close of the corresponding ones measured by absorption spectroscopy.

However, a better fit of the profile of the REP of the LO and TO G-modes occurs when interference effect are considered (black solid line in Figure 4.30).

Concerning the γ parameter: the γ values, obtained by the fit of the REPs of the TO G-mode of the inner tube are good agreement with the absorption data. The γ values, obtained by the fit of the REPs of LO and TO modes of outer wall, are also in relative good agreement with those derived from absorption.

In summary, the values of the energy positions (E_{ii}) and resonance window (γ) obtained in the framework of excitonic model with interferences gives values closer to the ones derived from absorption measurement. More elaborate models seem however necessary to go further.

	Absorption (eV)	Excitonic Interference				
		RBLM-L	RBLM-H	G^+ (LO)	G^- (TO) outer	G^- (TO) inner
E^S_{33-out}	1.44	1.440	1.441	1.437	1.432	
E^S_{44-out}	1.67	1.666	1.667	1.657	1.664	
E^S_{33-in}	1.81	1.806	1.816	1.812		1.811
E^S_{44-in}	2.15		2.165	2.164		2.140
γ^{out}_{33} (meV)	17.5	19.4	24.4	12.0	23.3	
γ^{out}_{44} (meV)	21.5	23.8	21.2	24.5	28.0	
γ^{in}_{33} (meV)	30	32.6	40.0	30.7		28.7
γ^{in}_{44} (meV)	48.5		36.4	67.6		
M^{out}_{33}		0.010	0.007	0.006	0.002	
M^{out}_{44}		0.027	0.006	-0.014	0.003	
M^{in}_{33}		0.015	0.041	0.015		0.006
M^{in}_{44}			0.013	-0.024		0.006
R^2		0.995	0.987	0.939	0.828	0.942

Table 4.11: *Comparison between the transition energies and the resonance window measured by absorption spectroscopy, and derived from the fit of the REP with interference effects (notice that all the parameters are free in the fit).*

	Absorption (eV)	Excitonic No-interference				
		RBLM-L	RBLM-H	G^+ (LO)	G^- (TO) outer	G^- (TO) inner
E^S_{33-out}	1.44	1.440	1.441	1.437	1.432	
E^S_{44-out}	1.67	1.666	1.667	1.650	1.668	
E^S_{33-in}	1.81	1.806	1.816	1.819		1.811
E^S_{44-in}	2.15		2.165	2.160		2.111
γ^{out}_{33} (meV)	17.5	20.0	24.8	16.1	11.0	
γ^{out}_{44} (meV)	21.5	23.9	21.6	24.9	25.3	
γ^{in}_{33} (meV)	30	32.7	40.1	36.7		27.3
γ^{in}_{44} (meV)	48.5		40.2	44.3		
M^{out}_{33}		0.010	0.007	0.008	0.0007	
M^{out}_{44}		0.027	0.006	-0.016	0.0027	
M^{in}_{33}		0.015	0.041	0.017		0.0056
M^{in}_{44}			0.015	-0.018		0.0035
R^2		0.995	0.987	0.830	0.729	0.913

Table 4.12: *Comparison between the transition energies and the resonance window measured by absorption spectroscopy, and derived from the fit of the REP without interference effects (notice that here all the parameters are free in the fit).*

4.5. Dependence of the G-modes of semiconducting inner tubes as a function of the inter-tube distance

4.5.1. The frequency shifts of LO and TO of inner walls

The features of G-modes (lineshape, frequencies, widths, relative intensity) in SWNTs are known to be extremely sensitive to strain [117, 118]. By applying a hydrostatic pressure, a lot of studies have investigated the shift of G-modes in SWNTs [117-121].

Concerning DWNT, a lot of experiments and calculations regarding the dependence of the Raman spectra under pressure have been published [122-127]. The Raman measurements on the DWNTs bundles observed an up-shift of G-modes with the increasing of the hydrostatic pressure. In addition, the authors in ref [122, 127] observed that, at high pressure and for SC@SC samples, the G band is splitted in two broad components which have been attributed to the internal and external SC tubes.

On the other hand, as shown by Liu *et al.* [112], and reported in chapter 2, an interlayer distance larger or smaller than 0.34 nm leads to an effective negative or positive pressure between the tubes. On Figure 4.31a, we plot the effective pressure as function of interlayer distance in graphite. The blue (green) line shows this relation when the interlayer distance at zero pressure is considered to be 0.34 nm (0.335 nm). An equilibration value of 0.34 nm (0.335 nm) is usually assumed for DWNT (graphite).

For an interlayer distance close of 0.34 nm, the effective pressure is close of zero (see Figure 4.31a). A negative (positive) pressure means a slight contraction (expansion) of the outer layer concomitant with the expansion (contraction) of the inner layer [128]. In this framework, a contraction (expansion) of nanotubes layer may leads to the downshift (upshift) of G-modes. However, we experimentally observe that the TO and LO frequencies of inner tubes are significantly affected by the inter-tube pressure while those frequencies of outer tubes are less sensitive. Consequently, in this section, we focus on the behavior of G-modes frequencies of the semiconducting inner tubes as a function of the diameter and inter-tube distance. We combine our data with other ones obtained by D. Levshov on index-identified DWNTs [90].

In the framework of this approach, the Figure 4.31b illustrates the expected dependence of the G-modes frequencies for two different inter-tubes distances. The open dots are the LO and TO frequencies of an inner tube when δr is equal at 0.34 nm and solid dots are LO and TO modes of an inner tube associated to a large distance δr (>0.34 nm). On this figure, the solid lines are the diameter dependence of the TO and LO modes in SWNTs [80]. A large inter-tube distance leads to a significant downshift of LO and TO modes of the inner tubes with respect to the frequencies

of the corresponding SWNTs. In the following, we study the shift of the LO and TO modes of an inner tube in comparison with G-modes of the corresponding SWNTs.

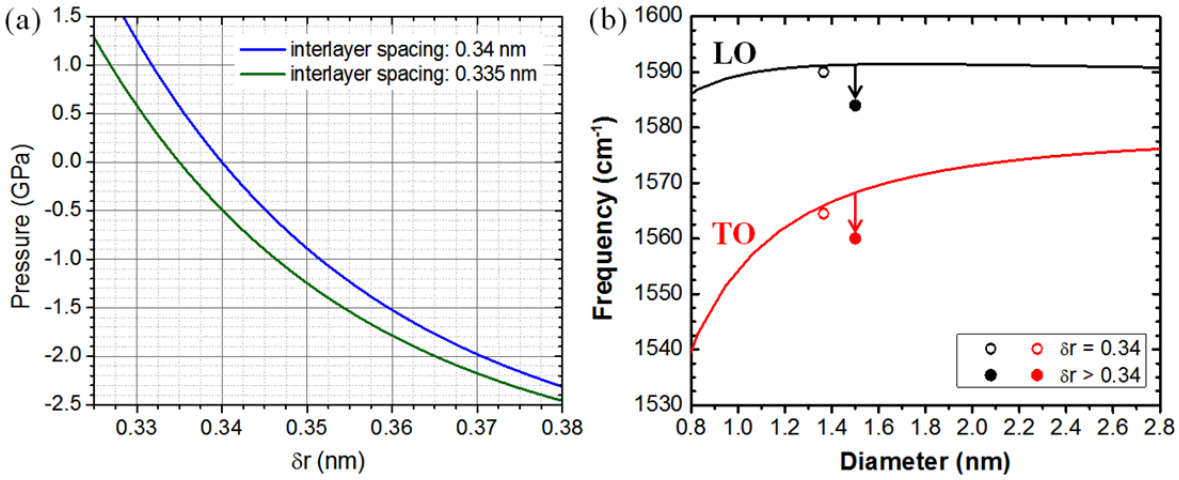

Figure 4.31*: (a) The relation between the distance and the effective pressure (adapted from ref [62, 113]). (b) Illustration of the dependence of LO and TO shift, with regards to the frequencies of the corresponding SWNTs, as a function of the inter-tubes distance (adapted from D. Levshov's thesis [90]).*

We compile in the Table 4.13, all the data [ref 90 and present work] concerning the amplitude of the downshift of LO and TO modes of the inner tube with respect to the frequencies of the same modes of the corresponding SWNTs as function of inter-tubes distance.

DWNT	Diameter of inner wall(nm)	Inter-wall distance (nm)	ω_{LO}^{exp} (cm^{-1})	ω_{TO}^{exp} (cm^{-1})	ω_{LO}^{SWNT} (cm^{-1})	ω_{TO}^{SWNT} (cm^{-1})	$\Delta\omega_{LO}$	$\Delta\omega_{TO}$
(16,12)@(27,10)	1.905	0.3453	1589	1569	1591.5	1573	2.5	4
(10,9)@(18,11)	1.289	0.3485	1585.5	1557	1590.7	1563	5.2	6
(11,6)@(18,9)	1.169	0.348	1586	1555.1	1591	1560.1	5	5
(12,8)@(16,14)	1.366	0.335	1589.5	1564.5	1591	1565	1.5	0.25
(20,4)@(20,16)	1.745	0.351	1587.5	1567.5	1591	1570.5	3.5	3
(13,9)@(24,7)	1.501	0.353	1584	1560.5	1591	1569	8.5	7
(22,11)@(27,17)	2.280	0.365	1583	1561.3	1591	1574	12.7	8

Table 4.13*: The comparison between the frequencies of LO and TO modes of inner tubes measured in index-identified DWNTs and those extrapolated from measurements in index-identified SWNTs. The data of DWNTs 4-7 have been obtained by D. Levshov [90].*

We report on the Figure 4.32 the downshift of the modes as a function of the inter-tube distance (bottom axis) and pressure (top axis). By this way, we unambiguously demonstrate the dependence of the frequencies of the G-modes on the distance between the inner and outer layers.

When the inter-layer distance is larger than the nominal van der Waals distance (close to 0.34 nm), a downshift of the inner-layer G-modes with respect to the corresponding modes in corresponding SWNTs is measured, and larger the inter-layer distance, larger the downshift of the LO and TO G-modes. The behavior of the G-modes is well understood by considering the effect of an effective pressure felt by the inner and outer layers. To the best of our knowledge, it is the first time that a clear relation between the shift of the G-mode and the inter-tubes distance is put in evidence in DWNT. An article, in which these results are reported and discussed, has been recently published on The Journal of Physical Chemistry C [116].

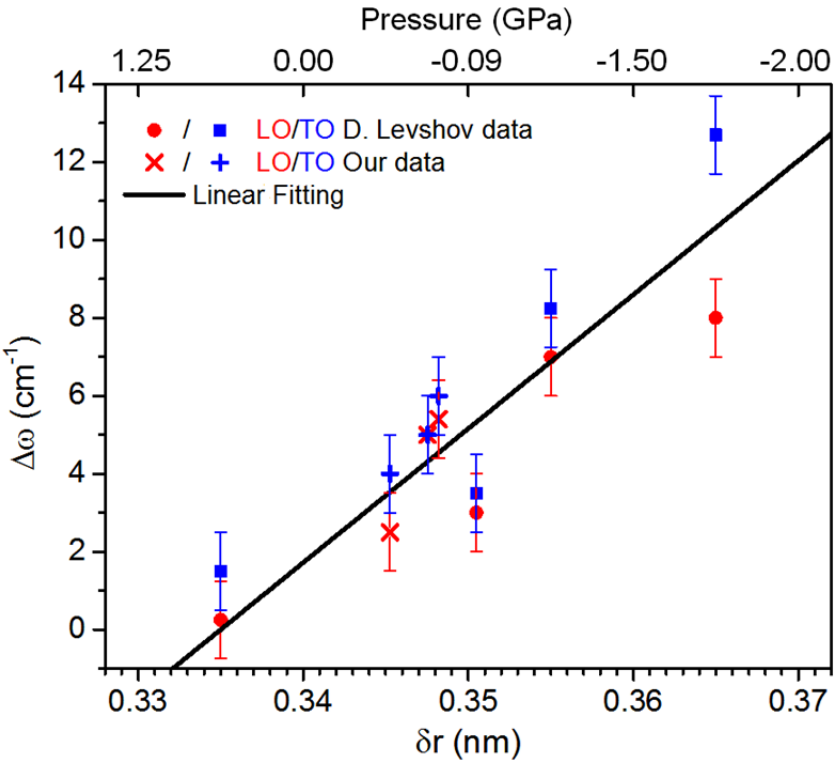

***Figure 4.32**: The relationship between G-modes shift and inter-tubes distance.*

4.5.2. The TO frequencies of (6,5)@outer walls

DWNTs prepared by using a specific thermal treatment of peapods (fullerenes inserted in nanotubes), can produce DWNTs with a large majority of (6,5) inner tube inserted in outer tubes of different diameters. Using this kind of DWNTs, F. Villalpando-Paez *et al.* [129] found 11 corresponding outer tubes with various wall-to-wall distances ranging between 0.29 – 0.38 nm. Especially, these authors measured the TO G-mode frequency of inner (6,5) tube in different individual DWNTs, and they observed that the downshift of TO G-mode increases with increasing the inter-tube distances. In this study, the authors derived the diameter of inner and outer tubes by using the following relationship between the RBM frequency and the diameter: $\omega_{RBM} = 218.3/d + 15.9$ [129, 130]. As discussed in section 4.1 and 4.2 of this chapter, such

approximation does not permit to derive the diameter and then the inter-tube distance between inner and outer tubes in DWNTs with a sufficient precision. In this section, we will use the RBLM model described in section 4.1 to derive the accurate diameter of outer tubes and to correct the initially reported inter-tubes distances. By following, the TO G-mode frequencies of (6,5) will be plotted as a function of the reevaluated inter-tube distance. The results will be compared with our results obtained on index-identified DWNTs.

We first consider all the possibilities of outer tubes which can be associated with an inner tube (6,5) (Figure 4.33).

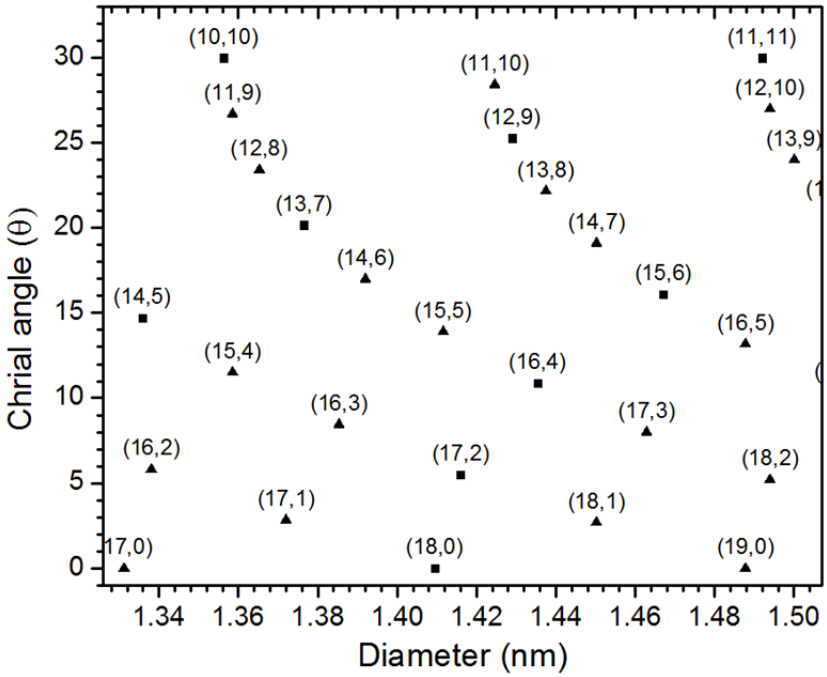

Figure 4.33: *All the possibilities outer walls for the same (6,5) inner tube.*

We calculate the frequencies of in-phase and out-of-phase RBLM for all these DWNTs by using the procedure described in section 4.1 (expressions 4.11 and 4.12). Two experimental situations are considered, namely the outer tube is environmental-free or not. In the first situation, a relation ω_{RBM} =228/d is used to describe the dependence of the RBM frequency with the diameter, and in the second situation we use the relation ω_{RBM} = 204/d+27.

We observe that the values of high-frequency RBLM are almost insensitive to this choice. By contrast, the frequencies of the low-frequency RBLMs change significantly. The relation between the RBLM frequencies of the in-phase and out-of-phase modes is displayed on the Figure 4.34 for the two simulated situations. Interestingly, the RBLM frequencies values of ref [129] range between the two simulated values. The best agreement of the experimental (6,5) RBLM with a calculated high-frequency RBLM of an index-identified DWNT permits to derive

the best candidate for the outer tube. For example, for the experimental high-frequency RBLM measured close of 331 cm^{-1}, the best match for the outer tube is the (13,7) leading to the assignment of this DWNT as (6,5)@(13,7). The group of four experimental RBLMs around 323 cm^{-1} is tentatively assigned as (14,6) outer tube and the corresponding DWNTs are (6,5)@(14,6), etc.

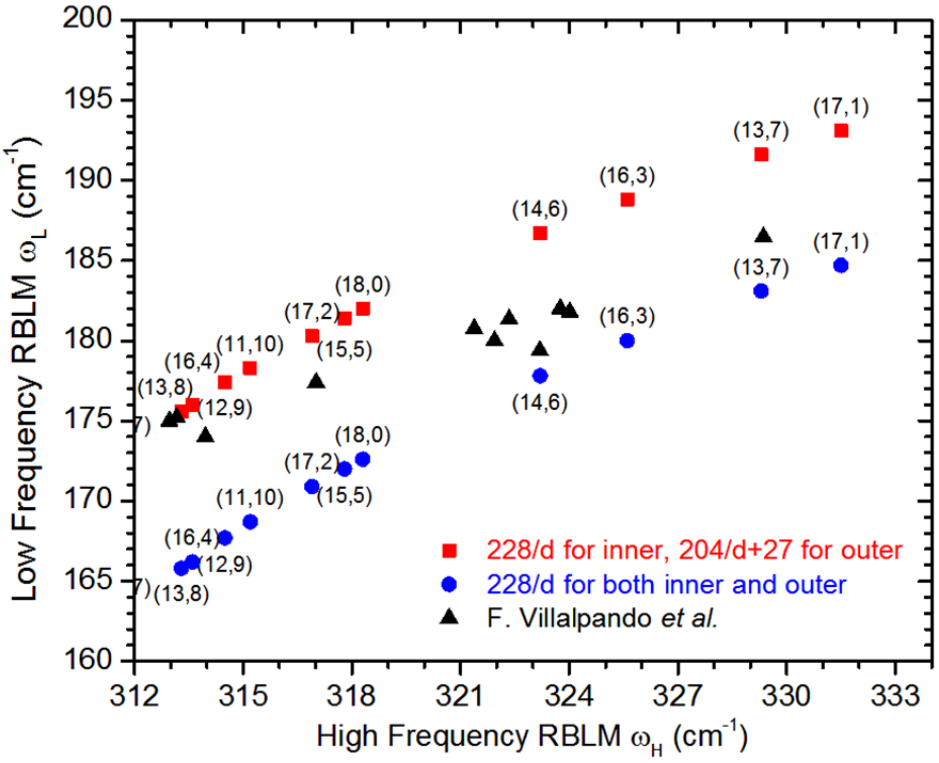

Figure 4.34: *The calculated RBLM frequencies of outer tubes corresponding to inner tubes (6,5). The blue and red dots are calculated by using RBLM model described in section 4.1.*

On the other hand, Pfeiffer *et al.* [58, 131] performed experiments using the same kind of samples. In order to calculate the RBLM frequencies of their different (6,5)@(n_o,m_o), they developed a continuum model by considering the tubes as an elastic cylinder coupled by Lennard-Jones potential (parameterized for graphite). The comparison between the experimental and calculated RBLMs permits also to propose the chiral indices of the outer tubes from the RBLM frequencies reported in [129].

In the Table 4.14, we compile all experimental RBLMs measured in ref [58, 129] and the corresponding assignments of (n_o,m_o). From these assignments, we can directly calculate the inter-tube distance (δr) for the DWNTs of ref [129]. As shown in Table 4.17, the values of δr derived from our analysis are about 0.02 nm larger than the ones estimated in ref [129] and both approaches (coupled oscillator model and ref. [58, 131]) give very close results.

From ref [129] (exp)		RBLM model (present work)		From ref [58] (exp)	
ω_H (cm^{-1})	ω_L (cm^{-1})	ω_H (cm^{-1})	(n,m)	ω_H (cm^{-1})	(n,m)
313	175	313.3	(13,8)	312.86	(11,10)
313.2	175.2	313.3	(13,8)	312.86	(11,10)
314	174	313.6	(16,4)	312.86	(11,10)
317	177.38	316.9	(17,2)	316.87	(18,0)
321.4	180.75	323.2	(14,6)	322.26	(14,6)
321.9	180	323.2	(14,6)	322.26	(14,6)
322.3	181.34	323.2	(14,6)	322.26	(14,6)
323.2	179.39	323.2	(14,6)	324.21	(16,3)
323.8	182	323.2	(14,6)	324.21	(16,3)
324	181.8	323.2	(14,6)	324.21	(16,3)
329.4	186.47	329.3	(13,7)	328.93	(17,1)

Table 4.14*: The outer tubes of (6,5) with the corresponding RBLM frequencies.*

From ref [129]			RBLM model			From ref [58]		
δr	$\omega_{TO}^{(6,5)}$	$\Delta\omega_{TO}^{(6,5)}$	(n,m)	δr	$\Delta\omega_{TO}^{(6,5)}$	(n,m)	δr	$\Delta\omega_{TO}^{(6,5)}$
0.31916	1526.312	1.388	(13,8)	0.34518	1.388	(11,10)	0.33876	1.388
0.31916	1522.360	5.340	(13,8)	0.34518	5.340	(11,10)	0.33876	5.340
0.32493	1527.084	0.616	(16,4)	0.34411	0.616	(11,10)	0.33876	0.616
0.31410	1526.152	1.548	(17,2)	0.33445	1.548	(18,0)	0.33227	1.548
0.30483	1530.968	-3.268	(14,6)or(18,0)	0.32243	-3.268	(14,6)	0.32243	-3.268
0.30917	1535.060	-7.360	(14,6)or(18,0)	0.32243	-7.360	(14,6)	0.32243	-7.360
0.30421	1531.396	-3.696	(14,6)	0.32243	-3.696	(14,6)	0.32243	-3.696
0.31309	1532.635	-4.935	(14,6)	0.32243	-4.935	(16,3)	0.3208	-4.935
0.30338	1536.375	-8.675	(14,6)	0.3208	-8.675	(16,3)	0.31921	-8.675
0.30388	1531.789	-4.089	(14,6)	0.3208	-4.089	(16,3)	0.31921	-4.089
0.29246	1541.184	-13.484	(13,7)	0.31468	-13.484	(17,1)	0.31245	-13.484

Table 4.15*: δr between inner tube (6,5) and corresponding outer tubes; the TO frequencies from ref [129], shift of the TO mode of inner (6,5) with respect to the TO mode in individual (6,5) SWNT. Assignment of the DWNTs from RBLM model and from ref [58].*

On Figure 4.35, we plot the TO G-mode frequencies shift of (6.5) inner tubes in DWNTs with regards to the TO G-mode frequencies in the corresponding SWNTs as function of δr evaluated by the three different ways. Obviously, corrected δr give a better agreement with the TO/δr dependence derived from index-identified DWNTs. The results unambiguously state that the TO frequencies are downshift (upshift) when the inter-tube distances are higher (lower) than a distance close of 0.34 nm.

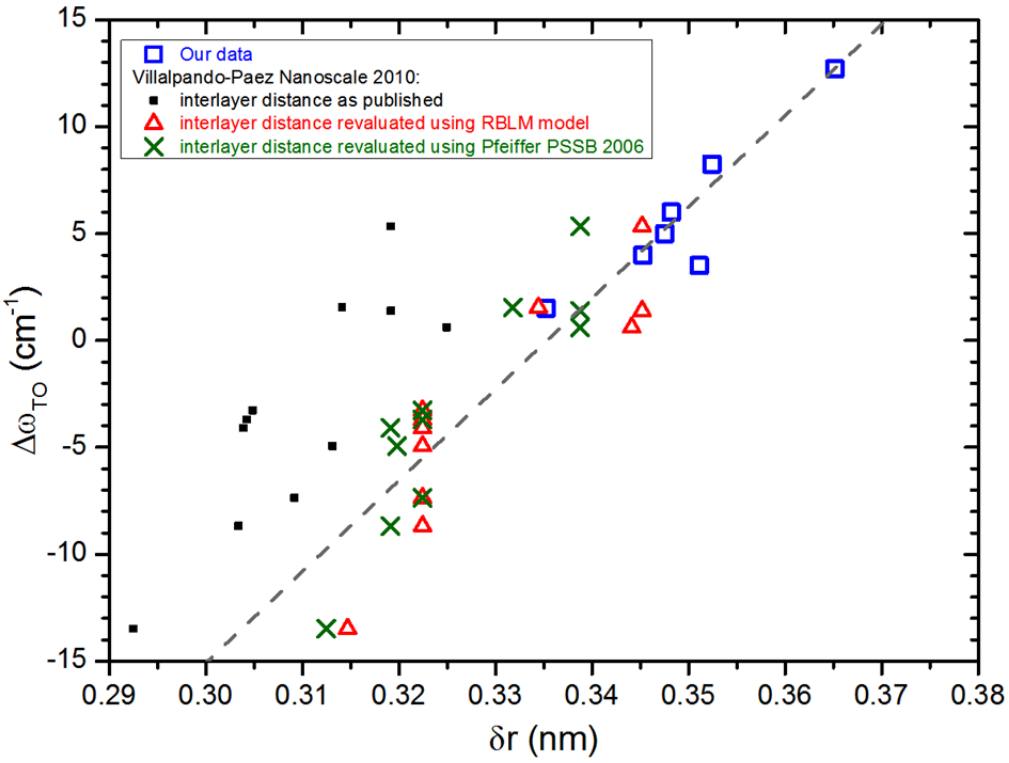

***Figure 4.35**: The TO frequencies shift ($\omega_{TO(SWNT)}$ - $\omega_{TO(DWNT)}$) as a function of the inter-tubes distance. The blue open squares correspond to index-identified individual suspended DWNTs. The black squares correspond to data from ref.[129] for (6,5)@(n_o,m_o) DWNTs, as published and the red open triangles (resp., green crosses) corresponds to the same data but with reevaluated inter-tube distances using the coupled oscillator model (resp. ref. [58, 129]).*

4.6. Summary

In the chapter 4, we have presented the model used to derive the diameters of the inner and outer tubes from the knowledge of the experimental in-phase and out-of-phase RBLMs. For the four DWNTs studied, the chiral structure of inner and outer tubes were assigned by combining the information derived by Raman, Electron diffraction pattern (EDP) and model.

For the four investigated index-assigned DWNTs, the assignments of absorption bands at inner and outer tubes were derived from the analysis of the absorption and Raman spectra. On the base of this assignment, the absorption energies were compared to the calculated energies of corresponding SWNTs. An overall downshift of the inner tubes transition energies of about 50-150 meV was found for most of the transition energies. By contrast, the shifts of the transition energies of outer tubes range from -100 meV (red-shift) to 100 meV (blue-shift).

The signature of quantum inferences was observed at some specific energy showing the strong effects on the Raman response of the concomitant resonant excitation of two closely spaced transitions. Interference effects produce striking behaviors on the dependence of the intensity of inner and outer tubes TO and LO G-modes with the excitation energy. Especially, constructive and destructive interferences cause anomalous excitation dependence of the TO/LO intensity ratio.

The quantum interference effects were also investigated from the REPs of the RBMs and G-modes of the (16,12)@(27,10) DWNT. The positions of the E_{33} and E_{44} energy transition of outer and inner tubes, derived from the fit of the REPs, for either interference or no-interference models, are very close of the corresponding energies measured by absorption spectroscopy. A better fit of the REPs of the LO and TO G-modes occurs when interference effect are considered.

Finally, the dependence of G-modes frequencies as a function of the inter-tube distance was investigated. When the inter-layer distance is larger than the nominal van der Waals distance (close to 0.34 nm), a downshift of the inner-layer G-modes with respect to the corresponding modes in corresponding SWNTs is measured, and larger the inter-layer distance, larger the downshift of the LO and TO G-modes. The behavior of the G-modes is well understood by considering the effect of the effective pressure felt by the inner layer in DWNT.

From these conclusions, previous results of F. Villalpando-Paez *et al.* [129] concerning the positions of G-modes measured on (6,5)@outer-tube DWNTs were revisited. Our RBLM model permits to propose a correct estimation of the inter-tube distance in these DWNTs. This assignment leads to a good agreement between the dependence of the position of the G-modes measured on the (6,5)@outer-tube DWNTs with the one observed in our individual index-identified DWNTs.

	Calculation ω_L / ω_H (cm^{-1})		Raman experiment
	model from ref [62]	our approach	
(10,6)@(15,13)	122/210	136/210	135/193
(11,7)@(15,13)	131/203	144/204	
(11,7)@(16,14)	114/187	129/187	
(13,8)@(17,15)	110/165	125/165	
(10,9)@(18,11)	123/188	137/189	
(11,9)@(19,12)	111/172	126/172	
(11,10)@(19,12)	116/173	130/173.5	
(11,10)@(20,12)	107/164	123/164	
(13,11)@(21,13)	106/154	121/155	

Table 4.16: *The calculated RBLM frequencies for all possible assignments of DWNT3 as compared to the one measured by Raman spectroscopy.*

PART B: EXPERIMENTAL INVESTIGATION OF THE PROPERTIES OF COVALENTLY AND NON-COVALENTLY FUNCTIONALIZED DOUBLE-WALLED CARBON NANOTUBES

CHAPTER 5 : OPTICAL INVESTIGATION OF DOUBLE CARBON NANOTUBES SUSPENSIONS AND THEIR FUNCTIONALIZATION

DWNTs are known as potential nanomaterials to fabricate hybrid devices based on the functionalization of their outer tubes, the properties of inner tubes being unaltered [132, 133]. Functionalized DWNTs have recently demonstrated excellent sensitivity and chemical selectively in thin film transistor based sensors [134]. In this chapter, we report results regarding the optical properties of pristine and functionalized-DWNTs (p/f-DWNTs). In this aim, we combine three experimental techniques: UV-Vis-NIR absorption, photoluminescence excitation (PLE), and Raman spectroscopy. Indeed:

- The absorption measurements put in evidence the functionalization through the change of the intensities of absorption bands.
- The PLE measurements show how the luminescence properties of nanotubes are affected after functionalization.
- The Raman spectroscopy is known as a powerful and accurate technique for the characterization of pristine (p-DWNTs) and functionalized (f-DWNTs) DWNTs from the changes of the RBLM and G-modes features as well as the one of the relative intensity of the D-band.

5.1. Covalent and non-covalent functionalization of carbon nanotubes

The chemical functionalization of carbon nanotubes is classified as covalent or non-covalent.

The covalent modification considers the attachment of functional groups on the nanotubes surface with chemical bonds. The covalent functionalization can preserve the electrical conductance of CNTs [135]. However, most of the functional groups that can be covalently attached to a CNT sidewall significantly change the hybridization from sp^2 to sp^3 on nanotubes surface and destroy simultaneously the π-conjugation of the system. As a result, the covalent functionalization has a significant influence on the optical [136] and electronic [137] properties of the CNTs.

The non-covalent modifications use adsorbed molecules to modify the surface energy of CNTs by using different interaction forces such as van der Waals or π–π interactions. The important advantage of non-covalent approach is that the chemical reaction does not destroy the π-conjugation system of CNTs sidewalls; therefore, the original properties of CNTs can be

mainly preserved. The main disadvantage of non-covalent functionalization is certainly the lack of stability due to the low nanotube/molecule interaction force involved.

SWNTs are extremely sensitive to changes of their environment because all the constituting atoms are surface atoms. Covalent functionalization of the nanotube sidewalls usually disrupts the periodicity of the lattice *via* the conversion of sp^2-hybridised trivalent carbon atoms to sp^3-hybridised tetravalent carbons upon the addition of moieties to the sidewall. These defect sites destabilize the band structure, resulting in the loss of available electronic transitions. On the other hand, for DWNTs, the inner walls are protected from the chemical functionalization by the outer walls. As shown in the Figure 5.1, the covalently functionalized SWNTs are becoming electrically insulating while f-DWNTs conductance only decreases by ~50% [133].

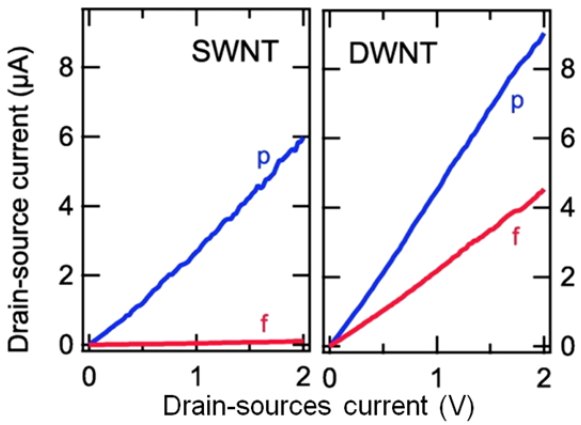

Figure 5.1: *Electrical current in an individual SWNT and DWNT device as a function of drain-sources voltage, in pristine (p-blue) and functionalized covalently (f-red) states (from ref [133]).*

In the following, we present investigation of the optical properties of DWNTs. The results focus on the comparison of the optical properties of the pristine (p-DWNTs) and functionalized DWNTs (f-DWNTs).

5.2. “Do inner tubes of DWNTs fluoresce or not?”: a short review

One challenge of the present work is to study the physical properties of inner tubes after chemical functionalization of the outer tubes of DWNTs. Among many techniques, the photoluminescence (PL) is a powerful technique to measure the optical properties of DWNTs, especially those of semiconducting inner tubes.

Although there are a large number of reports about the PL signal in DWNTs, the PL properties of DWNTs are still a highly debated subject. In this section, we provide a short review about the PL of DWNTs and on the debate: “Do inner tubes of DWNTs fluoresce or not?”

T. Okazaki *et al.* [138] performed experiments on DWNTs prepared from the thermal transformation at 1200°C of peapods (C_{60} inserted in SWNTs). No PL signal from small inner tubes of the DWNTs obtained by this synthesis route was observed. The authors measured PL signals in the range 1400-1600 nm with excitation at 800-950 nm. These peaks can be assigned to the emission of tubes with diameters in the 1.2-1.4 nm range, corresponding to outer tubes. The authors suggested that the PL of inner walls is quenched due to interlayer interaction and energy transfer from inner tubes to outer tubes. In addition, they show that the decrease of inter-wall distance enhances the PL quenching. Also, the absorption spectrum and HRTEM images suggest that the DWNTs samples contain a lot of bundles. Moreover, the amount of DWNTs is of about 50%. Therefore, it is suggested that the absence of PL signal associated to the inner tubes in this sample can be due to the presence of bundle and/or to a low amount of DWNTs.

H. Muramatsu *et al.* [139] also investigated the PL of DWNTs prepared from the thermal transformation of peapods. Different temperatures of treatment, from 1500°C to 2000°C, were used in order to obtain different inner tubes. In agreement with ref [138], the authors report the absence of PL signal of the inner tubes when the DWNTs are prepared at temperature below 1700°C, suggesting that those inner tubes are mainly metallic or form junctions. By contrast, PL signals assigned to inner tubes are measured when the temperature of synthesis is higher than 1700°C.

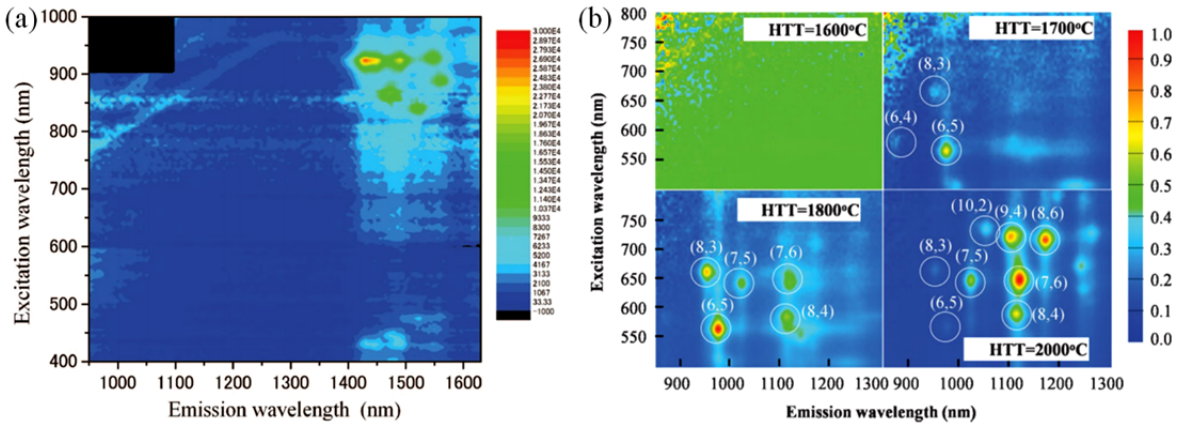

Figure 5.2: *The PLE of DWNTs grown by peapod method at (a)1200°C, (b)1600°C - 2000°C [138, 139].*

T. Hertel *et al.* [140], by using suspensions of DWNTs (prepared by CVD method) in water using sodium (or ammonium)-cholate as surfactant, observed signals in a broad range of excitation (550-900 nm) and emission (800-1600 nm). They assigned these signals to the PL of inner tubes. Furthermore, the PL decay from inner tubes in DWNTs suspension was found to be approximately three times longer than that of SWNTs in sodium dodecyl sulfate.

In another report, D. Shimamoto *et al.* [141] measured a higher PL intensity for inner tubes than those from SWNTs. Therefore, these experimental results support the conclusion that PL from DWNTs suspensions is dominated by the response of the inner tubes.

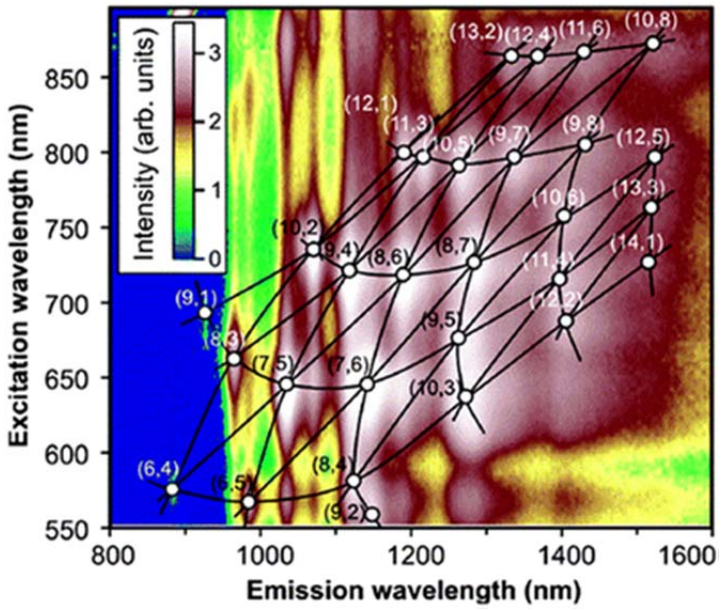

Figure 5.3: *Photoluminescence excitation spectrum of a DWNT-cholate suspension [140].*

K. Iakoubovskii *et al.* [142] report a complete optical characterization of DWNTs grown by CVD. Especially, they discuss the properties of DWNTs before and after oxidation (ozone etching and electrochemical doping). The absorbance spectra on DWNTs buckypaper showed that the absorption band of only the outer walls are significantly and irreversibly reduced after 40 minutes etching by ozone generated by UV illumination. Furthermore, the absorption spectra during electrochemical doping at high voltage (1.2 V) also assert the preservation of inner tube.

N. Kishi [143] measured the PL signal of DWNTs under thermal oxidation at different temperatures. The results suggest that: (i) from room-temperature to 570°C, the intensity of the PL of (6,5), (7,5), and (9,4) inner tubes decreases with increasing oxidation temperature, (ii) the PL intensity increases at higher temperatures.

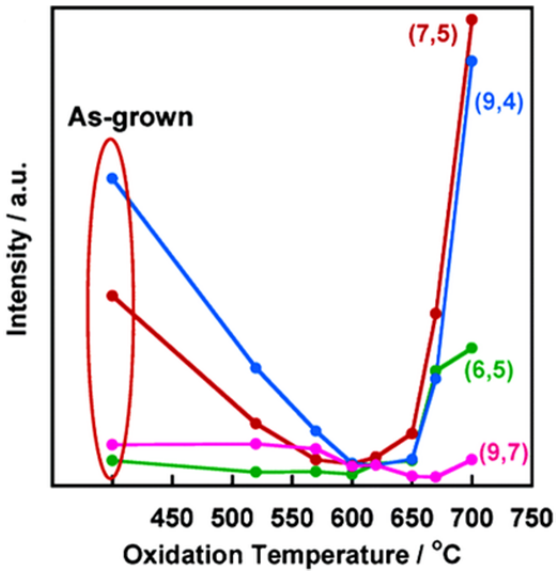

Figure 5.4: *Oxidation temperature dependence of absolute PL intensities of (6,5), (7,5), (9,4), and (9,7) [143].*

H. Hirori *et al.* [144] study the PL features (peak position and dynamics) of the inner tubes of DWNTs. They found that the PL peaks of the large inner tubes (> 0.8 nm) in DWNTs are red shifted as compared to the corresponding SWNTs and this redshift increases with the diameter. In addition, PL lifetimes of the inner tubes decrease with increasing inner tube diameter while the PL lifetime of SWNTs is almost independent on tube diameter. The results suggest that the inter-wall distance govern the PL features of the DWNTs. The difference in PL position and dynamics between DWNTs and SWNTs is caused by the screening effect due to the outer tubes and the exciton energy transfer between the inner and outer tubes.

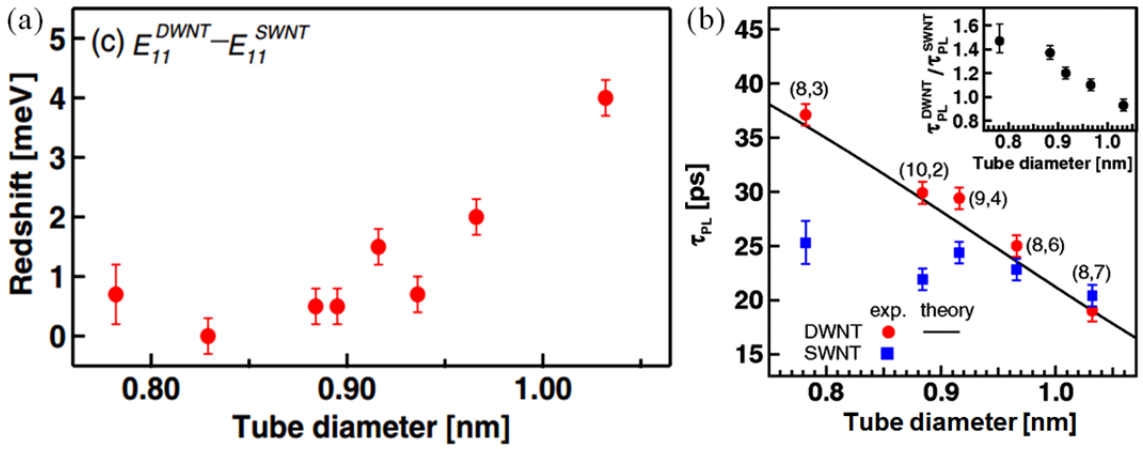

Figure 5.5: *(a) Diameter dependence of the PL peak shift of DWNTs compared to the SWNTs with the same chiral indices. (b) PL lifetimes τ_{PL}^{DWNT} and τ_{PL}^{SWNT} as a function of tube diameter in the DWNTs and SWNTs. The inset shows the PL lifetime ratio of $\tau_{PL}^{DWNT}/\tau_{PL}^{SWNT}$ as a function of the tube diameter [144].*

The investigations summarized above assigned the PL signal of DWNT to the emission of the inner tubes. However, opposite conclusion from experiments conducted on similar samples were reported by other authors.

D.A Tsyboulski *et al.* [145] performed experiments on suspensions in water of purified SWNTs and CVD-grown DWNTs (with 95% purity) using sodium-cholate as surfactant. The authors compare the emission spectra of suspensions of purified DWNTs and pristine SWNTs. By this way, they provided experimental evidence of the quenching of absorption and PL intensities in purified DWNTs as compared with those of SWNTs. On the other hand, fluorescence imaging of DWNT and SWNT suspensions reveal that the DWNT suspension contains a low concentration of emitters with features equivalent to the ones in SWNT suspension. These results suggest that the weak luminescence of DWNTs could result from the purification procedures. In a second approach, the authors performed covalent functionalization on sidewall of DWNTs. The PL quenching of the DWNT sample is significant and fast upon chemical functionalization via diazonium salts (Figure 5.6a, b). This result suggests that the emitting tubes are not preserved after covalent grafting and that the observed PL is due to SWNTs rather than inner tubes of DWNTs. Another property that can be probed by near-IR fluorescence microscopy is the mechanical stiffness of emissive long nanotubes (Figure 5.6c). The experimental results confirm here again that the emitting nanotubes are SWNTs (Figure 5.6d). Finally, using another approach, the authors identified near-IR emission measured on DWNTs purified by density gradient ultracentrifugation (DGU). The fluorescence quantum yield of inner walls is shown to be four orders of magnitude lower than the one of SWNTs with the same diameter. In conclusion, the authors show convincing evidences that the observed

luminescence of DWNT samples can be due to SWNTs impurities or released inner walls during treatment such as sonication and/or centrifugation.

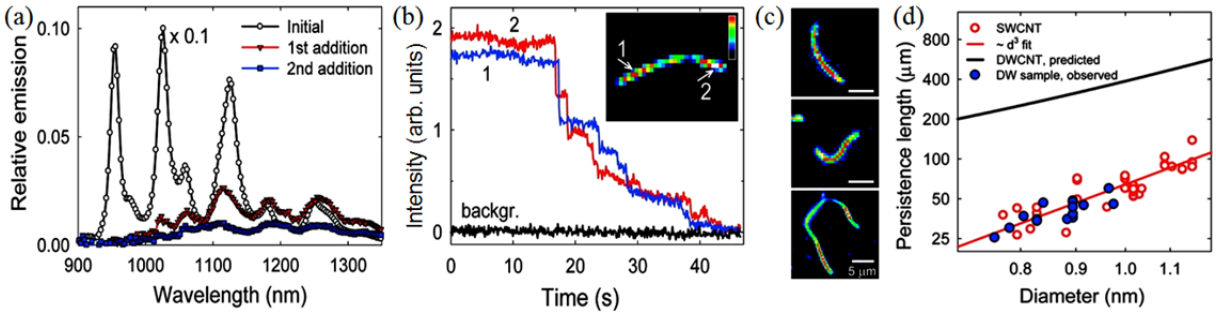

Figure 5.6: *Luminescence quenching of dispersed DWNTs functionalized by bromobenzene-diazonium. (a) Fluorescence spectra of f-DWNT suspension. (b) Stepwise fluorescence quenching of DWNTs dispersions in agarose gels. The inset shows locations of the segments whose emission intensities are plotted in the main frame. (c) Near-IR fluorescence images of "long" emissive nanotubes in a DWNT suspension reveal noticeable bending. (d) Persistence lengths measured for individual emissive nanotubes in samples of SWNTs (open circles) and DWCNTs (solid circles), plotted vs spectroscopically deduced diameter. The lower (upper) solid line represents the d^3 dependence expected for SWNTs (DWNTs) [145].*

A.A. Green and M.C. Hersam [146] conducted PL experiments on suspensions of isolated DWNTs, dispersed in co-surfactant containing sodium dodecyl sulfate (SDS) and sodium cholate (SC), and sorted by using density gradient ultracentrifugation (DGU) method. The fluorescence intensity of sorted inner tubes in DWNTs was observed to be two orders of magnitude lower than that of the semiconducting HiPCO-SWNTs (Figure 5.7a). This result provides evidence of inner-tubes fluorescence quenching due to the DWNT outer-tubes.

Recently, S. Yang *et al.* [147] prepared by CVD method samples which contents 77% DWNT. DWNTs are separated from other nanotubes by DGU method leading to high-purity DWNT samples. The luminescence is observed for only a few inner tubes while the luminescence of other inner tubes is completely quenched (Figure 5.7b). However, the authors provided no further explanation for these striking results.

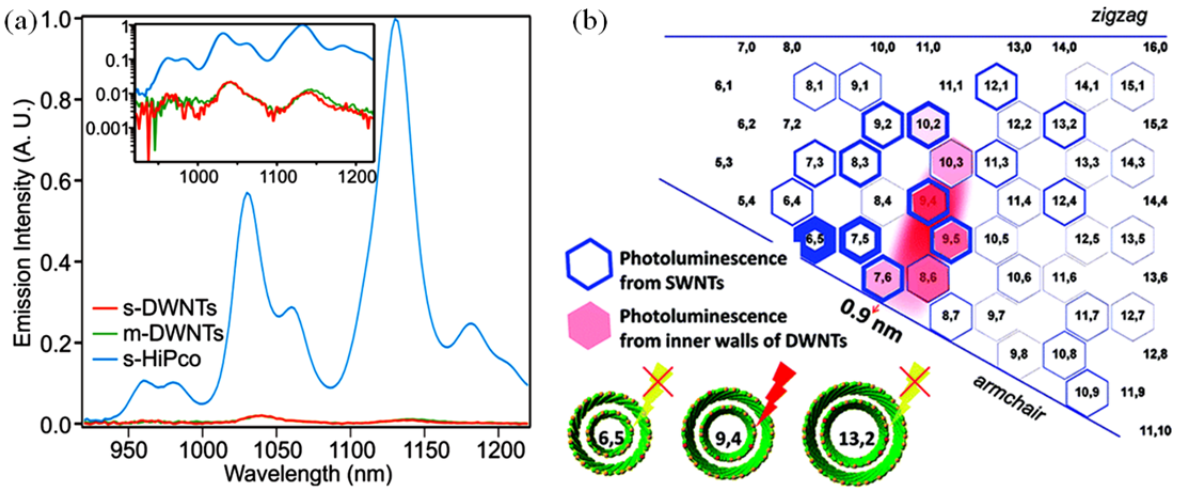

Figure 5.7: *(a) Photoluminescence spectra of electronic type separated DWNTs versus small diameter semiconducting SWNTs excited at 649 nm. Inset: PL spectra plotted on a logarithmic scale (from ref. [146]). (b) The (n,m) chirality map of the DGU separated SWNTs and DWNTs. Relative abundance is denoted by line thickness (SWNTs) or color gradient (DWNTs) (from ref. [147]).*

In conclusion, from the literature, we see that the luminescence of DWNTs is still an open question. The controversy is due to mainly three reasons:

- The presence of a small amount of semiconducting SWNTs in DWNTs samples can contribute to the PL.
- The possibility that inner tubes are extracted from the outer-tubes during the protocol of dispersion (*i.e.* during the sonication and centrifugation steps). These inner tubes become small SWNTs and these tubes can luminesce.
- The inter-tube interaction can cause the PL quenching due to the energy/charge transfer from inner tubes to outer tubes.

One of the objectives of this work is to contribute to the debate concerning the origin of the fluorescence in DWNTs' samples.

5.3. Samples preparation

In order to study the optical properties of inner tubes, we prepare DWNTs following two approaches: (i) starting with raw pristine DWNTs having a low amount of SWNTs, (ii) covalent functionalization via diazonium group on the surface of outer tubes. Moreover, the non-covalent functionalization of DWNTs permits to investigate the energy/charge transfer between inner and outer tubes, and between DWNTs and dye molecules.

5.3.1. Starting materials: Powder samples

E. Flahaut *et al.* (CIRIMAT) synthesized the pristine DWNTs (p-DWNTs) and two mixed double/triple-walled carbon nanotubes (D/TWNTs) samples by catalytic chemical vapour deposition (CCVD) [148]. A commercial HiPCO-SWNTs powder was purchased from CNI.

The first kind of samples contains approximately 80% DWNTs (Figure 5.8a) [140]. The residual tubes are SWNTs (20%) and a few triple-walled nanotubes (TWNTs). As shown on the graph (Figure 5.8a), the nanotubes with diameters below 1 nm correspond to the inner tubes of DWNTs. This information is important for the understanding of the results measured on this kind of DWNTs samples. However, the large number of SWNTs is a problem to identify unambiguously the origin of the luminescence in DWNT samples.

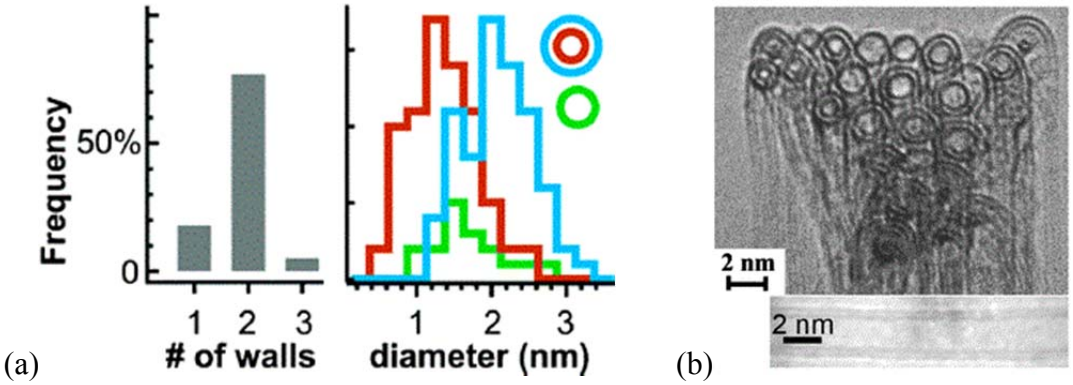

Figure 5.8: *(a) The diameter and number of walls distribution in a powder of pristine DWNTs samples, synthesized by CCVD, (b) HRTEM images of a DWNT bundle [140, 148].*

Nanotube	Percentage	Diameter distribution
SWNTs	~ 20 %	0.9 – 3 nm
DWNTs	~ 80 %	Inner tubes: ~ 0.4 – 2.6 nm Outer tubes: ~ 1.2 – 3.4 nm

Table 5.1: *The diameter distribution of the powder S/DWNTs samples.*

In order to minimize the number of SWNTs in raw p-DWNTs, a second kind of sample named DWNTs/TWNTs was synthesized. The TEM analysis of this sample shows that most of the nanotubes are DWNTs (~41%) or TWNTs (~43%) (Figure 5.9). Very importantly, the SWNTs content in these samples is very low, only ~ 1 %. In this sample, the luminescence signal, if it exists, could be attributed to the inner semiconducting of D/TWNTs rather than that of SWNTs. TWNTs contained three concentric tubes, and are called: namely inner@middle@outer tubes, are more complex for investigation. However, Figure 5.9c and d

suggest that all the tubes having a diameter smaller than 1 nm always correspond to inner tubes of DWNTs/TWNTs.

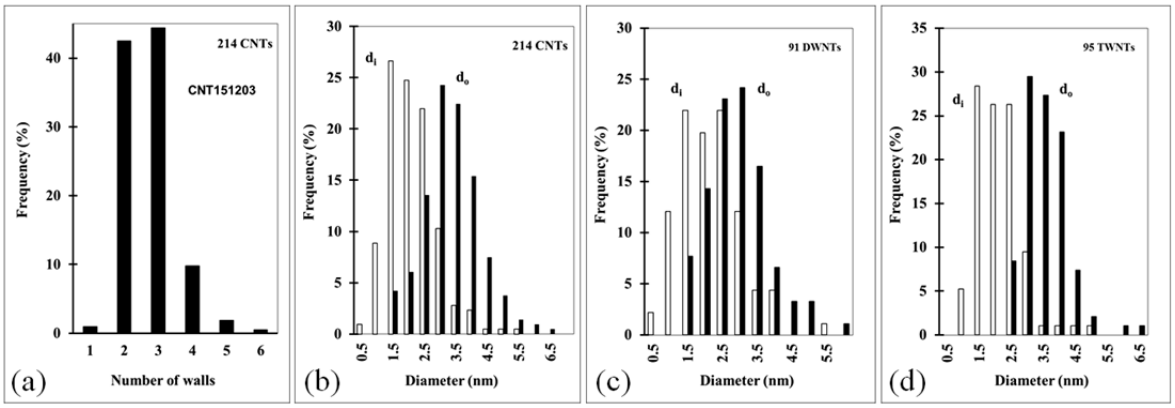

Figure 5.9: *The diameter and numbers walls distribution of D/TWNTs powder samples.*

5.3.2. Protocol for the functionalization of DWNTs

In this section, we introduced two methods of chemical functionalization using diazonium route and dye molecules. The aim of the functionalization is to permit the study of the optical properties of inner tube in DWNTs by the comparison with the corresponding ones in p-DWNTs. The functionalization DWNTs by diazonium group eliminates SWNTs and outer tubes. The functionalization with dye molecules allows us to fabricate hybrid systems.

5.3.2.1. Functionalization DWNTs via diazonium route

R. Aznar and J.-P. Lère Porte's team at ENSCM performed the chemical reaction between DWNTs and diazonium salts. The diazonium salts are organic compounds whose functional group is represented as $R{-}N_2H^+X$, in which R could be any organic compound and X an inorganic or organic anion. In my thesis, pristine powder DWNTs was functionalized via diazonium route following the approach illustrated on Figure 5.10. Iodobenzene molecules are grafted on the sidewall of outer tubes by chemical reaction with purified 4-iodoaniline, in presence of 1-Methyl-2-pyrolidone and isopentyl nitrite at 80^oC for 24 hours. The f-DWNTs are collected on a membrane filter by filtration. The collected powder f-DWNTs are washed by DMF, THF, CH_2Cl_2, acetone, ether. Finally, the membrane is dried in oven for 24 hours to collect the powder f-DWNTs. The functionalization for nanotubes by diazonium route is well-known, efficient, and reproducible [132, 133, 149]. Moreover, functionalization of the carbon nanotubes has been shown to be mostly reversible by heating [133, 150]. We performed two different degree of functionalization which have molar ratio of 1:1 and 4:1 between iodoaniline and carbon from the DWNTs.

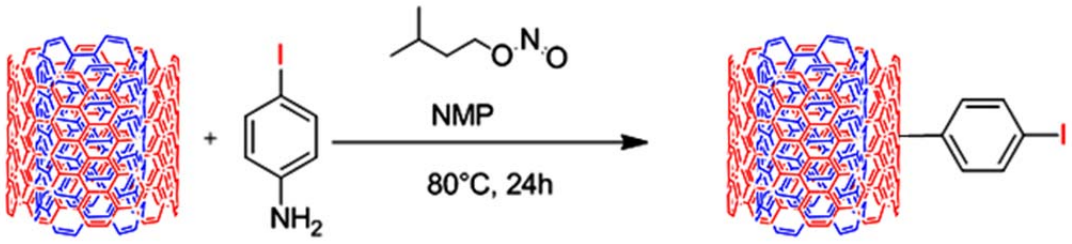

Figure 5.10: *Scheme of the DWNT functionalization reaction via the diazonium route.*

The mechanism of the CNTs functionalization by diazonium at high temperatures by refluxing the reaction mixture can be found in the ref [149, 151-154]. In brief (Figure 5.11), the reduction by heating creates aryl radical that covalently attaches to the carbon surface. This aryl radical is involved in a coupling reaction with CNTs, thereby forming a carbon-carbon bond with the wall of the nanotube. The reaction is thought to occur by injection of an electron from SWNTs into an aryl diazonium salt which induces then the formation of a reactive aryl radical, thereby releasing N_2 and resulting in the formation of a new nanotube-arene bond.

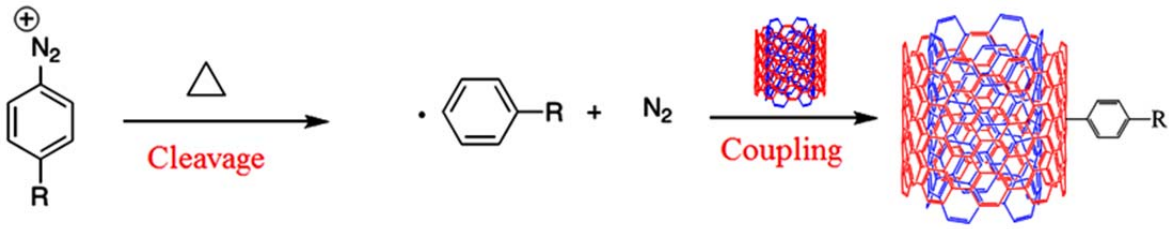

Figure 5.11: *The mechanism of diazonium functionalization on DWNTs (adapted from ref [153]).*

5.3.2.2. Functionalization DWNTs with dye molecules

In order to study the energy/charge transfer from molecules to DWNTs, the procedures of covalent and non-covalent (π-stacking) functionalization of DWNTs were performed with fluorescein isothiocyanate (FITC) by E. Flahaut's group at CIRIMAT. Figure 5.12 shows the molecules structure of fluorescein and FITC. The FITC is a derivative of fluorescein functioned with isothiocyanate (N=C=S). The isothiocyanate is very reactive towards NH_2 functions which allow a covalent functionalization. After FITC is covalently grafted on the DWNTs, the N=C=S group will be eliminated. These molecules are selected due to their strong luminescence in the visible range. FITC has an excitation (emission) peak approximately at 495 nm (520 nm) [155]. In the following, we study the optical properties of the pristine powder of DWNTs and dispersed DWNTs wrapped with surfactants in D_2O.

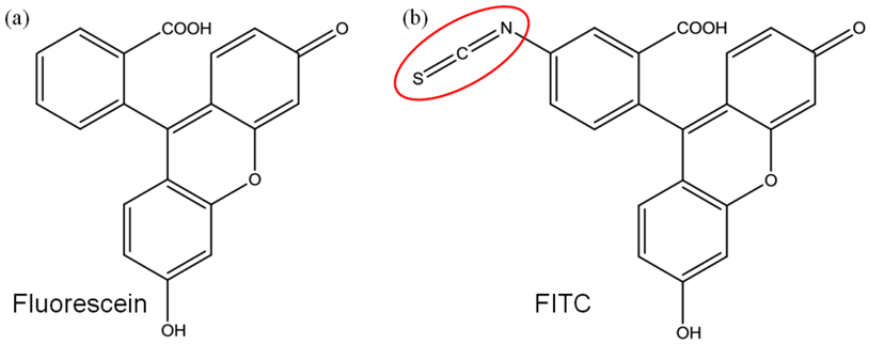

Figure 5.12: *The molecule structures of free fluorescein and FITC.*

Before functionalization with FITC, the p-DWNTs were oxidized by mixture of HNO_3/H_2SO_4 in order to purify them by removing traces of metallic catalyst and by burning amorphous carbon [156] (Figure 5.13a). Moreover, the oxidations also open the caps and increase the chemical reactivity on the CNTs surface by creation of functional groups, in particular carboxylic groups.

The covalent functionalization (DWNT-NH-FITC) and non-covalent functionalization (FITC@DWNTs) are then performed. The detail of functionalized DWNTs with FITC is presented in the thesis of Bortolamiol Tifania [156]. The scheme of oxidization and functionalization is illustrated in Figure 5.13b and c.

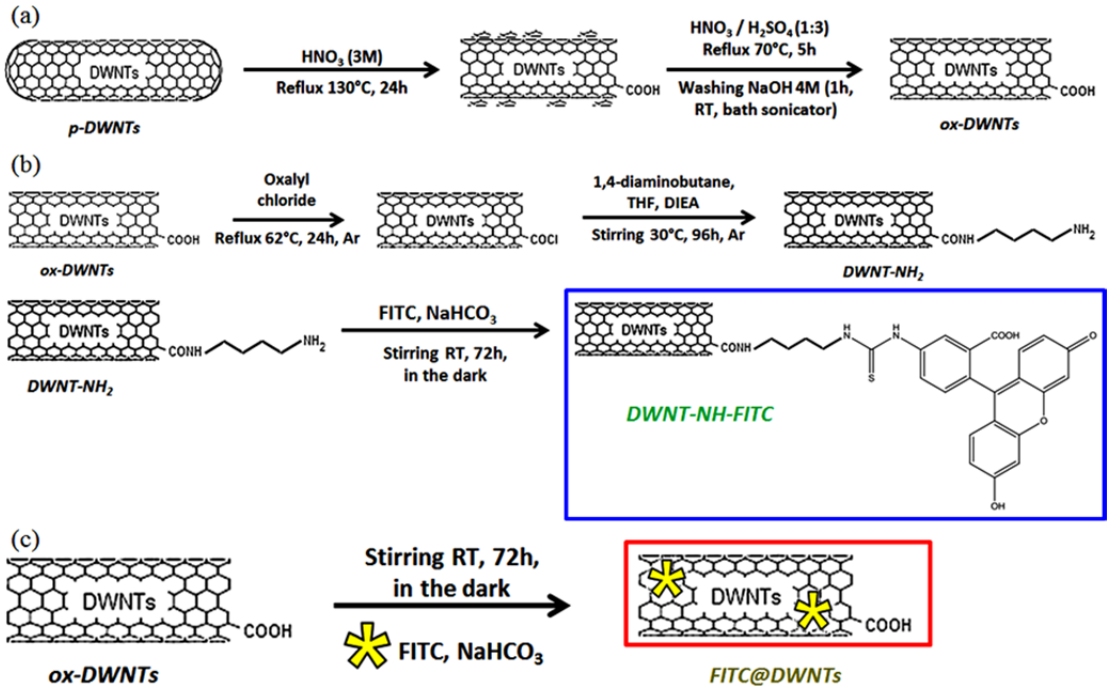

Figure 5.13: *Scheme of (a) oxidation p-DWNTs, (b) covalent functionalization p-DWNTs with FITC, and (c) non-covalent functionalization p-DWNTs with FITC (from the PhD thesis of T. Bortolamiol [156]).*

5.3.3. Protocol for the preparation of DWNT suspensions

The protocol below is applied to powder samples in order to disperse them with a surfactant in D_2O:

10 mg of each carbon nanotubes powder is dispersed by ultrasonication in a 10 ml solution of DOC (sodium deoxycholate) in D_2O (concentration of 1% in weight). D_2O (purity 99%) is used as the solvent instead of H_2O because of its superior near-infrared transparency. The isotopic frequency shift of the O-H stretching overtone increases the long wavelength cut-off of D_2O up to 1900 nm instead of 1350 nm in H_2O [157]. Here, the sodium deoxycholate (DOC) surfactant was preferred to other surfactants for preparing suspension of nanotubes because it was reported to yield to the higher absorption intensity and sharper peaks [140]. This result was also confirmed by our experiments from the comparison between data measured on DWNTs wrapped with DOC, SDBS (sodium dodecyl benzene sulfonate) and SDS.

In order to have suspensions of individual nanotubes, the following two-steps process was applied for dispersion:

- Bath sonication (USC500D, VWR International) for 30 minutes at the highest power level (45 kHz, 100 W).
- Micro-tip ultrasonication (Vibra Cell 75455; Bioblock Scientific) for 10 minutes; set value of pulse: 2s and amplitude: 40 W. During this step, the vial containing the nanotube suspension is put in an ice bath in order to avoid excessive heating.

After sonication, the suspensions of nanotubes were centrifuged during 10 hours (14500 rpm which corresponds to ~20000 g) in order to eliminate nanotube bundles and other residues. Finally, we carefully collected the supernatant for further analysis.

5.4. Properties of functionalized DWNTs (f-DWNTs) via diazonium route

In this section, we report and discuss the optical measurements performed on suspensions of pristine DWNTs (p-DWNTs), and functionalized DWNTs (f-DWNTs) at low and high degree of functionalization.

5.4.1. Characterization by Raman spectroscopy

The micro Raman spectra are recorded for nanotubes suspensions at different excitation energies. The samples were put in a quartz cuvette (5 mm width). A 50x microscope objective (numerical aperture = 0.5) is used to focus the excitation laser beam into the samples. The Raman signal was recorded and analyzed thanks to a monochromator with a diffraction grating either 1200 or 1800 groove/mm and liquid-nitrogen-cooled Si-CCD detector. The instrument is calibrated by using the peak position of the laser wavelength and silicon peak (520.7 cm^{-1}).

In the Figure 5.14, we plotted the Raman spectra of p-/f-DWNTs at different excitation energies in the RBLM (140 cm^{-1}-310 cm^{-1}), D-modes (1325 cm^{-1}), and G-modes (1590 cm^{-1}) ranges.

Because the RBLMs frequencies are known to be inversely proportional to nanotubes diameter, the RBLM features below (above) 200 cm^{-1} mainly correspond to outer (inner) tubes, respectively. The RBLM Raman spectra of p-/f-DWNTs are normalized on the RBLM peaks corresponding to inner tubes (around 300 cm^{-1}) because the inner tubes are expected to be protected by outer tubes from chemical reactions.

In order to study the influence of the level of functionalization on the Raman spectra, and then on the electronic structure via the changes in the resonance conditions, we record the RBLM feature at low and high degree of functionalization. Under functionalization, we clearly observe a general decrease of the low-frequency RBLMs corresponding mainly to outer tubes of DWNTs and residual SWNTs. We also demonstrate that the chemical sidewall functionalization of DWNTs with diazonium can be selective. Indeed, we observe that, in the spectra excited at 1.7 and 1.77 eV, the RBLMs assigned to metallic nanotubes are more significantly affected than the semiconducting ones after functionalization at molar ratio 1:1 (see Figure 5.14c-d). More precisely, by contrast with the RBLM of the metallic outer tubes, located around 170 cm^{-1}, the RBLM features around 130 cm^{-1} assigned to semiconducting outer tubes can still be observed when the level of functionalization is low. This observation is in good agreement with previous reports which showed that at low degree of functionalization the metallic SWNTs were functionalized by diazonium preferentially with respect to their semiconducting counterparts [158].

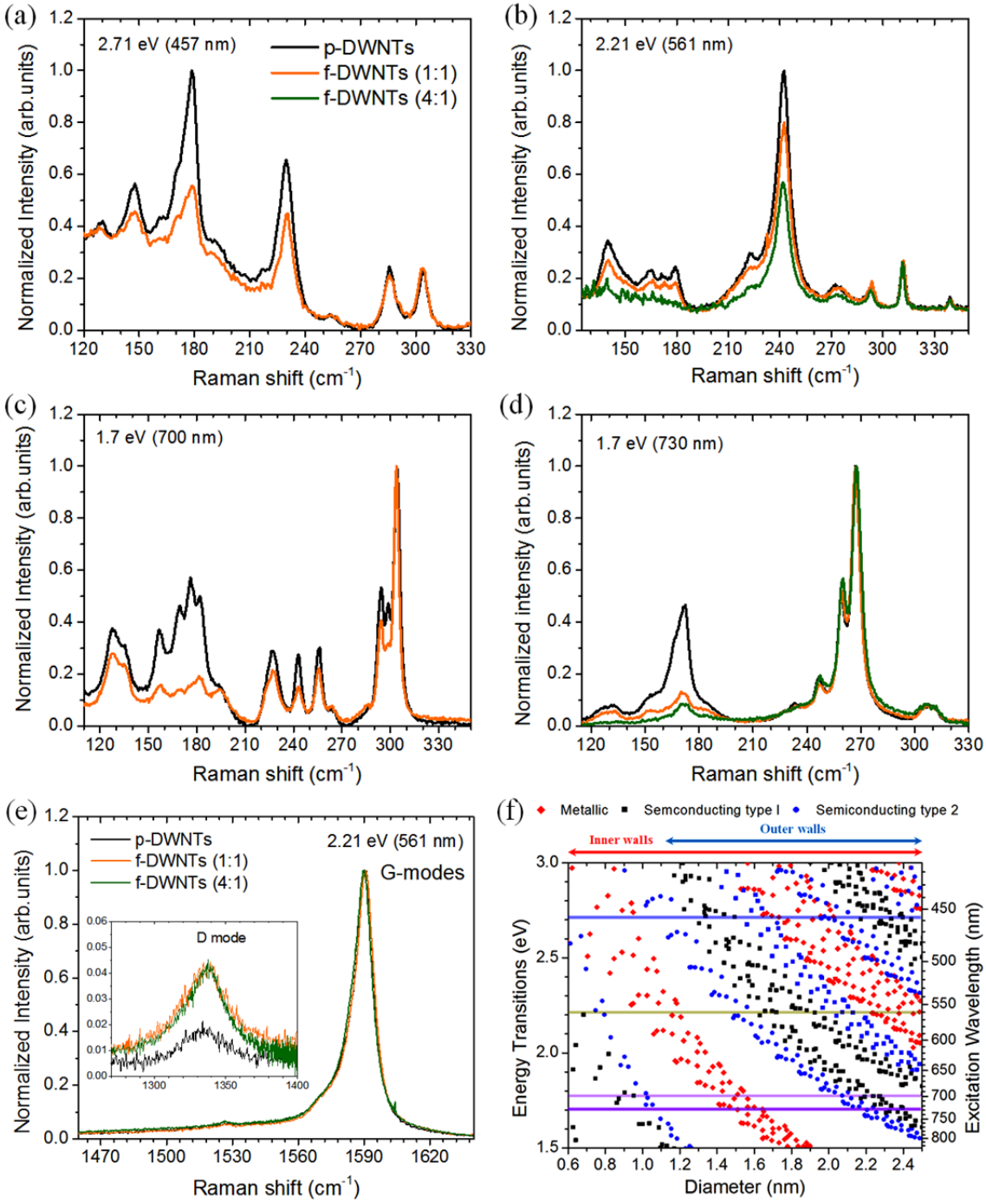

Figure 5.14: *The Raman spectrum excited at different energies for (a-d) RBLM, (e) G-modes. (f) Kataura plot with excitation energies used in this work.*

For the higher degree of functionalization (4:1), the vanishing of the low-frequency RBLMs (below 200 cm^{-1}) has to be related to a high level of defects on the outer nanotubes. In other words, the loss of features in the low-frequency RBLM region identifies a successful covalent functionalization of the outer walls. Despite of the high degree of functionalization, the presence of the high-frequency RBLM proves that the sp^2 hybridization of inner walls remains.

For instance, in the Raman spectrum excited at 2.21 eV, the RBLM features at low-frequency completely disappear while the intensity of the high-frequency RBLM is weakly affected. This observation suggests that the properties of the inner walls are protected, towards the covalent functionalization or in other words that the functionalization is only effective on the outer tubes of DWNTs.

In the high-frequency range, where appear the D-band and G-modes, the Raman spectra of p/f-DWNTs are normalized on the of G^+-mode. We observe that the line shape of G-modes is similar before and after functionalization. The D mode is significantly enhanced after the grafting of molecules on tubes. The intensity increase is related to the presence of sp^3 defects on the wall. The intensity ratio (I_D/I_G) is expected to increase with the degree of functionalization. However, our measurements show a close intensity ratio at low and high degree of functionalization, this intensity ratio I_D/I_G rising by a factor of 3 after functionalization (0.045 vs. 0.015).

5.4.2. Optical absorption measurements

The absorption spectra were recorded using a UV-Visible-NIR "CARY 5000" spectrometer which covers a 175–3300 nm wavelength range. The nanotubes suspensions were put in a 1 mm thick quartz cuvette. The baseline spectrum is obtained by measuring a blank sample, *i.e.* a 1 mm thick quartz cuvette containing a suspension of DOC in D_2O (DOC@ D_2O, 1% solution).

Figure 5.15 presents the absorption spectra of DWNTs suspension samples (before (a) and after (b) normalization) as function of the wavelength. The absorption spectra were normalized at 930 nm. The presence of separated sharp peaks, associated with specific optical transitions, suggests that after dispersion the nanotubes are individual. The energy bands $E_{ii}^{S/M-out(in)}$ correspond to optical transitions of outer (inner) semiconducting or metallic tubes.

The broad absorption band around 2000 nm (0.62 eV) corresponds to the first optical transitions of large diameter semiconducting tubes which are either outer or large inner walls of DWNTs. We found a significant decreasing of the band around 2000 nm after the functionalization. This 2000 nm feature decreases with increasing the degree of functionalization. This result suggests that the molecules are successfully grafted on the surface of outer walls at high degree of functionalization (molar ratio 4:1). Consequently, the optical transitions of these tubes are eliminated. The Kataura plot indicates that the lost transitions correspond to tubes with large diameter (above 2 nm) and thus assigned to outer tubes. The remaining intensity possibly corresponds to the absorbance of large diameter inner walls.

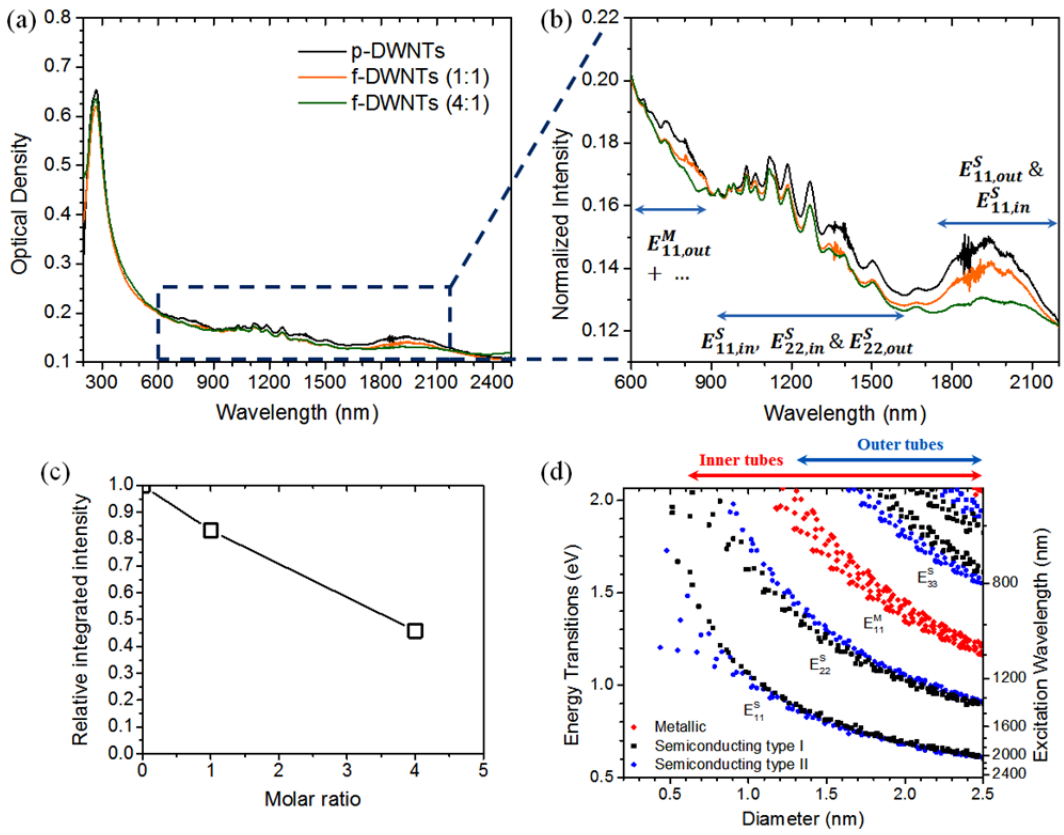

Figure 5.15: *(a) UV-Vis-NIR absorption spectra of the nanotubes suspensions: p-DWNTs (black), f-DWNTs 1:1 (orange), f-DWNTs 4:1 (olive). (b) zoom in the 600-20100 nm range,* $E^S_{ii,out}$ $(E^S_{ii,in})$ *is optical transitions of outer (inner) walls of DWNTs. (c) the relative intensity of the broad peak located around 2000 nm at molar ratio 1:1 and 4:1. (d) "Kataura" plot.*

From the Kataura plot, the features in the 900 - 1700 nm (1.55-0.72 eV) are assigned to the first and second optical transitions of inner and outer semiconducting tubes. The similar shape of p-DWNTs and f-DWNTs absorption spectrum in this range confirmed the presence of the E^S_{ii} transitions of individual inner tubes. In other words, the remaining absorption features can be assigned to inner tubes of f-DWNTs or extracted SWNTs. After functionalization, a slight decrease of absorption intensity is observed, and possibly assigned to the vanishing of the energy transitions of outer walls ($E^S_{22,out}$). On the other hand, comparison between the absorption of p-SWNTs and f-SWNTs shows that all the absorption peaks of SWNTs vanish after the functionalization [132, 152].

The peaks which appear under 900 nm can be assigned to E^M_{11} transition of metallic nanotubes. After the functionalization, with molar ratio 1:1 and 4:1 respectively, the progressive decreasing of small feature around 800 nm corresponds to the ones of the metallic outer tubes.

In agreement with previous result [133], the present data lead to the conclusion that the inner tubes are unaffected by chemical reaction thanks to the protection by outer walls.

5.4.3. Photoluminescence (PL) of pristine and functionalized DWNTs

Suspensions of pristine and functionalized DWNTs (dispersed DWNTs) are placed in a 5mm thick quartz cuvette.

The setup used for PL experiments is illustrated on the Figure 5.16. The main characteristics of the set-up are the following: a 300 groove/mm grating was used; the emitted signal in the infrared range is recorded by liquid-nitrogen-cooled InGaAs detector; some cutting filters are placed in front of spectrometer to remove the high-order peaks of the laser; for PLE measurement, we used as excitation source a Ti:Sapphire laser emitting in a broad wavelength range: from 700 nm to 1000 nm; measurements are recorded step by step, and a step of 3nm was used for the excitation wavelength.

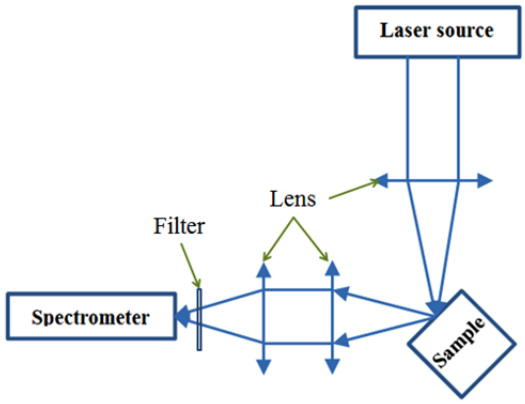

***Figure 5.16**: Scheme of the photoluminescence setup for the measurement of nanotubes suspensions.*

The PLE maps are plotted as contour graphs on the Figure 5.17. The results obtained on the pristine and functionalized DWNT suspensions are compared with those measured on HiPCO-SWNTs dispersed in SDS (white dots) in ref [28].

Figure 5.17 shows the PLE intensity as function of excitation and emission wavelength of isolated tubes in HiPCO, p-DWNTs, f-DWNTs, and D/TWNTs samples.

The PLE map of p-DWNTs (Figure 5.17b) clearly indicated that all the tubes with a diameter < 1 nm luminesce in good agreement with results from T. Hertel *et al.* [140]. However, it is unclear whether these tubes are inner tubes of DWNTs or remaining SWNTs of small diameter. An approach to distinguish fluorescence of SWNTs from DWNTs consists in the covalent functionalization of the tubes. Indeed, the covalent functionalization on p-DWNTs

eliminates the PL response of outer walls and residual SWNTs of the original sample while one expect that the electronic structure of inner walls remains intact. We measured the PL of dispersed f-DWNTs via diazonium group (Figure 5.17c). Interestingly, the measured PL of f-DWNTs shows close signal as compared with those of p-DWNTs.

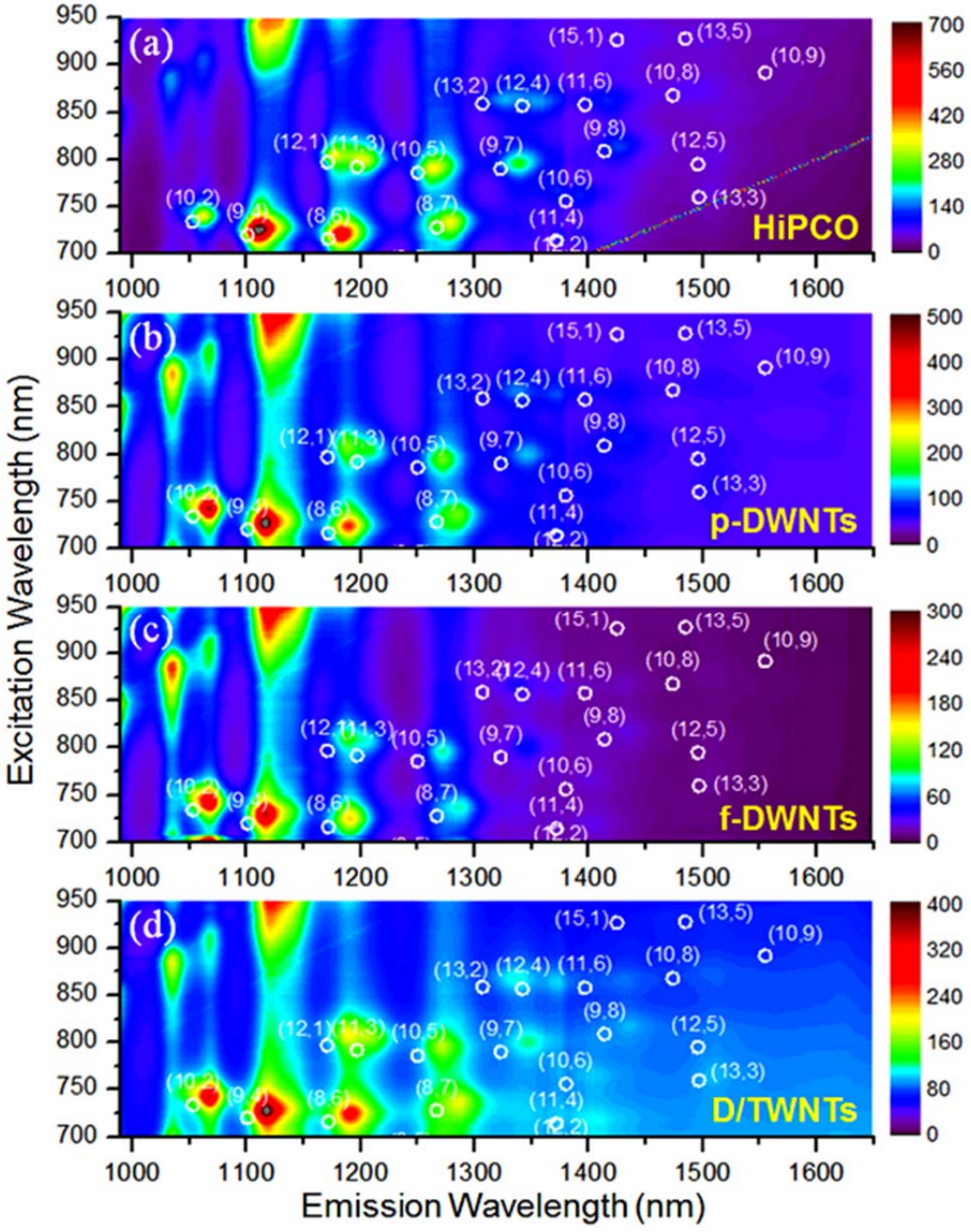

Figure 5.17: *The PLE maps of HiPCO, p-DWNTs, f-DWNTs, D/TWNTs suspensions at room temperature. (white dots are reference data from ref [28]). Intensity is normalized vs. incident laser power.*

Another approach consists on recording the PLE of D/TWNTs suspensions (with a low amount of SWNTs, 1%). The results also confirm the luminescence of small inner tubes (Figure 5.17d). The two approaches allow us to conclude that the amount of SWNTs contained in the original powder samples cannot explain the strong luminescence signal because of the elimination of SWNTs by covalent functionalization in f-DWNTs sample or selective synthesis in the D/TWNTs sample. Therefore, the observation of luminescence is the results of the emission either from inner tubes of DWNTs or from SWNTs extracted during the protocol of suspension.

We analyze in detail the position of PL peaks of p/f-DWNTs, D/TWNTs and SWNTs suspension by plotting the PL spectra excited at 728 nm (1.7 eV), and the excitation spectra of the PL emission at 1060 nm (1.17 eV). The absorption and emission peaks are fitted by using peak-fit software with Lorentzian functions. The results are presented in Figure 5.18.

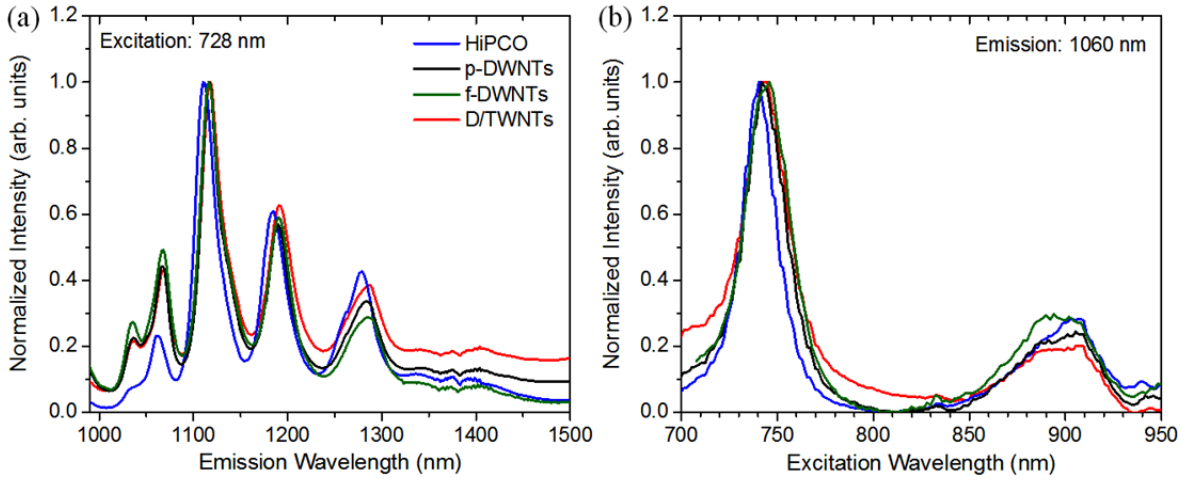

Figure 5.18: *PL spectra excited at 728 nm (1.7 eV), and excitation spectra of the PL emission at 1060 nm (1.17 eV).*

(n,m)	HiPCO	p-DWNTs	D/TWNTs	f-DWNTs	$\Delta E_{11}^{p-DWNTs}$ (meV)	$\Delta E_{11}^{D/TWNTs}$ (meV)	$\Delta E_{11}^{f-DWNTs}$ (meV)
(10,2)	1.17	1.163	1.163	1.163	-7	-7	-7
(9,4)	1.114	1.109	1.108	1.109	-5	-6	-5
(8,6)	1.046	1.042	1.040	1.041	-4	-6	-5
(8,7)	0.97	0.966	0.964	0.962	-4	-6	-8

Table 5.2: *Energy, and energy shift (with respect to position in the SWNT reference sample) of the luminescence peaks close of 1.16 eV in the different samples (excitation energy: 1.7 eV (728nm)).*

(n,m)	HiPCO	p-DWNTs	D/TWNTs	f-DWNTs	$\Delta E_{11}^{p-DWNTs}$ (meV)	$\Delta E_{11}^{D/TWNTs}$ (meV)	$\Delta E_{11}^{f-DWNTs}$ (meV)
(10,2)	1.674	1.667	1.667	1.665	-7	-8	-10

Table 5.3: *Excitation energy of the luminescence of the (10,2) nanotube, close of 1.17 eV (1060 nm), in the different samples, and shift of the excitation energy with respect to its position in the SWNT reference sample.*

Our results summarized in Table 5.2 and 5.3 show an average red-shift of the emission (excitation) energy, with respect to SWNTs, close of the E_{11} (E_{22}) transition energy of -6 meV (-8 meV) for nanotubes wrapped in DOC while a red shift of -4 meV was reported for DWNT@SBDS [141]. The small redshift of PL signal of p/f-DWNTs and D/TWNTs samples can be attributed to the different environments. Additionally, D.A Tsyboulski *et al.* [145] suggested that samples treatment of DWNTs (*i.e.* sonication and centrifugation) can also lead to the redshift of PL signal.

In summary, from the Raman, absorption and PL measurements performed on suspensions of pristine (p-DWNT) and DWNTs functionalized by diazonium (f-DWNT), we show that: (i) the functionalization is only effective on the outer tubes of each DWNT, (ii) the initial level of SWNTs in the pristine samples cannot explain the relative strong intensity of the PL signal measured on p/f-DWNTs, and consequently, (iii) the luminescence results from the emission either by inner tubes of DWNTs or by SWNTs extracted from DWNTs during the process used to prepare DWNTs suspensions.

5.5. Covalent and non-covalent functionalization of DWNTs with dye molecules

In this section, we performed optical measurements on different suspensions of DWNTs: pristine (p-DWNT), oxidized (ox-DWNT), covalently functionalized (DWNT-NH-FITC), and non-covalently functionalized (FITC@DWNT) with dye (FITC) molecules.

5.5.1. Characterization by Raman spectroscopy

The oxidized and functionalized DWNTs samples are analyzed by Raman spectroscopy to study the effect of the functionalization by FITC molecules on the structures of DWNTs. In the following, we will present the results of Raman measurements performed on powders and suspensions.

- **Powders**

On the Figure 5.19a, we plotted the Raman spectra, excited at 457 nm, measured on powders of pristine and functionalized DWNTs. These spectra are compared to the ones of FITC and fluorescein molecules. The Raman spectra of DWNTs are normalized on the intensity of the G-modes to help the comparison.

The Figure 5.19b compares the spectra of pristine and oxidized DWNT in the D and 2D range. We clearly observe a significant decreasing of D modes around 1360 cm^{-1} and of the band around 2960 cm^{-1}. Both features sign the presence of amorphous carbon in the pristine DWNTs and their decreasing implies that the amorphous carbon is eliminated under oxidation. A red-shift for D and 2D bands are observed in ox-DWNTs as compare to their frequencies in p-DWNTs (see Table 5.4).

Figure 5.19c compares the Raman spectra of FITC@DWNT and DWNTs-NH-FITC with the one of FITC and fluorescein molecules. We observe that the all characteristic bands of the fluorescein and FITC are presented in the Raman spectra of FITC@DWNT and DWNTs-NH-FITC. The presence of these bands confirms the presence of FITC molecules in the samples. We present in the Table 5.4 the frequencies of all the Raman peaks obtained by the fit of the different modes by using peak-fit software with a Lorentzian profile for each mode. These peaks relate to the vibration modes of FITC in powder and in functionalized DWNTs. The positions of these bands in the covalent or non-covalent f-DWNTs are very close to those in FITC.

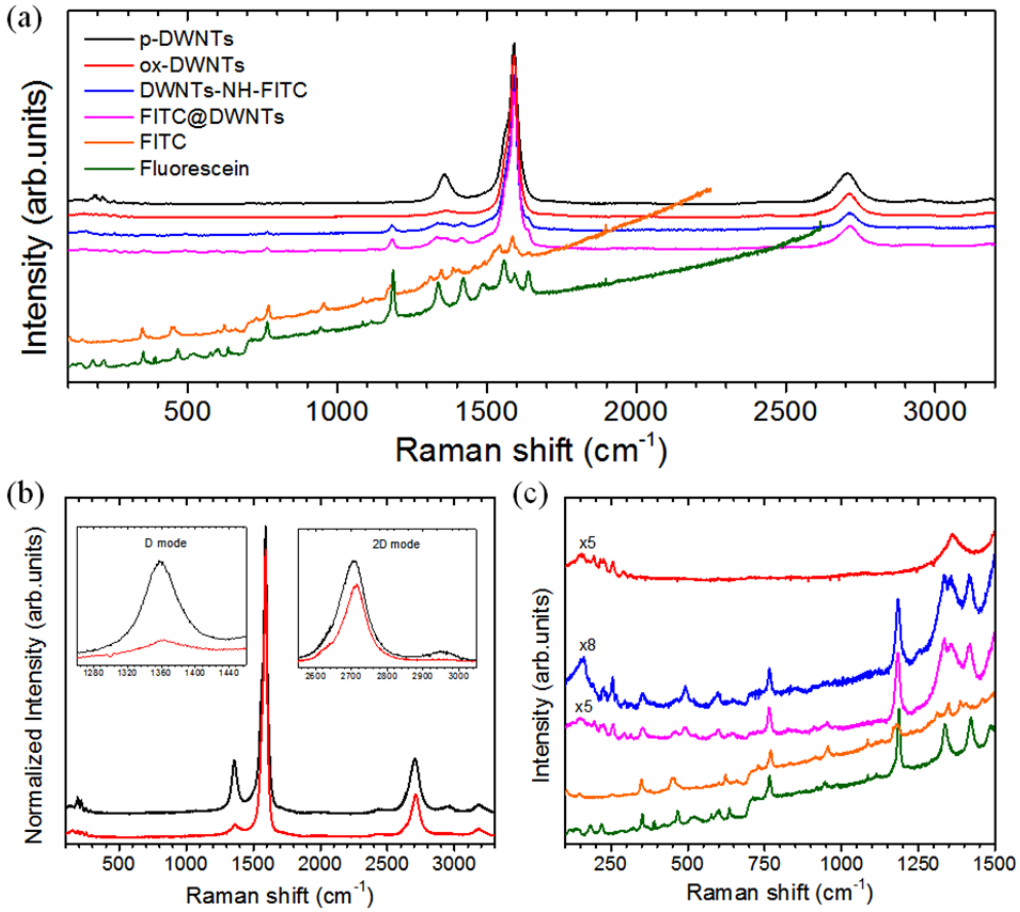

Figure 5.19: *Raman spectra excited at 457 nm of nanotubes and molecules powders. (a) full range for all samples, (b) p- and ox-DWNTs, (c) ox-DWNTs, FITC@DWNTs, DWNTs-NH-FITC, and free FITC.*

Vibrational modes	p-DWNTs	ox-DWNTs	fluorescein	FITC	FITC@DWNTs	DWNTs-NH-FITC
Hexasubstituted benzene			352	350	354	353
Deformation C-O			467	450	457	457
Deformation benzene ring			635	623	630	-
Substituted benzene			769	770	765	765
Elongation C-O-C			1187	1186	1183	1184
O-H deformation of phenol			1338	1348	1353	1346
Deformation C-O			1421	1404	1418	1419
D-modes	1360	1368		-	-	-
2D modes	2704	2711			2712	2713

Table 5.4: *Raman peaks positions (cm^{-1}) in the different powder samples DWNTs, molecules, and f-DWNTs.*

- **Suspensions**

We display, on the Figure 5.20a and 5.20c, the RBLM range of Raman spectra, excited at 730 nm, measured on suspensions of p-DWNTs, ox-DWNTs, FITC@DWNTs, and DWNTs-NH-FITC. The G-modes range of the Raman spectra, of the same samples excited at 561 nm, are reported on the Figure 5.20b and 5.20d. In the RBLM range, the spectra are normalized on the RBLM peaks assigned to inner tubes. In range of D and G-modes, the Raman spectra are normalized on the G^+ mode.

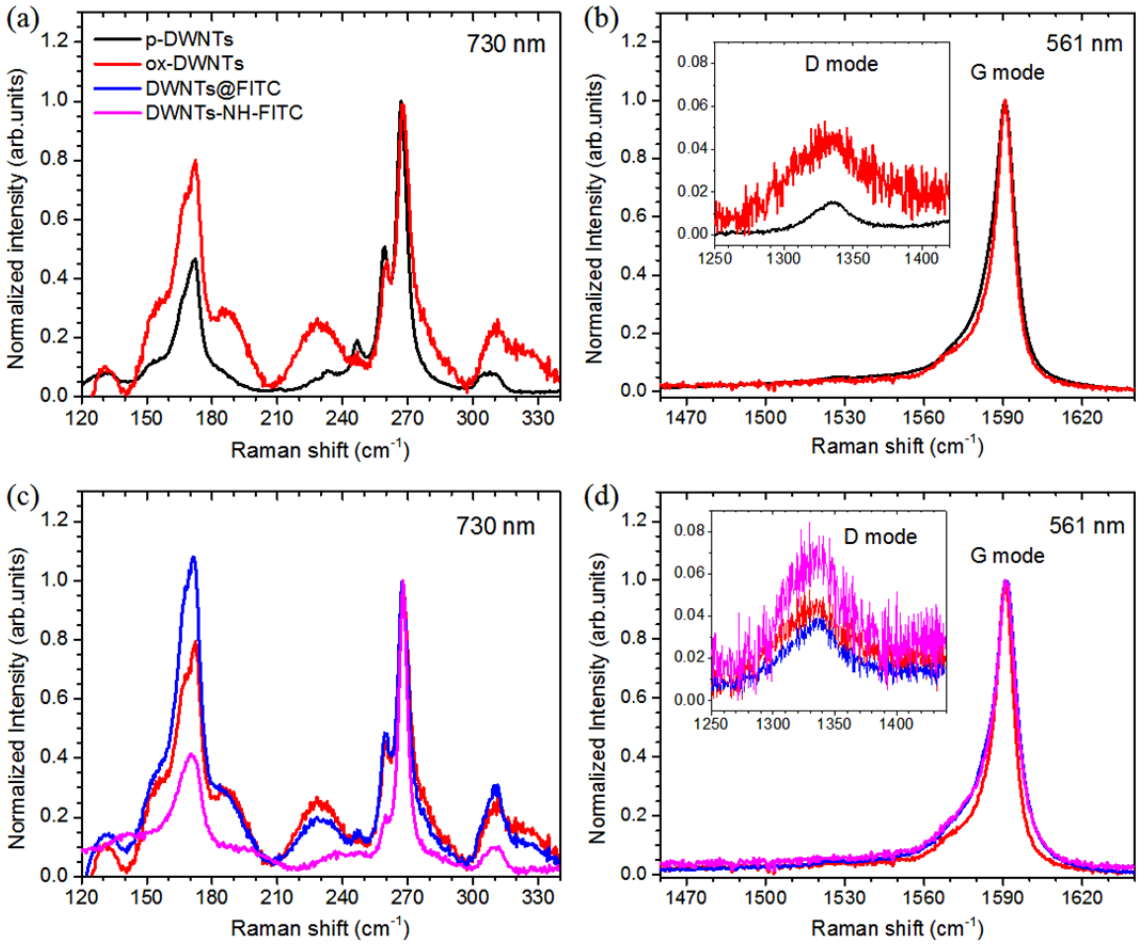

Figure 5.20: *Raman spectra of p/ox/f-DWNTs suspensions. (a,c) RBLM range excited at 730 nm; (b,d) D-modes and G-modes excited at 561 nm.*

The comparison between the RBLM part of the Raman spectra of p-DWNTs and ox-DWNT (Figure 5.20a) illustrates the change of the response of the outer tubes after oxidization. On the other hand, Figure 5.20c shows the evolution of the response of the outer tubes in covalent (DWNTs-NH-FITC) and non-covalent (FITC@DWNTs) functionalized DWNTs. Note that for a 730 nm excitation, metallic outer tubes and semiconducting inner tubes are in resonance (see the Kataura plot of the Figure 5.14f).

On Figure 5.20c, a decrease of the intensity of the RBLMs located below 200cm^{-1} (assigned to outer tubes) is observed upon covalent functionalization (DWNTs-NH-FITC). By contrast, the RBLMs of FITC@DWNTs are close of those measured in ox-DWNTs. These results probably rely on the selective dispersion of different categories of tubes depending on the initial type of sample.

Referring to the D band intensity in pristine DWNTs (p-DNWT) suspension, we observed that the D band intensity increases by factors of 4 in ox-DWNTs suspension (Figure 5.20b). This observation, which seems to be opposite to the one observed in the powders of p-DWNT and ox-DWNTs, can be understood as following: (i) it is well-known that the protocol of dispersion eliminate amorphous carbons in p-DWNTs, (ii) the increase of the D band in ox-DWNTs is referred to defects (carboxylic groups) created by the oxidation on the nanotubes surface. The increase of D-band intensity in DWNTs-NH-FITC as compare to ox-DWNTs, and FITC@DWNTs (Figure 5.20d) is unexpected. Indeed, as on Figure 5.13, the grafting of FITC should occur on defect sites already present in ox-DWNTs. As for RBLMs spectra, this could be due to the selective dispersion of the most defective nanotubes in DWNTs-NH-FITC sample.

5.5.2. Optical absorption

The absorption measurements focus on the absorbance bands of FITC either in suspensions of free molecules and in suspensions of functionalized DWNTs. The absorption measurement was performed by using the same condition as the ones described in section 5.4.1.

Figure 5.21a presents the optical absorption spectra of all materials in range 200-2500 nm. A strong and sharp absorption band at 492 nm, assigned to the absorbance band of the FTIC molecule, is observed in the suspensions of FITC, DWNTs-NH-FITC, and FITC@DWNTs. These results state that the FITC molecules form a hybrid material with DWNTs.

The shapes of absorption peak at 492 nm in covalently and non-covalently functionalized DWNTs are similar (Figure 5.21b). However, the stronger intensity of this band in FITC@DWNTs than in DWNTs-NH-FITC reflect the higher FITC loading provided by the non-covalent functionalization.

To help the comparison, the absorption of p-DWNTs and ox-DWNTs are normalized on the 263 nm band (Figure 5.21c). The sharp (broad) optical bands in p-DWNTs (ox-DWNTs) suggest that nanotubes in p-DWNTs are individual (individual defective tubes and small bundles).

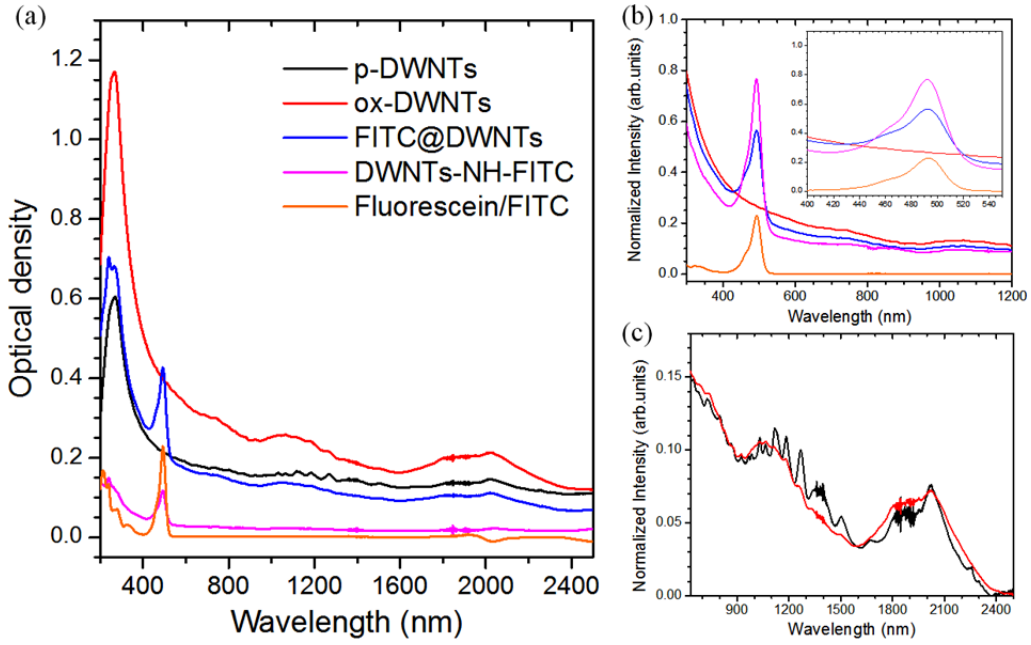

Figure 5.21: *(a) UV-Vis-NIR absorption spectra of different nanotubes suspensions; p-DWNT (black), ox-DWNTs (red), DWNTs@FITC (blue), DWNTs-NH-FITC (green), and FITC (orange). (b) zoom in the 300-1200 nm range, (c) spectra of p-DWNT and ox-DWNT normalized on the 263 nm band.*

5.5.3. Photoluminescence

Using a supercontinuum laser, we measured the PLE on the four DWNTs suspension samples: p-DWNTs, ox-DWNTs, FITC@DWNTs, DWNTs-NH-FITC. The luminescence of free FTIC molecules dispersed in D_2O has also been measured.

The experimental setup was described in section 5.4.3 (see Figure 5.16). The PLE maps are normalized with regards to the impinging laser power.

Figure 5.22a and 5.22b display the PLE map of p-DWNT and ox-DWNT suspensions, respectively. In both samples, PL provided by tubes having diameters below 1 nm is observed and assigned to semiconducting inner walls. The distribution of the PL intensity is changed after oxidation. In the pristine sample (p-DWNTs), the (8,3), (7,5) and (7,6) inner tubes exhibit the strongest PL intensities. The PL intensity of (6,5) inner tube dominates in the PLE map of the ox-DWNTs. This result suggests that the chiral distribution of inner tubes in ox-DWNTs is modified as compared to p-DWNTs. It might be that the larger inner tubes of DWNTs are burned selectively during oxidation.

It must be emphasized that no peak shift was observed when comparing the PLE maps measured on p-DWNTs and ox-DWNTs.

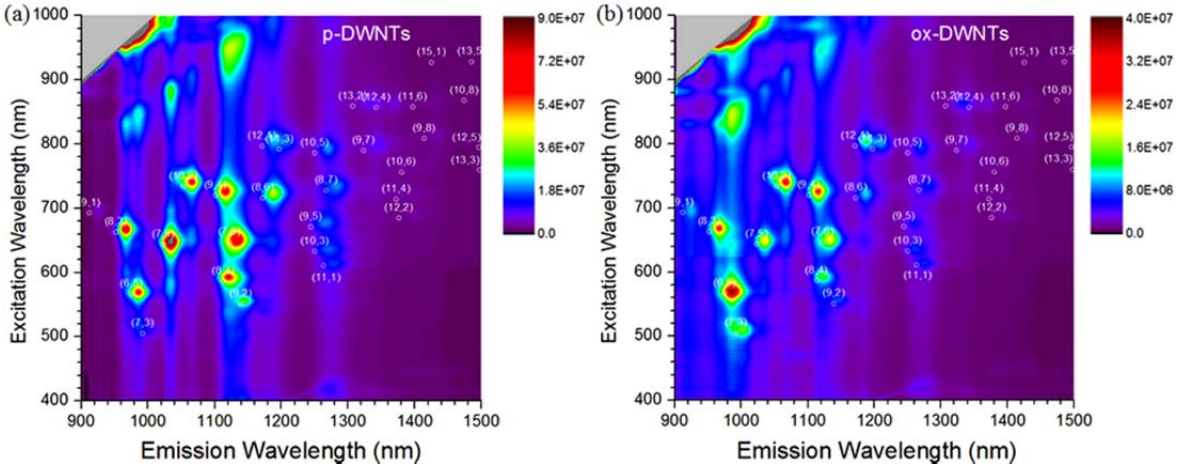

Figure 5.22: *PLE maps in the infrared range: (a) p-DWNTs, (b) ox-DWNTs. (white dots are data from ref [28]).*

The PLE maps of non-covalent (covalent) functionalized DWNTs are shown in the Figure 5.23a,b (Figure 5.23c,d) in the visible and infrared ranges. To help the comparison, the PL map of a free FTIC molecules suspension is shown in Figure 5.23e. A strong 520 nm (2.38 eV) PL peak excited around 493 nm (2.51 eV) is observed and assigned to the emission of FITC molecules. In the visible range, no difference is observed in the PLE maps measured on suspensions of free FITC molecules (Figure 5.23e) and suspensions of covalently and non-covalently f-DWNTs (Figure 5.23 a,c). In other words, the couple excitation-emission peaks at 490-525 nm confirm the presence of FITC in functionalized DWNTs.

In the infrared range, the PLE of DWNTs-NH-FITC (covalent functionalization) put clearly in evidence new emission peaks around 920 nm (1.34 eV) and 1000 nm (1.24 eV) (Figure 5.23d) for an excitation energy close of 493 nm (2.51 eV). The appearance of these peaks can be assigned to an energy transfer from grafted FITC molecules to the inner tubes. The process could be the following: the FITC molecules grafted on outer tubes absorb the energy at 493 nm; they transfer this energy to inner tubes; and the inner tubes emit in the 910-1000 nm the energy range. In addition, the transfer energy process seems to be selective for specific inner tubes. By contrast, the PLE spectrum of FITC@DWNTs (non-covalent functionalization) (Figure 5.23b) is close of the one measured on ox-DWNTs.

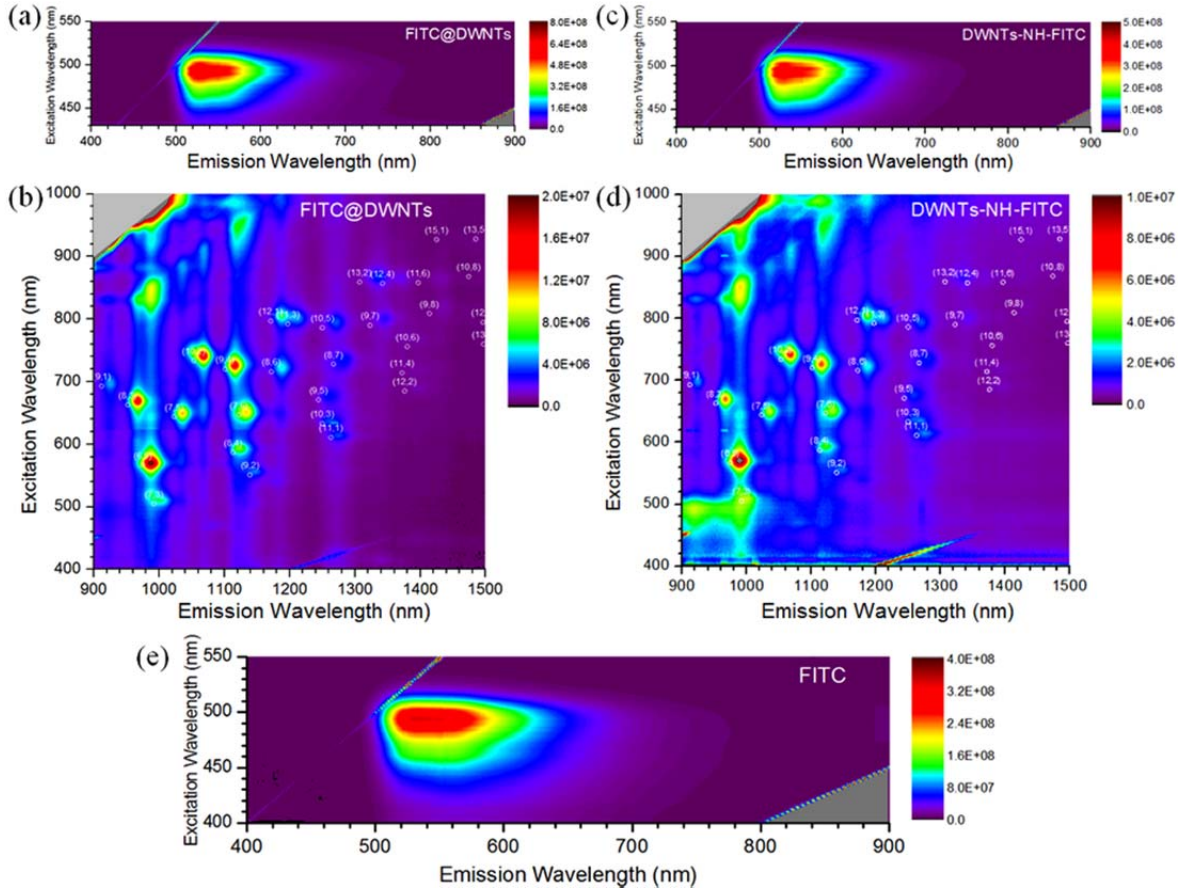

Figure 5.23: *The PLE of (a, b) FITC@DWNTs and (c,d) DWNTs-NH-FITC suspension recording in the (a, c) visible and (b, d) infrared range of emission. (white dots the reference data from ref [28]). (e) The PLE of free FITC.*

Figure 5.24 compares the luminescence spectra of suspensions of free FITC molecules, free fluorescein molecules, ox-DWNTs, FITC@DWNTs, and DWNTs-NH-FITC. On Figure 5.24a, we report the luminescence of FITC molecules (in the visible range), excited at 493 nm, for all the samples. In order to compare samples with the same amount of FTIC molecules, the intensity of the PL band (at 525 nm) of each sample is normalized by the intensity of the 492 nm absorption peak of FITC molecules in the corresponding samples (Figure 5.21). The PL emission at 525 nm is always observed in the suspensions of FITC@DWNTs and DWNTs-NH-FITC. The emitted signal can be assigned to either the FITC which are grafted on the nanotubes or to residual FITC's free molecules. The luminescence spectra allow us to discuss the nature of the interaction of FTIC with the nanotube surface, (*i.e.* non-covalent or covalent (chemical bonding) interaction). The normalized intensity of the 525 nm band is found to be significantly weaker in FITC@DWNTs than in DWNTs-NH-FITC. Thus, the non-covalent functionalization seems to lead to stronger interaction between the nanotubes and the FITC's molecules than covalent interaction. This quenching can be caused by photo-induced energy transfer or charge transfer.

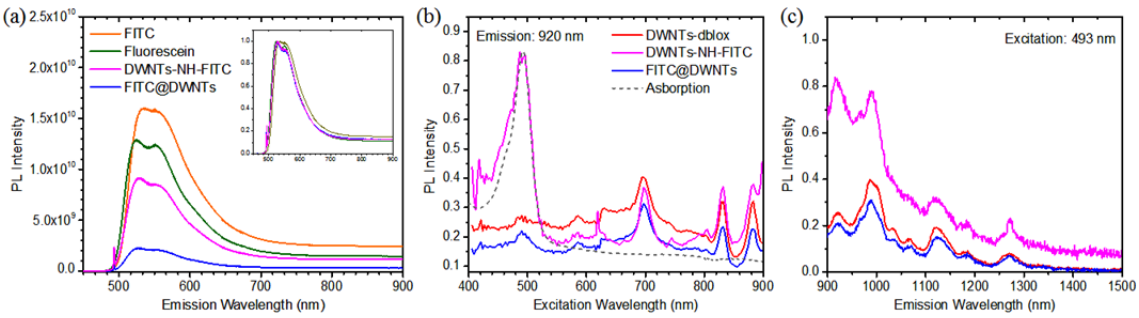

Figure 5.24: *Emission and excitation spectra measured on suspensions of FITC (orange line), fluorescein (green line), ox-DWNTs (red line), FITC@DWNTs (blue line), and DWNTs-NH-FITC (pink line): (a) The PL spectra, excited at 493 nm, is normalized by the intensity of the absorption peak of FITC at 492 nm, measured in the visible range. (b) The excitation spectrum of the PL emission at 920 nm (the dot line is the absorbance spectrum of FITC.), (c) the PL, excited at 493 nm, measured the IR range. In b and c, the spectra are normalized with the corresponding PL intensity of (8,3) nanotube of each sample.*

In order to study the luminescence of nanotubes after functionalization by FITC molecules, we discuss: (i) the excitation spectrum of the PL emission at 920 nm, (ii) the PL spectrum, in the infra-red range, exited at 493 nm (Figure 5.24b and c, respectively). The PL intensities are normalized by the PL peak of the (8,3) inner tubes excited at 670 nm because it is sufficiently far of the new emission/excitation peaks.

The excitation spectrum of the 920 nm PL emission shows a strong enhancement of this emission for an excitation around 493 nm in DWNTs-NH-FITC**.** More precisely, the PL spectrum excited at 493 nm shows two intense and well-defined features around 920 nm and 1000 nm in DWNTs-NH-FITC. Clearly, the significant enhancement of these emissions arises when the excitation matches the 493 nm absorption of FITC. These results can be understood by considering that the FITC were grafted successfully on the surface of DWNTs and that the new emission peaks observed in the visible range, for an excitation at 493 nm, signs an energy transfer from FITC to inner tubes. However, this process would imply the total quenching of the luminescence of FITC. The remaining PL of FITC molecules could be assigned to: (i) the efficiency of quenching, (ii) a selective energy transfer from FITC to specific inner tubes.

By contrast, no enhancement of the 493 nm band is observed in the excitation spectrum of the 920 nm emission in FITC@DWNTs. The excitation and emission spectra measured on FITC@DWNTs are close with the ones measured on oxidized DWNTs. In FITC@DWNTs (non-covalent functionalization), the similarity of the spectra line-shape of ox-DWNTs and FITC@DWNTs suggest that the π-stacked FITC molecules do not affect inner tubes. However, as shown previously, a strong quenching of the luminescence of FITC is observed in FITC@DWNTs. These results suggest that: (i) the energy can transfer from FITC to outer walls

which could give luminescence out of the range of our detector, (ii) charge transfer from FITC to inner tubes occur.

In summary, from Raman, absorption and PL measurements performed on suspensions of free FITC molecules, free fluorescein molecules, oxidized DWNTs, covalently (DWNTs-NH-FITC) and non-covalently (FITC@DWNTs) DWNTs, we have stated the main following points:

(i) the oxidation of pristine DWNTs causes a slight change of its chiral distribution,
(ii) the FITC molecules were successfully attached on the DWNTs,
(iii) the luminescence signal allow us to distinguish the nature of functionalization, namely covalent or non-covalent,
(iv) an energy transfer from FITC molecules to inner tubes is demonstrated in covalently functionalized DWNTs.

5.6. General conclusions

The Raman characterization and the studies of absorption and photoluminescence of covalently and non-covalently functionalized DWNTs have been performed. These investigations have permitted to state unambiguously different properties of the functionalized DWNTs. Especially, the presence of a PL signal in dispersions of individual DWNTs has been evidenced. The evolution of the PL signal, on one hand with the composition of the pristine DWNTs, and, on the other hand under the functionalization of DWNTs, suggests that PL arises from inner tubes. However, the assumption that the PL signal could be due to isolated inner tube extracted from DWNTs during the tubes dispersion process (the process leading to produce individual SWNTs) cannot be ruled out.

Other investigations are necessary to definitively solve the question of the origin of the PL signal in DWNTs. New approaches are necessary for that and some of them are discussed in the next paragraph.

5.7. Perspectives and preliminary results

One reminds that one of the objectives of this work was to contribute to the debate concerning the origin of the fluorescence in DWNTs. However, the previous studies have not given a definitive answer to this question. The ideal approach would be to combine TEM and PL measurements on individual DWNTs. However, the preparation of appropriate samples has not been achieved yet. In consequence, we propose different approaches to close this debate and we report preliminary results of these approaches.

5.5.1. PL mapping of individual DWNTs

First, we propose to investigate individual and isolated DWNTs. The procedure is summarized below:

(i) A low-density DWNTs solution is prepared, (ii) micrometric gold markers, with 100 µm spacing, are fabricated by photolithography on a glass substrate, these markers are used to locate nanotubes for PL mapping and Raman measurements, (iii) One drop of solution is spin-coated on the substrate, (iv) The PL mapping of sample is performed and the markers are used to identify the spatial coordinate of each nanotube which emits PL, (v) the structure of each emitted DWNT is obtained by Raman experiment performed at the same spatial positions as the PL measurement.

Concerning the PL experiments, preliminary results have been obtained. The yellow (561 nm) laser line was used as excitation source. The Si detector was used to record the emission signal. PL XY maps are measured at this laser wavelength on a large area. By this way, we can observe PL signal of particular individual nanotubes.

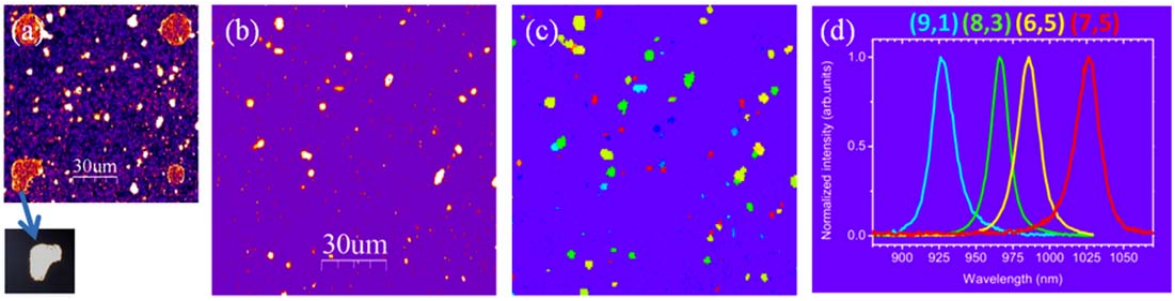

Figure 5.25: *(a) The luminescence of nanotubes and markers deposited on SiO_2 substrate (picture below is optical image; (b) the PL of individual nanotubes; (c) PL wavelength@λ_{max} of DWNT; (d) Typical PL spectra for individual DWNTs deposited on a SiO_2 substrate.*

Figure 5.25a presents the PL, excited at 2.21 eV (561 nm), of individual DWNTs deposited on glass and the background signal of the markers. Figure 5.25b presents the PL of nanotubes only. On the Figure 5.25c, the wavelength of the maximum PL intensity was color coded. For

example, blue dots correspond to nanotube (9,1). We focus our analysis on the response of specific nanotubes, namely: (9,1), (8,3), (6,5) and (7,5). These tubes are not luminescent in ref [147]. In our PL measurements, we observed the strong PL signal for these four tubes.

In a future step, thanks to the knowledge of the precise locations of individual tubes on glass, the measurements of the RBLM part of the Raman spectra will be performed at the same positions. By this way, we could be able to confirm that the PL signal occurs from inner tubes of DWNTs. This work is in progress.

5.5.2. In-situ functionalization DWNTs via diazonium

As discussed in the section 5.4, the covalent functionalization by diazonium of DWNTs powders, prior to the dispersions of the individual functionalized DWNTS wrapped by surfactant in D_2O, does not allow us to conclude about the origin of luminescence in DWNTs. The PL signals of tubes of diameter < 1 nm can be assigned to the emission of the inner tubes of DWNTs or to the extracted inner tubes during the protocol of dispersion (mainly during the sonication and centrifugation steps).

First, we propose a method based on the *"in situ"* covalent functionalization with aryl diazonimum salts of aqueous suspensions of dispersed DWNTs wrapped by surfactant. This approach leads to the attachment of molecules on the surface of dispersed DWNTs and SWNTs extracted from DWNTs during the dispersion protocol. By this way, the remaining PL signal, if it exists, is expected to only occur from inner tubes.

For the *in situ* functionalization of SWNTs and DWNTs, we use aryl diazonimum salts such as 4-bromobenzenediazonium tetrafluoroborate (Br-BDTFB) and 4-nitrobenzenediazonium tetrafluoroborate (NO_2-BDTFB). We followed the protocol of carbon nanotubes functionalization described in ref [159]. In the following, we present preliminary absorption measurements on *in situ* covalently functionalized SWNTs and DWNTs wrapped by different surfactants.

-DOC as surfactant

We performed absorption experiments on *in situ* functionalized (by Br-BDTFB and NO_2-BDTFB) SWNTs wrapped by DOC in D_2O. The absorption spectra of pristine and functionalized SWNTs are shown on Figure 5.26a, b. We observe the decreasing of some absorption peaks with the increase of the reaction time. However, the presence of relatively intense and well-resolved peaks at large exposition time is the signature that SWNTs are not efficiently functionalized, a possible reason for that being that the DOC form a tightly packed structure around the SWNTs [160]. The reaction rate of suspended SWNTs functionalized by NO_2-BDTFB is slightly faster than that of suspended SWNTs functionalized by Br-BDTFB. These results agree with the

previous report [159] and show that DOC is not good as surfactant to perform *in situ* functionalization with diazonium salts.

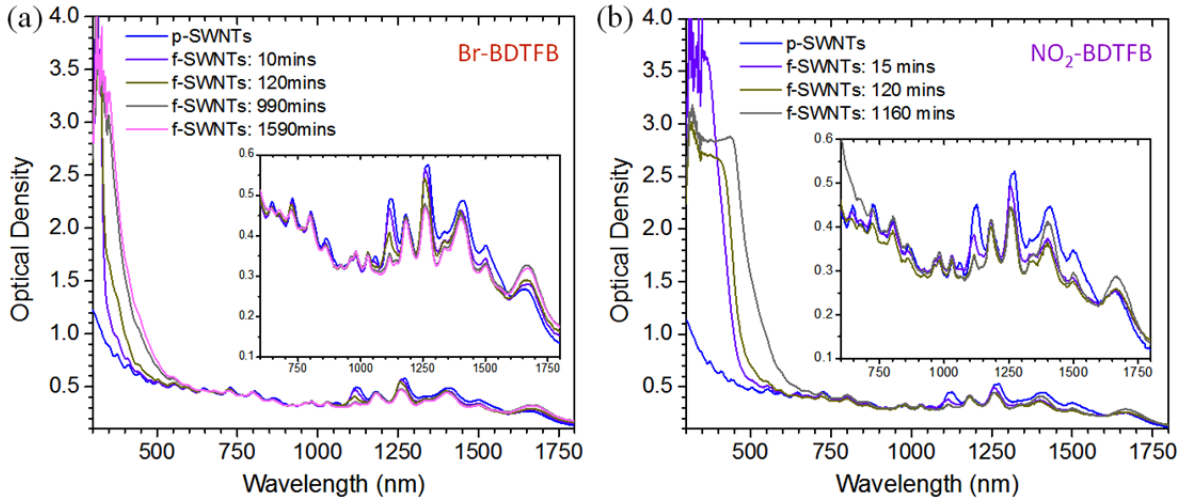

Figure 5.26: *The UV-Vis-NIR spectra recorded during the reaction between 2mM of Br-/NO_2-BDTFB and SWNTs dispersed in 1wt% DOC in D_2O. The molar ratio between nanotubes and molecules is 1:1.*

-SDS as surfactant

In order to have a faster reaction, we chose SDS as surfactant. Indeed, SDS has short alkyl chains and charged polar head groups [161]. Consequently, SDS molecules are expected to assemble as disordered layers around the nanotube surface. The dependence of the absorption spectra of aqueous (D_2O) dispersions of S/DWNTs wrapped by SDS on the time of exposure to NO_2-BDTFB is shown on Figure 5.27. The absorbance features of dispersions of pristine SWNTs wrapped by SDS are well resolved. The strong decrease of these absorption features after 15 minutes of exposure is a clear signature of the efficiency of the functionalization.

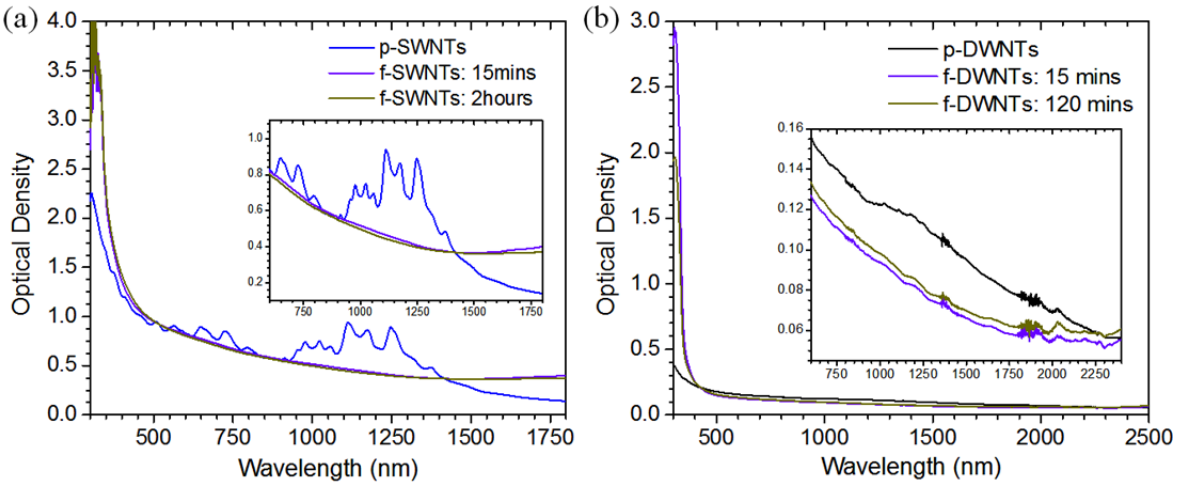

Figure 5.27: *The UV-Vis-NIR spectra recorded during the reaction (a) between 2mM NO_2-BDTFB and SWNTs dispersed in 1wt in SDS; (b) between 2mM NO_2-BDTFB and DWNTs dispersed in 1wt% in SDS. The molar ratio between nanotubes and molecules is 1:1.*

On the other hand, the absorbance spectra of pristine and functionalized DWNTs do not display well resolved peaks. These results show that SDS is not good as surfactant to disperse DWNTs.

-SCMC as surfactant

In order to optimize the dispersion of DWNTs and their functionalization, we choose SCMC (sodium carboxymethylcellulose) as surfactant to disperse S/DWNTs in D_2O. The polymeric SCMC may either wrap the nanotube helically or adsorb randomly along the sidewall [159, 162]. The dependence on the NO_2-BDTFB exposition time of the optical absorption of dispersions of SWNTs and DWNTs, wrapped by SCMC, is shown on Figure 5.28.

Clearly, both the absorbance features of pristine SWNTs (p-SWNT) and DWNTs (p-DWNTs) are well resolved.

We observed the decrease of the absorbance features of functionalized SWNTs (f-SWNTs) with the reaction time. After 10 minutes, some features show a small intensity and all the features vanish after a reaction time of 120 minutes.

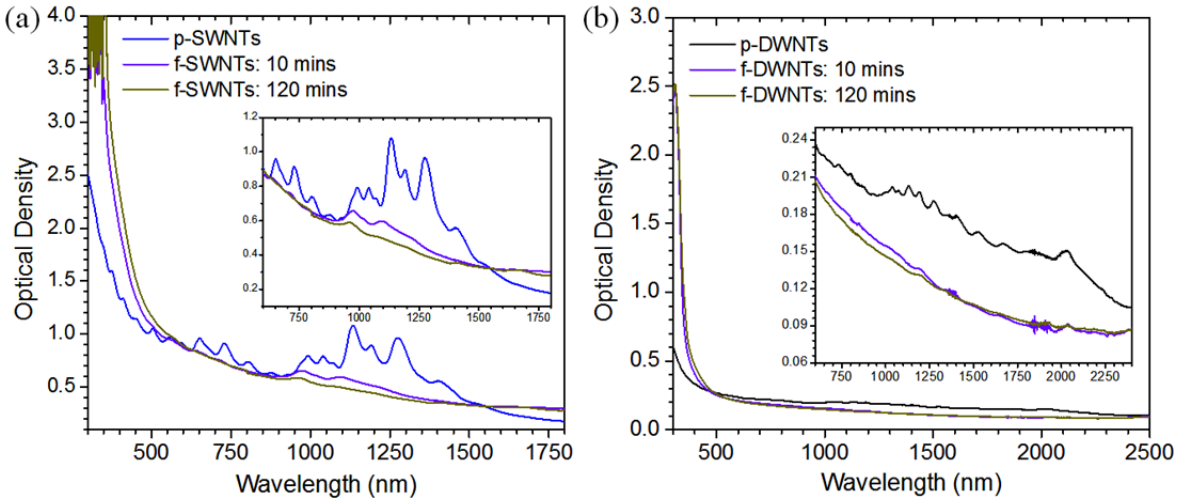

Figure 5.28: *The UV-Vis-NIR spectra recorded during the reaction (a) between 2mM NO_2-BDTFB and SWNTs dispersed in 1wt% in SCMC; (b) between 2mM NO_2-BDTFB and DWNTs dispersed in 1wt% in SCMC. The molar ratio between nanotubes and molecules is 1:1.*

By contrast, no absorbance peaks are observed in functionalized DWNTs. The visual inspection of the dispersions during the chemical reaction shows the presence of clusters in the suspensions, suggesting a fast re-aggregation of the nanotubes during the reaction. It is then still not possible to conclude. In the future, we propose to conduct such *in situ* functionalization experiments on thin films of DWNTs, deposited on glass which could allow both optical absorption and PL characterization.

CHAPTER 6 : CONCLUSIONS AND PERSPECTIVES

The first part of this manuscript was related to the understanding of some intrinsic properties of individual free-standing single-walled and double-walled carbon nanotubes. New information was obtained by coupling Raman spectroscopy data, including the measure of the excitation profiles of different modes, with optical absorption and electronic diffraction data. From a general point of view, we put in evidence the complementarity of the Raman spectroscopy and electronic diffraction for "the most likely" assignment of the structure of the nanotubes.

Among the results obtained on individual single-walled carbon nanotubes (SWNTs), one can underline: (i) the agreement between the experimental absorption energies measured in index-identified SWNTs with the calculated transition energies reported by V. N. Popov and F. Wang' group. (ii) the confirmation of the excitonic character of the optical transitions by combining optical absorption and Raman excitation profiles on the same nanotubes, and (iii) the evidence of an unexpected behavior of the relative intensity of the LO and TO components of the G-modes.

The study of the index-identified individual double-walled carbon nanotubes has permitted to understand the role of the inter-walls distance in the frequency shifts of the radial breathing-like modes (RBLM) and G-mode, by associating a given inter-walls distance to a negative (positive) pressure when this distance is larger (smaller) than 0.34 nm. On the other hand, the role of the effects of quantum interferences in the evolution with the excitation energy of the intensities of the LO and TO components of the G-modes of the inner and outer tubes was clearly identified. Finally, the assignment of the origin of the optical transitions of index-identified DWNTs, measured by absorption spectroscopy, was proposed.

The future studies on individual index-identified SWNTs and DWNTs will have as objectives to solve several open questions.

Concerning SWNTs, these objectives are: (i) the development of more elaborated models in order to reproduce quantitatively the Raman excitation profiles of Raman modes, especially in order to precise the effects of quantum interferences on the intensity of the Raman-active modes, (ii) the understanding of the origin of the unexpected behavior of LO and TO components of the G-modes.

Concerning DWNTs, these objectives are: (i) the acquisition of additional data of index-identified DWNTs in order to confirm some conclusions of the present work. In this framework, it seems important to studies DWNTs which contain metallic inner or/and outer tubes. (ii) to

precise the role of the inter-tube coupling on the energies of the optical transition, in particular, in order to assign the origin of the additional optical transitions (in the sense that they cannot be assigned as originating from inner or outer tubes), which appear in some DWNTs. (ii) to develop model in order to understand the resonance excitation profile of the RBLMs. Obviously, these models will have to take explicitly into account the inter-tube coupling and the interference effects.

From a general point of view, for both SWNTs as DWNTs, the development of close interactions with theoreticians is the way to achieve a complete understanding of our experimental results.

The second part of this work reports experimental investigations of the properties of covalently and non-covalently functionalized double-walled carbon nanotubes.

The study of the properties of functionalized DWNTs was performed by combining Raman spectroscopy, UV-visible-NIR absorption and photoluminescence (PL), including maps of photoluminescence excitation (PLE), on suspensions of DWNTs before and after functionalization: (i) covalently by using diazonium, (ii) covalently and non-covalently (π stacking) by using dye molecules.

The general objective of this work can be view as a contribution to the debate on an essential question for the use of the DWNTs in opto-electronic devices, namely: “Do the DWNTs luminesce? And if yes, what is the origin of the luminescence?". The presence of photoluminescence in our samples of DWNTs was established, and the study of its evolution with various kinds and degrees of functionalization states that PL can only result from internal tubes (intrinsic PL of DWNTs), or from SWNTs generated by the extrusion of the internal tubes of DWNTs during the preparation of the suspensions. On the other hand, one must emphasize the evidence of an energy transfer from the dye molecules towards the internal tube when the molecules covalently grafted on the external tube.

The future studies will have as main objectives; (i) to solve definitively the question of the existence or not of PL in DWNTs and of its origin. (ii) to precise the conditions to obtain an energy transfer from molecules, covalently attached to the outer tubes, towards the inner tubes. Two ways are proposed to solve these questions: (i) Combining PL and Raman mapping on individual and isolated DWNTs. (ii) to perform *in situ* covalent functionalization of aqueous suspensions of DWNTs wrapped by surfactants. This approach leading to the attachment of molecules on the surface of dispersed DWNTs and SWNTs extracted from DWNTs during the dispersion protocol, the remaining PL signal, if it exists, can only arise from inner tubes.

ANNEX: PROCEDURES AND EXPERIMENTAL SET-UP

A.1. The individual free-standing carbon nanotubes

A.1.1. About the interest of studying individual suspended (free-standing) carbon nanotubes

It is well-known that a substrate such as SiO_2/Si can strongly change the Raman spectrum of a CNT deposited on a such substrate as compared to the one measured on the same CNT suspended across a trench [95, 163-165]. A lot of authors gave experimental evidences that, with regards to suspended CNT, the Raman spectrum of supported CNTs show: (i) a blue-shift and a broadening of the resonance window (associated to shifted and broadened optical transition) [95], (ii) an upshift of the frequencies of RBM [164] and tangential modes [95], (iii) a significant quenching of the Raman signal [165] (Figure A.1a), (iv) the apparition of new modes, especially in the G-mode range [95, 163] (Figure A.1b). All these changes are due to the interaction between nanotubes and substrates.

The individual suspended CNTs have many advantages to investigate the intrinsic properties of carbon nanotubes, especially because there is no van des Waals interaction between the nanotube and a substrate, no deformation of the part of the nanotube in contact with the substrate, and no accidental doping via the substrate. For all these reasons, a large part of my work focuses on the optical properties of individual nanotubes suspended through a wide trench (free-standing CNT in air).

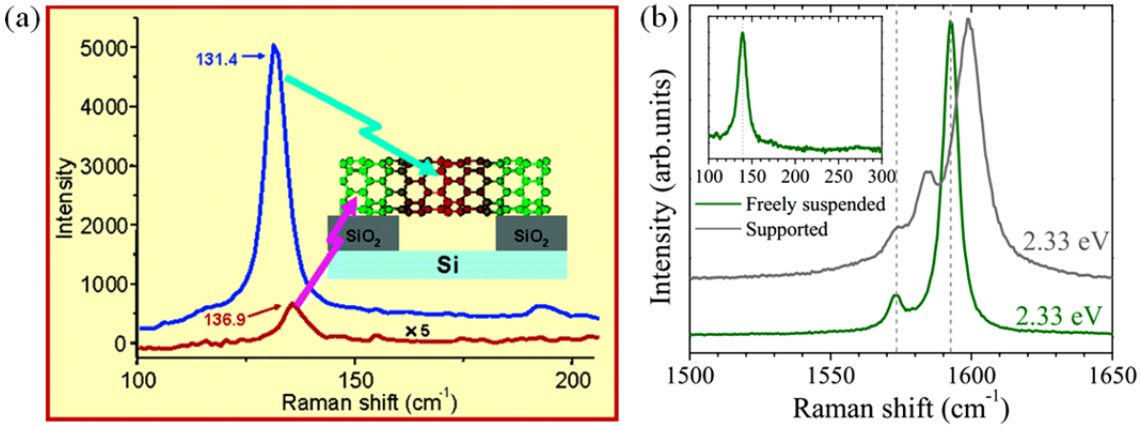

Figure A.1: *Comparison between the Raman spectra of supported and suspended (free-standing) individual SWNTs. (a) RBM [164, 165]. (b) G-modes (adapted from [95]).*

A.1.2. Synthesis of individual free-standing carbon nanotubes on silicon substrate.

Clean SiO_2/Si wafers, with <100> orientation, were used as substrates for the growth of CNTs. Before the synthesis, open-end slits were produced on the substrate by standard micro-fabrication techniques (KOH wet etching). The so-called "Kite-growth of ultra-long nanotubes" was used to prepare individual nanotubes suspended across trenches. The details of the synthesis procedure are described in ref [166, 167]. Examples of such suspended nanotubes are shown on Figure A.2

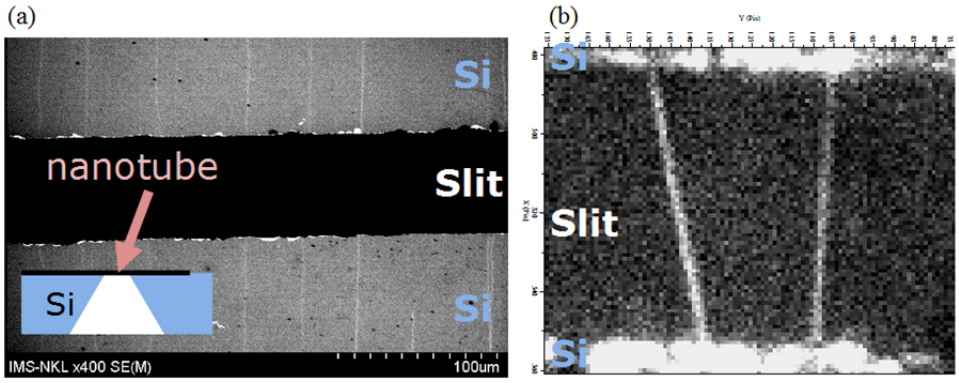

Figure A.2: *(a) Scanning electron microscopy image of ultra-long DWNTs suspended above a slit (black part), insert: side-view of the sample, (b) Raman global imaging of suspended DWNT above a 20μm wide slit.*

Using this procedure, SWNTs and DWNTs with relative large diameters (from 1.6 nm to 2.6 nm) were prepared.

We gratefully thank our coworkers for the sample fabrication.

- Dr. Xuan Tinh Than and Dr. Ngoc-Minh Phan – Laboratory of Carbon Nanomaterials, Institute of Materials Science, VAST, 100000 Hanoi, Vietnam.

A.2. The experimental set up

A.2.1. Electron diffraction

In this section, we will briefly summarize the method to identify the chiral structure of SWNTs and DWNTs by electron diffraction. The electron diffraction patterns (EDPs) have been recorded close to the edge of the SiO_2/Si substrate. The details about the analysis of EDPs are presented in ref [90, 168, 169]. In the following, we summarize the principal method to derive chiral index (n,m) of SWNTs, then further expand it for DWNTs.

- **EDP of SWNT**

This method consists of direct measurements of diameter and chiral angle from EDP pattern.

In a first step, the chiral angle θ is determined from the expression.

$$\theta = \arctan\left(\frac{1}{\sqrt{3}}\frac{d_2-d_1}{d_3}\right) = \arctan\left(\frac{1}{\sqrt{3}}\frac{2d_2-d_3}{d_3}\right) \qquad (1)$$

where d_i is the distance of i^{th} layer line from the equatorial line (see Figure A.3a). Note that calculation of the chiral angle is free from calibration of the EDPs and but is not independent of the tilt angle (inclination of the normal of the SWNT with respect the e-beam).

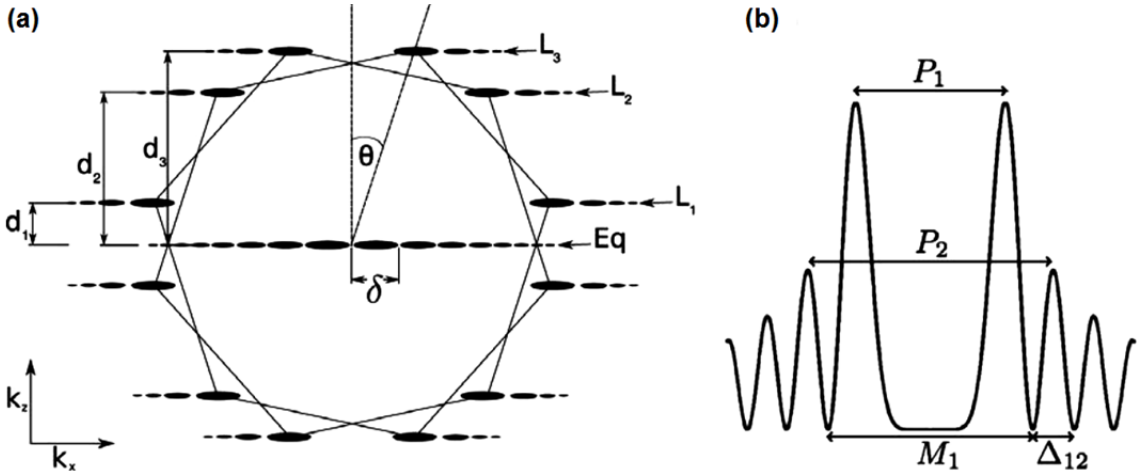

Figure A.3: *(a) A schematic depiction of the diffraction pattern obtained from a SWCNT. The hexagons mark the first order reflections from the graphene lattice. The first three layer lines are indicated (L_1–L_3) as is the equatorial oscillation (Eq) and its oscillatory pseudo period, d. The chiral angle θ is shown and the axial distances of each of the layer lines (d_1 to d_3) are marked. (b) The theoretical form of the radial intensity distribution of one of the layer lines. The separation of the first and second order peaks (P_1 and P_2) are shown as is the separation of the first order minima (M1) and the oscillatory period (Δ_{12}) [169].*

The second step consists to derive the diameter of the nanotube from the period of the equatorial oscillations, δ (in Å). For SWNT it is done by the formula:

$$D_0 = \frac{1}{\delta}. \qquad (2)$$

- **EDP of a DWNT**

Because the EDPs of a DWNT is basically the sum of the EDPs of each constituent SWNTs, the chiral angles determination is analogous to the SWNT case (see Figure A.4).

On the other hand, for a DWNT the equatorial oscillations provide information on the mean diameter $\overline{D}$ and the interlayer distance δD [170].

$$\overline{D} = \frac{1}{e}; \quad \delta D = \frac{1}{E} \qquad (3)$$

The inner (outer) diameter D_i (D_o) is then calculated from the relations:

$$\overline{D} = (D_o + D_i)/2; \; \delta D = (D_o - D_i)/2. \qquad (4)$$

It must be emphasized that the diameter calculated from eq. (2), (3) and (4) are not calibration-free.

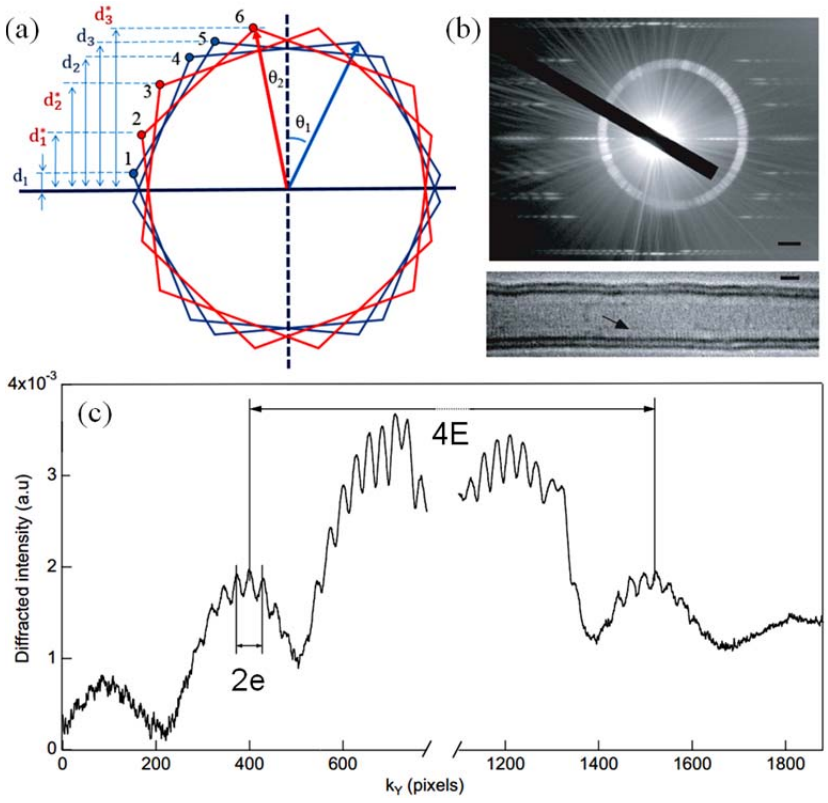

Figure A.4: *(a) The electron diffraction patterns of the double-walled nanotubes: general case of two chiral layers (adapted from ref [90]). (b) Diffraction pattern and image of a DWNT. (b) Intensity profile of the equatorial line. The central spot has been skipped for clarity (adapted from ref [171]).*

We emphasize that *a priori* we don't know which θ_i corresponds to what layer. Hence to assign definite (n,m) indices we consider two different combinations, namely:

$$(D_i@\theta_1)@(D_o@\theta_2)$$

$$(D_i@\theta_2)@(D_o@\theta_1)$$

We gratefully thank our coworker for the electron diffraction measurements:

- Dr. Raul Arenal, Laboratorio de Microscopias Avanzadas, Instituto de Nanociencia de Aragón, Universidad de Zaragoza, 50018 Zaragoza, Spain

A.2.2. The absorption spectroscopy set-up

The absorption cross-section measurements were performed by J.-C. Blancon at the "Institut Lumière Matière" of the University of Lyon [53, 95]. The absolute optical response of individual CNTs was studied by the spatial modulation spectroscopy (SMS) method. The SMS technique is based on modulating the position of a carbon nanotube placed under a tightly focused polarized light beam and detecting the induced modulation of the transmitted or reflected light energy. The experimental set-up uses a double microscope system focusing and collecting the light close to diffraction limit with two high-numerical aperture 100x objectives (Figure A.5). The incident light is polarized parallel to the nanotube axis in order to achieve maximum absorption.

The sample is fixed on a linear piezo-actuator, which permits fast spatial modulation of its position in the y direction at frequency f. An x–y positioning stage allows rastering of the sample with a sub nanometric precision. The modulated part of the transmitted, $\Delta T/T$, or reflected $\Delta R/R$ (collected by the focusing objective) light at frequency 2f is detected with a photodiode and a lock-in amplifier. In both cases, it directly provides the absolute absorption cross-section per unit length, C_{abs}, of the studied nanotube at the incident light wavelength. More details concerning SMS and R-SMS, as well as the positioning and orientation of CNTs, are available in ref. [172, 173]

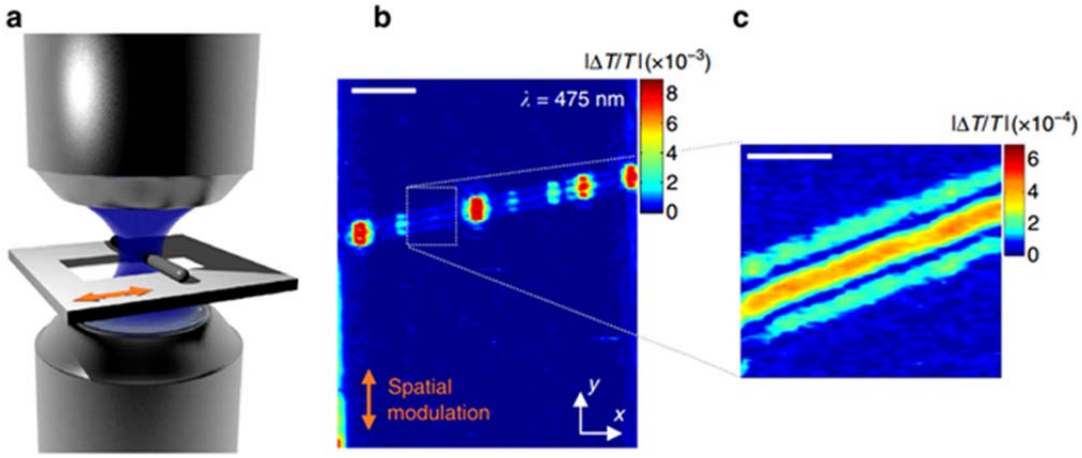

Figure A.5: *Absorption-based imaging of SWNTs. (a) Sketch of the SMS technique showing the double microscope system and the sample. The position of the sample is periodically modulated at frequency f (orange arrow) and the transmitted beam power is synchronously detected at 2f. (b) Transmission SMS image, |ΔT/T(x,y)|, of a region of the trench showing the free-standing (22,6) individual semiconducting SWNT. (c) Zoom on a clean section of this nanotube (adapted from [95]).*

We gratefully thank our coworkers for the absorption measurements:

- Dr. Jean-Christophe Blancon, Prof. A. San Miguel, Dr. Anthony Ayari, Dr. Natalia Del Fatti & Dr. Fabrice Vallée – Institut Lumière Matière, UMR5306 Université Lyon 1-CNRS, Université de Lyon, F-69622 Villeurbanne, France.

A.2.3. Raman spectroscopy set-up

In this section, I will describe the home-made micro-Raman system developed in our group at the Laboratoire Charles Coulomb of the University of Montpellier. Our micro-Raman spectroscopy set-up (Figure A.6) contains the following elements:

- Monochromatic light sources. Different lasers from visible to infrared, are available including single or multi-lines lasers as well as tunable lasers, dye laser containing Rhodamine 6G or DCM and Ti:sapphire laser pumped with Nd:YAG laser. The detail of the characteristic of each laser is listed in Table A.1.
- A home-made microscope. For Raman measurement on suspended CNTs, the scattered light is collected through a 100x objective using a backscattering geometry. Depending on the wavelength range investigated (visible or infrared), the type of 100x objective is selected in order to have the strongest intensity of the Raman signal (Table A.1).
- A piezo-actuator working in three directions xyz.

- A dispersive system (the spectrometer). It is a single monochromator (iHR 550 Horiba Jobin Yvon). Three diffraction gratings, namely: 1800 grooves/mm (blaze 400 nm), 1200 grooves/mm (blaze 750 nm), and 300 grooves/mm (blaze 1 μm) are available. The response of diffraction gratings depends on the polarization of the light with respect to the orientation (horizontal or vertical) of the grooves. The response of the gratings changes with the wavelength of the photons.
- The detector collects the dispersed photons. We use a detector, namely 2D charge-coupled device (CCD) (for Raman only Si CCD is used) and 1D InGaAs. The detectors are cooled (liquid-nitrogen) down at -133°C (-110°C) in order to reduce the noise of the detector.

Type of source	Wavelength (nm)	Type 100x objective
Laser diode	457, 561, 660.	Olympus MPFLN 100x/N.A= 0.9
Ar^+	466, 476, 488, 496, 514	Olympus MPFLN 100x/N.A= 0.9
Kr^+	647	Olympus MPFLN 100x/N.A= 0.9
Millenia (Nd-YAG)	532	Olympus MPFLN 100x/N.A= 0.9
Rhodamine 6G Dye laser	570-620	Olympus MPFLN 100x/N.A= 0.9
He:Ne laser	633	Olympus MPFLN 100x/N.A= 0.9
DCM Dye laser	620-670	Olympus MPlan 100xIR/N.A = 0.95
Titanium-sapphire	670-990	Olympus MPlan 100xIR/N.A = 0.95

Table A.1: *Classification of the excitation energies sources.*

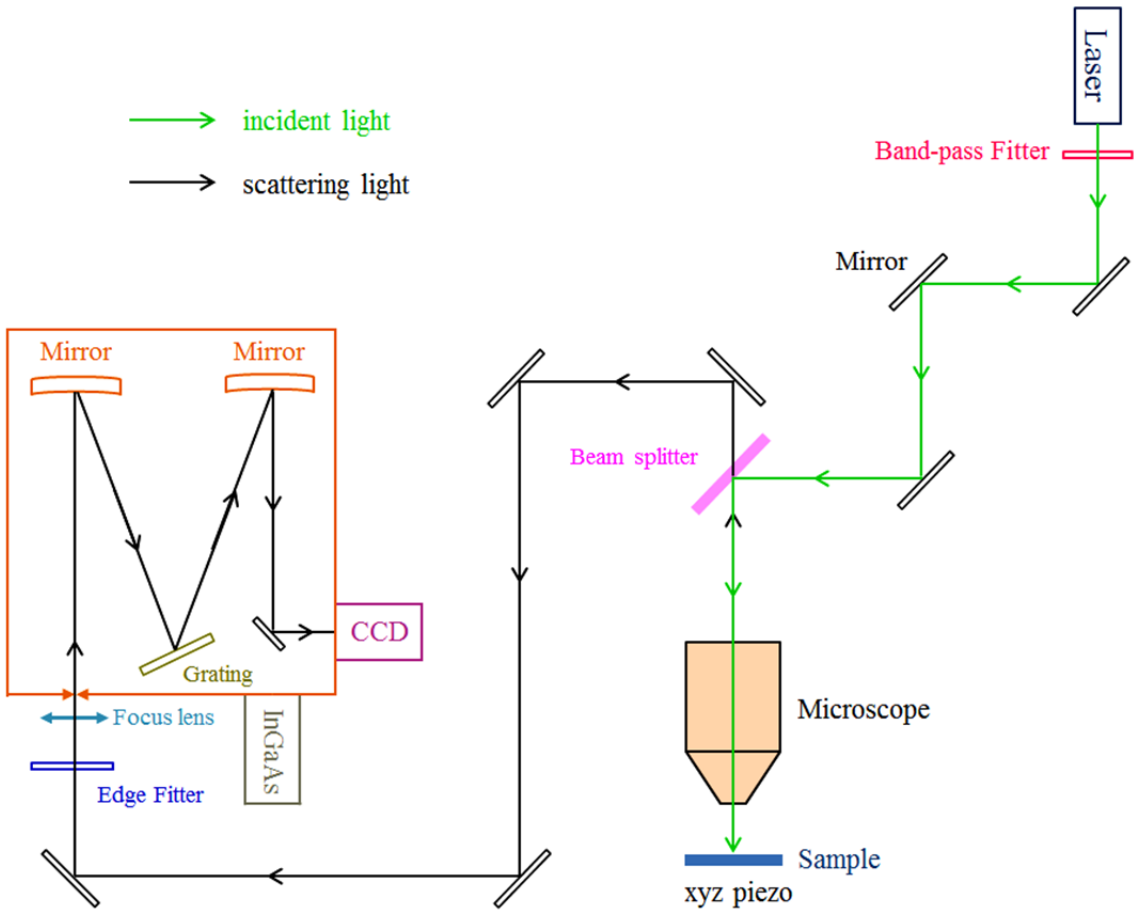

Figure A.6: *The experimental Raman system set-up.*

- **Procedures used in our Raman measurement**

-The incident power, directly measured at the exit of the laser, was kept below 2 mW. It must be emphasized that, in this condition, the power impinging the nanotube is less than 0.2 mW. Such incident power avoids the heating of the nanotube which could cause a shift of the Raman modes and energy transitions.

-The sample is fixed on a piezo-actuator. The sample is oriented in order to have the incident polarization along the nanotube axis under investigation. Its position can be adjusted with a high precision along the x, y, and z (focusing) directions in order to locate and focus the laser spot on a suspended nanotube. In practice, we always adjust the positioning in order to maximize the recorded Raman signal.

-A long-pass edge filter is placed in front of the monochromator to remove elastically scattered light. This filter transmits only wavelengths greater than its cut-off wavelength.

A.3. Calibration of the instrument

To measure the frequency and intensity of each Raman mode with a high precision, and especially to determine resonance excitation profiles, the Raman set-up needs to be calibrated [174-177].

Calibration consists to correct the raw data with regards to the set-up response in order to evaluate the intrinsic Raman response.

There are two key parameters that have to be calibrated in the dispersive Raman spectrometer: frequency calibration (X-axis) and intensity calibration (Y-axis). The frequency calibration refers to making sure that all pixels correspond to the wavenumbers they should refer to. The intensity calibration is a procedure which relates to the spectrometer response of the Raman scattering intensity.

A.3.1. Frequency calibration

Wavelength standards or Raman shift standards can be used to calibrate the frequency of the spectrometer.

-Wavelength standards such as the emission lines of calibration lamps are used to perform the wavelength calibration of our spectrometer.

-The peak at 520.7 cm^{-1} of silicon or the G-band of HOPG (1582 cm^{-1}) is also used as Raman shift standard in order to calibrate the Raman wavenumber shift (cm^{-1}). Especially, this Raman shift standard is used when the incident laser wavelength is not known with a sufficient accuracy (for dye laser for instance).

A.3.2. Intensity calibration

A spectrometer is not equally sensitive in all regions of the electromagnetic spectrum. Additionally, the transmission/reflection of all the optical elements, (including filters, lens, mirrors and gratings), along the incident and scattered light paths may selectively depend on the light wavelength. Therefore, we measured the response of spectrometer, including the transmission/reflection of the different optical elements, and the detector response.

Below, we report a method to measure the response curve of our set-up as function of wavelength by recording the spectrum of a calibrated white light spectrum. The calibrated curve is used to correct Raman intensities of RBM, G-modes by comparison with the reference Si sample. Especially, these corrections are very important to obtain the corrected REPs as presented in the manuscript from the experimental one.

- **Intensity calibration using white light**

The intensity calibration engine is a USB-powered, multi-LED light source with emission from 400 to 1100 nm. Each highly stable source is individually calibrated against a standard and the spectrum is recorded in the device's firmware[2]. The white light spectrum of this lamp was provided by supplier (called **Calibrated Signal**). To measure the spectrometer response, the lamp is placed in front of spectrometer as shown in Figure A.7.

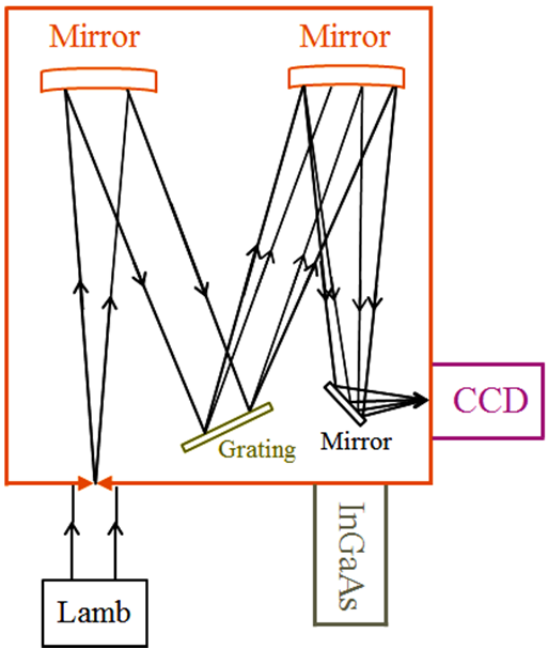

Figure A.7: *The experimental set-up for the calibration of the response of the spectrometer by using a calibrated white light source.*

- ***Polarization for intensity correction.***

In the CNTs, the polarization of light needs to be considered because the optical transitions are only allowed when the polarization of light is parallel to the nanotubes axis. For this reason, in order to define the correction factors, the white light spectra were recorded in two cases: with and without polarizer.

In our Raman setup, the diffraction grating of 1200 groove/mm is used when an excitation above 615 nm is employed. Otherwise, the diffraction grating of 1800 groove/mm is used. Therefore, the WL spectra were measured in two configurations of diffraction gratings.

The procedure of calibration to obtain the response of spectrometer (S) is followed by three steps:

[2] http://www.princetoninstruments.com/Uploads/Princeton/Documents/TechNotes/PI_Automated%20wave-length %20and%20intensity%20calibration%20routines_tech_note_A0.pdf

Step 1: the WL spectrum was recorded without polarizer (I_0). This spectrum is so-called un-polarized WL.

Step 2: the WL spectra corresponding to parallel ($I_{||}$) and perpendicular ($I_{\perp}$) configurations were recorded thanks to an analyzer. These spectra are so-called parallel and perpendicular WL.

The transmission (T) of the analyzer need to be taken account to correct the intensity of WL (Figure A.8a and Figure A.9a). It is calculated by expression:

$$T = (I_{||} + I_{\perp})/I_0$$

The parallel and perpendicular WL spectra corrected with the transmission (T) of analyzer are shown in Figure A.8b and Figure A.9b.

Step 3: normalization of the corrected WL spectra with the commercial calibrated WL spectrum to obtain the experimental spectrometer response.

We notice that the intensity of the measured WL spectra has a unit of counts per second (*i.e.* photon/s). On the other hand, the intensity of a commercial calibrated WL spectrum has a unit of "Relative Irradiance" (*i.e.* watts/cm^2). The conversion factor is shown by expression [177]:

$$I(photon\ s^{-1}\ cm^{-2}\ nm^{-1}) = \frac{\lambda}{hc} I(watts\ cm^{-2}\ nm^{-1})$$

Where: h is the Planck's constant, c is speed of light, λ is wavelength in nm.

The commercial calibrated WL spectrum is converted in counts/s by multiplying it by λ (black lines in Figure A.8b and Figure A.9b).

The experimental spectrometer response (S) is calculated by using expression (Figure A.8c and Figure A.9c):

$$S = \frac{\text{The measured WL spectra}}{T \times \text{the commercial calibrated WL spectrum} \times \lambda}$$

The incoming laser is polarized in parallel with CNTs axis. In addition, the A (A_{1g}) symmetry modes (RBM and G-modes) must be observed when both the incident and scattered light are polarized parallel to each other (VV configuration). For these reasons, only the red lines in Figure A.8c and Figure A.9c were used for the correction of Raman intensity.

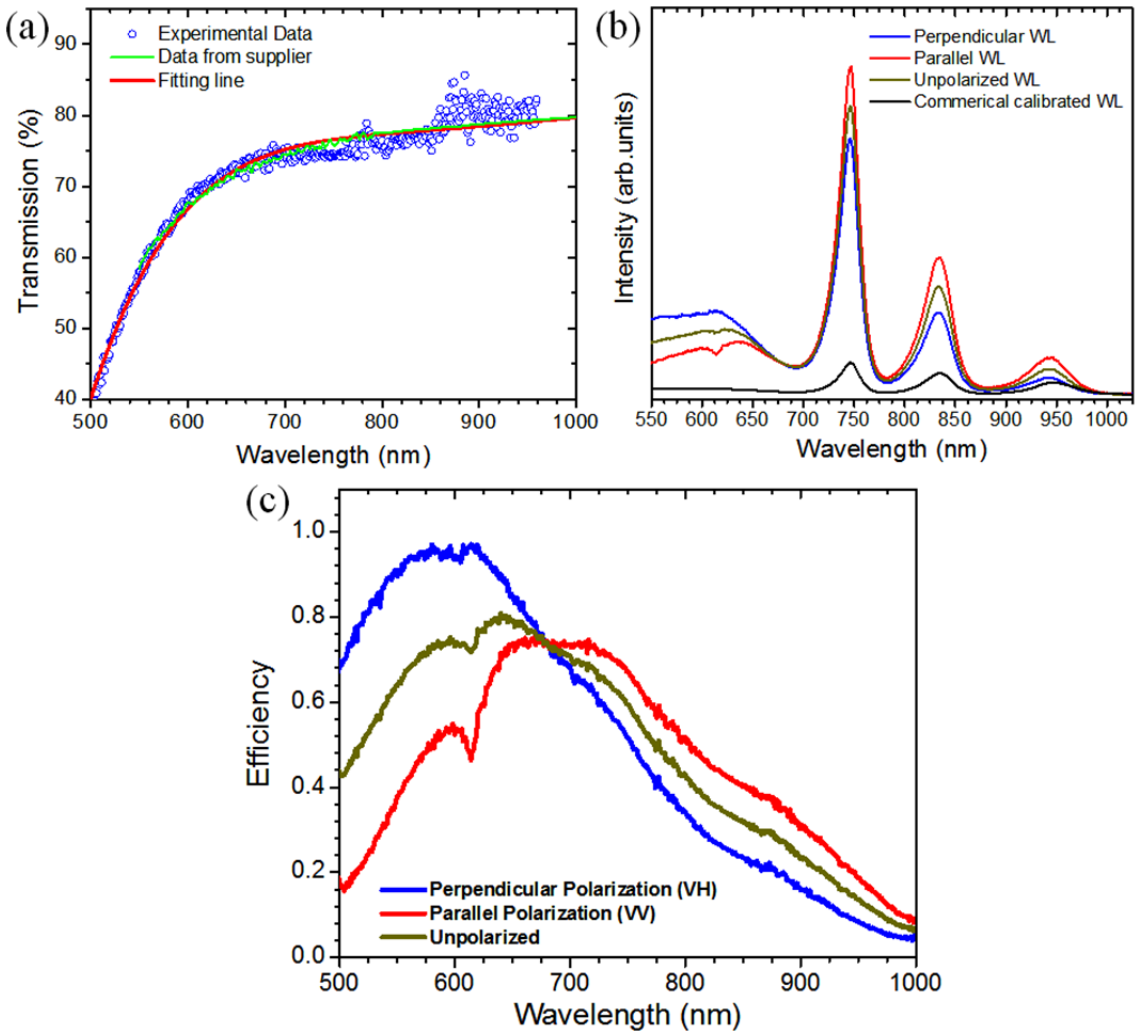

Figure A.8: *The white light (WL) measurement with diffraction grating of 1200 groove/mm (a) T Transmission of polarizer (T), (b) the measured WL spectra corrected by T at three configurations and the commercial calibrated WL spectrum after correction with wavelength, (c) response of spectrometer (S).*

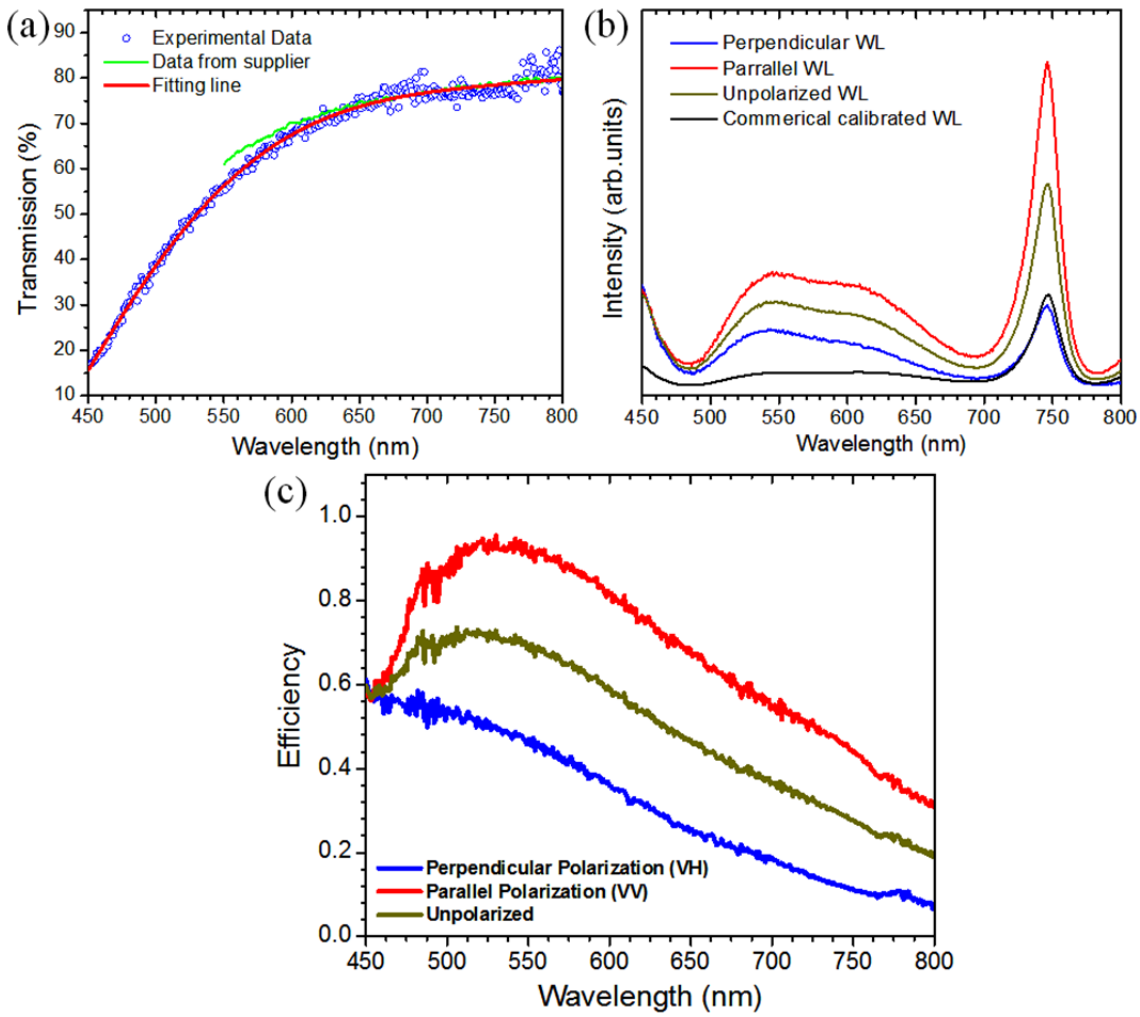

Figure A.9: *The white light (WL) measurement with diffraction grating of 1800 groove/mm (a) Transmission of polarizer (T), (b) the measured WL spectra corrected by T at three configurations and the commercial calibrated WL spectrum after correction with wavelength, (c) response of spectrometer (S).*

- **The procedure for normalization the relative intensity**

For normalization, the frequencies in cm^{-1} of phonon modes (including Si, RBM and G-modes) need to be converted to nm by using expression:

$$\lambda_{phonon\ modes}\ (\mathrm{nm}) = \frac{10^7}{\frac{10^7}{\lambda_{\mathrm{laser}}(\mathrm{nm})} - \lambda_{phonon\ modes}(\mathrm{cm^{-1}})}$$

The wavelength in nm of phonon modes is reported on the red lines in Figure A.8c and Figure A.9c to get the efficiency of response of spectrometer (S).

The relative intensity (A) of the features of RBM and G-modes in S/DWNTs is normalized with the relative intensity of silicon (reference) peak at each laser wavelength and corrected with the values of corresponding S. The normalized relative intensity is calculated by expression:

$$\text{Normalized relative intensity} = \frac{A_{\text{RBM (G-modes)}}}{A_{\text{Si}}} \times \frac{S_{\text{Si}}}{S_{\text{RBM (G-modes)}}}$$

An example of the raw and corrected data of REPs of (23,7) SWNT are displayed in Figure A.10. Although the so-corrected REPs are still altered by the Si substrate response, other attempts using CaF_2 for example were found to give aberrant results. Additional works are still in progress in order to perform the correction of the REP related to the Si substrate response. Such correction could slightly change the REPs line-shape especially when a broad wavelength range is considered, it should however not change the conclusions drawn in the manuscript.

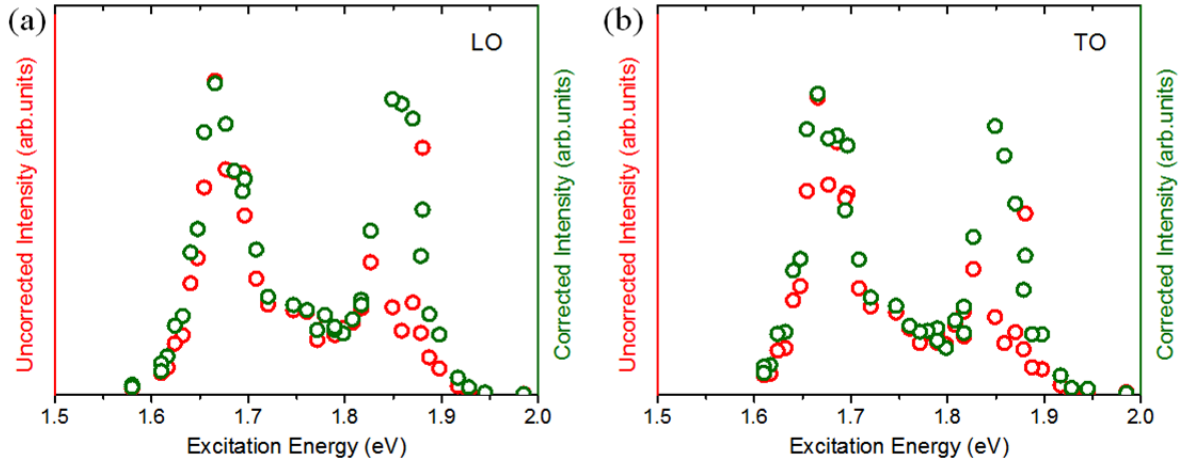

Figure A.10: *The REPs of (23,7) SWNT. (a) Uncorrected (red dots) and corrected (green dots) LO G-modes intensity as a function of excitation energy. (b) Uncorrected (red dots) and corrected (green dots) TO G-modes intensity as a function of excitation energy.*

Bibliography

1. Sazonova, V., et al., *A tunable carbon nanotube electromechanical oscillator.* Nature, 2004. **431**(7006): p. 284-287.
2. Treacy, M.M.J., T.W. Ebbesen, and J.M. Gibson, *Exceptionally high Young's modulus observed for individual carbon nanotubes.* Nature, 1996. **381**(6584): p. 678-680.
3. Wu, Y., et al., *Determination of the Young's Modulus of Structurally Defined Carbon Nanotubes.* Nano Letters, 2008. **8**(12): p. 4158-4161.
4. Ando, T., *The electronic properties of graphene and carbon nanotubes.* NPG Asia Mater, 2009. **1**: p. 17-21.
5. Avouris, P., Z. Chen, and V. Perebeinos, *Carbon-based electronics.* Nat Nano, 2007. **2**(10): p. 605-615.
6. Sun, D.-M., et al., *Mouldable all-carbon integrated circuits.* Nat Commun, 2013. **4**.
7. Avouris, P., M. Freitag, and V. Perebeinos, *Carbon-nanotube photonics and optoelectronics.* Nat Photon, 2008. **2**(6): p. 341-350.
8. Iijima, S., *Helical microtubules of graphitic carbon.* Nature, 1991. **354**(6348): p. 56-58.
9. Luis E. F. Foa Torres, S.R., Jean-Christophe Charlier., *Introduction to Graphene-Based Nanomaterials: From Electronic Structure to Quantum Transport*. 2014: Cambridge Unniversity Press. 421 pages.
10. Castro, L.d.C.e., *Modeling of Carbon Nanotube Field-Effect Transistors*. July 2006.
11. PAILLET, M., *Synthese et Proprietes Physiques de Nanotubes de Carbone Monofeuillets Individuels*. Mars 9, 2005.
12. Thomsen, C. and S. Reich, *Raman Scattering in Carbon Nanotubes*, in *Light Scattering in Solid IX*, M. Cardona and R. Merlin, Editors. 2007, Springer Berlin Heidelberg. p. 115-234.
13. Wallace, P.R., *The Band Theory of Graphite.* Physical Review, 1947. **71**(9): p. 622-634.
14. Saito, R., G. Dresselhaus, and M.S. Dresselhaus, *Trigonal warping effect of carbon nanotubes.* Physical Review B, 2000. **61**(4): p. 2981-2990.
15. Joselevich, E., *Electronic Structure and Chemical Reactivity of Carbon Nanotubes: A Chemist's View.* ChemPhysChem, 2004. **5**(5): p. 619-624.
16. Ali Javeey, J.K., *Carbon Nanotube Electronics Integrated Circuits and Systems*. Series on Integrated Circuits and Systems, ed. A. Chandrakasan. 2014: Springer. 262 pages.
17. Niyogi, S., et al., *Chemistry of Single-Walled Carbon Nanotubes.* Accounts of Chemical Research, 2002. **35**(12): p. 1105-1113.
18. Jeno, K., et al., *The geometry and the radial breathing mode of carbon nanotubes: beyond the ideal behaviour.* New Journal of Physics, 2003. **5**(1): p. 125.
19. Li, Z., *Electronic and vibrational properties of ultrasmall single-walled carbon nanotubes*, H.K.U.o.S.a. Technology, Editor. 2004. p. 36.

20. Charlier, J.-C., X. Blase, and S. Roche, *Electronic and transport properties of nanotubes.* Reviews of Modern Physics, 2007. **79**(2): p. 677-732.

21. Lin, H., et al., *Many-body effects in electronic bandgaps of carbon nanotubes measured by scanning tunnelling spectroscopy.* Nat Mater, 2010. **9**(3): p. 235-238.

22. Odom, T.W., et al., *Atomic structure and electronic properties of single-walled carbon nanotubes.* Nature, 1998. **391**(6662): p. 62-64.

23. Wilder, J.W.G., et al., *Electronic structure of atomically resolved carbon nanotubes.* Nature, 1998. **391**(6662): p. 59-62.

24. Kim, P., et al., *Electronic Density of States of Atomically Resolved Single-Walled Carbon Nanotubes: Van Hove Singularities and End States.* Physical Review Letters, 1999. **82**(6): p. 1225-1228.

25. Vl, A.M., E.E. Muryumin, and E.A. Gaiduk, *Optical second-harmonic generation from two-dimensional hexagonal crystals with broken space inversion symmetry.* Journal of Physics: Condensed Matter, 2013. **25**(19): p. 195302.

26. Odom, T.W., et al., *Structure and Electronic Properties of Carbon Nanotubes.* The Journal of Physical Chemistry B, 2000. **104**(13): p. 2794-2809.

27. Kataura, H., et al., *Optical properties of single-wall carbon nanotubes.* Synthetic Metals, 1999. **103**(1–3): p. 2555-2558.

28. Bachilo, S.M., et al., *Structure-Assigned Optical Spectra of Single-Walled Carbon Nanotubes.* Science, 2002. **298**(5602): p. 2361-2366.

29. Valentin, N.P., *Curvature effects on the structural, electronic and optical properties of isolated single-walled carbon nanotubes within a symmetry-adapted non-orthogonal tight-binding model.* New Journal of Physics, 2004. **6**(1): p. 17.

30. Popov, V.N. and L. Henrard, *Comparative study of the optical properties of single-walled carbon nanotubes within orthogonal and nonorthogonal tight-binding models.* Physical Review B, 2004. **70**(11): p. 115407.

31. Paillet, M., et al., *Raman Active Phonons of Identified Semiconducting Single-Walled Carbon Nanotubes.* Physical Review Letters, 2006. **96**(25): p. 257401.

32. Araujo, P.T., et al., *Third and Fourth Optical Transitions in Semiconducting Carbon Nanotubes.* Physical Review Letters, 2007. **98**(6): p. 067401.

33. Liu, K., et al., *An atlas of carbon nanotube optical transitions.* Nat Nano, 2012. **7**(5): p. 325-329.

34. Ajiki, H. and T. Ando, *Aharonov-Bohm effect in carbon nanotubes.* Physica B: Condensed Matter, 1994. **201**(0): p. 349-352.

35. Islam, M.F., et al., *Direct Measurement of the Polarized Optical Absorption Cross Section of Single-Wall Carbon Nanotubes.* Physical Review Letters, 2004. **93**(3): p. 037404.

36. Kim, Y., N. Minami, and S. Kazaoui, *Highly polarized absorption and photoluminescence of stretch-aligned single-wall carbon nanotubes dispersed in gelatin films.* Applied Physics Letters, 2005. **86**(7): p. -.

37. Miyauchi, Y., *Photoluminescence studies on exciton photophysics in carbon nanotubes.* Journal of Materials Chemistry C, 2013. **1**(40): p. 6499-6521.

38. Kane, C.L. and E.J. Mele, *Electron Interactions and Scaling Relations for Optical Excitations in Carbon Nanotubes.* Physical Review Letters, 2004. **93**(19): p. 197402.

39. Malic, E., et al., *Excitonic absorption spectra of metallic single-walled carbon nanotubes.* Physical Review B, 2010. **82**(3): p. 035433.

40. Berciaud, S., et al., *Excitons and high-order optical transitions in individual carbon nanotubes: A Rayleigh scattering spectroscopy study.* Physical Review B, 2010. **81**(4): p. 041414.

41. Maultzsch, J., et al., *Exciton binding energies in carbon nanotubes from two-photon photoluminescence.* Physical Review B, 2005. **72**(24): p. 241402.

42. Wang, F., et al., *The Optical Resonances in Carbon Nanotubes Arise from Excitons.* Science, 2005. **308**(5723): p. 838-841.

43. May, P., et al., *Observation of excitonic effects in metallic single-walled carbon nanotubes.* Physical Review B, 2010. **82**(19): p. 195412.

44. Yonglei, J., Y. Guili, and D. Jinming, *Higher energy optical transitions in semiconducting carbon nanotubes.* Nanotechnology, 2009. **20**(15): p. 155708.

45. Michel, T., et al., *E33 and E44 optical transitions in semiconducting single-walled carbon nanotubes Electron diffraction and Raman experiments.* Physical Review B, 2007. **75**(15): p. 155432.

46. Sato, K., et al., *Discontinuity in the family pattern of single-wall carbon nanotubes.* Physical Review B, 2007. **76**(19): p. 195446.

47. Jiang, J., et al., *Chirality dependence of exciton effects in single-wall carbon nanotubes: Tight-binding model.* Physical Review B, 2007. **75**(3): p. 035407.

48. Ohno, Y., et al., *Chirality-dependent environmental effects in photoluminescence of single-walled carbon nanotubes.* Physical Review B, 2006. **73**(23): p. 235427.

49. Kiowski, O., et al., *Photoluminescence microscopy of carbon nanotubes grown by chemical vapor deposition: Influence of external dielectric screening on optical transition energies.* Physical Review B, 2007. **75**(7): p. 075421.

50. Walsh, A.G., et al., *Screening of Excitons in Single, Suspended Carbon Nanotubes.* Nano Letters, 2007. **7**(6): p. 1485-1488.

51. Lee, H.W., et al., *Selective dispersion of high purity semiconducting single-walled carbon nanotubes with regioregular poly(3-alkylthiophene)s.* Nat Commun, 2011. **2**: p. 541.

52. Araujo, P.T., et al., *Diameter Dependence of the Dielectric Constant for the Excitonic Transition Energy of Single-Wall Carbon Nanotubes.* Physical Review Letters, 2009. **103**(14): p. 146802.

53. Blancon, J.-C., *Optical absorption and electronic properties of individual carbon nanotubes*. 2013, Université Claude Bernard - Lyon I.

54. Saito, R., et al., *Raman spectroscopy of graphene and carbon nanotubes.* Advances in Physics, 2011. **60**(3): p. 413-550.

55. Dresselhaus, M.S. and P.C. Eklund, *Phonons in carbon nanotubes.* Advances in Physics, 2000. **49**(6): p. 705-814.

56. Liu, K., et al., *Chirality-Dependent Transport Properties of Double-Walled Nanotubes Measured in Situ on Their Field-Effect Transistors.* Journal of the American Chemical Society, 2008. **131**(1): p. 62-63.

57. Pfeiffer, R., et al., *Fine structure of the radial breathing mode of double-wall carbon nanotubes.* Physical Review B, 2005. **72**(16): p. 161404.

58. Pfeiffer, R., et al., *Tube–tube interaction in double-wall carbon nanotubes.* physica status solidi (b), 2006. **243**(13): p. 3268-3272.

59. Popov, V.N. and L. Henrard, *Breathinglike phonon modes of multiwalled carbon nanotubes.* Physical Review B, 2002. **65**(23): p. 235415.

60. Levshov, D., et al., *Experimental Evidence of a Mechanical Coupling between Layers in an Individual Double-Walled Carbon Nanotube.* Nano Letters, 2011. **11**(11): p. 4800-4804.

61. Tomio, Y., H. Suzuura, and T. Ando, *Interwall screening and excitons in double-wall carbon nanotubes.* Physical Review B, 2012. **85**(8): p. 085411.

62. Liu, K., et al., *Quantum-coupled radial-breathing oscillations in double-walled carbon nanotubes.* Nat Commun, 2013. **4**: p. 1375.

63. Rahmani, A., et al., *Raman-active modes in finite and infinite double-walled carbon nanotubes.* Physical Review B, 2005. **71**(12): p. 125402.

64. Song, W., et al., *Electronic structures of semiconducting double-walled carbon nanotubes: Important effect of interlay interaction.* Chemical Physics Letters, 2005. **414**(4–6): p. 429-433.

65. Koshino, M., P. Moon, and Y.-W. Son, *Incommensurate double-walled carbon nanotubes as one-dimensional moiré crystals.* Physical Review B, 2015. **91**(3): p. 035405.

66. KREISEL, J., *Introduction to Raman scattering*. 2012. p. 36.

67. Zhang, D., J. Yang, and Y. Li, *Spectroscopic Characterization of the Chiral Structure of Individual Single-Walled Carbon Nanotubes and the Edge Structure of Isolated Graphene Nanoribbons.* Small, 2013. **9**(8): p. 1284-1304.

68. Ado Jorio, M.S.D., Riichiro Saito, Gene Dresselhaus *Raman Spectroscopy in Graphene Related Systems*. 2014: Wiley-VCH. 368 pages.

69. Dresselhaus, M.S., et al., *Raman spectroscopy of carbon nanotubes.* Physics Reports, 2005. **409**(2): p. 47-99.

70. Saito, R., et al., *Double resonance Raman spectroscopy of single-wall carbon nanotubes.* New Journal of Physics, 2003. **5**(1): p. 157.

71. Pimenta, M.A., et al., *Studying disorder in graphite-based systems by Raman spectroscopy.* Physical Chemistry Chemical Physics, 2007. **9**(11): p. 1276-1290.

72. Fantini, C., et al., *Optical Transition Energies for Carbon Nanotubes from Resonant Raman Spectroscopy: Environment and Temperature Effects.* Physical Review Letters, 2004. **93**(14): p. 147406.

73. Jorio, A., et al., *Structural (n, m) determination of isolated singlewall carbon nanotubes by resonant Raman scattering.* Physical Review Letters, 2001. **86**(6): p. 1118-1121.

74. Meyer, J.C., et al., *Raman Modes of Index-Identified Freestanding Single-Walled Carbon Nanotubes.* Physical Review Letters, 2005. **95**(21): p. 217401.

75. Araujo, P.T., et al., *Nature of the constant factor in the relation between radial breathing mode frequency and tube diameter for single-wall carbon nanotubes.* Physical Review B, 2008. **77**(24): p. 241403.

76. Milnera, M., et al., *Periodic Resonance Excitation and Intertube Interaction from Quasicontinuous Distributed Helicities in Single-Wall Carbon Nanotubes.* Physical Review Letters, 2000. **84**(6): p. 1324-1327.

77. Telg, H., et al., *Chirality Distribution and Transition Energies of Carbon Nanotubes.* Physical Review Letters, 2004. **93**(17): p. 177401.

78. Jorio, A., et al., *Resonance Raman spectroscopy (n,m)-dependent effects in small-diameter single-wall carbon nanotubes.* Physical Review B, 2005. **71**(7): p. 075401.

79. Liu, K., et al., *Intrinsic radial breathing oscillation in suspended single-walled carbon nanotubes.* Physical Review B, 2011. **83**(11): p. 113404.

80. Telg, H., et al., *Chiral Index Dependence of the G+ and G– Raman Modes in Semiconducting Carbon Nanotubes.* ACS Nano, 2011. **6**(1): p. 904-911.

81. Dresselhaus, M.S., et al., *Raman spectroscopy on isolated single wall carbon nanotubes.* Carbon, 2002. **40**(12): p. 2043-2061.

82. Jorio, A., et al., *Characterizing carbon nanotube samples with resonance Raman scattering.* New Journal of Physics, 2003. **5**(1): p. 139.

83. Rao, A.M., et al., *Diameter-Selective Raman Scattering from Vibrational Modes in Carbon Nanotubes.* Science, 1997. **275**(5297): p. 187-191.

84. Paillet, M., et al., *Probing the structure of single-walled carbon nanotubes by resonant Raman scattering.* physica status solidi (b), 2010. **247**(11-12): p. 2762-2767.

85. Michel, T., et al., *Indexing of individual single-walled carbon nanotubes from Raman spectroscopy.* Physical Review B, 2009. **80**(24): p. 245416.

86. Park, J.S., et al., *Fermi energy dependence of the G-band resonance Raman spectra of single-wall carbon nanotubes.* Physical Review B, 2009. **80**(8): p. 081402.

87. Brown, S.D.M., et al., *Origin of the Breit-Wigner-Fano lineshape of the tangential G-band feature of metallic carbon nanotubes.* Physical Review B, 2001. **63**(15): p. 155414.

88. Fano, U., *Effects of Configuration Interaction on Intensities and Phase Shifts.* Physical Review, 1961. **124**(6): p. 1866-1878.

89. Dubay, O., G. Kresse, and H. Kuzmany, *Phonon Softening in Metallic Nanotubes by a Peierls-like Mechanism.* Physical Review Letters, 2002. **88**(23): p. 235506.

90. LEVSHOV, D., *Raman modes in index-identified individual single-walled and multi-walled carbon nanotubes*. Demcember 16, 2013.

91. Piscanec, S., et al., *Optical phonons in carbon nanotubes: Kohn anomalies, Peierls distortions, and dynamic effects.* Physical Review B, 2007. **75**(3): p. 035427.

92. Dresselhaus, M.S., et al., *Defect characterization in graphene and carbon nanotubes using Raman spectroscopy.* Philosophical Transactions of the Royal Society of London A: Mathematical, Physical and Engineering Sciences, 2010. **368**(1932): p. 5355-5377.

93. Tuinstra, F. and J.L. Koenig, *Raman Spectrum of Graphite.* The Journal of Chemical Physics, 1970. **53**(3): p. 1126-1130.

94. BLANCON, J.-C., *Optical absorption and electronic properties of individual carbon nanotubes*. October 17, 2013.

95. Blancon, J.-C., et al., *Direct measurement of the absolute absorption spectrum of individual semiconducting single-wall carbon nanotubes.* Nat Commun, 2013. **4**.

96. Li, Z.M., V.N. Popov, and Z.K. Tang, *A symmetry-adapted force-constant lattice-dynamical model for single-walled carbon nanotubes.* Solid State Communications, 2004. **130**(10): p. 657-661.

97. Park, J.S., et al., *Raman resonance window of single-wall carbon nanotubes.* Physical Review B, 2006. **74**(16): p. 165414.

98. Canonico, M., et al., *Characterization of carbon nanotubes using Raman excitation profiles.* Physical Review B, 2002. **65**(20): p. 201402.

99. Doorn, S.K., et al., *Resonant Raman excitation profiles of individually dispersed single walled carbon nanotubes in solution.* Applied Physics A, 2004. **78**(8): p. 1147-1155.

100. Hároz, E.H., et al., *Enrichment of Armchair Carbon Nanotubes via Density Gradient Ultracentrifugation: Raman Spectroscopy Evidence.* ACS Nano, 2010. **4**(4): p. 1955-1962.

101. Telg, H., et al., *First and second optical transitions in single-walled carbon nanotubes: a resonant Raman study.* physica status solidi (b), 2007. **244**(11): p. 4006-4010.

102. Doorn, S.K., et al., *Excitons and exciton-phonon coupling in metallic single-walled carbon nanotubes: Resonance Raman spectroscopy.* Physical Review B, 2008. **78**(16): p. 165408.

103. Jiang, J., et al., *Intensity of the resonance Raman excitation spectra of single-wall carbon nanotubes.* Physical Review B, 2005. **71**(20): p. 205420.

104. Duque, J.G., et al., *Revealing new electronic behaviours in the Raman spectra of chirality-enriched carbon nanotube ensembles.* physica status solidi (b), 2010. **247**(11-12): p. 2768-2773.

105. Duque, J.G., et al., *Violation of the Condon Approximation in Semiconducting Carbon Nanotubes.* ACS Nano, 2011. **5**(6): p. 5233-5241.

106. Albrecht, A.C., *On the Theory of Raman Intensities.* The Journal of Chemical Physics, 1961. **34**(5): p. 1476-1484.

107. Moura, L.G., et al., *Raman excitation profile of the G band in single-chirality carbon nanotubes.* Physical Review B, 2014. **89**(3): p. 035402.

108. Bussi, G., et al., *Quantum interferences in the Raman cross section for the radial breathing mode in metallic carbon nanotubes.* Physical Review B, 2005. **71**(4): p. 041404.

109. Popov, V.N. and P. Lambin, *Resonant Raman intensity of the totally symmetric phonons of single-walled carbon nanotubes.* Physical Review B, 2006. **73**(16): p. 165425.

110. Duque, J.G., et al., *Quantum Interference between the Third and Fourth Exciton States in Semiconducting Carbon Nanotubes Using Resonance Raman Spectroscopy.* Physical Review Letters, 2012. **108**(11): p. 117404.

111. Jiang, J., et al., *Exciton-photon, exciton-phonon matrix elements, and resonant Raman intensity of single-wall carbon nanotubes.* Physical Review B, 2007. **75**(3): p. 035405.

112. Liu, K., et al., *Van der Waals-coupled electronic states in incommensurate double-walled carbon nanotubes.* Nat Phys, 2014. **10**(10): p. 737-742.

113. Hanfland, M., H. Beister, and K. Syassen, *Graphite under pressure: Equation of state and first-order Raman modes.* Physical Review B, 1989. **39**(17): p. 12598-12603.

114. Hasdeo, E.H., et al., *Electronic Raman scattering and the Fano resonance in metallic carbon nanotubes.* Physical Review B, 2013. **88**(11): p. 115107.

115. Farhat, H., et al., *Observation of Electronic Raman Scattering in Metallic Carbon Nanotubes.* Physical Review Letters, 2011. **107**(15): p. 157401.

116. Levshov, D.I., et al., *Interlayer Dependence of G-Modes in Semiconducting Double-Walled Carbon Nanotubes.* The Journal of Physical Chemistry C, 2015.

117. Lebedkin, S., et al., *Raman study of individually dispersed single-walled carbon nanotubes under pressure.* Physical Review B, 2006. **73**(9): p. 094109.

118. Levshov, D.I., et al., *Raman Probing of Uniaxial Strain in Individual Single-Wall Carbon Nanotubes in a Composite Material.* The Journal of Physical Chemistry C, 2010. **114**(39): p. 16210-16214.

119. Thomsen, C., et al., *Raman spectroscopy on single- and multi-walled nanotubes under high pressure.* Applied Physics A, 1999. **69**(3): p. 309-312.

120. Reich, S., H. Jantoljak, and C. Thomsen, *Shear strain in carbon nanotubes under hydrostatic pressure.* Physical Review B, 2000. **61**(20): p. R13389-R13392.

121. Amer, M.S., M.M. El-Ashry, and J.F. Maguire, *Study of the hydrostatic pressure dependence of the Raman spectrum of single-walled carbon nanotubes and nanospheres.* The Journal of Chemical Physics, 2004. **121**(6): p. 2752-2757.

122. Puech, P., et al., *Light scattering of double wall carbon nanotubes under hydrostatic pressure: pressure effects on the internal and external tubes.* physica status solidi (b), 2004. **241**(14): p. 3360-3366.

123. Gadagkar, V., et al., *Collapse of double-walled carbon nanotube bundles under hydrostatic pressure.* Physical Review B, 2006. **73**(8): p. 085402.

124. Cerqueira, T.F.T., et al., *Density-functional tight-binding study of the collapse of carbon nanotubes under hydrostatic pressure.* Carbon, 2014. **69**: p. 355-360.

125. Arvanitidis, J., et al., *Pressure screening in the interior of primary shells in double-wall carbon nanotubes.* Physical Review B, 2005. **71**(12): p. 125404.

126. Yang, X., G. Wu, and J. Dong, *Structural transformations of double-walled carbon nanotube bundle under hydrostatic pressure.* Applied Physics Letters, 2006. **89**(11): p. 113101.

127. Aguiar, A.L., et al., *Pressure-Induced Collapse in Double-Walled Carbon Nanotubes: Chemical and Mechanical Screening Effects.* The Journal of Physical Chemistry C, 2011. **115**(13): p. 5378-5384.

128. Wei, L., et al., *Aggregation-Dependent Photoluminescence Sidebands in Single-Walled Carbon Nanotube.* The Journal of Physical Chemistry C, 2010. **114**(14): p. 6704-6711.

129. Villalpando-Paez, F., et al., *Wall-to-wall stress induced in (6,5) semiconducting nanotubes by encapsulation in metallic outer tubes of different diameters: A resonance Raman study of individual C60-derived double-wall carbon nanotubes.* Nanoscale, 2010. **2**(3): p. 406-411.

130. Endo, M., et al., *Nanotube Coalescence-Inducing Mode: A Novel Vibrational Mode in Carbon Systems.* Small, 2006. **2**(8-9): p. 1031-1036.

131. Pfeiffer, R., et al., *Interaction between concentric tubes in DWCNTs.* The European Physical Journal B - Condensed Matter and Complex Systems, 2004. **42**(3): p. 345-350.

132. Piao, Y., et al., *Optical and Electrical Properties of Inner Tubes in Outer Wall-Selectively Functionalized Double-Wall Carbon Nanotubes.* The Journal of Physical Chemistry Letters, 2011. **2**(13): p. 1577-1582.

133. Bouilly, D., et al., *Wall-Selective Probing of Double-Walled Carbon Nanotubes Using Covalent Functionalization.* ACS Nano, 2011. **5**(6): p. 4927-4934.

134. Huang, J., et al., *Covalently Functionalized Double-Walled Carbon Nanotubes Combine High Sensitivity and Selectivity in the Electrical Detection of Small Molecules.* Journal of the American Chemical Society, 2013. **135**(6): p. 2306-2312.

135. Bouilly, D., J. Cabana, and R. Martel, *Unaltered electrical conductance in single-walled carbon nanotubes functionalized with divalent adducts.* Applied Physics Letters, 2012. **101**(5): p. 053116.

136. Liu, J., et al., *Sidewall functionalization of single-wall carbon nanotubes (SWNTs) through aryl free radical addition.* Chemical Physics Letters, 2006. **430**(1–3): p. 93-96.

137. Goldsmith, B.R., et al., *Conductance-Controlled Point Functionalization of Single-Walled Carbon Nanotubes.* Science, 2007. **315**(5808): p. 77-81.

138. Okazaki, T., et al., *Photoluminescence quenching in peapod-derived double-walled carbon nanotubes.* Physical Review B, 2006. **74**(15): p. 153404.

139. Muramatsu, H., et al., *Bright Photoluminescence from the Inner Tubes of "Peapod"-Derived Double-Walled Carbon Nanotubes.* Small, 2009. **5**(23): p. 2678-2682.

140. Hertel, T., et al., *Spectroscopy of Single- and Double-Wall Carbon Nanotubes in Different Environments.* Nano Letters, 2005. **5**(3): p. 511-514.

141. Shimamoto, D., et al., *Strong and stable photoluminescence from the semiconducting inner tubes within double walled carbon nanotubes.* Applied Physics Letters, 2009. **94**(8): p. 083106.

142. Iakoubovskii, K., et al., *Optical Characterization of Double-Wall Carbon Nanotubes: Evidence for Inner Tube Shielding.* The Journal of Physical Chemistry C, 2008. **112**(30): p. 11194-11198.

143. Kishi, N., et al., *Enhanced Photoluminescence from Very Thin Double-Wall Carbon Nanotubes Synthesized by the Zeolite-CCVD Method.* The Journal of Physical Chemistry B, 2006. **110**(49): p. 24816-24821.

144. Hirori, H., K. Matsuda, and Y. Kanemitsu, *Exciton energy transfer between the inner and outer tubes in double-walled carbon nanotubes.* Physical Review B, 2008. **78**(11): p. 113409.

145. Tsyboulski, D.A., et al., *Do Inner Shells of Double-Walled Carbon Nanotubes Fluoresce?* Nano Letters, 2009. **9**(9): p. 3282-3289.

146. Green, A.A. and M.C. Hersam, *Properties and Application of Double-Walled Carbon Nanotubes Sorted by Outer-Wall Electronic Type.* ACS Nano, 2011. **5**(2): p. 1459-1467.

147. Yang, S., et al., *Photoluminescence from Inner Walls in Double-Walled Carbon Nanotubes: Some Do, Some Do Not.* Nano Letters, 2011. **11**(10): p. 4405-4410.

148. Flahaut, E., et al., *Gram-scale CCVD synthesis of double-walled carbon nanotubes.* Chemical Communications, 2003(12): p. 1442-1443.

149. Schmidt, G., et al., *Mechanism of the Coupling of Diazonium to Single-Walled Carbon Nanotubes and Its Consequences.* Chemistry – A European Journal, 2009. **15**(9): p. 2101-2110.

150. Cabana, J. and R. Martel, *Probing the Reversibility of Sidewall Functionalization Using Carbon Nanotube Transistors.* Journal of the American Chemical Society, 2007. **129**(8): p. 2244-2245.

151. Ellison, M.D. and P.J. Gasda, *Functionalization of Single-Walled Carbon Nanotubes with 1,4-Benzenediamine Using a Diazonium Reaction.* The Journal of Physical Chemistry C, 2008. **112**(3): p. 738-740.

152. Bahr, J.L. and J.M. Tour, *Highly Functionalized Carbon Nanotubes Using in Situ Generated Diazonium Compounds.* Chemistry of Materials, 2001. **13**(11): p. 3823-3824.

153. CHEMINET, N., *Molécules pi-conjuguées fonctionnelles : synhèse et application à l'élaboration de nanomatériaux*. 2011. p. 312.

154. Dyke, C.A. and J.M. Tour, *Unbundled and Highly Functionalized Carbon Nanotubes from Aqueous Reactions.* Nano Letters, 2003. **3**(9): p. 1215-1218.

155. Schauenstein, K., E. Schauenstein, and G. Wick, *Fluorescence properties of free and protein bound fluorescein dyes. I. Macrospectrofluorometric measurements.* Journal of Histochemistry & Cytochemistry, 1978. **26**(4): p. 277-83.

156. Tifania, B., *Nanotubes de carbone biparois : fonctionnalisation et détection in vitro*. Mars 12 2015.

157. Weisman, R.B., *Chapter 5 Optical spectroscopy of single-walled carbon nanotubes*, in *Contemporary Concepts of Condensed Matter Science*, S. Saito and A. Zettl, Editors. 2008, Elsevier. p. 109-133.

158. Strano, M.S., et al., *Electronic Structure Control of Single-Walled Carbon Nanotube Functionalization.* Science, 2003. **301**(5639): p. 1519-1522.

159. Blanch, A.J., C.E. Lenehan, and J.S. Quinton, *Dispersant Effects in the Selective Reaction of Aryl Diazonium Salts with Single-Walled Carbon Nanotubes in Aqueous Solution.* The Journal of Physical Chemistry C, 2012. **116**(2): p. 1709-1723.

160. Lin, S. and D. Blankschtein, *Role of the Bile Salt Surfactant Sodium Cholate in Enhancing the Aqueous Dispersion Stability of Single-Walled Carbon Nanotubes: A Molecular Dynamics Simulation Study.* The Journal of Physical Chemistry B, 2010. **114**(47): p. 15616-15625.

161. Calvaresi, M., M. Dallavalle, and F. Zerbetto, *Wrapping Nanotubes with Micelles, Hemimicelles, and Cylindrical Micelles.* Small, 2009. **5**(19): p. 2191-2198.

162. Ohmori, S., et al., *Fractionation of Single Wall Carbon Nanotubes by Length Using Cross Flow Filtration Method.* ACS Nano, 2010. **4**(7): p. 3606-3610.

163. Steiner, M., et al., *How does the substrate affect the Raman and excited state spectra of a carbon nanotube?* Applied Physics A, 2009. **96**(2): p. 271-282.

164. Zhang, Y., et al., *Raman Spectra Variation of Partially Suspended Individual Single-Walled Carbon Nanotubes.* The Journal of Physical Chemistry C, 2007. **111**(5): p. 1983-1987.

165. Zhang, Y., et al., *Substrate-Induced Raman Frequency Variation for Single-Walled Carbon Nanotubes.* Journal of the American Chemical Society, 2005. **127**(49): p. 17156-17157.

166. THAN, X.T., *Croissance Catalytique Et Etude De Nanotubes De Carbone Multi-Feuillets Produits En Masse Et De Nanotubes De Carbone Ultra-Long Individuels A Quelques Feuillet*. November 21, 2011.

167. Tinh, T.X., et al., *Synthesis of individual ultra-long carbon nanotubes and transfer to other substrates.* Journal of Experimental Nanoscience, 2011. **6**(5): p. 547-556.

168. Lu-Chang, Q., *Electron diffraction from carbon nanotubes.* Reports on Progress in Physics, 2006. **69**(10): p. 2761.

169. Allen, C.S., et al., *A review of methods for the accurate determination of the chiral indices of carbon nanotubes from electron diffraction patterns.* Carbon, 2011. **49**(15): p. 4961-4971.

170. Kociak, M., et al., *Linking Chiral Indices and Transport Properties of Double-Walled Carbon Nanotubes.* Physical Review Letters, 2002. **89**(15): p. 155501.

171. Kociak, M., et al., *How accurate can the determination of chiral indices of carbon nanotubes be?* Eur. Phys. J. B, 2003. **32**(4): p. 457-469.

172. Christofilos, D., et al., *Optical Imaging and Absolute Absorption Cross Section Measurement of Individual Nano-objects on Opaque Substrates: Single-Wall Carbon*

Nanotubes on Silicon. The Journal of Physical Chemistry Letters, 2012. **3**(9): p. 1176-1181.

173. Arbouet, A., et al., *Direct Measurement of the Single-Metal-Cluster Optical Absorption.* Physical Review Letters, 2004. **93**(12): p. 127401.

174. Eom, T.J., et al., *Calibration and characterization protocol for spectral-domain optical coherence tomography using fiber Bragg gratings.* Journal of Biomedical Optics, 2011. **16**(3): p. 030501-030501-3.

175. Hutsebaut, D., P. Vandenabeele, and L. Moens, *Evaluation of an accurate calibration and spectral standardization procedure for Raman spectroscopy.* Analyst, 2005. **130**(8): p. 1204-1214.

176. Fryling, M., C.J. Frank, and R.L. McCreery, *Intensity Calibration and Sensitivity Comparisons for CCD/Raman Spectrometers.* Applied Spectroscopy, 1993. **47**(12): p. 1965-1974.

177. Griffiths, P.R., *Introduction to Vibrational Spectroscopy*, in *Handbook of Vibrational Spectroscopy*. 2006, John Wiley & Sons, Ltd.